AN E.P.R. STUDY OF SOME TRANSITION METAL IMPURITIES

IN SILVER CHLORIDE AND SILVER BROMIDE


b y


F.B.I. COOK


A dissertation

submitted to the University of Warwick

for admission to the degree of

Doctor of Philosophy

This dissertation is submitted to the University of Warwick in support of my application for admission to the degree of Doctor of Philosophy. It contains an account of my own work performed at the University of Warwick during the period October 1968 to December 1971 under the general supervision of Dr. M.J.A. Smith. No part of it has been used previously in a degree thesis submitted to this or any other University. The work described in this thesis is the result of my own independent research except where specifically acknowledged in the text.



F.B.I. Cook.



November 1972.

## ACKNOWLEDGEMENTS

ABSTRACT

The electron paramagnetic resonance (E.P.R.) and photosensitivity of silver chloride and silver bromide doped with a number of transition metal ions has been investigated. The valent state, lattice position and site symmetry of the impurities are discussed in relation to the E.P.R. spectra and the chemical properties of the ions.

The E.P.R. spectra of trivalent chromium in AgCl and AgBr are analysed. The principal spectrum at 95K in both halides has orthorhombic symmetry with axes in the $<100>$ directions. Subsidiary spectra are also observed with tetragonal and orthorhombic symmetries. The possible arrangements of the two charge compensating silver ion vacancies around the trivalent ion are discussed. The principal spectrum is shown to be consistent with a centre in which the $Cr^{3+}$ ion is associated with a nearest and a next nearest cation vacancy. The lines joining the vacancies to the $Cr^{3+}$ ion are at an angle of $135^{\circ}$. Other centres are proposed to explain the subsidiary spectra.

The $Cr^{3+}$ resonances are studied at temperatures up to 500K. The broadening of the fine structure lines at high temperatures is used to determine the activation energy for vacancy motion around the $Cr^{3+}$ ion in each of the centres observed. A set of lines which increase in intensity as the sample is warmed above room temperature is assigned to the $Cr^{3+}$ ion associated with a single next nearest cation vacancy.

The spin Hamiltonian parameters of the spectra of $Cr^{3+}$ in the chloride and the bromide are compared. The substitutional incorporation

of the $Cr^{3+}$ ion is contrasted with the interstitial incorporation of the $Fe^{3+}$ ion which has a similar radius.

A dewar and cavity for use at 4.2K are described. The E.P.R. spectra of ytterbium, erbium and dysprosium in AgCl are presented. The resonances are assigned to the trivalent state of these ions and the ground states are derived from the experimental g-values. The symmetries of the spectra are used to derive the probable arrangements of vacancies about the rare earth ions.

Preliminary investigations of the E.P.R. and optical properties of the remaining rare earths and the 4d and 5d series ions in AgCl are presented. The rare earths other than europium are thought to be present only in the trivalent state in AgCl. The stable valent state is discussed in relation to the chemical properties of the rare earths.

The E.P.R. and electrical measurements available to date on the lattice site and vacancy association of transition ions in AgCl and AgBr are summarised. The results are used to show that association with nearest neighbour vacancies is most likely for ions which are relatively large compared with the $Ag^{+}$ ion. Small impurity ions are shown to be more likely to be associated with next nearest cation vacancies.

Chapter Four :   Chromium in AgCl and AgBr

Chapter One :  General Introduction

1.1     Introduction

The silver halides have been in use as photographic materials for more than a century.  The photographic process is based on the reduction of the silver halide to silver and halogen on exposure to light. Photographic film usually takes the form of an emulsion in which silver halide microcrystals are embedded in gelatin.  The techniques of preparation and processing of emulsions are highly developed and complex. Mees and James[26] include in their book details of some of the complicated chemical processes involved.  Gelatin is a naturally occurring material with numerous impurities and the halide microcrystals are in random orientations in the gelatin and water matrix.  Emulsions are, therefore, difficult systems to control and study chemically or by electron paramagnetic resonance (E.P.R.).

Bulk silver halide crystals provide a comparatively simple system for a study of the foundations of the photographic process.  The detailed mechanism by which silver colloid is formed on exposure to light is not fully understood, although several theories have been proposed[1,2,3]. E.P.R. became a useful investigating tool when it was realised that silver colloid was not formed in the volume of pure silver halide crystals on exposure to light[4].  In 1958 Tucker[5] studied the E.P.R. of $Cu^{2+}$ in AgCl and observed that $Cu^{+}$ sensitized the AgCl for silver colloid formation.  Palma et al[6,7] later successfully showed by E.P.R. that $Cu^{+}$ was converted to $Cu^{2+}$ on exposure to light.  Subsequently E.P.R. studies of $Fe^{3+}$ [8,9], $Eu^{2+}$ [10], sulphur[11,12], $Se_2^{3-}$ and $Te_2^{3-}$ [13] and

$O^-$ [14] have shown that these impurities can act as hole traps when the silver halide is exposed to light at certain temperatures. Electron trapping at room temperature by impurities in silver halide has not been observed directly. However, E.P.R. studies of the double doped system $AgCl:Fe^{2+}:V^{3+}$ show that $V^{3+}$ can act as an electron trap on exposure of the crystals below 140K[34]. Hohne and Stasiw found that those $Ni^{2+}$ ions which are not associated with a vacancy can act as electron traps on irradiation at 20K [40].

## 1.2    Physical and chemical properties of the silver halides

The silver halides have continued to be the major photographic materials because of the unique combination of physical and chemical properties which they possess. Measurements of the lattice parameter as a function of temperature[15] show that the dominant defects in AgCl and AgBr at room temperature are of the Frenkel type (a silver ion vacancy and an interstitial silver ion). The ionic conductivity of the silver halides at room temperature is high due to the very mobile interstitial silver ions ($Ag_i^+$). Ionic conductivity measurements in AgCl give an activation energy for formation of a Frenkel pair of $1.3 \pm 0.1eV$, and an activation energy for $Ag_i^+$ migration of about 0.1eV at room temperature[16]. The interstitial silver ion mobility is $2.5 \times 10^{-8} m^2V^{-1}s^{-1}$ at 300K[22].

Haynes and Schockley[17] have measured the electronic conductivity of silver halides at 300K using pulsed electric fields to displace the silver colloid formed by exposure. They found an electron mobility of about $5 \times 10^{-3} m^2V^{-1}s^{-1}$. The electron lifetime could be increased from

2 to 10$\mu$s by careful annealing of the sample. The electrons were found to travel $2 \times 10^9$ lattice constants before being trapped. The results indicate that dislocations are the major electron trapping centres.

Hole currents are difficult to detect in the silver halides. Early work[18,19] showed that holes could be injected into the silver halides when they were placed in halogen atmospheres. Mitchell[2] deduced from this work that positive holes are more mobile than silver interstitials and are not trapped by silver ion vacancies at room temperature. Malinowski and co-workers, using very pure silver halides, have detected the movement of photo-produced holes. Pulsed fields were used to displace the holes after exposure to light and their presence was detected by the destruction of a layer of silver deposited on the surface. Their results are summarised in reference (3). The photo-holes were found to have drift mobilities of $1 \times 10^{-4} m^2 V^{-1} s^{-1}$ and lifetimes between 5 and 20$\mu$s.

The optical absorption of the silver halides is strong at wavelengths shorter than 400nm. The absorption has a long wavelength tail extending to 425nm in AgCl and to 500nm in AgBr. Irradiation with visible light in this tail produces electrons and holes with high efficiency in the conduction and valence bands. Brown[20] has studied the structure of the band edge. Theoretical calculations[21] confirm that indirect phonon-assisted transitions from maxima in the valence band not at $\underline{k} = 0$ to the minimum in the conduction band at $\underline{k} = 0$ account for the absorption edge.

The formation of silver colloid in the silver halides may be contrasted with F centre formation in the alkali halides[22]. The

alkali halides are transparent to visible light. Irradiation with U.V. or shorter wavelengths results in colouration of the alkali halides due to electrons trapped at halide ion vacancies (F centres). The lattice structure of both types of halide is face-centred cubic, but the dominant defect in the alkali halides is a Schottky defect (a cation vacancy and an anion vacancy). The Schottky defects are much less mobile than $Ag_i^+$, having activation energies for migration of the order of 0.75eV in NaCl[16]. Ionic conductivities in the alkali halides are, therefore, several orders of magnitude lower than in AgCl. Electron currents are hard to detect in the alkali halides because the point defects (halide ion vacancies) can act as electron traps, forming F centres. The alkali metals are more electropositive than silver and are, therefore, less likely to be reduced and form metallic precipitates. The more covalent nature of the silver halides as compared to the alkali halides is reflected in their lower melting points (AgCl:728K, NaCl:1074K) and the relative ease with which impurities may be added to the silver halides.

One final important property of the silver halides is their ability to be developed chemically. After short exposures of emulsions, invisible, stable latent images are formed with quantum efficiencies of very nearly unity. These small groups of silver atoms act as catalysts for the reduction of the silver halide by chemical reducing agents. Provided that the emulsion is not over-developed, only those micro-crystals in which a latent image is present will be reduced to silver and thus made visible. The development process results in the conversion of perhaps 4 atoms of silver to an entire microcrystal of about $10^9$ silver atoms. Development of bulk cyrstals is, at present, only possible in the surface regions, since the developer cannot penetrate the interior of the crvstals.

## 1.3   The photographic process in the bulk of the halide

The absorption of light in the silver halide lattice gives rise to an electron and a positive hole. The photo-electron is able to drift for considerable distances before being trapped. The original theory for the fate of the electron and the formation of silver colloid proposed by Gurney and Mott[1] is still the subject of discussion. The trapped electron is stabilized by the arrival of a mobile silver interstitial ion and a silver atom is formed. The process is then repeated until a stable group of silver atoms has formed, provided that the $Ag^o$ is not converted to $Ag^+$ by the arrival of a photo-hole.

Electronic conductivity measurements[17] and decoration of dislocations[2] show that the sites for electron trapping and formation of silver colloid are dislocations. Seitz[22] discusses a mechanism of trapping at dislocation jogs such that each $Ag^o$ formed has a charge of $+^e/_2$ to attract the next electron.

Gurney and Mott[1] were aware that, if the positive holes were more mobile than the silver interstitials, then recombination of electrons and holes was possible at the electron traps. Later experiments showed that the holes were the more mobile species, and Mitchell[2] suggested processes to overcome the problem of electron and hole recombination. He proposed that an interstitial silver ion is first absorbed at or near the trapping site which thereby acquires a positive charge to attract and trap an electron. The electron lifetime experiments of Brady and Hamilton[23] have shown that, in fact, the initial electron traps are shallow and are only stabilized by the later arrival of an $Ag_i^+$ ion.

Malinowski's recent work on the fate of the photo-excited holes[3,24,25] suggests that, even in the purest available silver halides, the holes are trapped in the lattice within a few microseconds of their creation and that the probability for recombination of electrons and holes is low. The holes are thought to be temporarily trapped, possibly at impurity cation sites, and the traps become neutral and permanent when a silver ion vacancy is formed. Malinowski[3] argues that the neutral hole complexes can diffuse and destroy the latent image unless sensitizing impurities are present.

## 1.4    The latent image and silver colloid

The latent image is thought to be a group of silver atoms of such a size that they efficiently catalyse subsequent reduction of the surrounding silver halide to silver by a developing agent. Mees and James[26] review the theories of formation and nature of the latent image. Experiments[26] have shown that motion of electrons and $Ag_i^+$ are involved in the build-up of the image. Low exposures show that a group of only three or four silver atoms is sufficient to form a latent image speck which is stable over a long period of time. This stable group is thought to form in stages. The nature of the less stable intermediate groups has been discussed by Mitchell and others[2,26], but direct evidence for their structure is not available.

The exposures used to investigate the impurities discussed in this thesis are high and produce visible darkening, or print-out, in sensitized materials. The optical absorption bands of the silver formed in bulk crystals after very low exposures[27] and after high exposures[28] are

very similar. The absorption is in a broad band with a peak between 550 and 600nm. Rohloff[29] calculated the absorption curves predicted by the Mie theory for spherical silver metal particles. Comparison with the experimental curves[4,28] indicated a particle size of 60nm. This particle size corresponds to a group of $10^{12}$ silver atoms, which is thought to be too high a number, particularly at low exposure levels. The absorption band may be selectively bleached with monochromatic light in the band[22] and it is probable that a number of different sizes and shapes of silver colloids are involved in the visible image. The Mie theory is not applicable to such a situation.

Direct information on the formation of the latent image and the nature of the silver colloid might be provided by electron spin resonance. Paramagnetic centres could be formed during the build-up of the latent image (for example, $Ag_2^+$, $Ag_2^-$). Silver metal colloids could give rise to conduction electron resonance, in spite of the large spin-orbit coupling of silver and consequent short conduction electron relaxation time, provided that their radius was small enough for the electron levels to be quantised[30]. Holland[30] suggests a radius of 10nm to be sufficiently small. Resonances have been seen in heavily exposed silver halides[31]. The lines observed did not have the characteristic temperature dependence of paramagnetic species, but their interpretation is not clear.

An attempt was made in this laboratory to form high concentrations of silver colloid particles. Silver chloride was placed in a tube with a fine bore lower section. The halide was heated until molten and allowed to fall in droplets through a stream of reducing gas (nitrogen or hydrogen) onto a glass plate. Many of the beads of silver chloride

formed were coloured pink, purple or black owing to the presence of
silver metal. Numerous intense resonances were observed in a proportion
of these particles at room temperature. The resonant lines were
usually broad and had a range of g values above g = 2. On cooling the
specimens the resonant intensity in most of the lines first increased
and then decreased. The temperature dependence, line widths and line
shapes are typical of a system which is coupled anti-ferromagnetically
below a certain temperature (for example, MnO, FeO, $MnO_2$). It is
thought that the resonances observed were most probably due to small
areas of partly oxidised impurities such as iron and manganese. Iron
was detected chemically in two of the samples giving resonances. The
temperatures for transitions to the paramagnetic behaviour were in the
region 100K to 150K, which indicates a high degree of exchange coupling.
Strong exchange coupling is not expected between the silver species
($Ag^o$, $Ag^+$) which may be present at high densities as a result of the
reduction process.

## 1.5    Silver halide emulsions

In emulsions the silver halide is present as small crystals
about 10nm across and 1nm thick suspended in a gelatin matrix. The
gelatin acts as a halogen acceptor and plays an important part in chemical
development[26]. The absorption of light in the microcrystals will
give rise to electrons and holes as in the bulk material. The
electron and hole trapping mechanisms may differ from those in the bulk
crystals. In the emulsion crystals one in four of the host ions lies
on the surface, whereas only one in $10^6$ will be on the surface of a
macroscopic crystal[26].

The surface of the emulsion grain can, therefore, be expected to play a much more important part in the process than the surface of a large crystal. Simple gelatin-based emulsions were made following a method given by Mueller[32]. Copper, europium and gadolinium chlorides were added to the starting materials. These impurities were found to produce no effect on the optical sensitivity of the emulsions. It can be concluded that the hole trapping in the emulsions is dominated by surface effects. Significantly, the rare earth doped emulsions darkened more quickly on exposure to X-rays than the undoped material. The heavy elements probably increase the X-ray absorption of the emulsions.

The latent image formation in emulsions may be very similar to the formation in the bulk, although the preferred sites may differ. The efficiency of emulsions for silver atom formation is almost 100%. Absorption of 3 or 4 quanta of light in one microcrystal gives rise to a single group of silver atoms. The means by which the electrons are trapped at one site per grain, on average, remains a problem[26]. A recent theory is based on the surface charge layer that exists in the microcrystals[33]. The sign of the charge depends on the concentration of divalent cation impurities. For a concentration of a few p.p.m. the surface charge is expected to be negative. The photo-holes are, therefore, quickly attracted to the surface and absorbed by the gelatin. The photo-electrons are repelled by the surface and wander in the crystal lattice until they find a sensitivity speck, possibly $Ag_2S$, where the sign of the surface charge is reversed locally.

## 1.6    E.P.R. and the silver halides

E.P.R. has produced valuable evidence on the role of the
sensitizers $Cu^+$, $Fe^{2+}$ and $Eu^{2+}$, which act as hole traps in the silver
halides[6,7,9,10]. In addition to information relevant to the
photographic process, E.P.R. reveals the site symmetry of paramagnetic
impurities dissolved in the lattice. The positions of the charge
compensating vacancies can be deduced from the site symmetry. The
activation energy for motion of the vacancy around the impurity can be
found from the broadening of lines seen at room temperature. The
binding energy of the impurity-vacancy complex can be estimated from
the relative numbers of associated and unassociated impurity ions as
a function of temperature. Manganese has been studied in AgCl and
$AgBr$[35] by E.P.R. and is shown to be incorporated substitutionally in
association with a next nearest cation vacancy. Resonances from
nickel[36] and cobalt[37] in silver halides have been seen at low
temperatures. $V^{2+}$ has been studied in $AgCl$[38] and is incorporated
substitutionally in association with a next nearest cation vacancy below
room temperature.

A review of the paramagnetic properties of the iron transition
series in the alkali halides has been published[39]. No similar
review has been made of paramagnetic impurities in the silver halides.
Very little work has been published on the rare earths in monovalent
lattices.

## 1.7 <u>References</u>

1     R.W. Gurney and N.F. Mott,   Proc. Roy. Soc. (London), A164, 151 (1938).

2     J.W. Mitchell,   Rep. Prog. Phys. 20, 433 (1957).

3     J. Malinowski,   Contemp. Phys., 8, 285 (1967).

4     F. Moser, N.R. Nail and F. Urbach,   J. Phys. Chem. Solids, 9, 217 (1959).

5     R.F. Tucker,   Phys. Rev., 112, 725 (1958).

6     I.S. Ciccarello, M.B. Palma-Vittorelli and M.U. Palma,   Phil. Mag., 5, 723 (1960).

7     L. Bellomonte, M.B. Palma-Vittorelli and M.U. Palma,   Phys. Rev. Lett. 9, 84 (1962);
and Proc. 1st Int. Conf. on Paramagnetic Resonance, Jerusalem 1962, Ed. W. Low, Vol.2, p 790 (Academic Press, New York).

8     W. Hayes, J.R. Pilbrow and L.M. Slifkin,   J. Phys. Chem. Solids, 25, 1417 (1964).

9     K.A. Hay, D.J.E. Ingram and A.C. Tomlinson,   J. Phys. C., 1, 1205 (1968).

10     S.U. Cheema and M.J.A. Smith,   J. Phys. C., 4, 1231 (1971).

11     I. Ebert,   Z. Naturf. 15a, 279 (1960).

12     J. Busse and K. Hennig,   Phys. Stat. Sol. 7, K83 (1964).

13     M. Höhne and M. Stasiw,   Phys. Stat. Sol. 20, 657 (1967); Ibid., 20, 667 (1967).

14     M. Höhne, K.H. Segsa and M. Stasiw,   Phys. Stat. Sol. 35, 717, (1969).

15     C.R. Berry,   Phys. Rev. 82, 422 (1951).

16     P. Suptitz and J. Tetlow,   Phys. Stat. Sol. 23, 9 (1967).

17     J.R. Haynes and W. Schockley,   Phys. Rev. 82, 935 (1951).

18     G.W. Luckey and W. West,   J. Chem. Phys. 24, 879 (1956).

19     R.C. Harrison,   J. Phys. Chem. 66, 2376 (1962).

20     F.C. Brown,   J. Phys. Chem. 66, 2368 (1962).

21     F. Bassani, R.S. Knox and W.B. Fowler,   Phys. Rev. 137, A1217 (1965).

22     F. Seitz,   Rev. Mod. Phys. 23, 328 (1951).

23    L.E. Brady and J.F. Hamilton,   J. Appl. Phys. 37, 2268 (1966).

24    A. Buroff and J. Malinowski,   Phys. Stat. Sol. 26, 267 (1968).

25    M. Georgiev, E. Zagorska and J. Malinowski,   Phys. Stat. Sol. 28, 725 (1968).

26    C.E.K. Mees and T.H. James,   The Theory of the Photographic Process,   Macmillan, New York (1966), Chapter 5.

27    R. Hilsch and R.W. Pohl,   Z. Physik, 64, 606 (1930).

28    F.C. Brown and N. Wainfan,   Phys. Rev. 105, 93 (1957).

29    E. Rohloff,   Z. Physik, 132, 643 (1952).

30    B.W. Holland,   Proceedings of 14th Colloque Ampere, Ljubljana (1966), p 468.

31    M.J.A. Smith, K.A. Hay and D.C. Lainé,   Paramagnetic Resonance, Vol. 2, p 785, Ed. W. Low, Academic Press, N.Y. (1963).

32    Photographic Theory, Liège Summer School 1962, The Focal Press, London 1963, Chapter 1.

33    E. Fatuzzo and S. Coppo,   J. of Phot. Sci. 20, 43 (1972).

34    S.U. Cheema and M.J.A. Smith,   Phys. Stat. Sol. 42, 179 (1970).

35    M. Daehler,   Ph.D. Thesis, (1962), University of Wisconsin.

36    M. Höhne, M. Stasiw and A. Wettesich,   Phys. Stat. Sol. 34, 319 (1969).

37    T.R. Sliker,   Phys. Rev. 130, 1749 (1963).

38    S.U. Cheema and M.J.A. Smith,   J. Phys. C., 2, 1751 (1969).

39    .G.O. Sootha and S.K. Agarwal,   Phys. Stat. Sol. (a) 5, 293 (1971).

40    M. Höhne and M. Stasiw,   Phys. Stat. Sol. 33, 405 (1969).

Chapter Two :   The Theory of Electron Paramagnetic Resonance

## 2.1    The resonance phenomenon

Resonance has been observed from a large number of paramagnetic ions in many different host materials and several reviews of the experimental results[1-4] and the theory[4-9] have been made.  This chapter will outline those aspects of the theory which are relevant to the paramagnetic resonance results described later in the thesis.

An isolated ion with a total angular momentum $J\hbar$ possesses an associated magnetic moment $-g_L\beta\underline{J}$ where $g_L$ is the Lande g-factor (given by equation (5)), $\beta$ is the Bohr magneton, and $\hbar = \frac{h}{2\pi}$ where h is Planck's constant.  When the ion is placed in a steady magnetic field B, the magnetic moment will precess about B with an angular velocity $\omega_L = \frac{g_L\beta}{\hbar} B$.  If a rotating magnetic field of magnitude $B_1$ is applied perpendicular to B so that it rotates about B in the same sense and with the same frequency, $\omega_L$, as the magnetic moment, it will exert a constant couple on the magnetic moment.  In the frame rotating at $\omega_L$ the magnetic moment precesses about $B_1$ with an angular velocity $\omega_1 = \frac{g_L\beta}{\hbar} B_1$ and an alternating component of magnetic moment is produced in the direction of B.  The magnetic ion can, therefore, exchange energy with the oscillating field.  In practice the rotating magnetic field is obtained from a linearly polarised radio-frequency magnetic field, oscillating at right angles to B, which may be resolved into two circularily polarised fields rotating in opposite senses.

The resonance is detected by placing the sample in a region of high oscillating magnetic field in a resonant cavity.

in the sample from an applied field $B_1 \cos \omega_l t$ is given by

$$P_s = \frac{\omega \chi''}{2\mu_o} \int B_1^2 \, dV_s$$

$\chi''$ is the imaginary part of the susceptibility of the sample and $V_s$ is the sample volume. The power absorbed in the cavity at resonance is given by

$$P_c = \frac{\omega}{2\mu_o Q_o} \int B_1^2 \, dV_c$$

$Q_o$ is the quality factor of the cavity and $V_c$ is the volume of the cavity. For detection of the resonance the ratio $\frac{P_s}{P_c}$ must be large. $\frac{P_s}{P_c} = \chi'' Q_o \eta$, where $\eta$ is the filling factor $\frac{\int B_1^2 dV_s}{\int B_1^2 dV_c}$, and so $Q_o$ and the filling factor must be large.

In quantum terms the ion with total angular momentum $J\hbar$ has energy levels $m_J g \beta B$ in a magnetic field B where $m_J$ is the magnetic quantum number. g is the effective g-factor or the spectroscopic splitting factor of the ion and will be equal to $g_L$ only when the surroundings of the ion have a negligible effect on the ion. The r.f. magnetic field can induce magnetic dipole transitions between those levels for which the selection rule $\Delta m_J = \pm 1$ applies. The frequency required, $\nu_o$, is given by $h\nu_o = g \beta B$                                      (1)
so that the quantum of microwave energy is equal to the separation between the magnetic energy levels.

The probability for absorption of energy by the ion from the r.f. field at the resonant frequency $\nu_o$ is equal to the probability for stimulated emission[8]. The net amount of energy taken from the r.f. field is governed by the population difference between the two levels since spontaneous emission can be neglected at microwave frequencies.

In thermal equilibrium the population $n_i$ of a level with energy $E_i$ is given by the Boltzmann distribution function

$$n_i \; \propto \; \exp \left( \frac{-E_i}{kT} \right)$$

so that the difference $\Delta n_o$ between the number of ions $(n_1)$ in the lower state and the number $(n_2)$ in the higher state is given by

$$\Delta n_o \; = \; n_1 - n_2 \; = \; (n_1 + n_2) \cdot \frac{1 - \exp(\frac{-h\nu_o}{kT})}{1 + \exp(\frac{-h\nu_o}{kT})} \qquad (2)$$

For $h\nu \ll kT$, which is a good approximation down to about 4K, equation (2) becomes

$$\Delta n_o \; = \; \tfrac{1}{2} (n_1 + n_2) \frac{h\nu_o}{kT} \qquad (3)$$

and the resonant intensity is proportional to $\frac{1}{T}$. At thermal equilibrium $n_1 > n_2$ and energy is taken from the r.f. field and the population of the upper level will be increased. When the populations of the two states become equal, no more power is absorbed and saturation occurs. For an ion in a crystal field there are paths by which the ion can relax from the higher to the lower energy state without giving a quantum of energy to the microwave field. As a result, saturation of the absorption and the associated distortion of the absorption line does not usually occur for low values of $B_1$.

## 2.2 The free ion

The properties of a paramagnetic ion in a crystal are derived by first considering the energy levels of the free ion. Only the unfilled electron shell, which gives rise to the paramagnetic properties of the

ion, is considered. The Hamiltonian of the free ion in a magnetic

field will have the form (4)

$$H = H_C + H_{LS} + H_{SS} + H_Z + H_N + H_I .\qquad (4)$$

The terms are arranged in descending order of magnitude and represent

the following interactions (approximate magnitudes are given in

parentheses[10]):

$H_C (10^5 cm^{-1})$:  the coulombic interaction of the electrons with the

nucleus and with each other.

$H_{LS} (10^2 cm^{-1})$:  the interaction between the spin and orbital magnetic

moments of the electrons.

$H_{SS} (1 \ cm^{-1})$:  the spin-spin interaction between the electrons.

$H_Z (1 \ cm^{-1})$:  the effect of the external field on the electrons.

$H_N (10^{-2} \ cm^{-1})$:  the interaction of the magnetic moment of the

nucleus with the net magnetic moment of the electrons, and the

electrostatic quadrupole interaction of the nucleus and the electrons.

$H_I (10^{-3} \ cm^{-1})$:  the effect of the external magnetic field on the

nucleus.

The last term is usually neglected.  In the Russell-Saunders coupling

scheme the terms $H_C$ and $H_{SS}$ are combined and split the free ion

electronic configurations (for example, $3d^3$, $4f^2$) into levels characterised

by the total orbital angular momentum and the total spin momentum of the

electrons (for example, $3d^3$, $^4F$;  $4f^3$, $^4I$).  The level (or term) which

lies lowest in energy can be found using Hund's rules[8].

$H_{LS}$ will couple the magnetic moment vectors $\underline{L}$ and $\underline{S}$ into a total

magnetic quantum number $\underline{J}$.  $\underline{J}$ is formed by the vector addition of $\underline{L}$ and

$\underline{S}$.  For a shell less than half filled with electrons the lowest state

has J of magnitude L - S, and for a more than half-full shell J = L + S

will have the lowest energy. The ground state of the ion has 2J + 1

degenerate magnetic levels which will be split in an external magnetic

field. Resonance may be observed between the levels with the

selection rule $\triangle J = \pm 1$. The g-factor is given by the Landé expression

$$g_L = 1 + \frac{J(J + 1) - L(L + 1) + S(S + 1)}{2J(J + 1)} \tag{5}$$

## 2.3 The crystal field

The effect of the crystal field around the ion in a lattice is

now considered. The interaction of the ion and the field may be larger

than $H_C$. These strong fields occur when there is large covalent or

chemical bonding between the ion and the ligands. Hund's rules no

longer apply, the orbital motion of the electrons is quenched, and

the electron spins line up in their strong field configurations[7]. Low

spin states result as seen in the cyanides of the iron group (for

example, $K_3Fe(CN)_6$ [4]) and usually in the 4d and 5d ions.

Intermediate crystal fields giving interactions less than $H_C$

but larger than $H_{LS}$ are more common in the iron group. Hund's rules

apply but L and S are not combined to a vector J. The ligand ions

reduce the degeneracy of the various d orbitals ($d_{3z^2-r^2}$, $d_{x^2-y^2}$, $d_{xy}$

etc.). In a qualitative description the energy of those orbits where the

electron cloud passes near the negative ligands is raised. The orbits

which do not approach near the negative ligands are reduced in energy.

The electrons will occupy these orbits in order of increasing energy.

Electron-electron repulsion will remove further degeneracy of the orbits when two or more electrons are present and triplet $(t_2)$, doublet $(e)$ and singlet orbital levels will form in a general cubic field.

In rare-earth complexes the crystal field effect is usually less than $H_C$ and $H_{LS}$. The 4f electrons lie well inside the ion[11] and the crystal field effects are shielded by the full 5s and 5p shells. The crystal field is considered as a perturbation on the spin-orbit coupled J states.

Group theory provides a powerful method for determining how the crystal field will split the $(2J + 1)$ degenerate states. The symmetry group of the field surrounding the paramagnetic ion is first determined. All the symmetry operations of this group must commute with the Hamiltonian of the system since these operations do not alter the system. Any finite symmetry group has a finite number of irreducible representations. The number of irreducible representations is essentially equivalent to the number of different types of symmetry operators in the group[11]. Each representation can be written as a matrix of a certain order or dimension.

For a particular symmetry, represented by a symmetry group S, each energy level of the Hamiltonian belongs to a particular irreducible representation of S. The wave-functions of the energy level transform in the same way as the matrices of the representation to which it belongs and the degeneracy of the level is given by the dimension of the representation. The relation between the site symmetry and the level structure was established by Bethe[12] and his notation is used

in this thesis. Reviews of group theory methods and character tables for the crystal point groups are given by Heine[13] and Knox and Gold [14].

Two useful theorems derived by Kramers[15] and Jahn and Teller[16] simplify the analysis of the effects of the crystal field. Kramers theorem, a result of time reversal symmetry, states that if a system with an odd number of electrons is placed in a crystal field, the degeneracy of the system cannot be less than two. A crystal field cannot remove the spin degeneracy of a Kramers ion, whereas it can for a non-Kramers ion. The Jahn-Teller theorem states that non-linear complexes of non-Kramers ions with orbitally degenerate ground states will distort so as to remove the orbital degeneracy.

For a non-Kramers ion in a general cubic field (4, 6 or 8 coordinated) the cubic O group applies and singlet ($\Gamma_1$, $\Gamma_2$), doublet ($\Gamma_3$) and triplet ($\Gamma_4$, $\Gamma_5$) levels can arise. For a Kramers ion time reversal symmetry adds an additional operator.

The double cubic group $O^+$ applies and doublet ($\Gamma_6$, $\Gamma_7$) and quartet ($\Gamma_8$) levels are formed. Abragam and Bleaney[9] tabulate the wave-functions appropriate to these levels for each value of J. Lower symmetry fields are usually treated as a perturbation on the general cubic field, or on a general trigonal field.

## 2.4   Calculation of the crystal field potential

The crystal field potential surrounding the ion is usually calculated using a point charge model in which the ligands are assumed to be static

and the electrons are localised on the ions. In certain cases where considerable covalent bonding is present this model is poor and configuration interaction or molecular orbital methods are introduced. For the study of ions in silver halides, the point charge model should be fairly satisfactory as the bonding is expected to be predominantly ionic in character. The silver halides are, however, less ionic than the corresponding alkali halides. Evidence of covalent overlap of orbitals has been found in the E.P.R. spectra of interstitial $Fe^{3+}$ in $AgCl$[17] but the point charge model is still useful. The potential V is calculated by adding the coulombic potentials of each ligand ion at a general position (x, y, z) with the origin of the coordinates at the paramagnetic ion. In E.P.R. work only the first neighbour shell is considered, although the effect of more distant neighbours has been taken into account in calculations of defect energies[18]. The crystal field effects on the 4f electrons in rare earth ions may be altered from the point charge model by distortions of the outer-electron shells[19]. In general such effects have been ignored.

The electric field surrounding the paramagnetic ion will obey Laplace's equation and so may be expanded as a series of spherical harmonics[20]

$$V = \sum_{n,m} A_n^m \, r^n \, Y_n^m \, (\theta, \phi) \tag{6}$$

where $Y_n^m$ are spherical harmonics, $A_n^m$ are coefficients depending on the nature of the surroundings and $m \leqslant n$. It should be noted that the spherical harmonics with m odd are imaginary whereas the potential must be real. The article by Hutchings[21] defines combinations of the $Y_n^m$ into real tesseral harmonics and also clarifies the different notations and expansions used in the literature.

The matrix elements of the perturbing Hamiltonian with the free ion wave functions have to be found so that the secular equation may be formed. The solutions of this equation give the energy levels and wave-functions of the ion. The matrix elements will include a term $\langle \psi_m^* | -eV_n^m | \psi_m \rangle$ in which the free ion wave-function $\psi_m$ may be expanded in spherical harmonics

$$\psi_m = \psi_{nlm}(r, \theta, \emptyset) = R_{nl}(r) \, \Theta_{lm}(\theta) \, \emptyset_m(\emptyset) \qquad (7)$$

The rules for multiplication of spherical harmonics show that for 3d electrons (n = 2) terms in the crystal field expansion with n > 4 will give zero matrix elements. For 4f electrons terms with n > 6 can be ignored. The term with n = 0 gives only a constant factor and is ignored. Terms with n odd do not occur when there is a centre of symmetry and parity conservation shows that the odd terms can only connect states of different configurations and are usually ignored in E.P.R. work (they do affect optical spectra). Additional simplification arises in dealing with the $Cr^{3+}$ ion since this has an orbital singlet ground state with $S = \frac{3}{2}$ and only terms with $n \leqslant 3$ will give non-zero matrix elements.


## 2.5   Operator equivalent methods

The matrix elements $\langle \psi_m^* | -eV_n^m | \psi_m \rangle$ can be calculated directly using the cartesian equivalents of the harmonic expansions[11,12] and the chosen free ion wave-functions. The evaluation can be made considerably simpler by the use of operator equivalents[20,22,23]. The coordinates x, y and z throughout the cartesian expression of the crystal field potential are replaced by appropriate angular momentum operators. These are Sx, Sy and Sz for spin only ground states (for example, $Cr^{3+}$ in

octahedral field) and Jx, Jy and Jz for the rare earth ions. The

substitution is not completely simple because x, y and z commute whereas

Sx, Sy and Sz do not. As a result, for example, xy is replaced by

$\frac{SxSy + SySx}{2}$ (22). The matrix elements are then calculated using the

well-known properties of these operators.

Stevens[22] has shown that the operator equivalents give matrix

elements proportional to those of the original potential functions, and

that the constant of proportionality is the same for all operators of the

same order acting on a single J state. The constants are found by

calculating the matrix element for a chosen simple case in cartesian

form. The elements are integrals over r, $\theta$ and $\phi$ and involve a radial

integral of the type $\int_0^\infty [f(r)]^2 r^n r^2 dr$. The radial integral cannot

usually be evaluated since the radial part of the electronic wavefunction

f(r) is not well known. The unknown factor is usually expressed as

$\langle r^n \rangle$ where $\langle r^n \rangle = \int_0^\infty [f(r)]^2 r^n r^2 dr$. The values of the proportionality

constants $\alpha$, $\beta$ and $\gamma$ for second, fourth and sixth order terms are tabulated

for 4f electrons by Elliott and Stevens[23] and for 3d electrons by

Bleaney and Stevens[4].

A form which is frequently used for the contribution of the crystal

field to the total Hamiltonian is

$$H_V = \sum_{n,m} B_n^m O_n^m \qquad (8)$$

where $O_n^m$ are the operators tabulated by Hutchings[21] and Low[6] and by

others. $B_n^m$ are the experimentally determined constants and are related

to the $A_n^m$ given above by $A_n^m \langle r^n \rangle = B_n^m$. In the study of transition

series ions only terms with n ⩽ 4 are needed and the substitutions

$B_2^0 \equiv \frac{1}{3}D$, $B_2^2 \equiv E$ and $B_4^0 \equiv \frac{1}{180}F$ are usually made.

## 2.6   The spin Hamiltonian

In the majority of cases, and particularly those where the crystal field has less than cubic symmetry, an orbital singlet ground state is formed. The excited orbital states are usually of the order of 100 $cm^{-1}$ higher in energy. At room temperature and below only the ground state will be appreciably populated. The spin Hamiltonian is introduced to express, in a convenient, shorthand form, those quantities which can be derived from a paramagnetic resonance experiment. $H_S$ describes only the ground orbital level[4,10]. The crystal field interaction $H_V$ is added to the total Hamiltonian of equation (4) and those interactions which do not split the ground-state are ignored. The spin Hamiltonian has the general form:

$$H_s = H_Z + H_V + H_N \qquad\qquad (9)$$

The degeneracy of the state is expressed by means of an effective spin S. There are (2S + 1) degenerate spin states $|M\rangle$ where M takes integral values between S and -S. $H_S$ operates on these levels. Where S occurs subsequently in this chapter it is the effective spin. $H_C$ and $H_{SS}$ of equation (4) are accounted for in deriving the free ion configurations. $H_{LS}$ is used to derive the spin-orbit coupled scheme which holds for the rare-earth ions. For the 3d ions $H_{LS}$ gives zero contribution in the ground state since $\langle L \rangle = 0$ for an orbital singlet[4]. The Zeeman interaction is usually the largest of the remaining terms. $H_Z$ has the general form

$$H_Z = \beta \underline{B} \cdot (\underline{L} + 2\underline{S}) \qquad\qquad (10)$$

which reduces to

$$H_Z = \beta \underline{B} \cdot g \cdot \underline{S} \qquad\qquad (11)$$

for an orbital singlet. The g-factor is a tensor which may not have a

value exactly equal to the free electron value of 2.0023 because the crystal field can mix excited levels with the ground state. The off diagonal terms in the g-tensor ( $g_{xy}$, $g_{yz}$ etc.) are zero if the site has reflection symmetry and have been shown to have negligible effects for $S = \frac{1}{2}$ states[24]. In orthorhombic symmetry the Zeeman term reduces to

$$H_Z = (g_x B_x S_x + g_y B_y S_y + g_z B_z S_z) \tag{12}$$

Equation (12) is used for both 3d and 4f ions where $(2S + 1)$ is the degeneracy of the state. The eigenstates of the 4f ions are not pure spin states but are formed by a combination of spin and orbital magnetic moments. The spin Hamiltonian operates on the $(2J + 1)$ degenerate states $|J_z\rangle$ where $J_z$ takes integral values from $+J$ to $-J$. The wave-functions are usually combinations of several $|J_z\rangle$ states and the g-values vary greatly from 2. The excited states of 4f ions may not be widely separated from the ground state and resonance from excited states has been observed[25]. However, at the low temperatures required to observe resonance, only the lowest level is significantly populated.

The crystal field interaction takes the form described in section 2.4. For example, in a general cubic field:

$$H_V = B_4(0_4^0 + 50_4^4) + B_6(0_6^0 - 21.0_6^4) \tag{13}$$

The contribution for a 3d ion with $S < \frac{5}{2}$ in an orthorhombic field is $H_V = B_2^0 \, 0_2^0 + B_2^2 \, 0_2^2$ , which is usually written as

$$H_V = D\left[S_z^2 - \frac{1}{3}S(S + 1)\right] + E\left[S_x^2 - S_y^2\right] \tag{14}$$

$H_N$ represents the magnetic and quadrupole nuclear interactions. The quadrupole effects only arise when the nuclear spin is greater than $\frac{1}{2}$ and can be most clearly detected in forbidden hyperfine lines. These

were not distinguished in the systems studied and the effect will be ignored. The magnetic interaction between the nuclear spin and the electron spin is expressed in the form $H_N = \underline{S}.A.\underline{I}$, which reduces to

$$H_N = A_x S_x I_x + A_y S_y I_y + A_z S_z I_z \tag{15}$$

in orthorhombic symmetry.

## 2.7 The spin Hamiltonian and the ground state

The properties of the ground state are determined by setting up the secular equation of $H_S$ with suitable wave-functions for the ion. Usually $H_Z$ is the largest term and $H_V$ and $H_N$ are treated by perturbation theory.

For example, in the case of $Cr^{3+}$ $(3d^3)$ the appropriate spin Hamiltonian in orthorhombic symmetry is

$$H_S = g\beta\underline{B}.\underline{S} + D\left[S_z^2 - \tfrac{1}{3}S(S+1)\right] + E\left[S_x^2 - S_y^2\right] \tag{16}$$

The matrix formed using the spin states $|\tfrac{3}{2}\rangle$, $|\tfrac{1}{2}\rangle$, $|-\tfrac{1}{2}\rangle$ and $|-\tfrac{3}{2}\rangle$ can be solved for B∥Z, and solutions for B∥X and B∥Y can be found using the transformations of Jones et al[26]. For a general direction of B the above spin states are no longer eigenstates of $H_Z$ and off-diagonal terms of $g\beta\underline{B}.\underline{S}$ arise. For B>D,E perturbation theory can be used to find the energy levels, and hence the resonant fields, provided that B only occurs in diagonal terms. The matrix is made diagonal in $H_Z$ by either chosing new basis states that are eigenstates of $H_Z$[8] or by rotation of the coordinates of $H_S$ so that the new Z axis is parallel to the external field B, not the crystal field Z axis (see Appendix I ).

If the nucleus has a magnetic moment then the hyperfine interaction is treated in the same way by perturbation theory. Bleaney[27] gives a complete expression for the energies of the hyperfine transitions in a field of axial symmetry.

For the rare earth ions a similar approach is used to find the energy levels of the spin Hamiltonian although the calculation is more complex since crystal field terms up to $B_6^6$ are needed and J can have values up to $\frac{15}{2}$. Lea, Leask and Wolf (LLW)[28] have determined the eigenvalues and eigenfunctions of all the trivalent 4f ions in 4, 6 and 8 fold cubic coordination. The general cubic field is given in equation (13) and for tetrahedral fields

$$B_4 = -\frac{7}{36}\frac{Ze^2}{R^5}\langle r^4 \rangle \beta \qquad B_6 = +\frac{1}{18}\frac{Ze^2}{R^7}\langle r^6 \rangle \gamma \qquad (17)$$

For octahedral fields

$$B_4 = +\frac{7}{16}\frac{Ze^2}{R^5}\langle r^4 \rangle \beta \qquad B_6 = \frac{3}{64}\frac{Ze^2}{R^7}\langle r^6 \rangle \gamma \qquad (17)$$

The eigenvalues are plotted by LLW as a function of a parameter x defined by

$$\frac{x}{1 - |x|} = \frac{F(4)\ B_4}{F(6)\ B_6} \qquad (18)$$

where $-1 < x < 1$ and F(4) and F(6) are common factors within each J state. The energy levels (and eigenfunctions in the case of $\Gamma_8$ states) depend on x and hence upon the ratio of the fourth to the sixth degree crystal terms. For $x = 0$ $B_4$ is zero and for $x = 1$ $B_6$ is zero. The energies are plotted in terms of a scale W where W is defined by

$$B_4 F(4) = Wx$$
$$B_6 F(6) = W(1 - |x|) \qquad (19)$$

The sign of x is determined by the ratio of $B_4/B_6$ since LLW show that F(6) and F(4) are both positive for all J's. The sign of x can be seen in (17) to change in going from 4-fold (and 8-fold) to 6-fold coordination. The actual value of x for a given coordination will vary according to the values of $\beta$ and $\gamma$ and these are tabulated by LLW. The sign of W will depend on $B_6$, since $(1 - |x|)$ is always positive for $|x| < 1$, and hence the sign of W depends only on $\gamma$ since the multiplying factors in $B_6$ are always positive.

Tetragonal and lower symmetry fields are treated as a perturbation on the cubic field states and may mix excited states with the ground state as discussed in Chapter Five.


## 2.8    Relaxation processes

It was shown in section 2.1 that saturation of the resonance line will occur unless there are relaxation processes present. In dilute systems where the paramagnetic ions are dissolved in a diamagnetic host material, the dominant relaxation mechanism is one in which the ions in the excited state can give up a quantum of energy to the lattice. The spin-lattice relaxation time is characterised by $T_1$. The population difference ($\Delta n$) at time t between the upper and lower states is given by

$$\Delta n = \Delta n_o \left[ 1 - \exp(\frac{-t}{T_1}) \right] \tag{20}$$

where $\Delta n_o$ is the equilibrium value of $\Delta n$.

Kroning[29] described a mechanism for the coupling of the spins to the lattice which gives good agreement with experimental results. Thermal

vibrations of the lattice will give rise to a continuous range of phonon frequencies up to a maximum corresponding to the Debye temperature of the solid. The lattice waves modulate the crystal electric field surrounding the paramagnetic ion and by means of the spin-orbit coupling the lattice waves influence the spin magnetic moment. The ion may relax by giving up a single phonon of the appropriate energy to the lattice (direct process) or by absorbing a phonon of frequency $\nu_1$ and emitting a phonon of frequency $\nu_2$ such that $\nu_2 - \nu_1 = \nu_0$ where $\nu_0$ is the resonant frequency (Raman process). The direct process is more probable since it requires only one phonon of the correct energy and usually dominates at temperatures of 4K since there are few phonons present. At higher temperatures the Raman process is more important since it can involve phonons of a range of frequencies and there are large numbers of phonons present.

Kroning[29] and Van Vleck[30] have estimated values for $T_1$. The analysis for Kramers and non-Kramers ions is not the same since the crystal electric field cannot directly affect a Kramers doublet[15] and the spins and the lattice can only be coupled by means of excited levels. For $g\beta B < kT$ the direct process gives

$$\frac{1}{T_1} \propto \frac{\lambda^2 T \nu_0^4}{\delta^4} \qquad \text{for Kramers ions} \qquad (21)$$

where $\lambda$ is the spin-orbit coupling parameter, $\delta$ is the separation of the ground and first excited orbital levels, T is the absolute temperature and $\nu_0$ is the resonant frequency. For non-Kramers ions

$$\frac{1}{T_1} \propto T \nu_0^2 |\langle a|V|b \rangle|^2 \qquad (22)$$

where $\langle a|V|b \rangle$ is the matrix element of the crystal field potential V with the two spin states a and b.

Orbach[31] has discussed the two-phonon processes in detail and he considered the situation where the energy equivalent to the Debye phonon frequency, $k\theta_D$, is greater than the separation $\Delta$ of the two lowest excited states. Phonons of energies of the order of $\Delta$ are preferentially absorbed or emitted by the spin system. The ion can then relax via a transition to the excited orbital level (Orbach process). For temperatures where these two phonon processes are likely, Orbach finds for Kramers ions:

$$k\theta_D > \Delta \qquad T_1 \propto \exp(\frac{\Delta}{kT}) \qquad \text{(Orbach process)}$$

$$k\theta_D < \Delta \qquad T_1 \propto T^{-9} \qquad \text{(Raman process)}$$

and for non-Kramers ions:

$$k\theta_D > \Delta \qquad T_1 \propto \exp(\frac{\Delta}{kT}) \qquad \text{(Orbach process)}$$

$$k\theta_D < \Delta \qquad T_1 \propto T^{-7} \qquad \text{(Raman process)}$$

It is assumed that the time taken for energy to be passed from the lattice to the external thermal reservoir is much shorter than the spin-lattice relaxation time so that lattice heating from a build up of phonons (phonon bottleneck) does not occur.

For a Kramers ion such as $Cr^{3+}$ for which a cubic field gives a singlet orbital ground state well separated from the higher states, equation (21) shows that the relaxation times should be long. Resonance is expected to be observed at room temperature. In $Ti^{3+}$, however, the lowest orbital doublet is only split by fields of less than cubic symmetry and $\delta$ is small. The spin-lattice relaxation times are short and low temperatures are usually required for the observation of a

resonance. For the rare-earths the spin-orbit coupling parameter $\lambda$ is large and orbital magnetic moment is present in the ground states (except for $Eu^{2+}$ and $Gd^{3+}$). The ions are strongly coupled to the lattice and have short spin-lattice relaxation times.

Spin-spin relaxation occurs when the paramagnetic ions are sufficiently close for the magnetic field of one magnetic ion to affect a nearby ion. The relaxation times are not dependent on temperature. This mechanism is not expected to be important in the dilute systems studied in AgCl and AgBr.

## 2.9    Line width and line shape

Paramagnetic resonance is usually observed using a fixed frequency r.f. field and varying the static magnetic field. In general, resonant absorption takes place over a range of magnetic fields on either side of the magnetic field value which fulfills the resonant condition (equation (1))

The line width may be dominated by one of a number of different mechanisms. The lifetime ($\Delta t$) of the excited electronic state is associated with a band width ($\Delta E$) of the energy level by the uncertainty principle

$$\Delta E.\Delta t \simeq \frac{h}{2\pi}$$

The uncertainty in the energy will give rise to a line width of

$$\Delta \nu = \frac{1}{2\pi\Delta t} \tag{23}$$

The line width in field units may be obtained from (23) by means of the resonant condition (1).

$$\Delta B = \Delta \nu \cdot \frac{h}{g\beta} = \frac{h}{g\beta} \cdot \frac{1}{2\pi\Delta t} \tag{24}$$

Strictly speaking, $\Delta B = (\frac{\partial B}{\partial \nu}) \cdot \Delta \nu$ and $\frac{\partial B}{\partial \nu}$ can be large, for example, when the magnetic field is not parallel to a principal axis. The line width in field units is not then directly related to the true frequency width.

If the limited lifetime of the excited state is the major source of line width then a homogeneously broadened line is produced. The absorption line shape is Lorentzian and the derivative curve recorded by the spectrometer will have the form[32]

$$Y'(B) = \frac{16 \, y'_m \left( \frac{B - B_o}{\frac{1}{2}\Delta B_{pp}} \right)}{\left[ 3 + \left( \frac{B - B_o}{\frac{1}{2}\Delta B_{pp}} \right)^2 \right]^2} \tag{25}$$

$y'_m$ is the derivative amplitude, $\Delta B_{pp}$ is the peak-to-peak line width and $B_o$ is the resonant field.

In the early paramagnetic resonance work concentrated samples were used and spin-spin interactions were important contributions to the line width and relaxation times. The line is broadened because the local magnetic field of each ion is the sum of the external field and that of the surrounding magnetic dipoles in random orientations. Resonance occurs over a range of external fields when the local field at each ion obeys the resonance condition (1). If the surrounding ions are unlike the resonant ion, an inhomogeneous line shape results. Similar neighbouring ions can give rise to spin-spin relaxation. Van Vleck[33] and Pryce and Stevens[34] have studied the dipolar interactions between identical ions. They also show that in highly concentrated systems cooperative or exchange interactions are important and can give rise to line widths smaller than

those expected from dipolar broadening alone. For the majority of the impurities studied in the silver halides the dilution is such that the dipolar interactions will be negligible in comparison with the other broadening mechanisms present. Orton[8] shows that for concentrations below 0.1% the dipolar interaction can be expected to contribute less than 0.1 mT to the line width.

Random strains or local variations in the crystal lattice, and random arrangements of other magnetic ions in the structure, can give rise to inhomogeneous broadening. The associated line shape is usually Gaussian. The Gaussian derivative curve has the following form[32]

$$Y'(B) = e^{\frac{1}{2}} y'_m \left(\frac{B - B_o}{\frac{1}{2}\Delta B_{pp}}\right) \exp\left[-\frac{1}{2}\left(\frac{B - B_o}{\frac{1}{2}\Delta B_{pp}}\right)^2\right] \qquad (25)$$

where the symbols are interpreted as for equation (24).

An important source of broadening in the silver halides arises from the nuclear magnetic moments of the adjacent ions. These magnetic moments may be oriented in a finite number of ways with respect to the external magnetic field. The superposition of the resonance lines corresponding to each of the possible internal fields gives rise to a broadened line. The line shape is approximately Gaussian when the structure due to a number of orientations of nuclear moments is not resolved. In AgCl:$Fe^{3+}$ this line broadening is resolved into ligand hyperfine structure[17]. In AgCl:$Cr^{3+}$ and AgBr:$Cr^{3+}$ unresolved interaction with the halogen ions probably accounts for the line widths of 1.2mT and 5mT. These values contrast with the line width of 0.075mT observed in MgO:$Cr^{3+}$ where the neighbouring $O^{2-}$ ions have zero nuclear moment[35].

The Lorentzian and Gaussian derivative curves may be conveniently distinguished by comparison with the table of amplitudes at multiples of $\frac{1}{2}\Delta B_{pp}$ from the centre of the line ($B_0$) given by Poole[32]. The Lorentzian curve is sharper at the centre than the Gaussian, but the amplitude of the Lorentzian falls off much less quickly beyond the half amplitude points.

## 2.10    The appearance of the spectrum

The combination of the calculated energy levels, as discussed in section 2.7, and the selection rules gives the resonant lines which will be seen. The considerations of sections 2.8 and 2.9 will govern the temperatures at which a resonance can be observed, and the expected line width. For $S > \frac{1}{2}$ the crystal field can split the spin states into doublets and fine structure is seen. 2S lines are observed for a given lattice site at a general orientation to the external field. The transition probabilities are not equal for each of the magnetic dipole transitions involved. The intensity of the transition $|m\rangle$ to $|m-1\rangle$ is given by Bleaney[27] and for an $S = \frac{3}{2}$ ion three lines are expected with intensities in the ratio 3:4:3.

The hyperfine transitions have the selection rule $\Delta m = 0$, where m is the nuclear magnetic quantum number. Each electronic spin transition is split into $(2I + 1)$ components by the $(2I + 1)$ possible orientations of the nuclear magnetic moment. Since all the orientations are equally likely, the lines are of equal intensity.

The fine structure splittings are equal and symmetrical about $B_0$, where $h\nu_0 = g\beta B_0$, to first order of $\frac{D}{B_0}$. To first order the hyperfine

transitions are also equally spaced about the fine structure line positions corresponding to $I = 0$. Second and higher order terms in general shift the lines to lower fields. The corrections are larger at lower fields and when the external field is not parallel to the principal axes of the site.

Rare-earth Kramers ions in axial or lower symmetry have doubly degenerate states ($S = \frac{1}{2}$). The crystal field terms cannot be determined from the ground state resonance. Excited state resonances and optical spectra are required to determine the $B_n^m$ values. g-values varying widely from 2 and with large anistropies are found because of the orbital contribution to the wave functions.

## 2.11    References

1    K.D. Bowers and J. Owen, Rep. Prog. Phys. 18, 304 (1955).

2    J.W. Orton, Rep. Prog. Phys. 22, 204 (1959).

3    J.H.E. Griffiths, J. Owen and I.M. Ward, Proc. Roy. Soc. (London), A219, 526 (1953).

4    B. Bleaney and K.W.H. Stevens, Rep. Prog. Phys. 16, 108 (1953).

5    D.J.E. Ingram, Spectroscopy at Radio and Microwave Frequencies, Butterworths, London (1955).

6    W. Low, Paramagnetic Resonance in Solids, Solid State Physics Suppl. 2, Academic Press (1960).

7    H.M. Assenheim, Introduction to Electron Spin Resonance, Hilger and Watts Ltd. (1966).

8    J.W. Orton, Electron Paramagnetic Resonance, Iliffe (1968).

9    A. Abragam and B. Bleaney, Electron Paramagnetic Resonance of Transition Ions, Clarendon Press, Oxford (1970).

10    A. Abragam and M.H.L. Pryce, Proc. Roy. Soc. (London), A205, 135 (1951).

11    G.H. Dieke, Spectra and Energy Levels of Rare Earth Ions in Crystals, J. Wiley & Sons Inc., New York (1968).

12    H. Bethe, Ann. Physik. 3, 133 (1929).

13    V. Heine, Group Theory in Quantum Mechanics, Pergamon (1964).

14    R.S. Knox and A. Gold, Symmetry in the Solid State, Benjamin, New York (1964).

15    H.A. Kramers, Proc. Acad. Sci. Amsterdam, 33, 959 (1930),

16    H.A. Jahn and E. Teller, Proc. Roy. Soc. A161, 220 (1937).

17    W. Hayes, J.R. Pilbrow and L.M. Slifkin, J. Phys. Chem. Solids 25, 1417 (1964).

18    F. Bassani and F.G. Fumi, Il Nuovo Cimento, 11, 274 (1954).

19    R.E. Watson and A.J. Freeman, Phys. Rev. 133, A1571 (1964).

20    R.J. Elliott and K.W.H. Stevens, Proc. Roy. Soc. (London), A215, 437 (1952).

21    M.T. Hutchings, Solid State Physics, 16, 227 (1964).

22    K.W.H. Stevens, Proc. Phys. Soc., A65, 209 (1952).

23    R.J. Elliott and K.W.H. Stevens,  Proc. Roy. Soc. (London), A218, 553 (1953).

24    J.E. Lowther,  Phys. Stat. Sol. B46, K19-21 (1971).

25    R.W. Bierig and M.J. Weber,  Phys. Rev. 132, 164 (1963).

26    D.A. Jones, J.M. Baker and D.F.D. Pope, Proc. Phys. Soc. 74, 249 (1959).

27    B. Bleaney,  Phil. Mag. 42, 441 (1951).

28    K.R. Lea, M.J.M. Leask and W.P. Wolf,  J. Phys. Chem. Solids 23, 1381 (1962).

29    R. de L. Kroning,  Physica 6, 33, (1939).

30    J.H. Van Vleck,  Phys. Rev. 57, 426 (1940).

31    R. Orbach,  Proc. Roy. Soc. (London) A264, 458 (1961).

32    C.P. Poole,  Electron Spin Resonance,. J. Wiley & Sons Inc., New York (1968).

33    J.H. Van Vleck,  Phys. Rev. 74, 1168 (1948).

34    M.H.L. Pryce and K.W.H. Stevens,  Proc. Phys. Soc. A63, 36 (1950).

35    J.E. Wertz and P. Auzins,  Phys. Rev. 106, 484 (1957).

Chapter Three :  Experimental Methods

## 3.1     Sample preparation

### 3.1.1   Synthesis of AgCl and AgBr

The photosensitivity and the E.P.R. of silver halide crystals are very sensitive to low levels of impurities.  For example, the optical density of the silver colloid produced on exposure to blue light increases by a factor of $10^2$ if 2ppm of $Cu^+$ are present[1].  The E.P.R. system used at room temperature could detect a concentration of 0.1ppm of the common paramagnetic impurities (iron and manganese) present in a typical AgCl sample

Pure AgCl was prepared from silver and chlorine in vacuo by a method similar to that described by Malinowski[2].  A diagram of the apparatus is shown in fig. 3.1.  The chlorine was prepared by electrolysis of NaCl solution with platinum electrodes.  The gas was passed into a container held in a dry ice-acetone bath, and liquified.  This procedure removed any contaminating gases of lower boiling point, such as $O_2$ and $CO_2$.

Pure silver was prepared by repeated electrolysis of silver through "Analar" silver nitrate solutions (fig. 3.1a).  Sintered glass filters were placed at the base of the anode and at the centre of the cell to prevent insoluble deposits from the anode silver reaching the cathode. Silver, and the other noble metals (Cu, Au, Hg) have very positive standard electrode potentials (S.E.P.) as compared to other common metals.  For
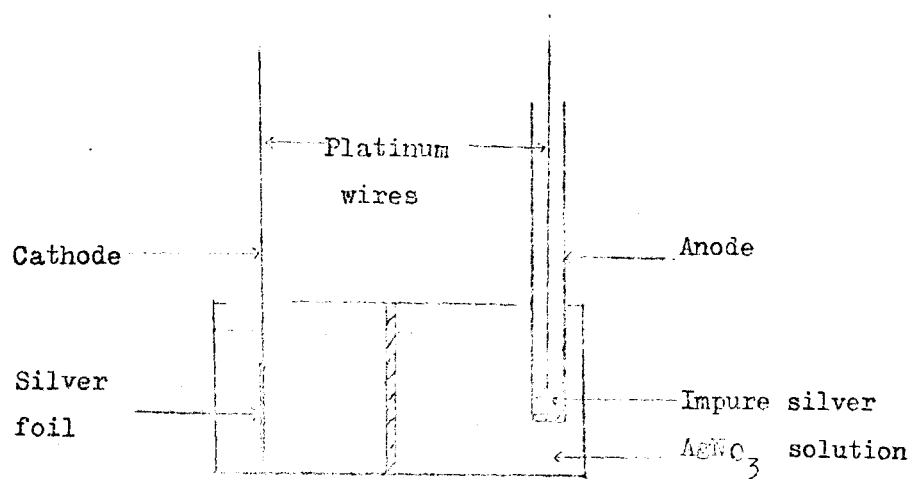
Fig. 3.1.(a) The purification of silver metal.
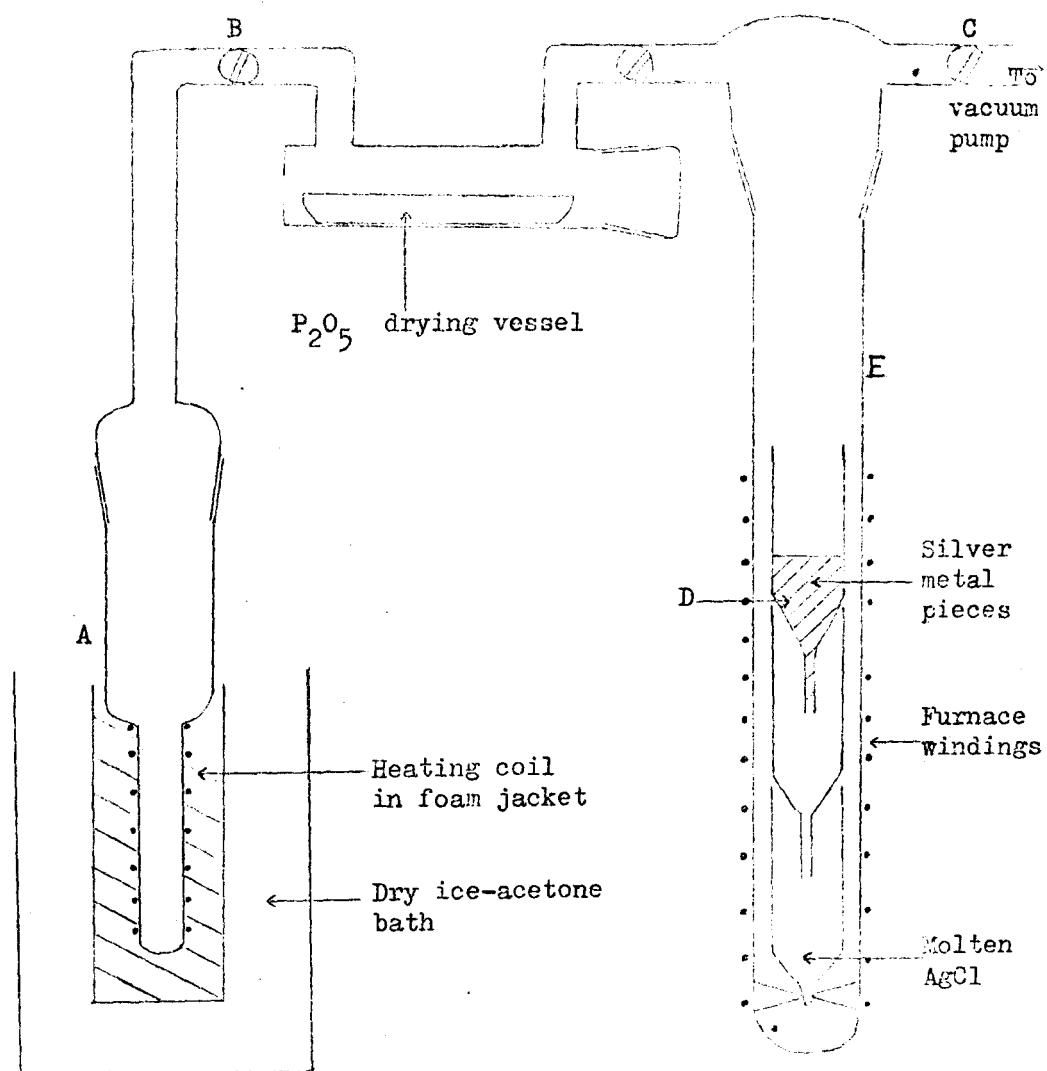
example, the S.E.P.'s of Ag, Cu and Fe are +0.8V, +0.35V and -0.44V respectively measured against a standard hydrogen electrode[3]. Provided that low voltages are used all those metals of S.E.P. about 0.4 volts more negative than silver are not expected to be deposited at the cathode. The current densities were kept correspondingly low to prevent appreciable solution polarisation which would cause the effective cathode potential to rise. Typical values of the voltage across the solution and the current density were 5V and 25mA/cm$^3$.

The initial electrolysis was carried out through dilute $AgNO_3$ solution because the solution quickly became contaminated. Repeated electrolysis was then carried out through saturated $AgNO_3$ solutions which refine the silver more effectively. Thermodynamic considerations[3] show that

$$E = E_o + \frac{RT}{ZF}\ln\left[M^{z+}\right] = E_o + \frac{0.059}{Z}\log_{10}\left[M^{z+}\right]$$

where $E_o$ = standard electrode potential in volts.

$E$ = effective electrode potential in volts.

$\left[M^{z+}\right]$ is the molar concentration of the $M^{z+}$ ion expressed in gram molecular weights per litre.

$T$ = absolute temperature, taken as 298K.

$F$ = Faraday's constant.     $R$ = gas constant.

As $AgNO_3$ is very soluble, a molar concentration of 10 or more could be obtained. The silver potential became more positive by 0.06V whilst the potentials of the dilute impurities present in the original solution at, say, 10ppm became more negative by about 0.3V. Electrolysis was repeated three or four times in fresh solutions.

The liquified chlorine was placed in the container A (fig. 3.1b) which had a heating coil around it and was initially in a dry ice-acetone bath. By means of the taps B and C and by warming the liquid chlorine, the system was flushed through with chlorine. The silver in D was then heated to 720 - 760K under vacuum. Chlorine gas was then allowed into the vessel E and reacted with the silver to form molten silver chloride. This passed slowly through the narrow portions of the silica tubes where a certain amount of organic material was filtered out. The silver chloride was removed from the final container after cooling the system to room temperature in chlorine.

A similar method was used to prepare silver bromide. Bromine gas was not prepared as there is no simple electrolytic preparation of the gas, which is only semi-volatile at room temperature. The commercially supplied material was also stored in glass phials, not in metal cylinders as in the case of chlorine, and was, therefore, less likely to contain metallic impurities. To provide sufficient gas for the reaction, the bromine was heated to 350K in a water bath. No drying reagent was used and the upper part of the furnace vessel and gas transfer tube were warmed with a heating coil to prevent condensation of the bromine. The silver reacted very much more quickly with the bromine ($\simeq \frac{1}{2}$ hour) than with the chlorine ($\simeq 4$ hours).

The silver chloride prepared was colourless and usually showed negligible volume darkenability when exposed to light and represented a considerable improvement over typical commercial material. The silver bromide samples were a clear yellow colour and also showed no bulk sensitivity to light. E.P.R. tests for Fe, Mn and Cu after annealing in nitrogen and halogen atmospheres compared favourably with readily available

commercial materials. Manganese was detected in some samples, but at levels of less than 1ppm, in contrast to 5ppm of Mn present in B.D.H. 'Optran' material. The samples were annealed in vacuo and then in a halogen atmosphere and tested for sensitivity to light after each anneal. An increase in the volume sensitivity after annealing in $N_2$ would indicate the presence of sensitizing impurities such as copper[1]. No such increase was detected and the overall cation impurity levels are believed to be below 1ppm. These pure samples were used for tests of light sensitivity and some E.P.R. work. However, when high levels of impurity were to be added to the samples, commercial material was used.

## 3.1.2 Doping of samples

Several methods were used to introduce the required cation impurity into the silver halide. The most effective method with a large number of impurities was to dip a strip of the metal into the molten silver halide for a few seconds in the appropriate halogen atmosphere. This method was generally successful, even for metals which oxidised readily, provided that care was taken to exclude air by maintaining a steady flow of halogen gas over the sample. With some of the rare earths, for example cerium, neodymium and samarium, the temperature of the molten halide had to be held only just over the melting point to prevent spontaneous combustion of the dopant material.

Where the metal was unobtainable, or was very unstable in air (for example europium), doping was achieved by the addition of the metal halide to the molten silver halide under a halogen atmosphere. The metal halide could also be added by diffusion into the silver halide at

temperatures just below the melting point. This method was not used, except in the case of thin film samples because it was slow and often gave uneven doping. In some cases the chloride reduced to the metal and failed to diffuse.

With metals which did not appear to dissolve easily in the molten halide (for example cerium and samarium) a current was passed through the halide while doping was taking place. The metal dopant was connected to the positive terminal of a low voltage supply and a silver metal electrode to the negative terminal. Passing a current of 0.1A for a few seconds was found to increase the amount of metal dissolving in the silver halide and was particularly useful in the case of large impurity ions.

As described, doping in the presence of excess halogen was found most successful. The heavily doped material was diluted with pure halide. The valent state of the impurity ion was then, when required, reduced by annealing at temperatures just below the melting point in nitrogen or in vacuo. When reduction of the impurity ion was difficult, the sample was placed in contact with metallic silver to encourage diffusion of electrons into the sample.

### 3.1.3  Crystal growth

Crystals were grown using the Bridgman-Stockbarger method. The silver halide was placed in a pyrex tube of external diameter 1cm. The tubes were made with conical ends to encourage the crystal to grow from a single point. They were evacuated to $10^{-5}$mm Hg while being heated to about 500K to remove water vapour and were sealed with a glass hook. In cases

where doping was difficult, halogen gas was then allowed into the tube at a pressure below one atmosphere and the boule was sealed. Growth of the crystal under a halogen atmosphere usually maintained a higher concentration of dopant in the final crystal than growth in vacuo.

The sample tube was attached to a short length of copper wire which was suspended by a cotton thread wound on an axle. A belt and pulley system driven by a Velodyne was used to obtain a constant velocity drive which could be set to any value within an order of magnitude range. The flexible drive system was used to prevent vibration from the motor being transferred to the sample and furnace. The furnace was placed on the floor and the Velodyne on a bench a short distance from the furnace. After melting in the hot zone of the furnace, the sample was lowered at a rate of 4 - 6mm per hour.

The furnace was designed to provide an 8cm region where the temperature was above the melting point of the halide, followed by a sharp temperature drop of 100K in 1cm over the melting point, and then a region where the temperature fell gradually to room temperature. This was achieved by using a single silica tube of 13mm O.D. wound with two Nichrome coils separated by 5mm (fig. 3.2). The furnace was contained in a syndanio box to reduce the effects of air currents. The absence of thermally insulating packing ensured that a sharp temperature gradient could be set up. The sample tube was only slightly smaller than the furnace tube and both were narrow so that the temperature profile across the tube was quite flat. The two furnace windings were supplied through variable auto-transformers from an "Advance" constant voltage supply to minimize the effects of mains voltage fluctuations.

Pyrex tube

Syndanio
box

Upper
furnace
windings

Lower
furnace
windings
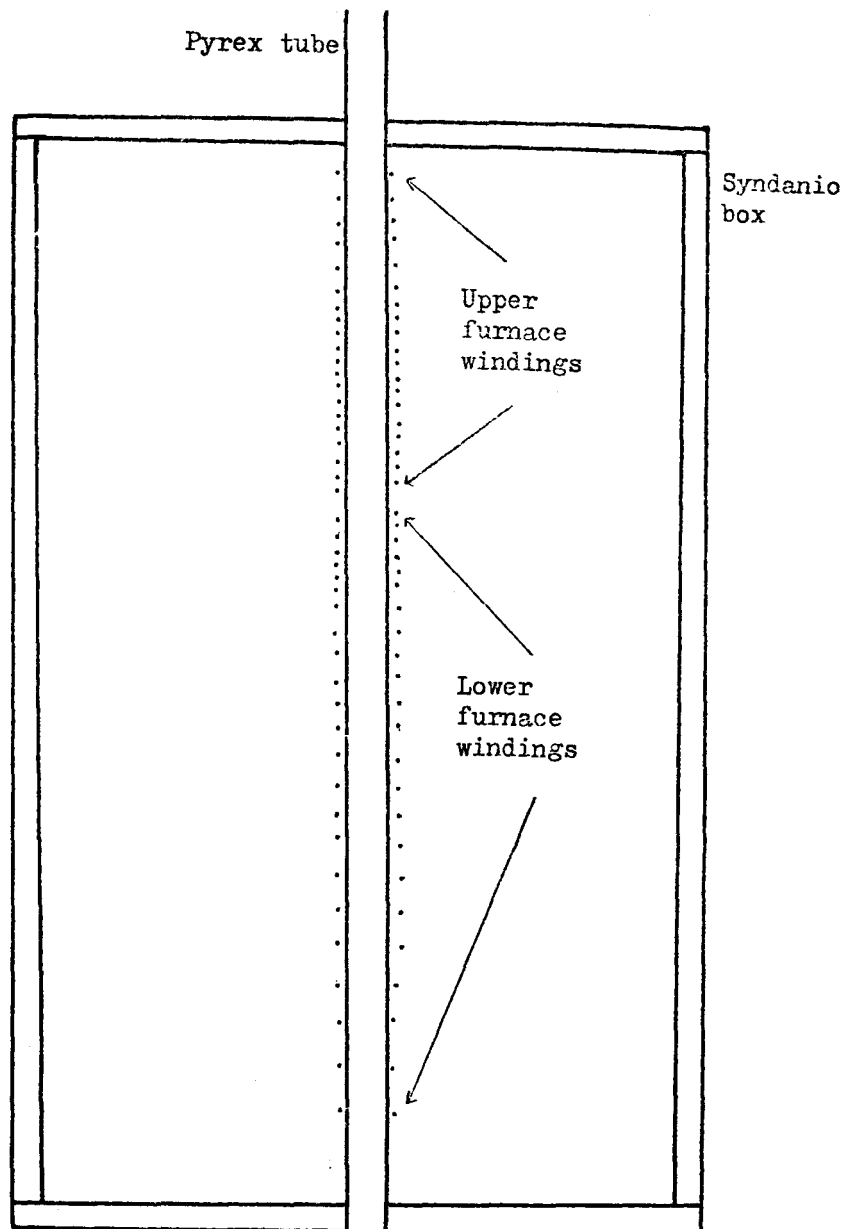
Fig. 3.2. The crystal growing furnace.

Crystal growth was carried out at night when vibrations and fluctuations in ambient temperature were at a minimum. The steep temperature gradient and the relatively high rate at which the sample passed through it made electronic temperature control of the furnace unnecessary.


3.1.4  Crystal orientation


The silver halides do not cleave at room temperature and mechanical cutting can cause damage to the crystals. In order to reduce the damage the crystals were cut by a string chemical saw using dilute sodium thiosulphate (hypo) solution. A nylon thread was passed back and forth over the crystal and through the hypo solution by means of a motor whose direction was reversed automatically approximately every 30 secs. The speed of the motor and the tension in the thread could be adjusted.


The crystals were polished on soft cloths soaked in dilute hypo and washed for 2 - 3 minutes in hypo solution, distilled water, dilute HCl to remove any metallic or sulphur deposits, and finally in distilled water again. X-rays of wavelength about 1Å penetrate less than 0.1mm below the surface[4] and so the quality of the X-ray pictures obtained depended critically on careful preparation of the surface. Poor quality crystals could be identified from the grain boundaries revealed by etching in hypo solution.


The nature of the polished plane was determined from Laue back-reflection X-ray photographs[5]. Exposure times of half an hour were used with a Phillips 3cm camera and X-ray set run at 40kV and 15mA. The prominent lines of spots on the film are produced by planes in the same zone in the crystal. These zones were measured using a Greninger chart

and were plotted on a stereogram with a Wulff net. The angles between
the zone axes, which can be considered equivalent to planes in the case
of these cubic crystals, were measured. Indices were assigned to the
faces by comparison of the angles with those between prominent faces of
cubic crystals.

The crystal was then turned so that a required face was directed
towards the X-ray beam and was re-polished. Further X-ray photographs
were taken and their self-consistency was used to establish the single
crystal nature of the specimen. Usually {100} and {110} faces were
prepared so that the crystal could be mounted on these faces and
rotated in these planes. The simplification of the E.P.R. spectrum
when the magnetic field was aligned with an axis of low indices and the $90^{\circ}$
repetition of the spectrum in the {100} plane provided a precise means
of final alignment.

### 3.1.5 Other samples

For some optical sensitivity and resolution work thin crystal
sheets were prepared as described by Clark and Mitchell[6]. A thick
stainless steel slab was heated at one end with bunsen burners. Molten
halide was placed between two silica sheets separated by glass spacers.
The sheets were moved slowly down the slab by a metal bridge attached to
a rotating screw thread. After cooling, the silica sheets were soaked in
dilute HCl solution until the halide could be removed from the glass.
Etching showed single crystal areas about 0.5cm across. The dopant
added to the melt was often partly removed by zone refining during this
preparation. Diffusion doping was used afterwards to restore the required
impurity level.

In a photographic film the silver halide is in the form of an
emulsion in which microcrystals of the halide are held in gelatin. The
present studies of silver halide E.P.R. were carried out on bulk samples.
These have the advantages over the emulsions that single crystals rather
than randomly oriented microcrystals are used and that volume effects
will certainly dominate over surface effects. However, it might be
argued that an investigation of emulsions would be more relevant to the
photographic process. A normal water-based emulsion is inconvenient as
it reduces the Q-factor of the microwave cavity because of the molecular
absorption by water at microwave frequencies. A non-water based
emulsion was successfully prepared using glycerol. Both $AgNO_3$ and KCl
dissolve in glycerol[7]. $AgNO_3$ was dissolved in fresh dry glycerol by
warming the mixture very gently. KCl was dissolved in another beaker of
glycerol and the contents of the two beakers were then mixed. A thick
precipitate of AgCl formed gradually. The emulsion was sensitive to
light, but time did not permit further experiments to be made on this
system.

## 3.2    The Decca E.P.R. spectrometer

### 3.2.1  Microwave system and cavity

E.P.R. measurements were made using a DeccaXI spectrometer
operating in the simple detection mode. The standard cavity and
associated dewar were used in the temperature range 573K to 95K. This
is an X-band (9270 MHz) reflection system in which the signal kylstron
may be phase-locked via a reference oscillator to a quartz crystal

frequency standard to reduce klystron F.M. noise. A harmonic generator provides a 9300 MHz signal from the 30 MHz frequency standard. The beat frequency between this and the signal klystron is compared in phase with a reference voltage controlled oscillator operating at about 30 MHz. Any phase difference is used to provide the necessary change in klystron reflector voltage.

In the simple detection mode high frequency field modulation at 100 KHz is used to reduce crystal noise. Phase sensitive detection at 100 KHz is also used to reduce the bandwidth and, hence, the noise of the detecting system. Modulation coils are fixed in the cavity walls on either side of the sample beneath glass sheets plated with a thin layer of gold which is transparent to 100 KHz but not to microwave frequencies.

The rectangular cavity operates in the TE102 mode with the sample placed at its centre. The cavity is tuned to the klystron by reducing the reflected signal to zero using the variable coupling and tuning controls provided. For maximum sensitivity the cavity must remain tuned to the klystron while the spectrum is swept. The E.P.R. signals investigated were, in general, well above the noise level of the system and so the klystron was usually locked directly to the cavity while sweeping a spectrum, although this rendered the klystron frequency phase-lock inoperative. The direct cavity lock provided a larger range of klystron frequencies (9270 $\pm$ 10 MHz) than the alternative cavity-corrected phase-lock which did not override the klystron phase-lock to the reference oscillator.

The quoted sensitivity of the system is $4 \times 10^{11}$ spins per 0.1mT linewidth at 1mW microwave power and one second time constant.

The Decca gas flow system and automatic temperature controller provided continuously variable temperatures in the range 573K to 95K to within ± 2 K. A device was constructed to provide a continuous supply of nitrogen gas at the high flow rates required for several hours. Gas cylinders were found inconvenient as they did not last sufficiently long. Liquid nitrogen prepared in the Department of Physics was readily available. Electric coil heaters were placed in the liquid nitrogen dewars and the gas which boiled off was used to operate the low temperature system in the usual way. The voltage across the heaters was altered to provide the required gas flow rate.

### 3.2.2 Newport 11" magnet

The Newport 11" magnet provided automatic field sweeps at a number of different rates. An integrating magnetometer provided a signal accurately proportional to the field change from the start of the sweep. The signal was used to drive the Y axis of the pen recorder. The field was calibrated by a proton resonance magnetometer and a frequency standard provided a range of marker pips appropriate to fields from 0.2T to 0.6T at various intervals down to 1mT. 50Hz field modulation coils were also provided for visual display of resonances on an oscilloscope. The quoted homogeneity of the field, using pole pieces spaced 3 inches apart, was a few parts in $10^6$ over a volume of $1.0 \text{cm}^3$.

### 3.2.3 Sample support

Samples were attached by "Durofix" to one end of a silica rod, the other end of which was attached to a goniometer graduated in degrees. This

arrangement enabled the sample to be rotated about a vertical axis in the

cavity. A modification to the sample mount was made (fig. 3.3) so that

small angle rotations about a horizontal axis were possible. The sample

was attached to a small P.T.F.E. platform which was supported by a fine

horizontal silica rod set in a P.T.F.E. support held in the end of a

silica tube. Two nylon cords, which were attached to the platform, passed

around the support and through the silica tube to a horizontal axle above

the goniometer table. The height of the axle was adjustable so that the

tension in the cords could be maintained over the range of temperatures

used. The axle was turned by means of a 20:1 reduction gear. This

arrangement provided a convenient method of fine adjustment of the plane

of rotation of the sample. The setting was checked by observation of the

E.P.R. spectrum.


## 3.3    The low temperature E.P.R. system


### 3.3.1  Cavity and microwave system

To enable measurements to be made at temperatures below 95K a

dewar and cavity were constructed. The system was designed to be compatible

with the Decca spectrometer described in section 3.2.1. From considerations

of size, weight and ease of construction, a single mode rectangular TE 101

cavity was used. This was milled from two pieces of brass screwed

together as shown in fig. 3.4. As the cut was made across the currents

in the cavity wall[8], the high conductivity joint which is required if the

cavity Q is to be maintained was achieved by placing thin copper shims

between the sections. The inside of the cavity was gold plated to

Scale: $\frac{1}{2}$ actual
       size

Silica tube

Nylon cords

Actual size

Side      Front
view      view

Cords

Fine
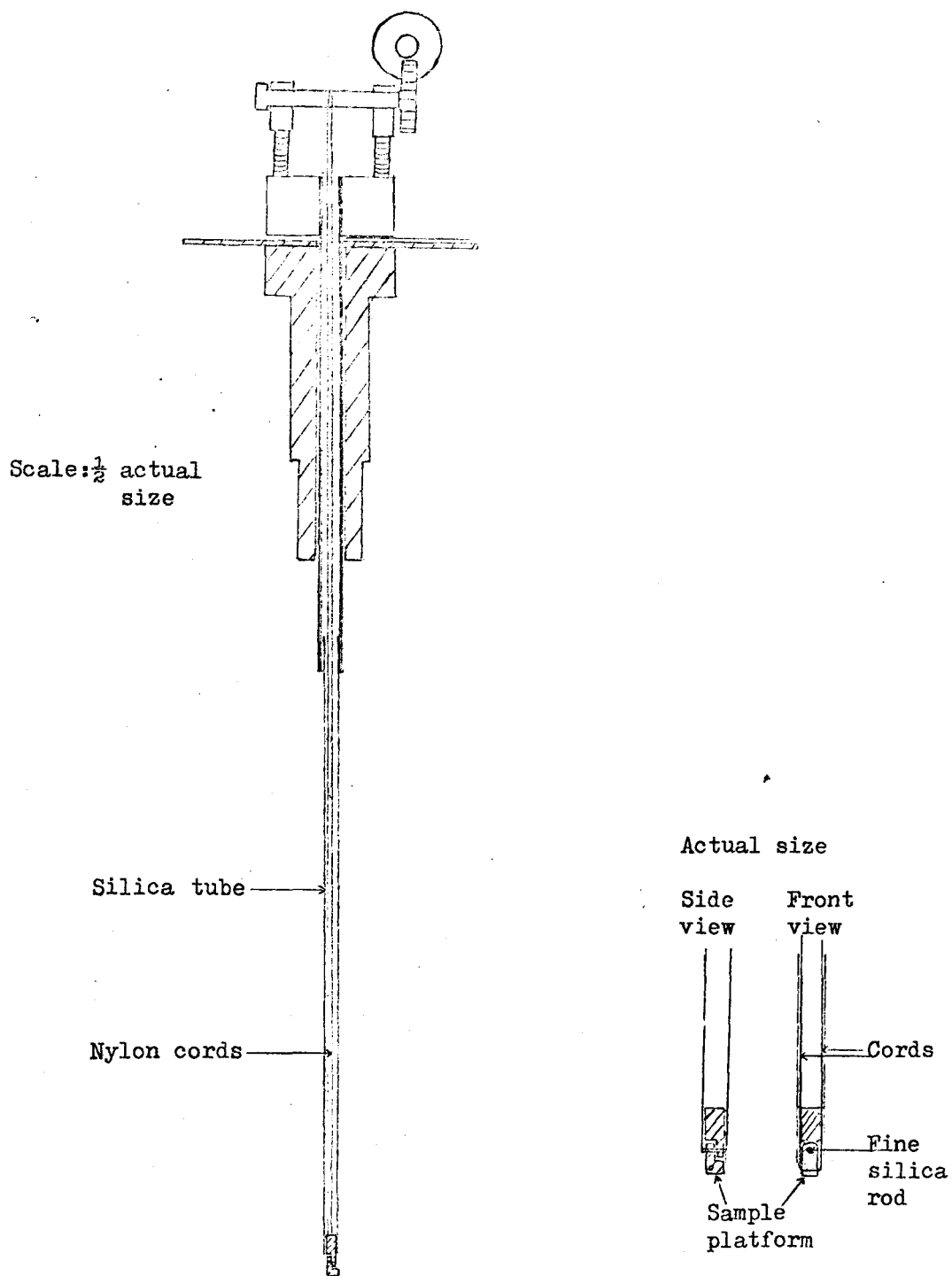silica
rod

Sample
platform

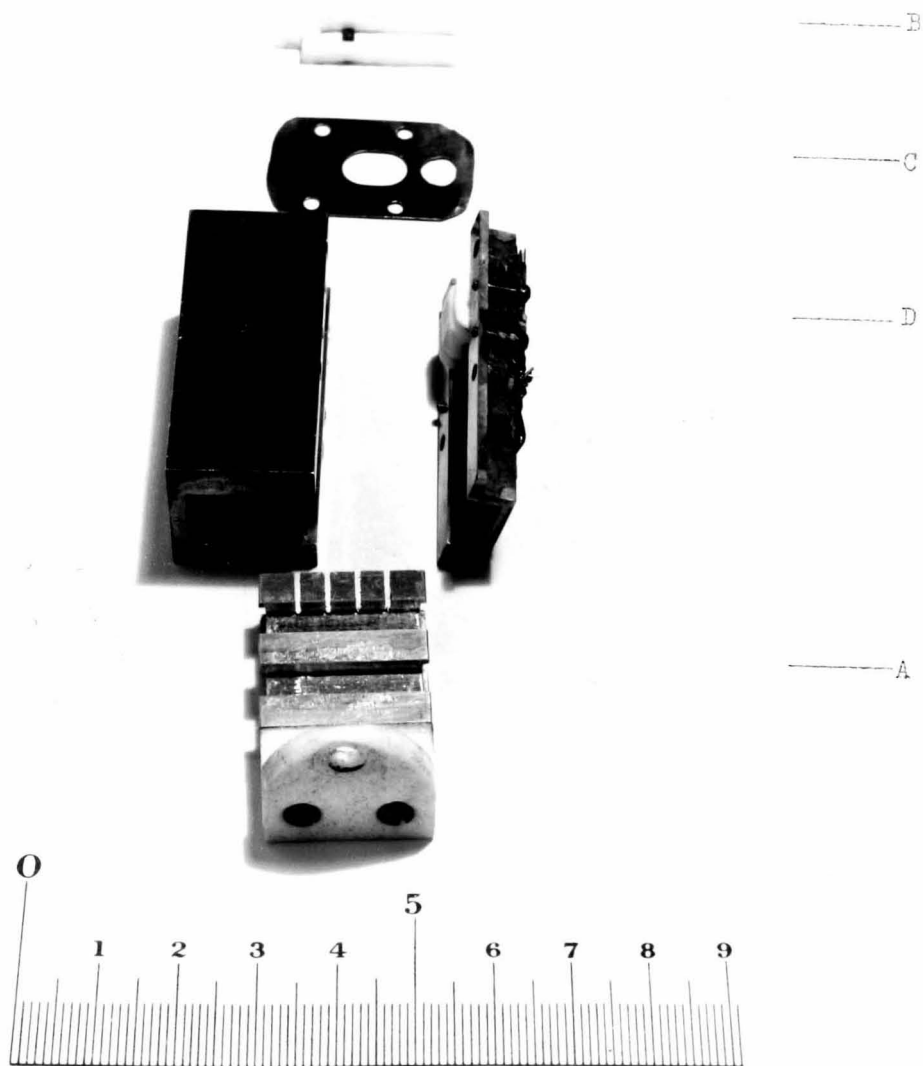Fig. 3.3. The sample support for the Decca cavity.

Fig. 3.4. The cavity and tuning arrangements.

improve the surface conductivity and reduce the cavity background signal. The cavity was tuned to the frequency of the klystron by making its lower end from a standard moveable waveguide short circuit component (fig.3.4A).

The cavity was offset by about 4mm from the stainless steel wave-guide[9] to allow for the introduction of the samples (fig. 3.5). The samples were placed in thin-walled silica tubes attached by "Durofix" to a P.T.F.E. screw which was fixed into the end of a long stainless steel tube.

The upper end of the cavity was formed from a thin (0.2mm) copper sheet bolted to the body of the cavity by means of a flange on the wave-guide. A hole of 4mm diameter in the copper sheet was located between the centres of the cavity and the waveguide (fig.3.4C). This arrangement gave optimum coupling between the waveguide and the cavity. A capacitive variable coupling arrangement provided small changes in coupling coefficient. A small rectangular piece of copper sheet set in a P.T.F.E. support was moved over the coupling hole, about 2mm above it, and gave a sufficiently large variation of coupling coefficient (fig. 3.4B). However, in some later experiments, this device was thought to be vibrating at low temperatures and causing unacceptably large variations in reflection coefficient. It was, therefore, removed and a slide-screw tuner placed in the waveguide outside the dewar system to cancel out any small changes in reflected signal from the frequency tuned cavity at zero field (fig. 3.7).

Since the cavity was to be used with 100KHz modulation, and the walls were thick, the modulation coils were placed on either side of the sample in a P.T.F.E. support inside the cavity. The coils were constructed from five turms of 35 S.W.G. silk covered copper wire. The
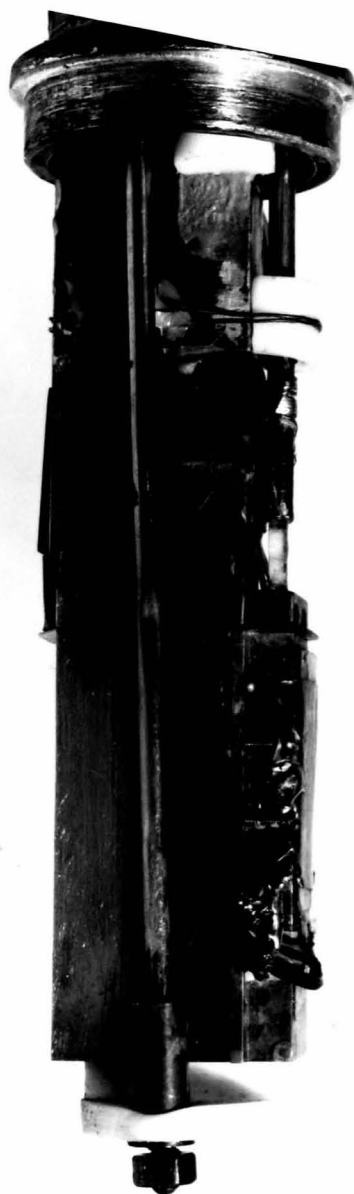
Fig. 3.5. The cavity, wave-guide and sample in position.

coils were placed in a region of small or zero cavity electric field and perpendicular to this field in order that they should have the minimum effect on the cavity Q-factor and would not act as microwave probes[8,10]. The leads to the coils were passed through small holes in the cavity walls placed to give minimum interference with the wall currents. The leads were oriented so that they were not parallel to the electric field or, otherwise, they would couple strongly to the microwave field[10]. In spite of the above precautions, considerable problems were encountered with microwave leakage through the coil leads which altered the cavity Q and gave rise to changes in the resonant cavity frequency if the wires were in any way free to move. These problems were largely eliminated by fixing the leads rigidly to a sandwich of mica and copper sheet on the outside wall of the cavity (fig. 3.4D). The sandwich acted as a short circuit at microwave frequencies but not at 100KHz. The low impedance modulation coils were matched to the higher impedance of the Decca 100KHz supply by means of a tuned air cored transformer coil. In use the modulation depth near the sample was calculated to be 0.2 - 0.3mT using the usual expression for a pair of Lorentz coils.

The cavity Q was measured directly on a test bench using a klystron with 50Hz modulation to display the cavity resonance at 9270 MHz on an oscilloscope. With the modulation coils and sample in place the Q-factor was about 1,000 at room temperature. In view of the number of holes and joins in the cavity, the Q-factor was not expected to increase at low temperature as a result of the increased conductivity of the walls. The spin sensitivity at 4.2K was estimated by recording the spectrum from a sample of coke which had been calibrated by comparison with weighed samples of D.P.P.H. in the Decca cavity at room temperature. The low temperature system could detect about $10^{15}$ spins per mT linewidth

at 4.2K with a 0.1s time constant. At high microwave power and high 100 KHz amplifier levels a background signal proportional to both the steady and 100 KHz magnetic fields made detection of small resonance lines at low fields difficult.


3.3.2 Cooling arrangements


The 3" magnet gap enabled glass to be used for part of the system. The outer liquid nitrogen dewar was double-walled silvered glass, with an unsilvered portion for observation of the liquid level. In the original design the lower sections of the inner liquid helium bath and cavity jacket were made of glass so that the sample could be illuminated directly from the front of the magnet through windows in the cavity. The limited space available meant that the helium resevoir had to be made of metal. The different metals used (copper and stainless steel) and the glass to metal seals involved created numerous vacuum leaks which could not be overcome. The liquid helium dewar was, therefore, finally constructed entirely of thin walled stainless steel by the Oxford Instrument Co. Ltd. The entire waveguide and sample section was isolated from the liquid helium by a further stainless steel tube. The lowest section of the inner tube, which surrounded the cavity, had to be slightly larger than the section above the cavity and the parts were joined with a demountable Woods metal seal to allow easy access to the cavity (fig. 3.6).

Liquid helium condensed in the dewar within 20 minutes of slow cooling from 77K using $\frac{1}{2}$ litre of liquid helium. In use, the boil-off rate was approximately $\frac{1}{2}$ litre of liquid helium per hour and the system could hold about $1\frac{1}{2}$ litres of the liquid. It was found necessary to fill

N

O

Vacuum pumps

A. Moveable short-circuit .
B. Brass cavity .
C. Sample
D. Coupling control rod .
E. Sample guide tube .
F. Wood's metal seal .
G. Tuning control rod .
H. Stainless steel wave-guide.
I. Liquid helium dewar.
J. Liquid helium inlet.
K. Goniometer.
L. Pointer.
M. Mica wave-guide vacuum seal.
N. Helium gas outlet.
O. Rotary pump and helium
   gas supply.

J

I

H

Scale: ½ actual size
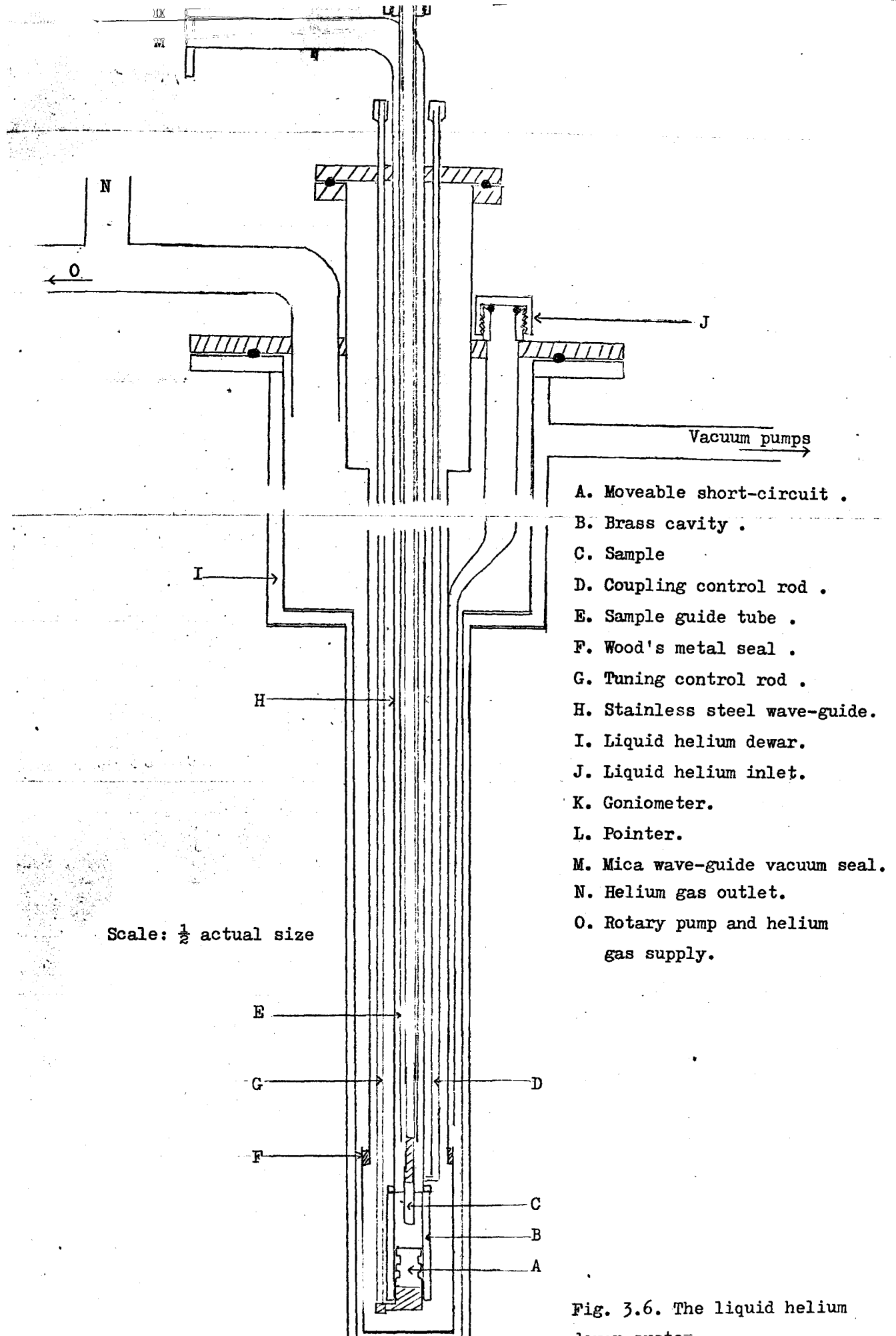
E

G                    D

F

C

B

A

Fig. 3.6. The liquid helium

the entire waveguide and cavity section with helium gas to bring the sample temperature down to 4.2K. If this space remained evacuated the sample temperature was about 18K.

The sample could be changed after warming the system to 77K. Excess helium pressure was then maintained in the sample section while the sample was changed, and successfully prevented icing up at 77K. At temperatures below this, however, even with considerable excess helium gas pressure, it was found impossible to prevent oxygen entering and freezing in the system. Fig. 3.7 shows the dewar and vacuum systems. A combination of rotary and diffusion pumps was used to evacuate the dewars to $10^{-5}$ Torr or less. A second rotary pump was used for rough evacuation and flushing with helium gas of the sample section and the helium well before use. All the inner dewars and sections were filled with helium gas to expedite the initial cooling to 77K with liquid nitrogen.

The sample and cavity temperature was measured using a gold and 0.03% iron with chromal thermocouple. This was calibrated by direct immersion in liquid helium and in nitrogen and by interpolation in the interval. The thermocouple voltage was measured with a "Comark" multimeter.

## 3.4 Optical measurements

The silver halide crystals were exposed using a projector with a 100 W quartz-iodine bulb and gelatin and glass colour filters. The projector was used for illuminating samples in the Decca cavity, via the cavity windows, with suitable lenses. A silica rod was placed inside the
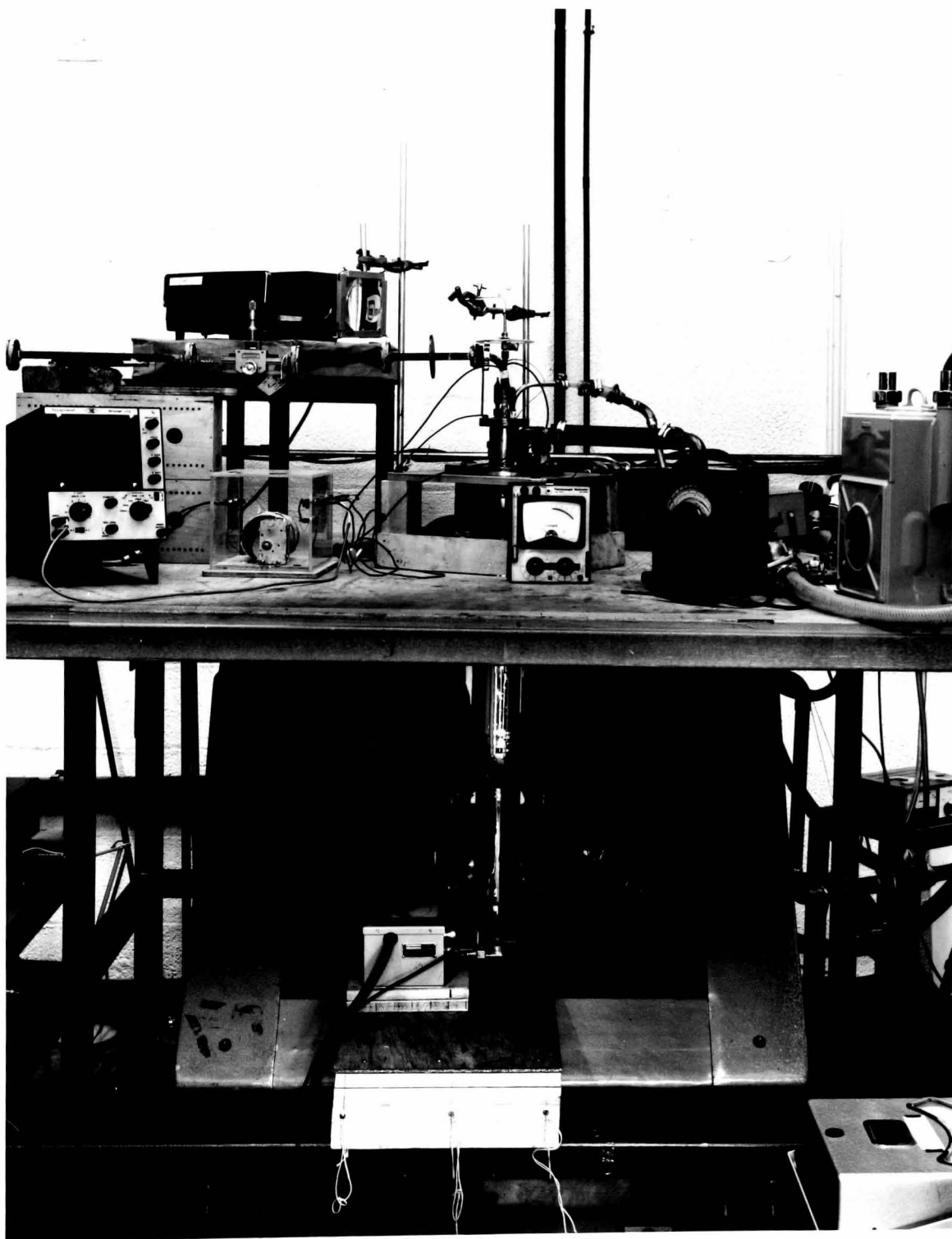
Fig. 3.7. The low temperature system.

stainless steel sample support tube in the liquid helium system and acted as a light guide for illumination of the samples (fig. 3.8).

Other optical sensitivity and optical absorption measurements were made using a Perkin-Elmer Model 450 double beam spectrophotometer. A dewar was also used with the spectrophotometer to cool the sample to 90K and 20K with liquid nitrogen and helium. Exposure of these samples was also carried out with the projector or a mercury lamp while they were in the Perkin-Elmer sample holder. Typical illumination intensities were $10^{17}$ photons/$cm^2$ sec. estimated using a Hilger Schwarz thermopile and Keithley electrometer.

Irradiation of samples with wavelengths below the band edge of AgCl (420nm) produced high surface colouration since the light is strongly absorbed by the material. Light absorption in the bulk of the samples can be achieved by using wavelengths in the long wavelength tail of the band edge[1]. Irradiation was, therefore, carried out using a Barr and Stroud 450 - 500nm band pass filter or a Grubb Parsons filter which passed 434 ± 7nm wavelengths.

Fig. 3.8. Irradiation of samples in the low temperature system.

54

## 3.5   References

1    F. Moser, N.R. Nail and F. Urbach,   J. Phys. Chem. Solids, 99, 217 (1959)

2    J. Malinowski,   J. Photog. Sci., 8, 69 (1960).

3    J.A.V. Butler,   Chemical Thermodynamics, Chap.VII,   Macmillan (1965).

4    C.E.K. Mees and T.H. James,   The Theory of the Photographic Process, Macmilland, New York (1966).

5    F.C. Phillips,   An Introduction to Crystallography,   Longmans (1963).

6    P.V. McD. Clark and J.W. Mitchell,   J. Photog. Sci., 4, 1 (1956).

7    Handbook of Chem. and Phys., The Chemical Rubber Co., Cleveland, Ohio (1969).

8    R.S. Alger,   Electron Paramagnetic Resonance,   J. Wiley, New York (1968).

9    W.D. Ohlsen,   Rev. Sci. Inst., 33, 492 (1966).

10   D.E. Cark and H.J. Mead,   Electronic, Radio and Microwave Physics, Heywood (1961).

54

Chapter Four :  Chromium in AgCl and AgBr

4.1    Introduction

Several members of the iron transition series have been studied

as impurities in the silver halides.  E.P.R. measurements have been made

on $V^{2+}$ [1], $Mn^{2+}$ [2], $Fe^{3+}$ [3,4], $Co^{2+}$ [5], $Ni^{2+}$ [6,7] and $Cu^{2+}$ [8,9,10].

Chromium was chosen for this study as it is most likely to give E.P.R. in

the trivalent state and would provide information on the surroundings and

behaviour of a trivalent ion in a monovalent lattice.  The only trivalent

ion studied previously by E.P.R. in the silver halides is $Fe^{3+}$ [3,4].

$Fe^{3+}$ is incorporated in the lattice in an interstitial position and is

surrounded, at low temperatures, by four $Ag^+$ vacancies at the corners of

a tetrahedron (provided that the trivalent state is not produced at low

temperatures).  $Cr^{3+}$ is a $3d^3$ ion with a zero nuclear spin in 90% of the

isotopes.  In an octahedral field of intermediate strength the ground

state is a singlet orbital level with four-fold spin degeneracy.  The

spectrum is expected to be reasonably simple and detectable at room

temperature.

Chromium has been studied in AgCl and AgBr by optical absorption[11],

thermal depolarization currents (T.D.C.)[12], dielectric loss[13] and

ionic conductivity measurements[11].  These papers conclude that the

$Cr^{2+}$ and $Cr^{3+}$ ions are incorporated substitutionally in the halide

lattice and that the $Cr^{3+}$ ion is associated with two vacancies at low

temperatures.  Annealing in vacuo produces $Cr^{2+}$ and annealing in an halogen

atmosphere produces $Cr^{3+}$.  Busse has observed the E.P.R. of $Cr^{3+}$ in AgCl

but was not able to analyse it[11].

The incorporation, vacancy association and photolytic behaviour of divalent and trivalent chromium will be discussed. The system may be compared with $AgCl:V^{2+}/V^{3+}$ and $AgCl:Fe^{2+}/Fe^{3+}$ which have already been investigated[1,4].

## 4.2    Experimental details

Chromium doped silver halide was prepared from chromium metal and the molten halide as described in section 3.1.2. The single crystals were generally grown in vacuo. The AgBr:Cr crystals were more sensitive to conditions of growth than AgCl:Cr and some were grown in a bromine atmosphere. Those grown in vacuo were a clear yellow (AgCl:Cr) or yellow-green (AgBr:Cr) colour. The crystals were heated to 580-630K in the appropriate halogen atmosphere to convert the ions to the trivalent state and ensure complete dispersal of the precipitates. They were cooled to room temperature over a period of 10-20 minutes. The crystals were then clear and orange to red-brown in colour. Samples were grown with concentrations of chromium in the following ranges:

| | |
|---|---|
| low-doped | 5-10ppm |
| medium-doped | $\sim$ 100ppm |
| high-doped | 1,000-5,000ppm |

E.P.R. measurements were made in the temperature range 95K to 550K on crystals oriented in {100} or {110} planes. Samples were oriented using Laue back reflection X-ray photographs and the symmetry properties of the spectrum. No E.P.R. was observed from the $Cr^{2+}$ state at room temperature, 95K or 4.2K.

## 4.3     Experimental results for AgCl

### 4.3.1   The spectrum at 95K

Figs. 4.1, 4.2 and 4.3 show the spectra observed with the applied magnetic field B parallel to the $<100>$, $<110>$ and $<111>$ directions in a medium-doped sample. There are more lines present than would be expected for a single $S = \frac{3}{2}$ centre. As the sample was rotated all the extreme positions of the lines occurred at $<100>$ or $<110>$ directions, not at $<112>$ or $<111>$ directions, indicating that all centres involved have $<100>$ or $<110>$ principal axes. However, one line labelled Z (fig. 4.4) reached minimum and maximum fields at $<100> \pm 4^{\circ}$. The line widths of some of the outer fine structure lines increased up to 5mT as the crystals were rotated away from B parallel to $(/\!/) <100>$. The line widths and the overlapping of the lines between 0.29 and 0.35T made it difficult to follow the movement of the lines as the sample was rotated.

The same spectra were obtained in the low-doped samples. In the high-doped samples a broad central line appeared at g = 1.98 with a width of approximately 6mT and the outer lines decreased proportionately in size (fig. 4.5).

### 4.3.2   The spectrum at room temperature and above

Fig. 4.6 shows the spectrum at 300K with B$/\!/<100>$. On warming from 95K to 300K the outer lines broadened and decreased in intensity while a central line at 0.3345T increased in intensity. The remaining central lines also decreased in intensity. Most of the outer, fine structure
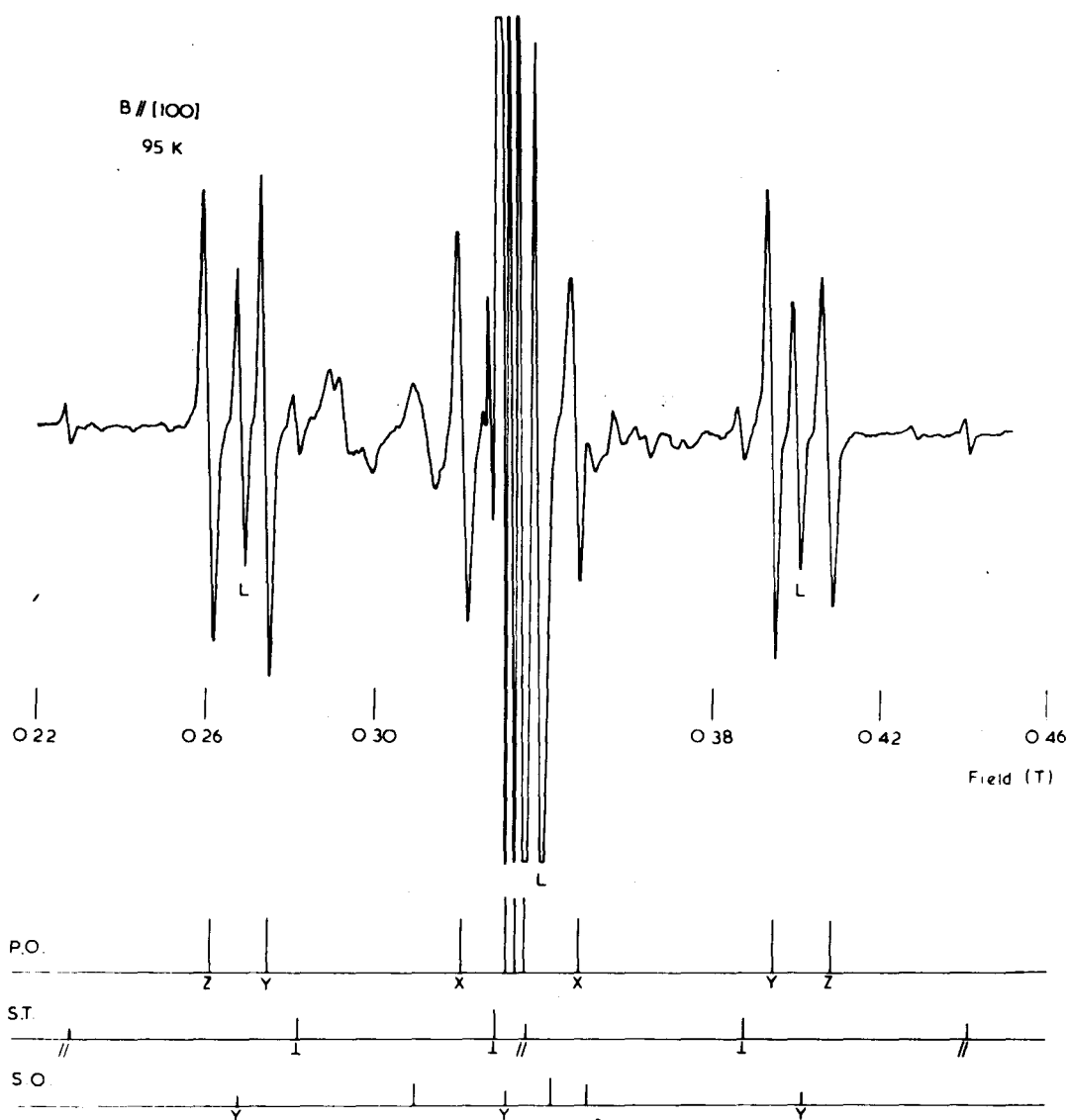
Fig. 4.1. The E.P.R. of $Cr^{3+}$ in AgCl at 95K with B $//<100>$.
The line positions calculated using the spin Hamiltonian
parameters given in the text are shown for the principal orthorhombic
centre (P.O.), the subsidiary tetragonal centre (S.T.) and the
subsidiary orthorhombic centre (S.O.) .
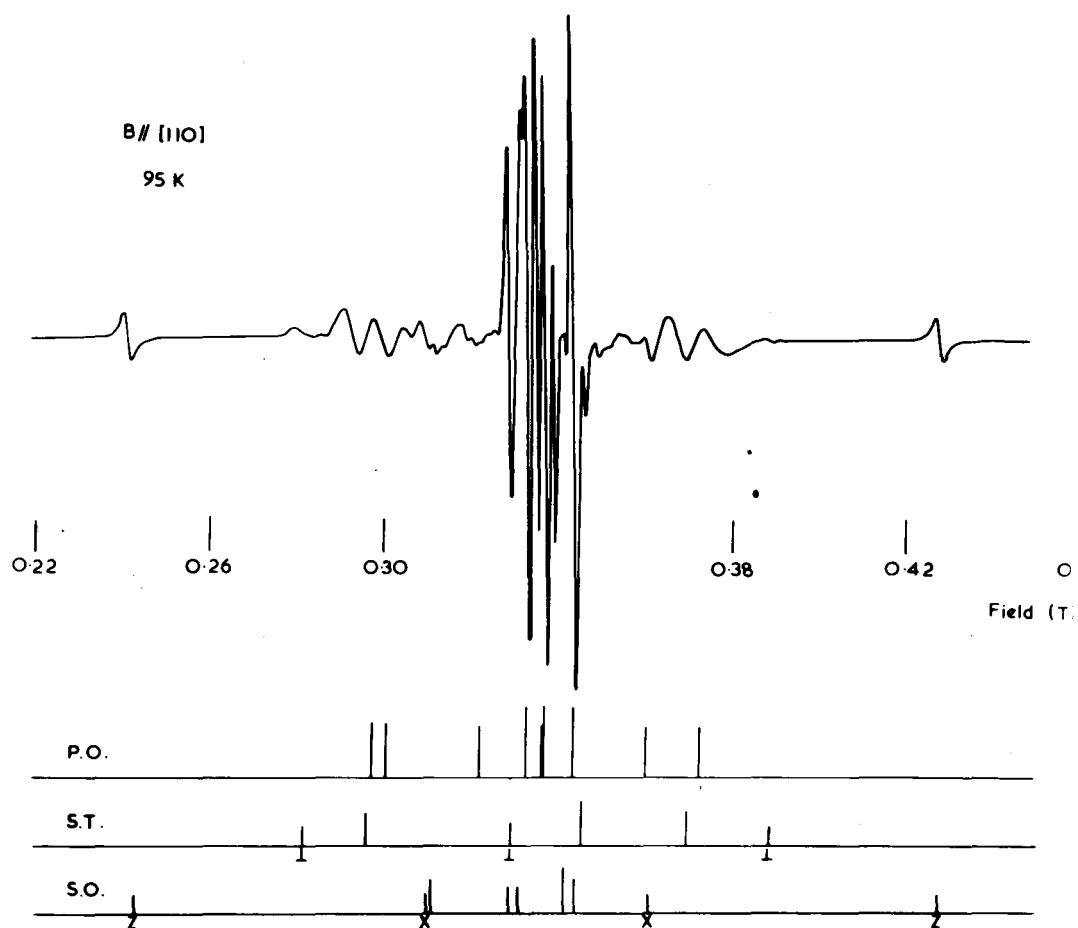
Fig. 4.2. The E.P.R. of $Cr^{3+}$ in AgCl at 95K with B $//\langle 110 \rangle$.
The calculated line positions are shown as in fig. 4.1.

B // (III)

95 K

O 28    O 30    O 32    O 36    O 38    O 40

Field (T)

P O

S T

S O
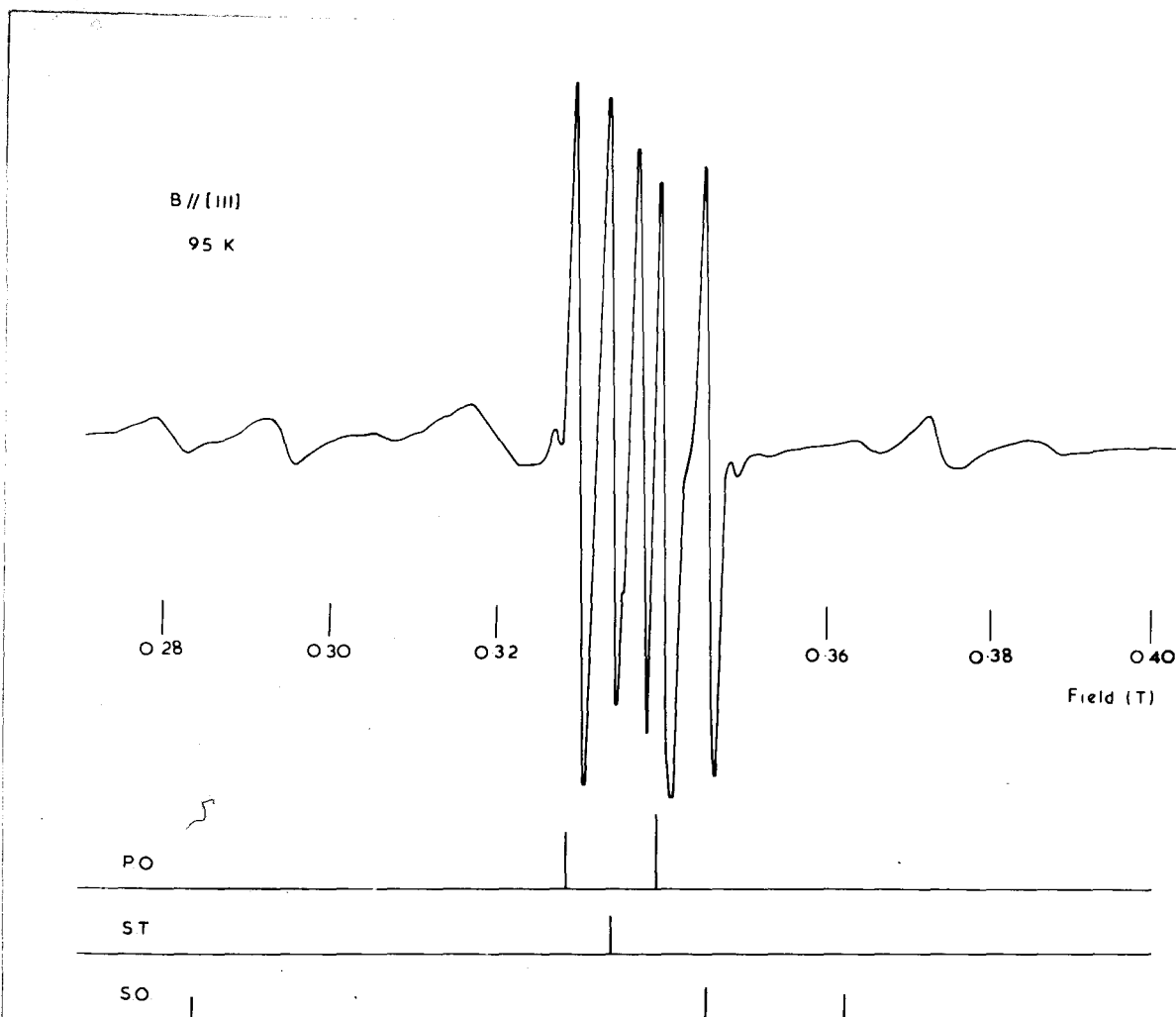
Fig. 4.3. The E.P.R. of $Cr^{3+}$ in AgCl at 95K with B // $\langle 111 \rangle$ .

The calculated line positions are shown as in fig. 4.1.
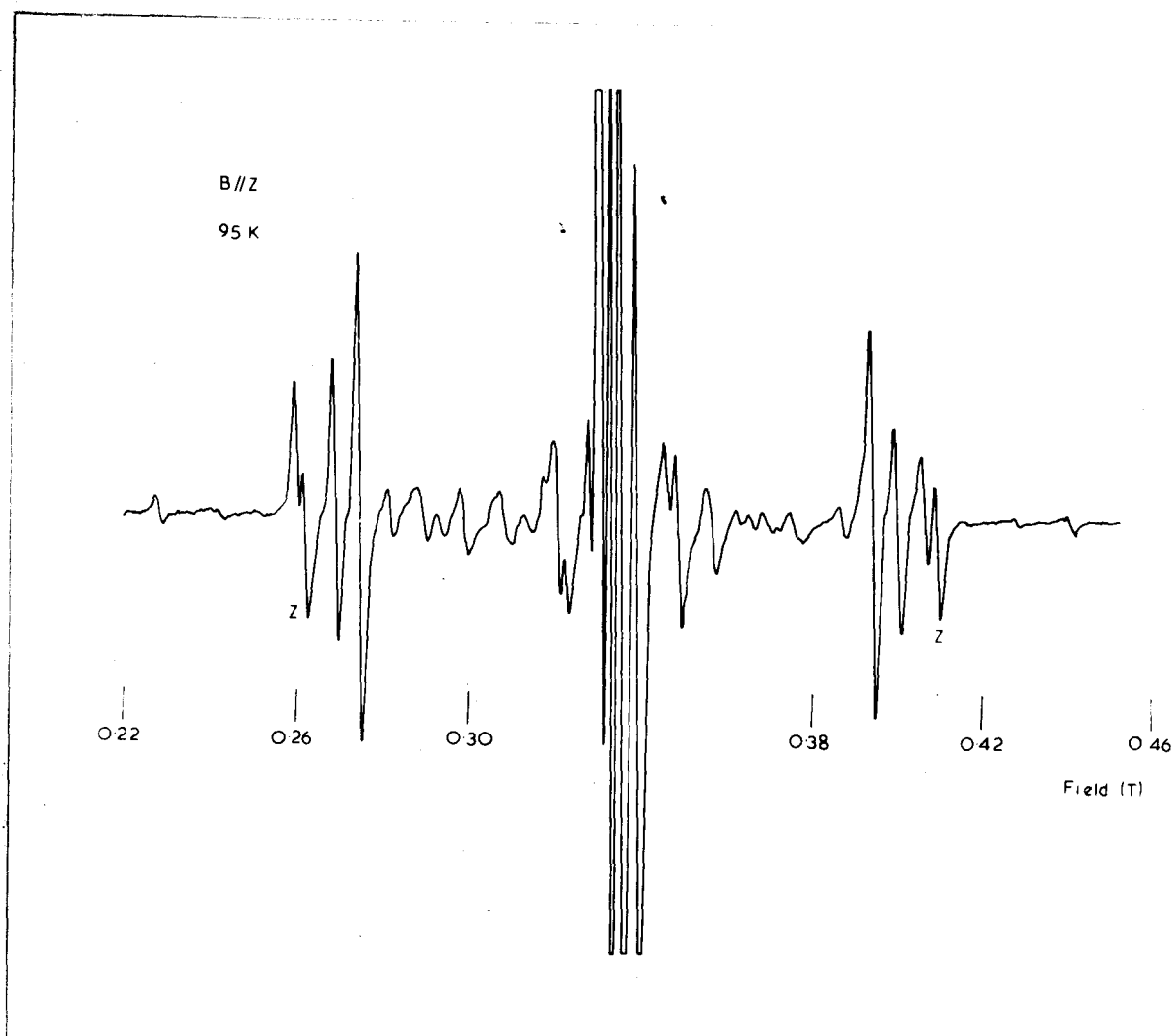
Fig. 4.4. The E.P.R. of $Cr^{3+}$ in AgCl at 95K with B parallel to the Z axis of the principal orthorhombic centre. The fine structure lines from centres with B // Z are labelled Z.

B // [100]

95 K

0.30

0.38

Field (T)

C
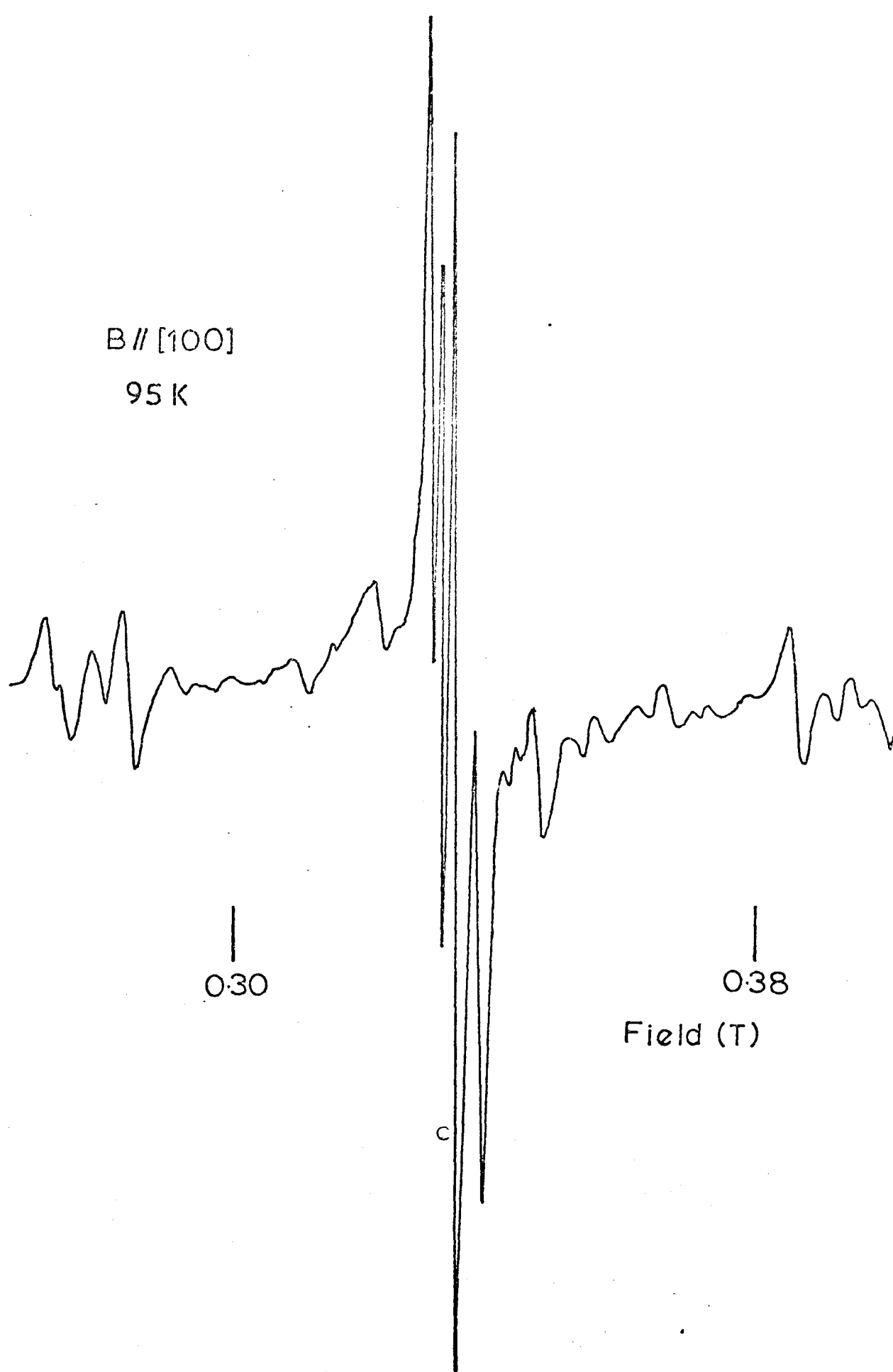
Fig. 4.5. The E.P.R. of $Cr^{3+}$ in a high-doped sample of AgCl at
central line is labelled C.
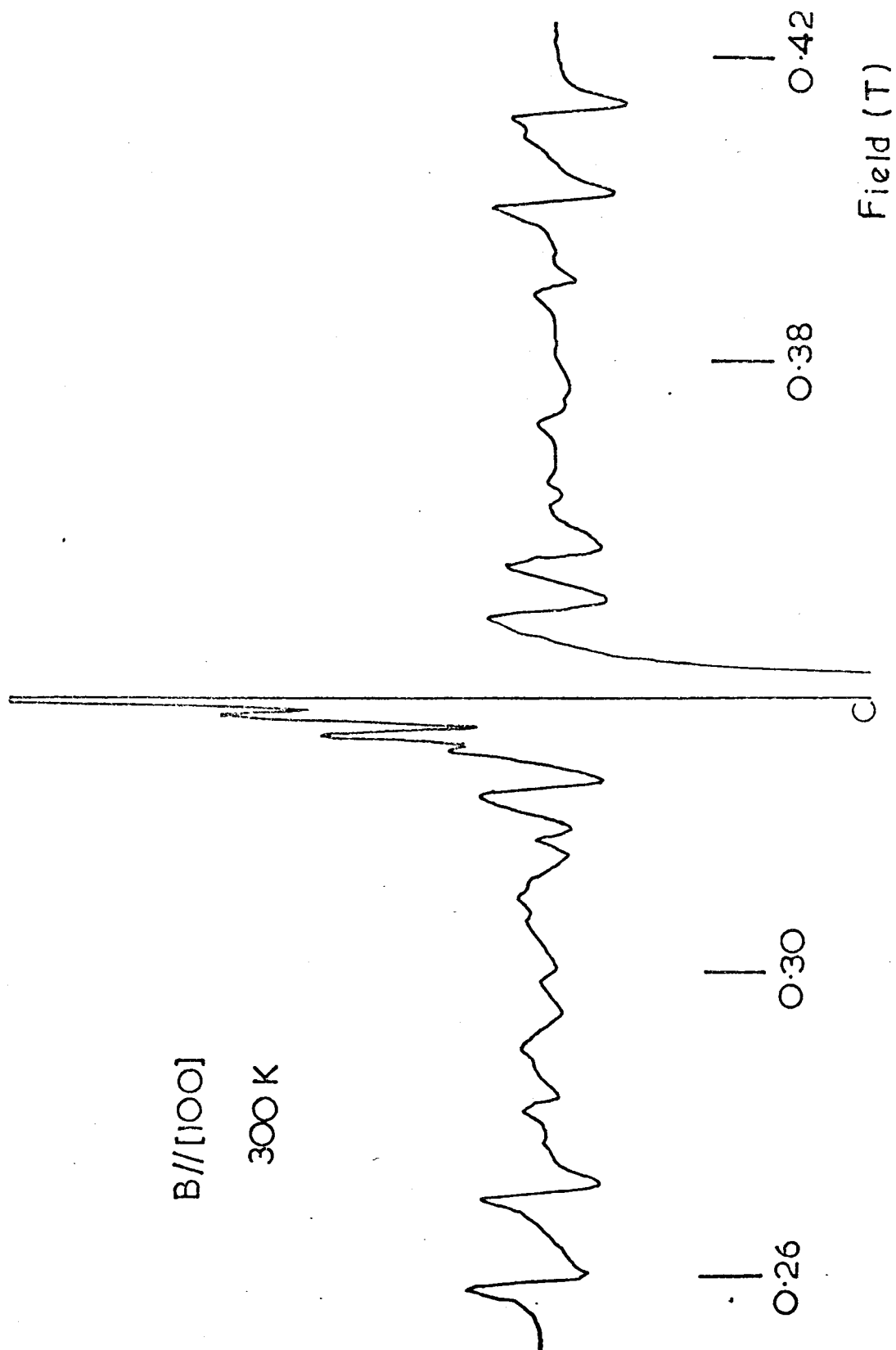
Fig. 4.6. The E.P.R. of $Cr^{3+}$ in AgCl at 300K with B // $\langle 100 \rangle$.

is labelled C .

lines broadened abruptly and disappeared over the temperature range 273K to 373K. However, a set of three lines (labelled L in fig. 4.1) decreased in intensity to zero without broadening between 150K and 300K. The intensity of the line at 0.3345T increased up to 400K and then remained approximately constant within the experimental error.

As the temperature was increased from 300K to 350K the majority of the lines decreased in intensity faster than the $1/_T$ dependence of the Boltzmann factor. However, there is a set of fine structure lines which appear to increase in intensity relative to the other lines over this temperature range. These are shown (labelled S) on the low field side of $g = 2$ in fig. 4.7. The profusion of broad overlapping lines with B//<110> made it impossible to distinguish any similar lines with the samples in that direction.

Fig. 4.8 shows the spectrum at 383K with B//<100>. The spectrum is now cubic. The total integrated intensity of the spectrum was estimated by graphical addition of the area under the derivative curve and ᵃᵉ ᵗ.ᵉ multiplying the result by the line width and is the same as that of the spectrum at 95K to within ± 5%, once allowance is made for the Boltzmann factor. The low intensity lines due to residual $Mn^{2+}$ impurity ions in a cubic environment can just be seen at 383K.

The rate at which the sample was cooled to 95K was varied from a few minutes up to two hours but had no appreciable effect on the spectrum. Nor did long anneals of the samples at 580-630K in chlorine affect the resonance. No change in the spectrum was detected after irradiation of the divalent or trivalent state. After storing in the dark for several months the intensity of the resonance in the outer fine structure lines decreased and a broad central line appeared.
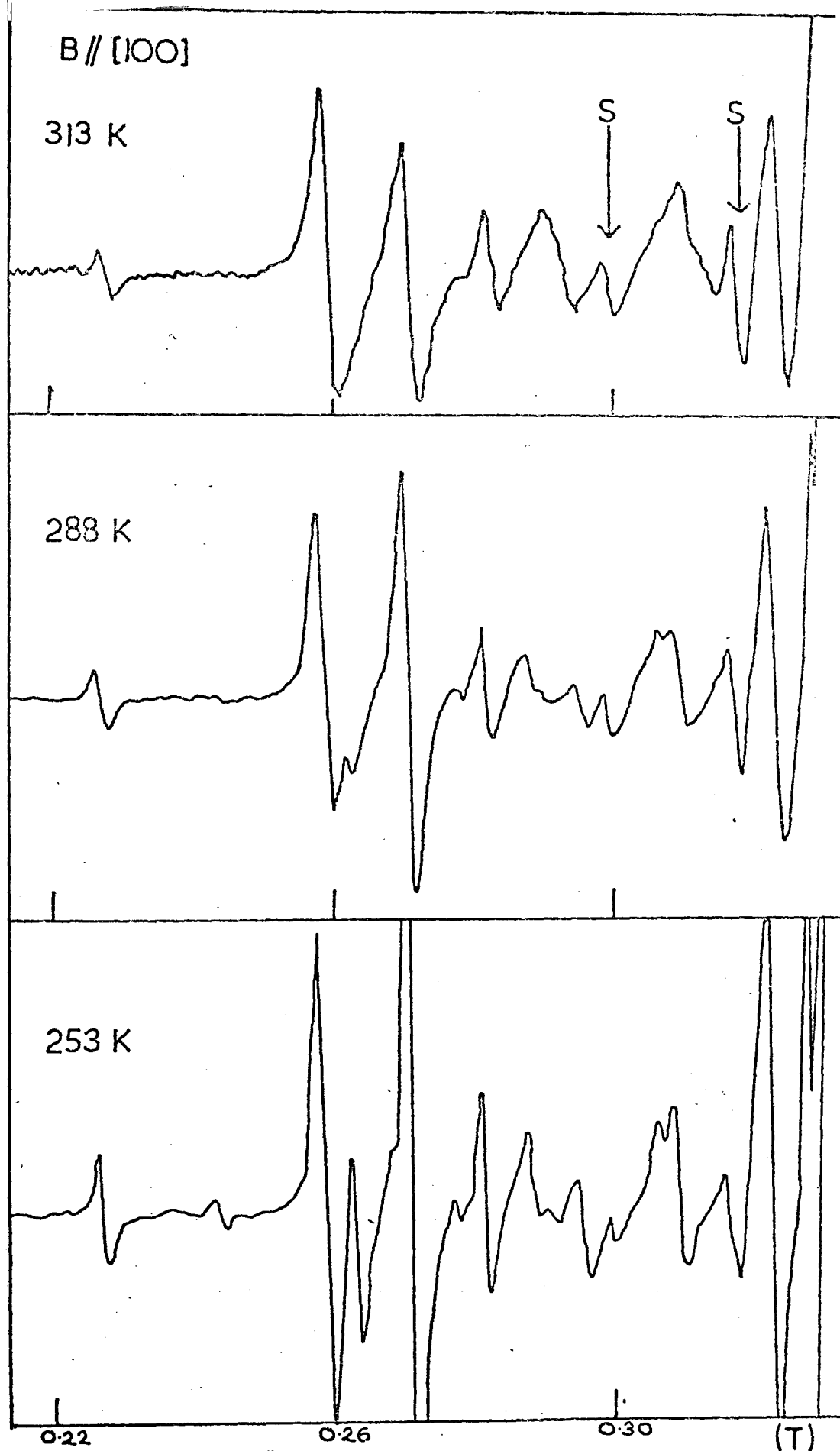
Fig. 4.7. The E.P.R. of $Cr^{3+}$ in AgCl above 250K with B // $\langle 100 \rangle$.

The upper trace is on a vertical scale twice that of the lower traces.

B//[100]

383 K

0.30    0.34    0.38

Field (T)
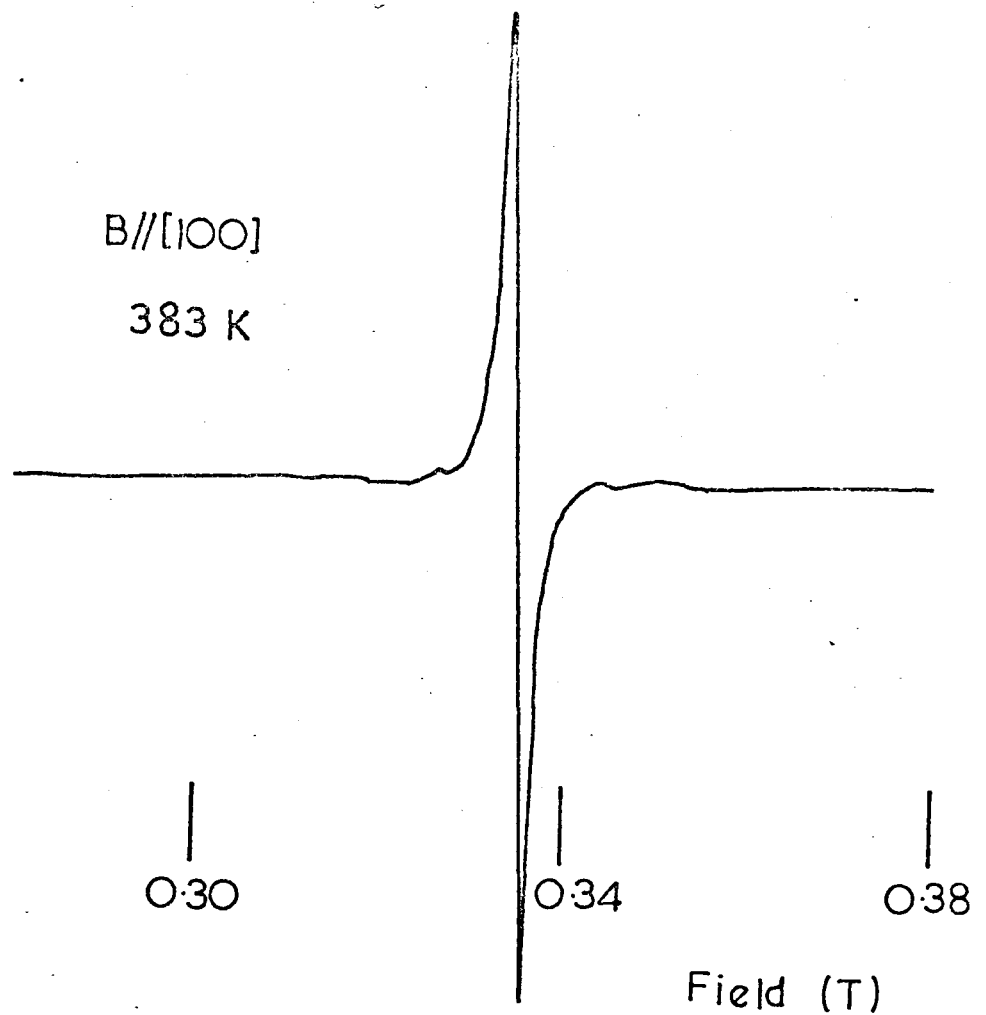
Fig. 4.8. The E.P.R. of $Cr^{3+}$ in AgCl at 383K with B // $\langle 100 \rangle$.
The spectrum has reduced to a single cubic line .

## 4.4    Interpretation of the spectrum for AgCl

### 4.4.1    A spin Hamiltonian for monoclinic symmetry

The $Cr^{3+}$ ion has a double excess positive charge over the silver halide lattice.  It is expected to be locally charge compensated at sufficiently low temperatures.  Kunze and Müller[12], as discussed below, interpret their T.D.C. measurements by means of a centre with the $Cr^{3+}$ ion in a cation site associated with a nearest cation vacancy and a next nearest cation vacancy arranged as shown in fig. 4.9.  The local symmetry of this site is monoclinic.  It has only a mirror plane of symmetry (crystal class m, $C_{1h}$).

A resonant spectrum will always have three mutually perpendicular principal axes which corresponds to orthorhombic symmetry.  However, the monoclinic symmetry of the Kunze and Müller centre will add a term in xy to the crystal field potential.  In terms of the spherical harmonic expansion of the crystal field surrounding the paramagnetic ion (section 2.4) this is the $A_2^{-2}$ term given by Dieke[14].  Stevens[15] gives the form of the potential appropriate to this term, in cartesian coordinates as $V_2^{-2} = 2xy$.  The operator equivalent of (xy) is $(\frac{S_xS_y + S_yS_x}{2})$ [15,16] and hence the spin Hamiltonian is

$$H = g\beta\underline{B}.\underline{S} + D\left[S_z^2 - \frac{1}{3}S(S + 1)\right] + E(S_x^2 - S_y^2) + K(S_xS_y + S_yS_x)$$

and it is Hermitian.

A calculation of the effect of this Hamiltonian on the energy levels of an $S = \frac{3}{2}$ ion was undertaken in order to determine if the final term would have a detectable effect on the resonant lines.
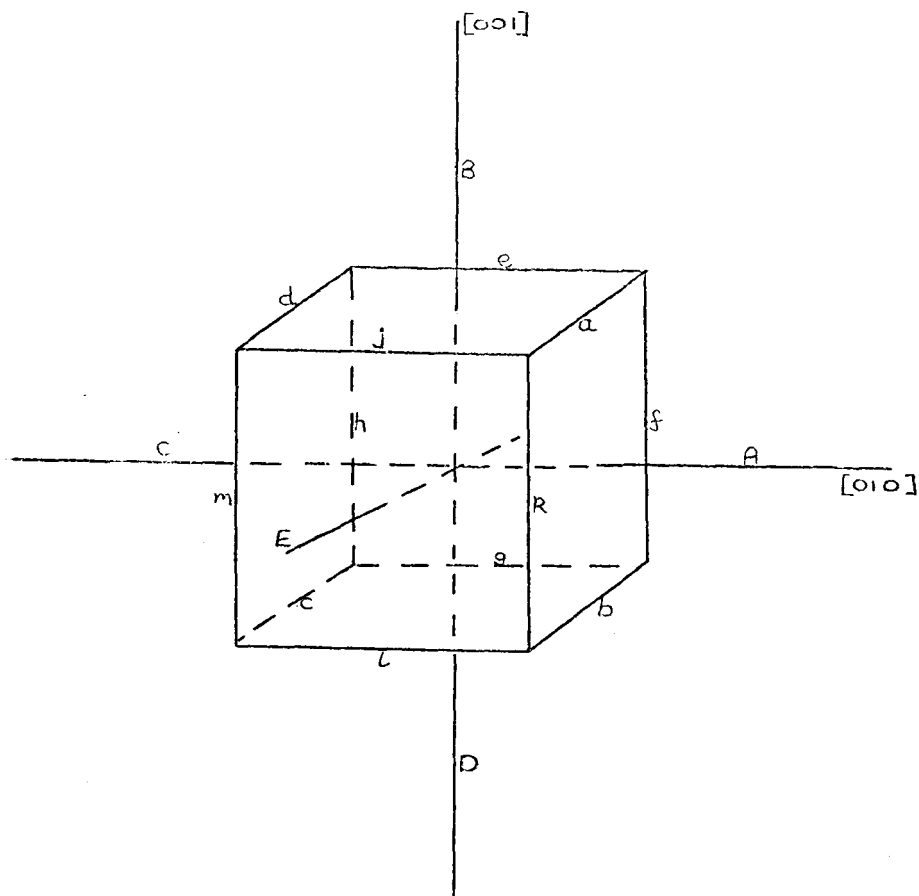
The next nearest cation vacancy A is associated with one of the
nearest cation vacancies c,d,h or m.
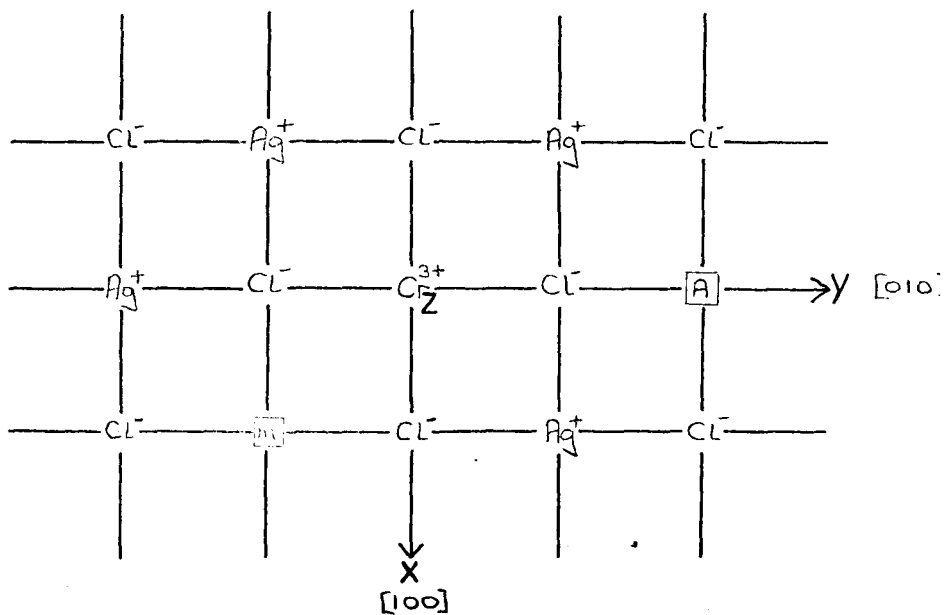


Fig. 4.9. The centre proposed by Kunze and Muller for $Cr^{3+}$ in AgCl .

The matrix appropriate to this Hamiltonian cannot be solved exactly as $E(S_x^2 - S_y^2)$ and $K(S_xS_y + S_yS_x)$ give off-diagonal terms with the usual base states which are diagonal with respect to $g\beta B_zS_z$ and $D(S_z^2 - \frac{1}{3}S(S + 1))$. Approximate solutions may be found provided that $D \ll g\beta B$ and $E, K < D$ which is a good approximation for $AgCl:Cr^{3+}$. To find solutions for a general direction of B the Hamiltonian is first transformed to be diagonal in $g\beta \underline{B}.\underline{S}$ so that the off-diagonal elements are small compared to the diagonal elements.

The relative energy levels, and hence the transition energies, have been calculated (see Appendix I). The calculation was restricted to angles varying within the three principal planes ZX, ZY and XY. The expressions derived for the transitions, calculated to second order in $\frac{D}{B}$, agree with those given by Low[17] (with minor corrections) and by Henderson[18] for all angles within these planes if K is put equal to zero. For D, E and K in field units the results are:

ZX plane : ($\theta$ is the angle between the magnetic field and Z)

$$\pm\tfrac{3}{2} \leftrightarrow \pm\tfrac{1}{2} \quad B = B_0 \mp \left[D(3\cos^2\theta - 1) - 3E(1 - \cos^2\theta)\right]$$
$$- \frac{6}{B_0}\left[(D + E)^2\sin^2\theta\cos^2\theta + K^2\sin^2\theta\right]$$

$$+\tfrac{1}{2} \leftrightarrow -\tfrac{1}{2} \quad B = B_0 + \frac{6}{B_0}\left[(D + E)^2\sin^2\theta\cos^2\theta + K^2\sin^2\theta\right]$$
$$- \frac{3}{4B_0}\left[\{D\sin^2\theta - E(1 + \cos^2\theta)\}^2 + 4K^2\cos^2\theta\right]$$

ZX plane : ($\theta$ is the angle between the magnetic field and Z)

$$\pm\tfrac{3}{2} \leftrightarrow \pm\tfrac{1}{2} \quad B = B_0 \mp \left[D(3\cos^2\theta - 1) + 3E(1 - \cos^2\theta)\right]$$
$$- \frac{6}{B_0}\left[(D - E)^2\sin^2\theta\cos^2\theta + K^2\sin^2\theta\right]$$

$$+\tfrac{1}{2} \leftrightarrow -\tfrac{1}{2} \quad B = B_0 + \frac{6}{B_0}\left[(D - E)^2\sin^2\theta + K^2\sin^2\theta\right]$$

$$- \frac{3}{4B_0}\left[\{D\sin^2\theta + E(1 + \cos^2\theta)\}^2 + 4K^2\cos^2\theta\right]$$

XY plane : ($\theta$ is the angle between the magnetic field and X)

$$\pm\tfrac{3}{2} \leftrightarrow \pm\tfrac{1}{2} \quad B = B_0 \mp \left[D + 3E(2\cos^2\theta - 1) - 3K\sin2\theta\right]$$

$$- \frac{6}{B_0}\left[E\sin2\theta - K(2\cos^2\theta - 1)\right]^2$$

$$+\tfrac{1}{2} \leftrightarrow -\tfrac{1}{2} \quad B = B_0 + \frac{6}{B_0}\left[E\sin2\theta - K(2\cos^2\theta - 1)\right]^2$$

$$- \frac{3}{4B_0}\left[D + E(2\cos^2\theta - 1) + K\sin2\theta\right]^2$$

## 4.4.2 The principal spectrum at 95K

There are three sets of lines with high intensity in the spectrum at B//<100> all of which have similar temperature dependence. The behaviour of these lines as the orientation of the crystal was changed (fig. 4.10) suggests that they are produced by a centre of orthorhombic symmetry with axes in the directions <100>, $4^\circ$ off <010> and $4^\circ$ off <001>.

For the magnetic field parallel to the principal axes of the centre the transitions derived above reduce to:

B//Z

$$\pm\tfrac{3}{2} \leftrightarrow \pm\tfrac{1}{2} \quad B = B_0 \mp 2D$$

$$+\tfrac{1}{2} \leftrightarrow -\tfrac{1}{2} \quad B = B_0 - \frac{3E^2}{B_0}$$

B//Y

$$\pm\tfrac{3}{2} \leftrightarrow \pm\tfrac{1}{2} \quad B = B_0 \pm (D + 3E) - \frac{6K^2}{B_0}$$

$$+\tfrac{1}{2} \leftrightarrow -\tfrac{1}{2} \quad B = B_0 + \frac{6K^2}{B_0} - \frac{3}{4B_0}(D - E)^2$$
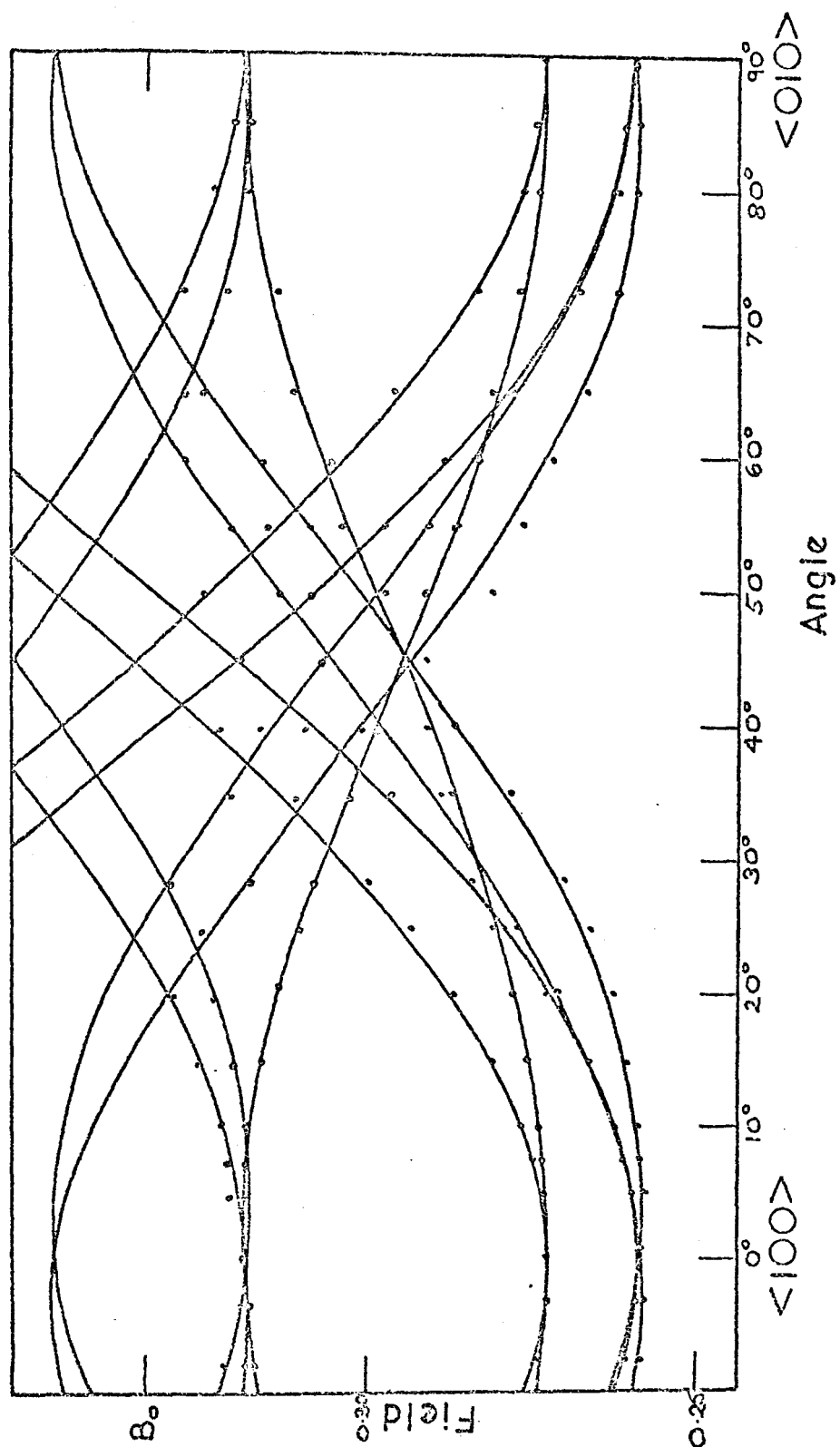
Fig. 4.10. The angular dependence of the fine structure lines of the principal spectrum in AgCl:Cr$^{3+}$ in the {100} plane on the low field side. The full lines indicate the theoretical values and the circles the experimental ones.

$$\pm\frac{3}{2} \leftrightarrow \pm\frac{1}{2} \qquad B = B_o \pm (D - 3E) - \frac{6K^2}{B_o}$$

B//X

$$+\frac{1}{2} \leftrightarrow -\frac{1}{2} \qquad B = B_o + \frac{6K^2}{B_o} - \frac{3}{4B_o}(D + E)^2$$

The lines which reach extreme fields with the largest separation at $\langle 100 \rangle \pm 4°$ are labelled Z. The Y lines extreme at $\langle 100 \rangle$ and the X lines at $\langle 100 \rangle \pm 4°$ (fig. 4.1). The terms in E and K appear only in third order for the $\pm\frac{3}{2} \leftrightarrow \pm\frac{1}{2}$ transitions with B//Z. D was calculated from the splitting of these lines and $g_z$ was calculated from their midpoint. The centre of the fine structure lines with B//X and B//Y did not differ greatly from that of the B//Z lines and so g was taken to be isotropic within the experimental accuracy. The term in K contributes in the same sense to the fine structure lines at B//X and B//Y and E was calculated and checked from the separation of these lines. The K term contributes only in second order to all the transitions. An upper limit was set on K by determining the possible separation ($\not> 0.5$mT) of the centre of the fine structure lines with B//X and Y, and that with B//Z. The separation was within the experimental error.

The spectrum may be fitted to the Hamiltonian with

$$g = 1.980 \pm 0.004$$

$$|D| = 37.5 \pm 0.2\text{mT} = (346 \pm 2) \times 10^{-4}\text{cm}^{-1}$$

$$|E| = 7.8 \pm 0.1\text{mT} = (72 \pm 1) \times 10^{-4}\text{cm}^{-1}$$

$$|K| \leqslant 5.4 \pm 0.2\text{mT} \leqslant (50 \pm 2) \times 10^{-4}\text{cm}^{-1}$$

The line positions calculated using these parameters are shown in figs. 4.1, 4.2 and 4.3. At B//$\langle 100 \rangle$ the calculated positions agree with

the observed lines within the experimental error. At B//<110> the fit of the centre lines is good but the fit of the outer lines is poor, although the general features are in agreement. The fine structure lines from centres with B at $45^{\circ}$ to Z and X or X and Y lie outside the centre region and are obscured by the number of overlapping, broad lines. The fine structure lines from centres with B at $45^{\circ}$ to Z and Y lie in the central region, and are clearly present in the spectrum, but are not close to the calculated positions. The discrepancy may arise because of the increasing inaccuracy of the perturbation approach as the magnetic field is turned away from a principal axis. At B//<111> the magnetic field is at the same orientation to each equivalent distortion of any particular centre. For the centres with <100> axes the first order fine structure splitting is zero. The spectrum simplifies considerably at B//<111> (fig. 4.3) and the fit of calculated and observed lines is good near g = 2.

A plot of the experimental line positions as $\theta$ varies in a {100} plane over those angles where the lines can be clearly followed is shown in fig.4.10. Also shown are the calculated resonant fields for the D and E values given above and K = 5.4mT.

The widths of the outer lines in the spectrum when B is not parallel to <100> are unusual for this type of crystal. In identically prepared AgCl:$V^{2+}$ and AgCl:$Eu^{2+}$ samples the maximum line widths present in well oriented samples at B//<110> were 2.0mT. The line widths in AgCl:$Cr^{3+}$ may be due to a degree of misalignment of grains within the crystal. A very small misorientation of grains ($2^{\circ}$) will give only a 0.16mT increase in line width at B//<100> and an increase of 4mT at B//<110>. However, there may be considerable local strain around the $Cr^{3+}$ ion leading to small differences in the local field at each ion.

### 4.4.3 The subsidiary spectra at 95K

There are numerous lines in the spectrum at 95K with smaller intensity than the principal set. One set of these (labelled S.T. in figs. 4.1, 4.2 and 4.3) may be fitted to a tetragonal spin Hamiltonian

$$H = g\beta\underline{B}.\underline{S} + D(S_z^2 - \frac{1}{3}S(S + 1))$$

where $g = 1.980 \pm 0.002$

$$|D| = 54.0 \pm 0.1mT = (499 \pm 1) \times 10^{-4}cm^{-1}$$

The fit of the calculated and observed line positions as a function of angle in the {100} plane is shown in fig. 4.11. These centres account for approximately 5% of the total $Cr^{3+}$ ions.

With $B//\langle 110\rangle$ a pair of lines can be clearly seen to reach maximum and minimum fields and also a pair of lines at intermediate fields extreme at this orientation. The lines are most probably from a centre of orthorhombic symmetry with axes $Z\langle 110\rangle$, $X\langle\bar{1}10\rangle$ and $Y\langle 001\rangle$. At $B//\langle 110\rangle$ the outer pair of lines are from centres with $B//Z$ and the inner pair from centres with $B//X$. The positions of these lines give

$$g = 1.980 \pm 0.005$$

$$|D| = 46.25 \pm 0.5mT = (426 \pm 0.5) \times 10^{-4}cm^{-1}$$

$$|E| = 6.9 \pm 0.1mT = (63.6 \pm 1) \times 10^{-4}cm^{-1}$$

The calculated line positions for the subsidiary orthorhombic centre are shown in figs. 4.1, 4.2 and 4.3. The other lines from this centre at $B//\langle 110\rangle$ and the lines at $B//\langle 100\rangle$ cannot be clearly distinguished in the spectrum because they are broad or they overlap with other lines. This centre, if present, accounts for about 10% of the $Cr^{3+}$ ions.
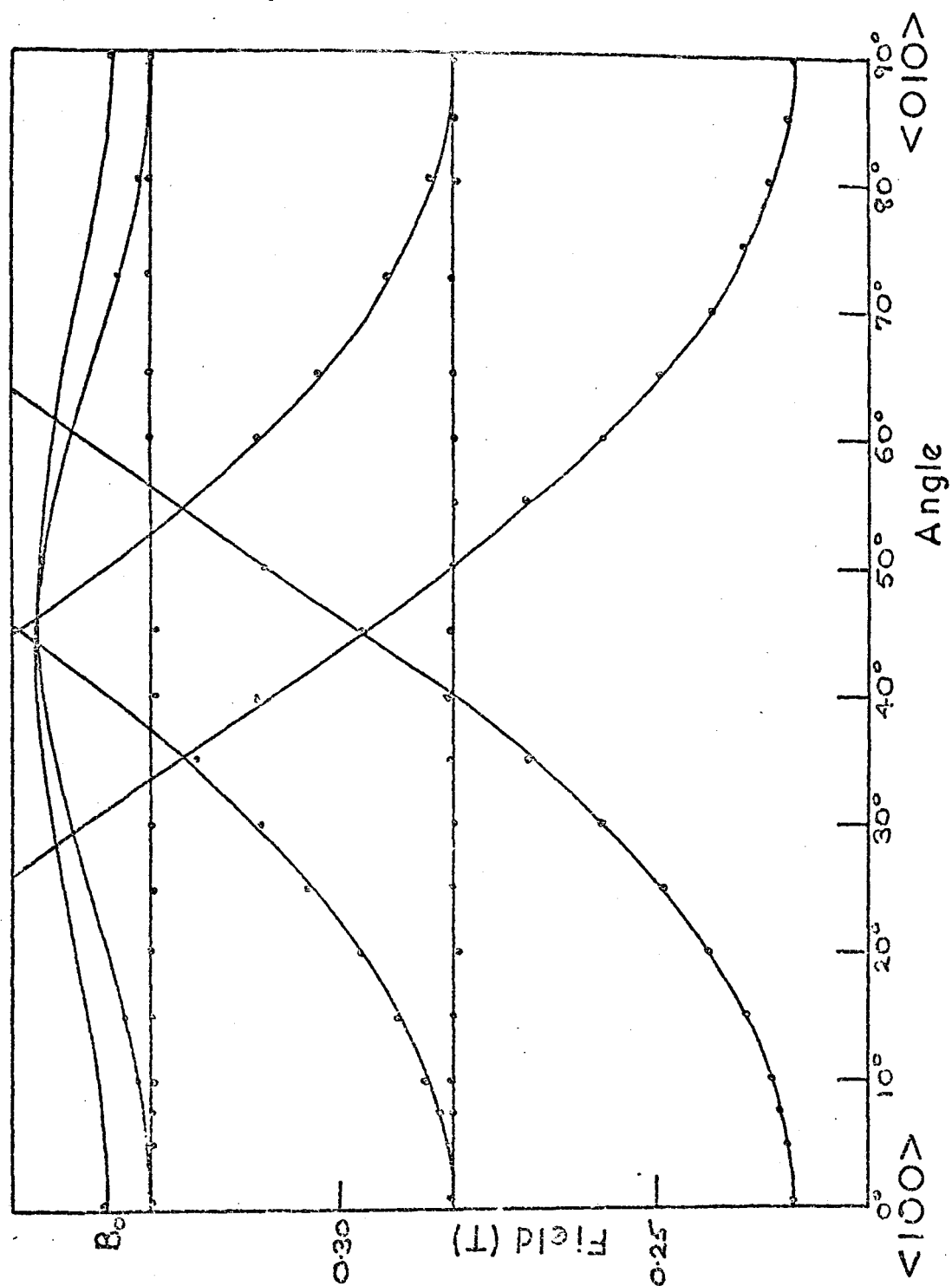
Fig. 4.11. The angular dependence of the subsidiary tetragonal centre in AgCl:$Cr^{3+}$ in the {100} plane below $B_o$ .
The full lines indicate the theoretical values and the circles the experimental ones.

No explanation has been found at present for the set of three lines labelled L in fig. 4.1. The lines, L, are seen at B//⟨100⟩ and disappear without broadening as the temperature is warmed to 280K and re-appear on cooling. No corresponding set of lines can be found at B//⟨110⟩ or B//⟨111⟩ nor are there any other similar lines at B//⟨100⟩. The separation of the outer pair of lines reaches a maximum at B//⟨100⟩ and no part of the lines can be seen to move to lower fields as the crystal is rotated over the $20^{\circ}$ where the lines can be distinguished. It follows that ⟨100⟩ is a major axis of the site. However, the centre line is displaced to high field relative to $B_o$ ($B_o = \frac{h\nu}{g\beta}$ where g = 1.980). For B parallel to a principal axis the centre $\pm\frac{1}{2}$ transitions are displaced to low field by second and third order correction terms. A low g-value (1.955) combined with large third order shifts to low field of the $\pm\frac{3}{2} \leftrightarrow \pm\frac{1}{2}$ transitions would explain the positions of the L lines. These corrections are of order $\frac{3D^3}{8B_o^2}$, and a value of $D \simeq 0.1T$ is required to give the 2.5mT shift. However, the absence of lines at other orientations and the temperature dependence remain to be explained.

### 4.4.4 Line broadening and activation energies

As the temperature of the sample is raised above 180K the vacancies surrounding the $Cr^{3+}$ ion become increasingly mobile. Broadening of the outer fine structure lines occurs when a silver ion vacancy, or pair of vacancies, jumps to a new position and alters the local crystal field within the relaxation time of the excited spin state. The increase in line width is related to the temperature T by

$$\frac{1}{\tau} = \frac{1}{\tau_o} \exp\left(\frac{-E}{kT}\right) \tag{8.19}$$

where the line shape at low temperatures is assumed to be Lorentzian so

that the width is related directly to $\tau$. E is the activation energy for the process involved and $\frac{1}{\tau_o}$ is a constant.

Fig. 4.12 shows the line width in excess of the line width at 95K plotted against $1/_T$ for those lines in the spectrum whose broadening can be clearly followed. The Y lines of the principal spectrum give a good straight line graph with

$$E_a = 0.21 \pm 0.04 \text{ eV}$$

The Z lines at B//⟨100⟩ give a higher activation energy probably because the broadening caused by vacancy motion is compensated by a narrowing as the component of asymmetry which gives the Z axis $4^o$ away from ⟨100⟩ is lost.

The tetragonal centre lines give $E_a = 0.41 \pm 0.04$eV. The subsidiary orthorhombic centre line with B//Z at B//⟨110⟩ gives $E_a = 0.32 \pm 0.04$eV.

The fraction p of $Cr^{3+}$ ions associated with two vacancies was estimated at a number of different temperatures between 95K and 350K. It was assumed that all the ions were associated with vacancies at 95K. The intensity of the principal centre was determined from the $\pm\frac{1}{2}$ transition from the centre with B//Y. The $\pm\frac{1}{2}$ line with B⊥Z was used for the tetragonal centre. Both these lines were displaced from the cubic line and did not broaden at high temperature. Watkins[19] uses the simple mass action law $\frac{p}{(1 - p)^2} = Ce^{-E_b/kT}$ where C is a constant and $E_b$ is the binding energy of the vacancy to the impurity. The results for $AgCl:Cr^{3+}$ could be approximately fitted to this law and, assuming that all the
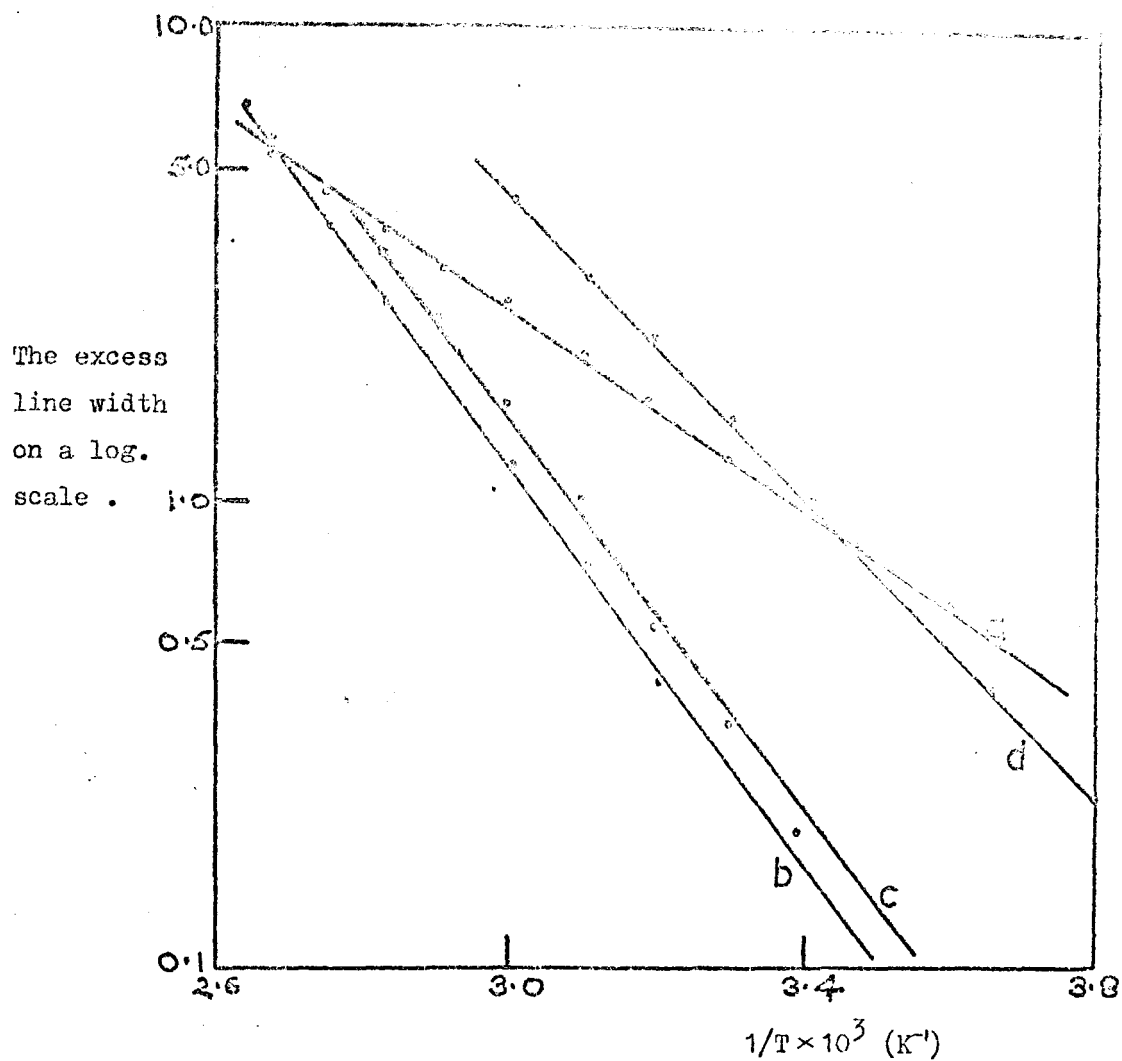
Fig. 4.12. The log. of the excess line width in $AgCl:Cr^{3+}$ plotted against 1/T for (a) the principal orthorhombic line with B // Y,

(b) the principal orthorhombic line with B // Z,

(c) the subsidiary tetragonal line with B // Z

and    (d) the susidiary orthorhombic line with B // Z .

centres have similar binding energies for the vacancy which leaves at the lower temperature, gives $E_b \simeq 0.18 \pm 0.05eV$.

### 4.4.5 The spectrum at high temperatures

At 300 K the lines from centres with low symmetry have decreased considerably in intensity. The decrease is due to fast motion of the silver ion vacancies about the $Cr^{3+}$ ion, or to the motion of the vacancies away from $Cr^{3+}$ which can be detected in conductivity measurements[11].

The principal orthorhombic spectrum now has

$$g = 1.980 \pm 0.005$$

$$|D| = 38.0 \pm 0.5mT = (354 \pm 5) \times 10^{-4}cm^{-1}$$

$$|E| = 8.7 \pm 0.1mT = (80.4 \pm 1) \times 10^{-4}cm^{-1}$$

(K was not estimated.) E has increased by 11%, and D by only 1.3%, over their values at 95K.

The single cubic line present at temperatures above 400K is considered to be due to isolated $Cr^{3+}$ ions in cubic sites. Conductivity measurements show that all the vacancies present in the crystal are highly mobile at these temperatures. The fact that the intensity of the cubic line remains approximately constant from 400K to 550K suggests that there is not any undetected intensity in outside lines made very broad by fast motion of the silver ion vacancies around the $Cr^{3+}$ ion.
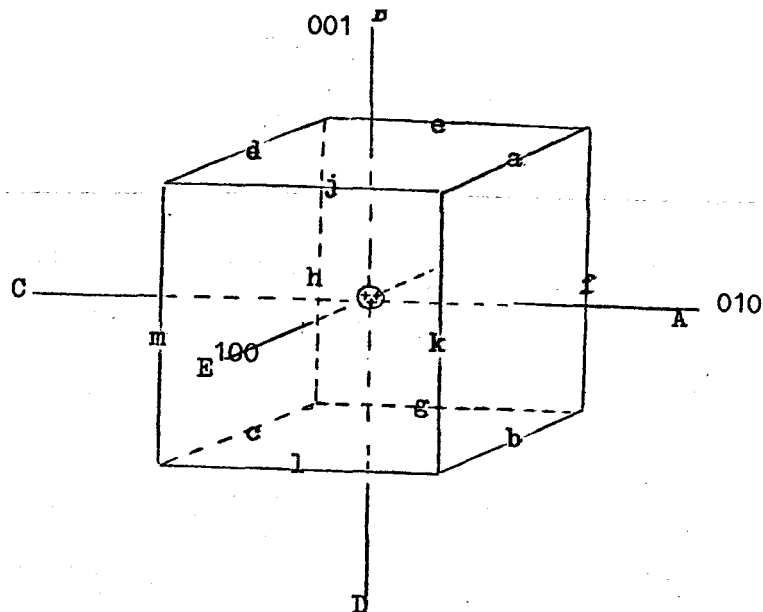
| θ | Example of vacancy positions | Site symmetry | Symmetry axis of site | Probable axes of the Spin Hamiltonian | Symmetry of the field on point-charge model |
|---|---|---|---|---|---|
| 180° | A, C | Tetragonal, 4/mm, $C_{4h}$ | $\langle 100 \rangle$ | 100 | Tetragonal |
| 90° | A, B | Orthorhombic, 2m, $C_{2v}$ | $\langle 110 \rangle$ | (100,010,001) | Tetragonal |
| 90° | A, e | Monoclinic, m, $C_{1h}$ | $\langle 110 \rangle$ | (010,101,$\bar{1}$01) | Orthorhombic |
| 135° | A, m | Monoclinic, m, $C_{1h}$ | $\langle 100 \rangle$ | (010,100,001) | Monoclinic |
| *45° | A, k | Monoclinic, m, $C_{1h}$ | $\langle 100 \rangle$ | (010,100,001) | Monoclinic |
| 90° | k, m | Orthorhombic, 2m, $C_{2v}$ | $\langle 100 \rangle$ | (110,1$\bar{1}$0,001) | Orthorhombic |
| *60° | k, a | Monoclinic, m, $C_{1h}$ | $\langle 112 \rangle$ | (1$\bar{1}$1,110,$\bar{1}$12) | Monoclinic |
| 120° | j, b | Monoclinic, m, $C_{1h}$ | $\langle 110 \rangle$ | ($\bar{1}$11,101,12$\bar{1}$) | Monoclinic |
| 180° | k, h | Orthorhombic, mmm, $D_{2h}$ | $\langle 110 \rangle$ | (110,1$\bar{1}$0,001) | Orthorhombic |

θ is the angle between the lines joining the $Cr^{3+}$ ion to each of the vacancies.

* These arrangements are unlikely because of the proximity of the vacancies

Fig. 4.13. The possible arrangements of two vacancies within the first two cation shells about a substitutional impurity ion.

The set of lines which appear to increase in intensity above 300K are tentatively assigned to a number of $Cr^{3+}$ ions which have lost one of the two vacancies. Since these lines are well defined at $B//\langle 100\rangle$ and are at even spacings about $B_o$ they are thought to arise from a tetragonal centre.

If this is so, then $g = 1.980 \pm 0.005$ and $|D| = 18.0 \pm 0.5mT$ $(166 \pm 5) \times 10^{-4} cm^{-1}$ at 300K. However, the lines may appear to increase in intensity because of a change in the overlap of the existing lines, or they may be from a centre which is present at low temperature and which remains associated to higher temperatures than the other centres.

The broad cubic line observed in highly-doped specimens and in old specimens is assigned to a proportion of precipitated $CrCl_3$ phase. E.P.R. from $Cr^{3+}$ in hydrated and anhydrous $CrCl_3$ has been observed with line widths varying from 5 - 14mT in the anhydrous crystals and g-values of $1.99^{[20,21]}$.

## 4.5    Experimental results for AgBr

### 4.5.1    The spectrum at 95K

The spectra observed at $B//\langle 100\rangle$ and $B//\langle 110\rangle$ are shown in figs. 4.14 and 4.15. The spread of the spectrum is very much larger than in $AgCl:Cr^{3+}$ and there are resonances at zero field. The majority of the lines reach extreme positions at $B//\langle 100\rangle$ and none extreme at $B//\langle 111\rangle$ or $B//\langle 211\rangle$. The large number of lines, particularly on the low field side
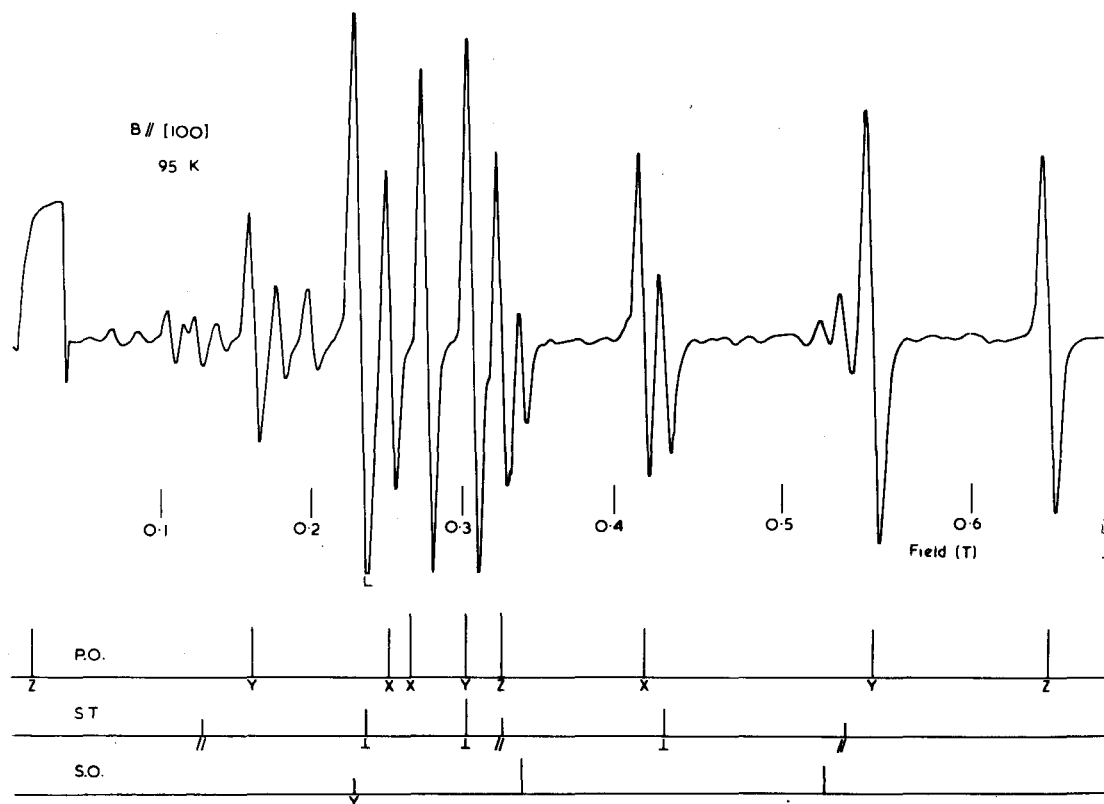
Fig. 4.14. The E.P.R. of $Cr^{3+}$ in AgBr at 95K with B $// \langle 100 \rangle$.

The line positions calculated using the spin Hamiltonian

parameters given in the text are shown for the principal orthorhombic

centre (P.O.), the subsidiary tetragonal centre (S.T.) and the

subsidiary orthorhombic centre(S.O.).

Several lines from the subsidiary orthorhombic centre are not shown

as they lie at fields either below zero or above 0.7 T .
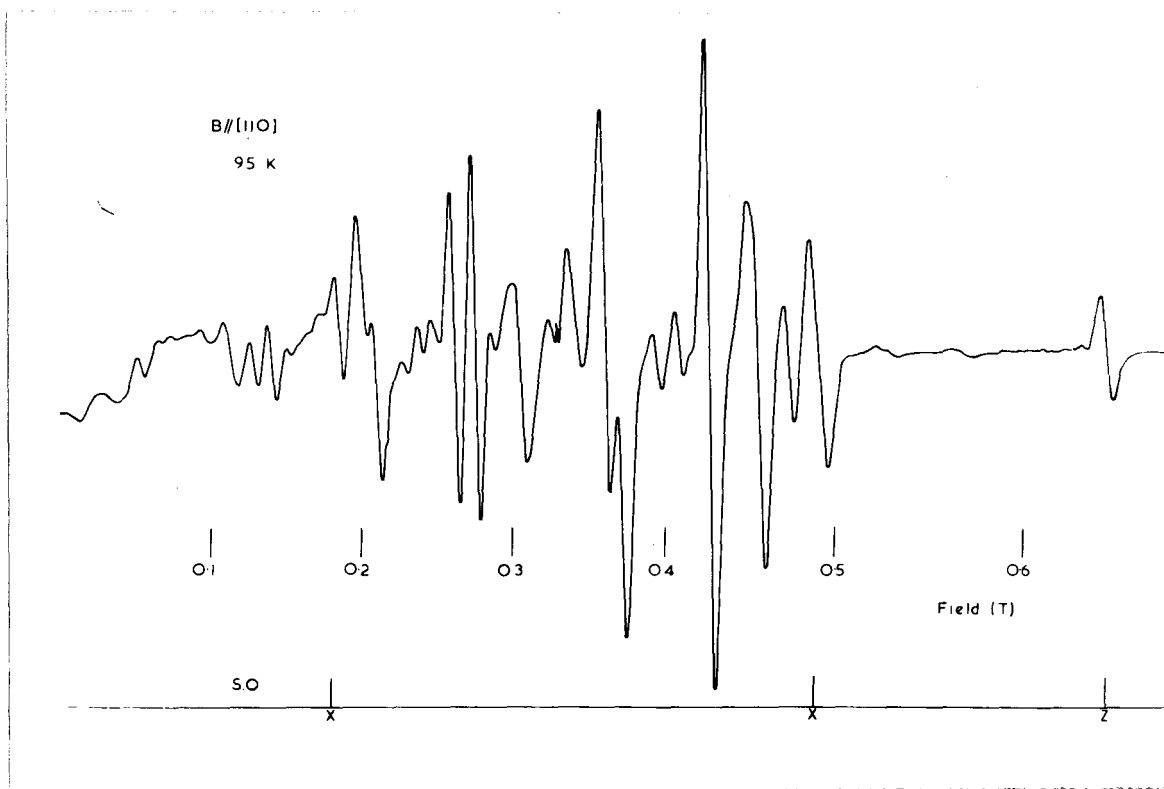
Fig. 4.15. The E.P.R. of $Cr^{3+}$ in AgBr at 95K with B $//\langle 110\rangle$.

The fine structure lines from the subsidiary orthorhombic

centres (S.O.) with B $//$ Z and B $//$ X are labelled Z and X respectively.

of g = 2, made it difficult to follow the angular dependence of the spectrum over more than 25$^{o}$ on either side of B//<100>.

The line widths are large at all angles, typically about 6mT. The line labelled L, where it could be followed, was not isotropic but moved slightly to higher field as the sample was rotated.

### 4.5.2 The spectrum at room temperature and above

As the sample was warmed above 95K the intensity of the outer lines gradually decreased and that of the central line at 0.333T increased. Between 290K and 400K the outer lines broadened. The line L moved to higher field between 100K and 250K, obscuring the neighbouring lines (figs. 4.14, 4.16 and 4.17), and then decreased sharply in intensity without broadening between 240K and 300K. The overall spread of the spectrum had decreased at 300K so that the low field fine structure lines were clearly observed at room temperature (fig. 4.17).

The spectrum reduced to a single cubic line at 0.332 ± 0.005T of width 15mT at 430K. However, the total intensity of the spectrum increased steadily up to 560K. The total intensity at 560K was 95(± 10)% of that at 95K once allowance was made for the Boltzmann factor.

Between 273K and 300K the central line at 0.332T increased in intensity and a set of lines appeared which increased in intensity when compared to the other lines present. The set is labelled S in figs. 4.17 and 4.18.
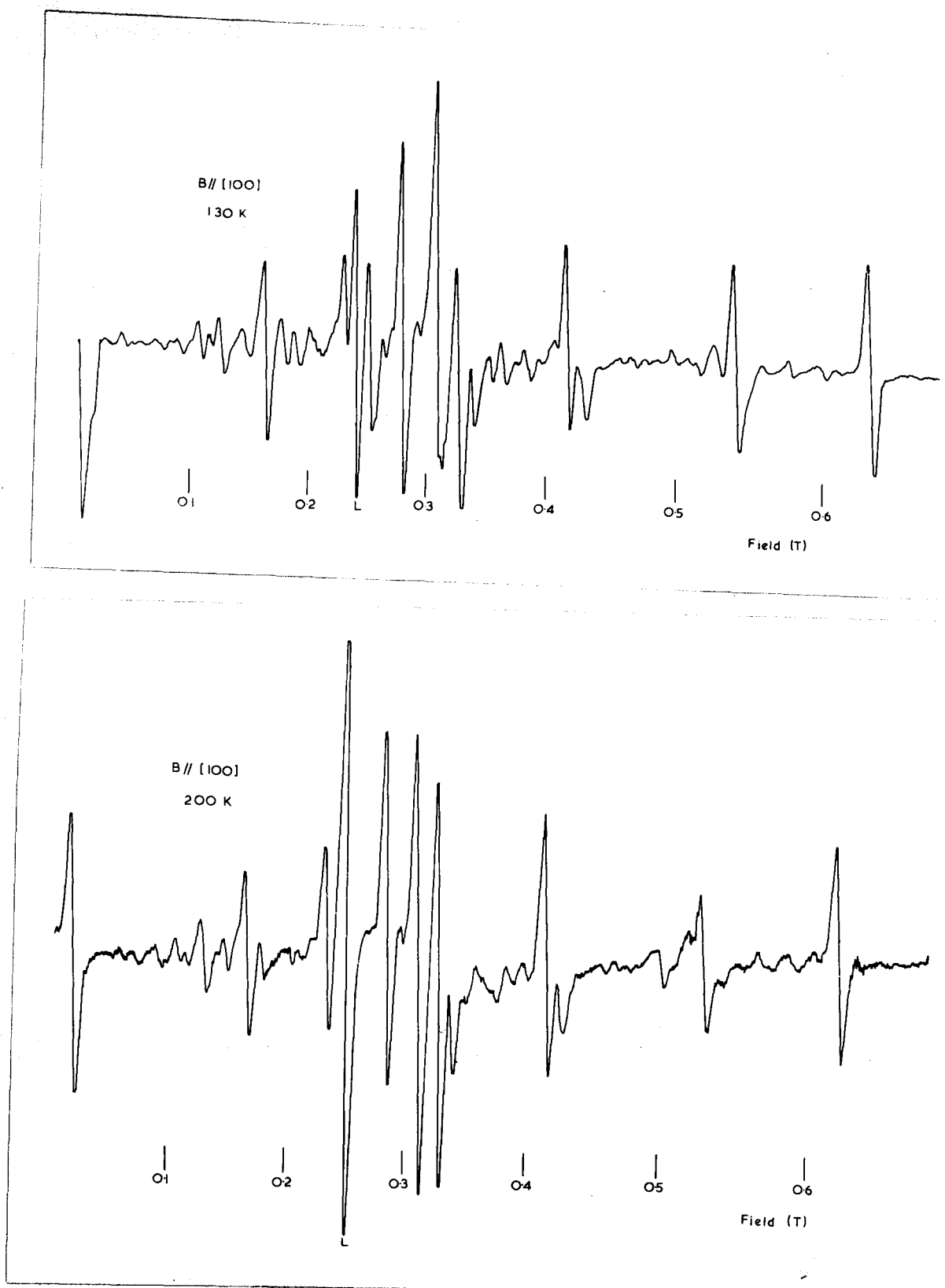
Fig. 4.16. The E.P.R. of Cr$^{3+}$ in AgBr at 130K and 200K with B //< 100>
showing the movement with temperature of the line L.
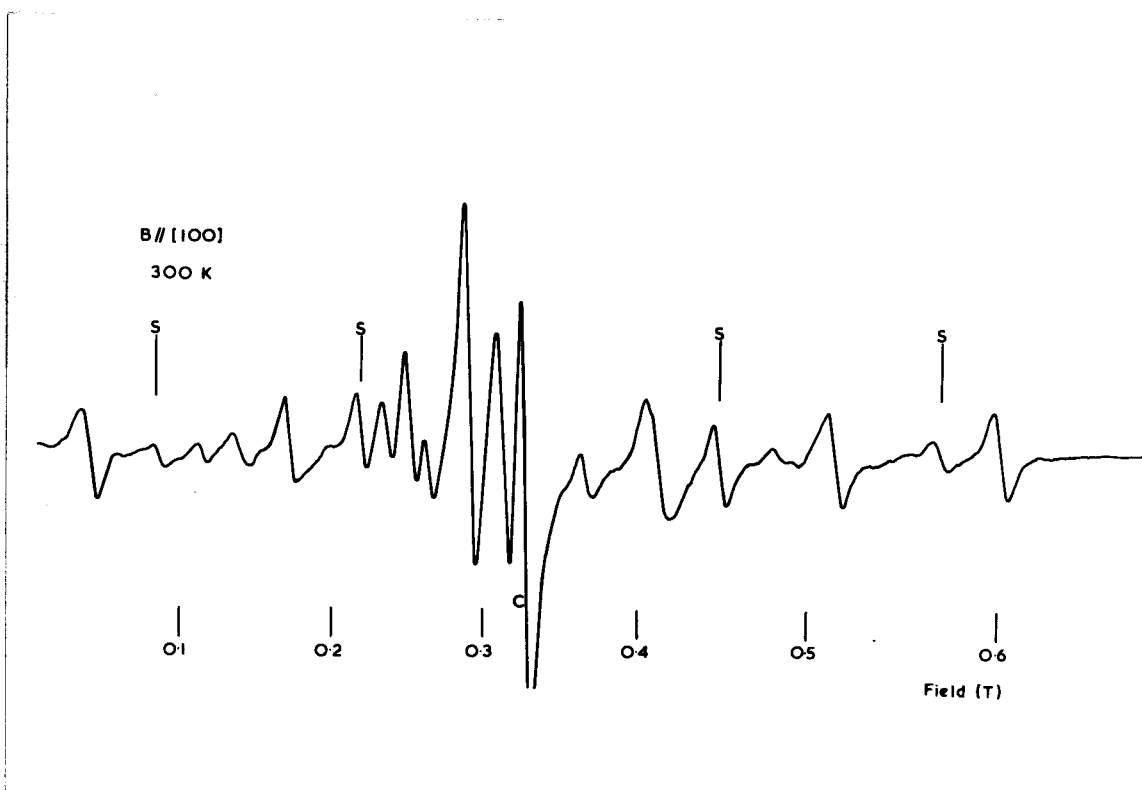
Fig. 4.17. The E.P.R. of $Cr^{3+}$ in AgBr at 300K with B $//<100>$.
The lines labelled S increase in intensity relative to the rest
of the sprectrum as the temperature rises.
The central isotropic line is labelled C .
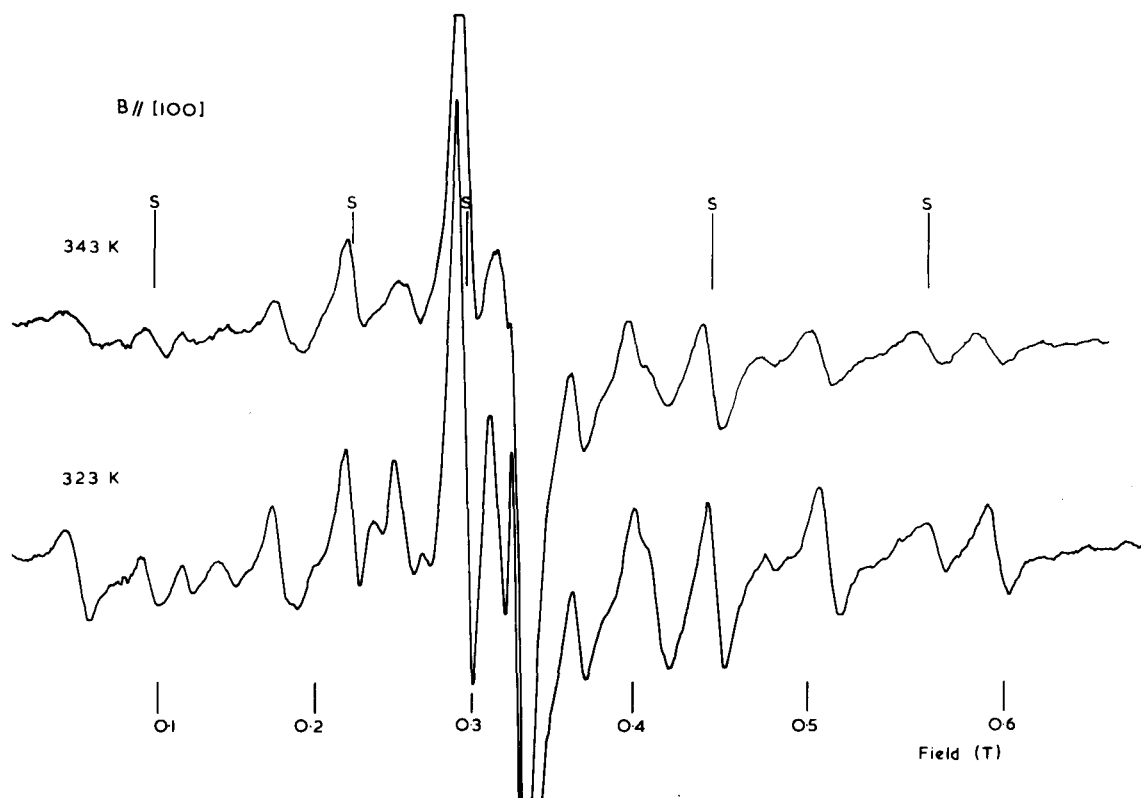
Fig. 4.18. The E.P.R. of $Cr^{3+}$ in AgBr above 300K with B $// <100>$.
The lines labelled S increase in intensity relative to the rest
of the spectrum as the temperature rises .

At all temperatures there were more lines present below $g = 2$ than above. These extra lines are thought to be due to forbidden transitions.

## 4.6 Interpretation of the spectrum for AgBr

### 4.6.1 The principal spectrum at 95K

A set of nine lines with high intensity at 95K extreme at $B /\!/ \langle 100 \rangle$ and all have similar temperature dependences. These lines have been fitted to the orthorhombic Hamiltonian

$$H = g\beta \underline{B}.\underline{S} + D(S_z^2 - \tfrac{1}{3}S(S + 1)) + E(S_x^2 - S_y^2)$$

The large spread of the spectrum shows that $2D \simeq 0.3T$. $\frac{D}{B}$ is not, therefore, a small quantity and perturbation theory will not give a satisfactory solution to the Hamiltonian. However, for the fine structure lines on the high field side of $g = 2$ corresponding to $B /\!/ Z$ and $B /\!/ Y$, the second and higher order terms in $\frac{D}{B}$ will be comparatively small. The positions of these lines, and the position of the cubic line at high temperatures, were used to estimate $B_o$, D and E. The g-value was assumed to be isotropic within the experimental error as for $AgCl:Cr^{3+}$. The position of the high field line from the centre with $B /\!/ X$ was calculated as a check on the chosen values of D and E.

The second and third order corrections to all the lines at fields below $B_o$ are significant (1mT or more). Therefore, plots were made of the energy levels of the system as B varied for B parallel to Z, X and Y using the estimated values of $B_o$, D and E. These energy level plots are

exact, being calculated from the solutions of the matrix of the above Hamiltonian and the usual base states $|\pm\frac{3}{2}\rangle$ and $|\pm\frac{1}{2}\rangle$ [16].

For B//Z

$$E_n = \begin{cases} \frac{1}{2}B \pm \left[(D + B)^2 + 3E^2\right]^{\frac{1}{2}} \\ -\frac{1}{2}B \pm \left[(D - B)^2 + 3E^2\right]^{\frac{1}{2}} \end{cases}$$

For B//Y

$$E_n = \begin{cases} \frac{1}{2}B \pm \left[(-\frac{1}{2}(3E + D) + B)^2 + \frac{3}{4}(D - E)^2\right]^{\frac{1}{2}} \\ -\frac{1}{2}B \pm \left[(-\frac{1}{2}(3E + D) - B)^2 + \frac{3}{4}(D - E)^2\right]^{\frac{1}{2}} \end{cases}$$

For B//X

$$E_n = \begin{cases} \frac{1}{2}B \pm \left[(\frac{1}{2}(3E - D) + B)^2 + \frac{3}{4}(D + E)^2\right]^{\frac{1}{2}} \\ -\frac{1}{2}B \pm \left[(\frac{1}{2}(3E - D) - B)^2 + \frac{3}{4}(D + E)^2\right]^{\frac{1}{2}} \end{cases}$$

where $E_n$, E and D are in field units.

Transitions occur at $\triangle E_n = B_o$ where $h\nu = g\beta B_o$.

The energy levels are shown in fig. 4.19 together with the transitions. The theoretical transition fields taken from the graphs are also shown in fig. 4.14. The constants used were

$$g = 1.990 \pm 0.003$$

$$|D| = 0.1555 \pm 0.0005T = (1443 \pm 5) \times 10^{-4} \text{cm}^{-1}$$

$$|E| = 0.022 \pm 0.001T = (20.4 \pm 1) \times 10^{-4} \text{cm}^{-1}$$

The principal centre accounts for about 70% of the total resonant intensity.
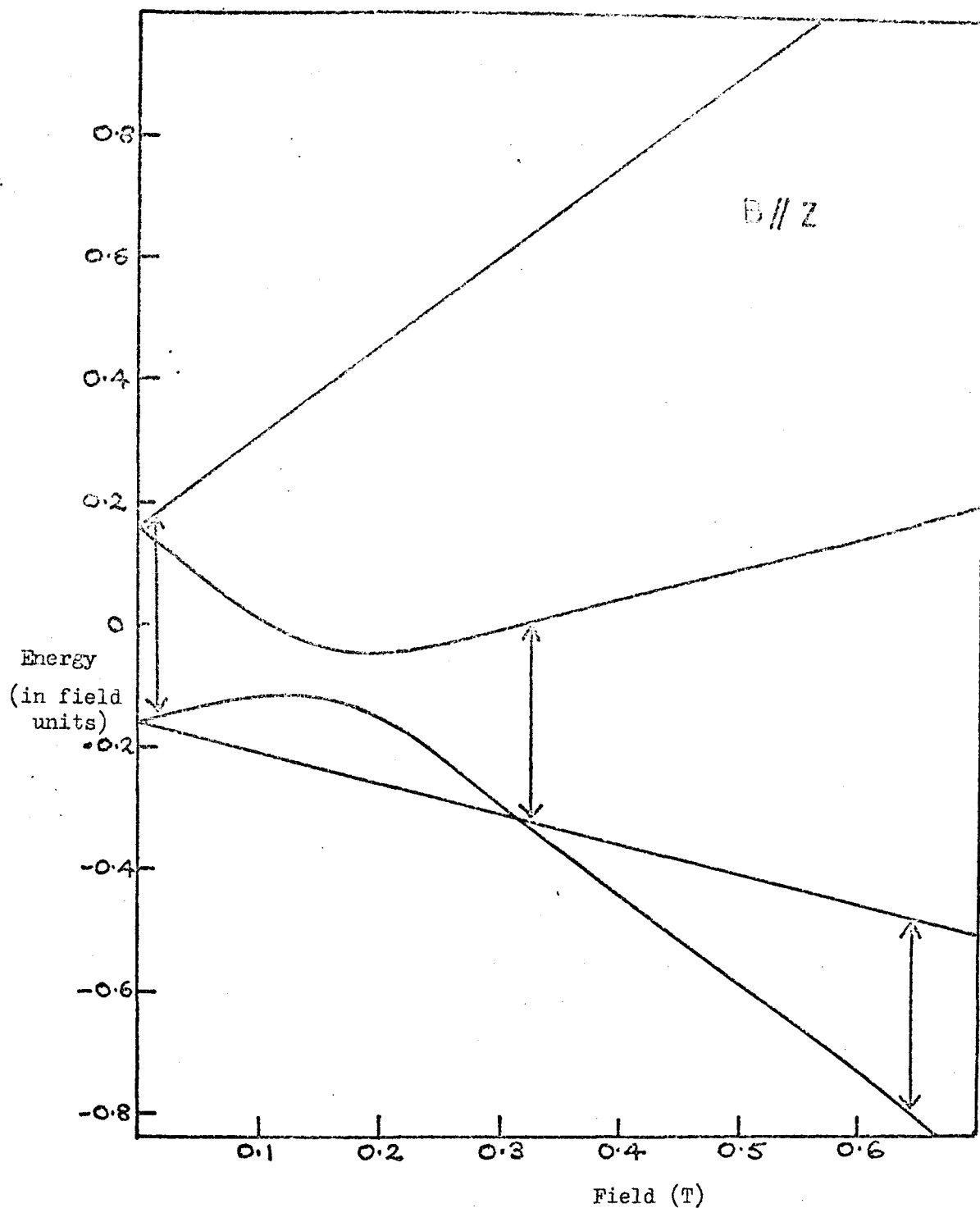
Fig. 4.19a. The relative energy levels of the principal orthorhombic centre in AgCl:Cr$^{3+}$ with B // Z as the external field varies. The spin Hamiltonian parameters given in the text were used to calculate the levels. The transitions observed are shown by arrows .
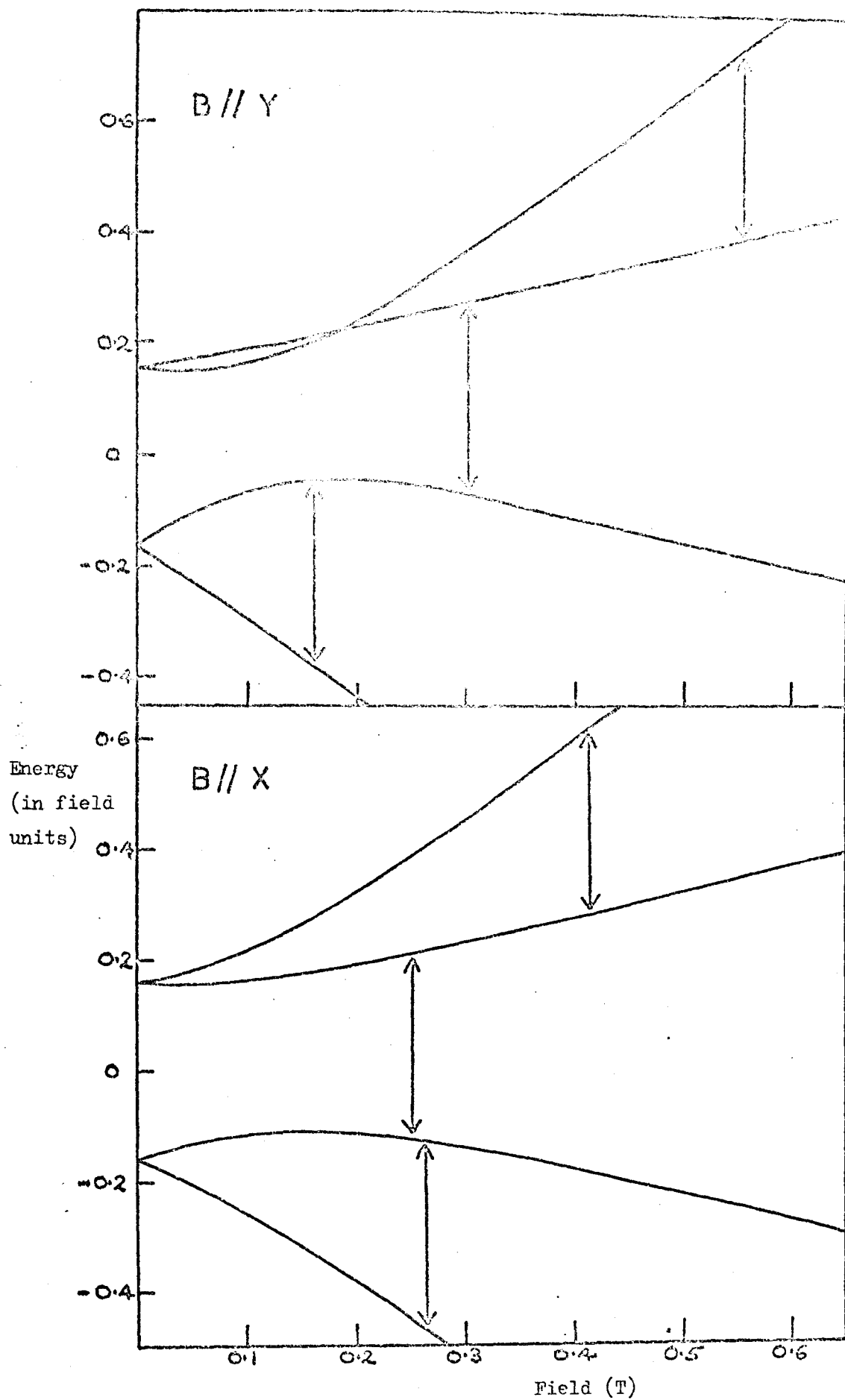
Fig.4.19b. The relative energy levels with B // Y and B // X .

### 4.6.2  The subsidiary spectra at 95K

One set of low intensity lines observed at 95K was fitted to a spin Hamiltonian of tetragonal symmetry

$$H = g\beta\underline{B}.\underline{S} + D(S_z^2 - \frac{1}{3}S(S + 1))$$

where g = 1.990 ± 0.003

$$|D| = 0.1025 \pm 0.0002T = (950 \pm 2) \times 10^{-4} cm^{-1}$$

The lines on the high field side of $B_o$ can be fitted exactly to this Hamiltonian using the expressions for the transition fields with B//Z and B⊥Z correct to third order. These lines are shown in fig. 4.14. The low field transitions are also shown, and were calculated from graphs showing the variation of the energy levels with B. At B//<110> the lines arising from centres with B⊥Z are clearly present. The resonant lines from centres with B at 45° to Z cannot be positively identified and a perturbation calculation cannot be used to find the resonant fields as $\frac{D}{B_o}$ is significantly large. The centre accounts for about 10% of the total intensity.

There is a low intensity line which reaches a maximum field of 0.8T at B//<100>. Another line of similar intensity reaches a maximum field at 0.648T when B is parallel to <110>. These two lines and another near 0.535T with B//<100> are tentatively assigned to an orthorhombic centre with <110>, <001>, <1$\bar{1}$0> as the Z, Y and X axes respectively. The Hamiltonian is then

$$H = g\beta B.S. + D(S_z^2 - \frac{1}{3}S(S + 1)) + E(S_x^2 - S_y^2)$$

and                    g = 1.990 ± 0.003

$$|D| = 0.158 \pm 0.001T = (1470 \pm 10) \times 10^{-4} cm^{-1}$$

$$|E| = 0.103 \pm 0.001T = (956 \pm 10) \times 10^{-4} cm^{-1}$$

The transitions for B//Z and X (at < 110>) and B//Y (at < 100>) are shown on figs. 4.14 and 4.15. The lines from centres with other orientations cannot be readily identified as perturbation theory calculations of the fields are again not valid. This centre accounts for about 10% of the $Cr^{3+}$ ions.

### 4.6.3 Line broadening and activation energies

As the temperature of the sample increases above 200K the outer lines of the spectrum start to broaden. This is interpreted as in $AgCl:Cr^{3+}$. Jumping of the vacancies around or away from the $Cr^{3+}$ ion changes the symmetry of the site and reduces the lifetime of the resonant state. Fig. 4.20 shows the excess line width (the observed line width minus the line width at 95K-150K) plotted against $\frac{1}{T}$ for the two lines which are clearly separated from nearby lines at B//<100>. These are the high field $\frac{3}{2} \leftrightarrow \frac{1}{2}$ transitions from those principal centres with the magnetic field parallel to Z and Y. The activation energy is the same for both lines.

$$E_a = 0.35 \pm 0.03 \text{ eV}$$

### 4.6.4 The spectrum at high temperatures

At 300K the intensity of the non-cubic centres has decreased and the intensity of the isotropic line at 0.3320T has increased, allowing for the Boltzmann factor (fig. 4.17). (The area under the derivative curves was estimated directly to correct for broadening of the outer lines.) As Ulrici has shown from conductivity measurements[11], the vacancies associated with the $Cr^{3+}$ ion are moving into the lattice at these temperatures.
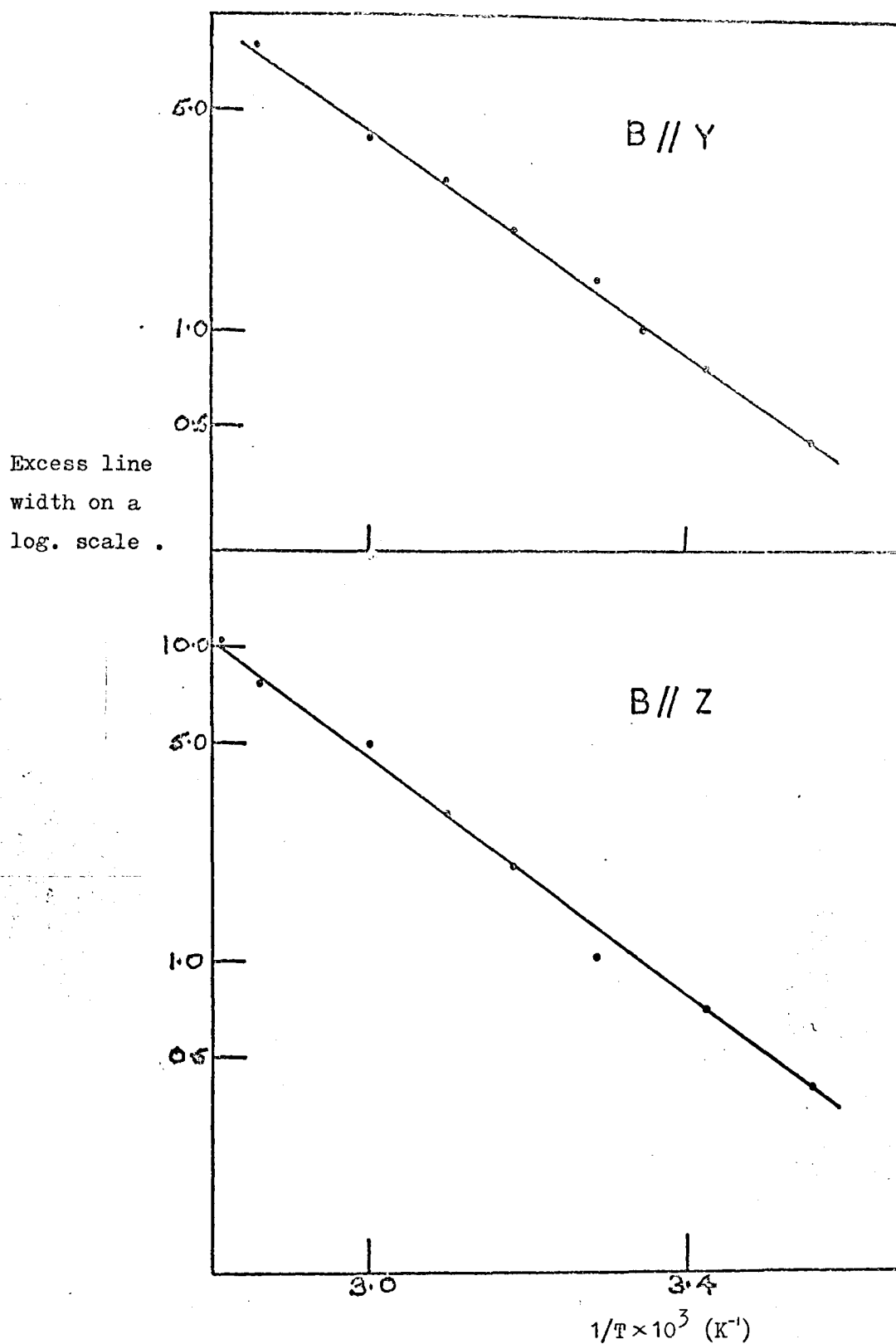
Fig. 4.20. The log. of the excess line width in AgBr:Cr$^{3+}$ plotted against 1/T for the principal orthorhombic centre .

The overall spread of the principal orthorhombic centre has decreased considerably so that the low field lines are seen. The spectrum may be fitted to the orthorhombic Hamiltonian with

$$g = 1.990 \pm 0.003$$

$$|D| = 0.137 \pm 0.001T = (1270 \pm 10) \times 10^{-4} cm^{-1}$$

$$|E| = 0.015 \pm 0.001T = (139 \pm 9) \times 10^{-4} cm^{-1}$$

$|D|$ has decreased by about 15% from 95K, and $|E|$ has decreased by about 30%.

Since the intensity of the spectrum increases up to 550K the apparently cubic spectrum at 430K is probably due to those $Cr^{3+}$ ions which are associated with one vacancy. If this vacancy jumps rapidly about the $Cr^{3+}$ ion, the outside lines will be too broad to be detected and the central lines will overlap the cubic line by a motional narrowing effect. The $Cr^{3+}$ ion is thought to be isolated at 550K.

The set of lines labelled S in figs. 4.17 and 4.18 are assigned to a new centre of $Cr^{3+}$ with one vacancy which becomes the major centre at temperatures above 350K. The lines at B//<100> may be fitted to an axial Hamiltonian with tetragonal symmetry. At 300K

$$g = 1.990 \pm 0.003$$

$$|D| = 0.1205 \pm 0.0005T = (1120 \pm 5) \times 10^{-4} cm^{-1}$$

The fine structure lines from centres with B parallel to and perpendicular to the principal axis can be seen. The central $\pm \frac{1}{2}$ transitions for centres with B⊥Z is resolved from the central cubic line because of second order shifts to low field. The resonance probably arises from $Cr^{3+}$ ions associated with a single next nearest cation vacancy.

## 4.7  Discussion of the surroundings of the $Cr^{3+}$ ion

### 4.7.1  Possible vacancy models

There are numerous possible arrangements of the two vacancies which are expected to be associated with the $Cr^{3+}$ ion at low temperatures. In view of the previous work on vacancy association in silver chloride[2-8,22] it seems probable that the vacancies will lie within the first two cation shells surrounding the $Cr^{3+}$ ion.

The possible arrangements of two vacancies are listed in fig. 4.13, together with the symmetry of the resulting site and the probable crystal field axes. Arrangements where the vacancies are in adjacent positions are unlikely because of the mutual repulsion of the vacancies.

The only two vacancy centre which will give a perfect tetragonal centre is that with both vacancies in next nearest cation sites in a line. The tetragonal centre is, therefore, considered to arise from this type of centre. The vacancies probably lie on opposite sides of the $Cr^{3+}$ ion because of their mutual repulsion. A centre of this kind is suggested by Cheema[22] for $V^{3+}$ in AgCl.

There are several arrangements of two vacancies which might give an orthorhombic centre with $\langle 110 \rangle$ $\langle \bar{1}10 \rangle$ and $\langle 001 \rangle$ axes. A likely centre, because the two vacancies are well separated, is that with two nearest cation vacancies at $180°$.

The centre which is most likely to give strong orthorhombic, or lower symmetry, with $\langle 100 \rangle$ axes is that suggested by Kunze and Müller[12]

None of the other centres are likely to give orthorhombic symmetry combined with <100> axes unless the vacancies are displaced considerably from the normal lattice sites.

## 4.7.2 The Kunze and Müller model and a crystal field calculation

·This model is shown in fig. 4.9. It has monoclinic symmetry $(m, C_{1h})$ and gives rise to the term $K(S_x S_y + S_y S_x)$ in the spin Hamiltonian. In order to establish whether the principal spectrum observed can be assigned to this centre a crystal field calculation was undertaken. A simple point charge model was used following Watkins[19]. The potentials found confirm the presence of the (xy) term, but can only be fitted to the usual form in D, E and K if the correct axes are chosen. These axes are shown on fig. 4.9.

The spectrum observed in AgCl has two axes (Z, X) displaced by $\pm 4°$ from the <100> directions. The planar nature of the centre, and the mutual repulsion of the vacancies makes it probable that the off-axis components will arise within the plane of the two vacancies and the $Cr^{3+}$ ion. The spectrum axis Z is therefore re-assigned to Y′ for the crystal model, and Y to Z′, and X to X′.

The analysis of the spectrum is not altered but new D, E values are required. These are:

$$|D'| = 30.5 \pm 0.2 \text{ mT} = (281 \pm 2) \times 10^{-4} \text{cm}^{-1}$$

$$|E'| = 14.8 \pm 0.1 \text{ mT} = (137 \pm 1) \times 10^{-4} \text{cm}^{-1}$$

The crystal field calculation predicts (Appendix II)

$$D = -k \left[ \frac{3e}{8\sqrt{2}a^3} + \frac{e}{32a^3}(3 + 72\eta) \right]$$

$$E = +k \frac{e}{32a^3}(3 + 72\eta) \qquad\qquad K = k\frac{6e}{a^3}(\varepsilon - \frac{1}{8\sqrt{2}})$$

where k is an unknown constant relating the crystal field potential to the observed energy level splittings. a is the mean distance from the impurity ion to the halogens. $\eta$a is the displacement towards the $Cr^{3+}$ ion of the halide ion between the $Cr^{3+}$ and the next nearest cation (N.N.C.) vacancy. |e| is the numerical charge on the electron.

The ratio of $\frac{D}{E}$ may be used, in the case of AgCl, to calculate $\eta$ if the sign of E is taken to be opposite to that of D. The experimental values for $AgCl:Cr^{3+}$ give $\eta = 0.07$. The value of K, predicted by this simple model, does not depend on $\eta$ but only on $\varepsilon$. $\varepsilon$a is the displacement of halide ions produced by the nearest cation vacancy. Thus the model will not provide confirmation that the E.P.R. results have been interpreted correctly. However, the ratio of $\frac{E}{K}$ was used to investigate whether a reasonable value of $\varepsilon$ could be found using the maximum K value allowed by the spectrum (5.4mT). The value of $\varepsilon$ found is 0.11 which is a reasonable value and larger than $\eta$ as might be expected.

For $AgBr:Cr^{3+}$ the accuracy of the E.P.R. results at X-band does not permit an estimate of K. To obtain a positive value of $\eta$ it was necessary to change the assignment of the axes of the spectrum, as for $AgCl:Cr^{3+}$. Z and Y were interchanged to give new values for D and E:

$$|D'| = 0.1107 \pm 0.001T$$

$$|E'| = 0.0668 \pm 0.001T$$

and then $\eta = 0.14$.

This value of $\Omega$, although larger than for AgCl, is still reasonable and compatible with values suggested by Watkins[19] and Bassani and Fumi[23] for divalent impurities in NaCl.

## 4.8    Discussion and comparison of AgCl and AgBr

### 4.8.1    The centres observed

All the spectra are assigned to trivalent chromium ions. The chemistry of chromium and the method of production by halogenation confirm that the trivalent state is the most probable. E.P.R. has been observed from $Cr^{5+}$ and $Cr^{4+}$ but only at 20K and below. The E.P.R. of $Cr^{2+}$ and $Cr^{+}$ have also been observed but only at very low temperatures. No nuclear hyperfine structure was detected. 90.5% of chromium isotopes have zero nuclear spin. The remaining isotope ($^{53}Cr$) has a nuclear spin of $\frac{3}{2}$ and is expected to give four hyperfine lines each of intensity about 2% of the central line. The hyperfine separation is typically about 1.8mT[29] and is too small to be detected around the numerous central lines in AgCl and AgBr.

Table 4.1 summarises the E.P.R. results in AgCl:$Cr^{3+}$ and AgBr:$Cr^{3+}$. The number of centres observed is unusual in the silver halides. For the majority of the divalent ions studied ($Fe^{2+}$, $Co^{2+}$, $V^{2+}$, $Eu^{2+}$) only one centre is needed to explain 98% of the spectrum at 77K. A cubic resonance due to isolated ions is also seen in AgCl:$Ni^{2+}$. $Fe^{3+}$ gives only a single interstitial centre under these conditions at these temperatures[3,4]. It seems likely that, when two vacancies are needed to neutralize a small

Table 4.1

| | | AgCl:$Cr^{3+}$ | AgBr:$Cr^{3+}$ |
|---|---|---|---|
| Principal centre at 95K | g | 1.980 ± 0.004 | 1.990 ± 0.003 |
| | D | 37.5 ± 0.2mT | 155.5 ± 0.5mT |
| | E | 7.8 ± 0.1mT | 22 ± 1mT |
| | K | ⩽ 5.4 mT | - |
| Tetragonal centre at 95K | g | 1.980 ± 0.002 | 1.990 ± 0.003 |
| | D | 54.0 ± 1mT | 102.5 ± 0.2mT |
| Approximate % of $Cr^{3+}$ | | 5% | 10% |
| Subsidiary orthorhombic centre at 95K | g | 1.980 ± 0.005 | 1.990 ± 0.003 |
| | D | 46.25 ± 0.5mT | 158 ± 1mT |
| | E | 6.9 ± 0.1mT | 103 ± 1mT |
| Approximate % of $Cr^{3+}$ | | 10% | 10% |
| Principal centre at 300K | g | 1.980 ± 0.005 | 1.990 ± 0.003 |
| | D | 38.0 ± 0.5mT | 137 ± 1mT |
| | E | 8.7 ± 0.1mT | 15 ± 1mT |
| Tetragonal centre arising above 300K | g | 1.980 | 1.990 |
| | D | 18.0 ± 0.5mT | 120.5 ± 0.5mT |
| Activation energies ($E_a$) | | | |
| Principal centre | | 0.21 ± 0.04eV | 0.35 ± 0.03eV |
| Tetragonal centre | | 0.41 ± 0.04eV | - |
| Orthorhombic centre | | 0.32 ± 0.04eV | - |
| Binding energy ($E_b$) of first vacancy to $Cr^{3+}$ | | 0.18 ± 0.05eV | 0.20 ± 0.05eV |

substitutional ion, the changes in binding energy between different possible arrangements are small. Estimates of the binding energies for the various centres observed in AgCl and AgBr show only small differences The T.D.C. curves for the trivalent ions $Ti^{3+}$, $Cr^{3+}$, $V^{3+}$ (12b) increase in complexity in that order, again suggesting that there are a number of centres involved.

The principal and subsidiary centres present at 95K are thought to be the same in both lattices. The main spectrum is interpreted with the Kunze and Müller model for both AgCl and AgBr. Although the absolute magnitudes of the zero field splittings are different, the ratios of $\frac{D}{E}$ in each case are similar enough for the same explanation to apply to both. Smaller percentages of tetragonal and orthorhombic centres are observed in both matrices. Also, on warming, a new centre appears which can be interpreted as a single N.N.C. vacancy associated with the $Cr^{3+}$ ion. This centre can be more clearly seen in AgBr:$Cr^{3+}$ because of the larger field splittings. It might be thought that the nearest cation (N.C.) vacancy would be more tightly bound to the impurity ion and would, therefore, constitute the single vacancy centre seen at temperatures near 320K. However, dielectric, conductivity and other E.P.R. measurements show that the jump frequency for any associated vacancy will be high at these temperatures. A N.C. vacancy can jump around the impurity ion by means of the N.N.C. sites with the result that mobile N.N.C. and N.C. vacancies cannot be distinguished at these temperatures. The appearance of the tetragonal symmetry spectrum shows that the vacancy spends longer in the N.N.C. site than in the N.C. site. The activation energy for jumping of the tetragonal centre (two N.N.C. vacancies) in AgCl is higher than that for the subsidiary orthorhombic centre (two N.C. vacancies). (Table 4.1).

## 4.8.2 Line widths and g-values

Table 4.2 gives a list of previous E.P.R. and optical results obtained for impurity ions in both AgCl and AgBr. A list of relevant parameters for the two lattices is included. The spectra of $Co^{2+}$, $Ni^{2+}$ and $Fe^{3+}$ have been studied in both lattices and, in general, show that the spectra in AgBr have two or three times larger line widths than in AgCl, and are harder to detect. The $Cr^{3+}$ lines have widths 1.2mT and 5mT in AgCl and AgBr respectively in agreement with the usual trend. The low temperature line width is almost certainly due to unresolved ligand hyperfine structure. The overlap of metal and ligand orbitals, or covalency, is greater in AgBr than in AgCl, as would be expected from the relative positions of bromine and chlorine in the periodic table.

The difference in g-values for the two matrices is also due to increased covalency in the AgBr lattice. The g-value of $Cr^{3+}$ is expected to be related to the free spin value by

$$g = 2 - \frac{8\lambda}{\Delta} \tag{16}$$

where $\lambda$ is the spin-orbit coupling parameter, and $\Delta$ is the cubic field splitting. $\Delta = 10Dq$ in the usual terminology of optical absorption measurements. The free ion value of $\lambda$ for $Cr^{3+}$ is $91cm^{-1}$, and using the $\Delta$ values of Ulrici[11] this gives expected g-values of 1.95 and 1.94 for AgCl and AgBr respectively.

The reduction in g-values quoted above arises when the coupling of the ground state $^{4}A_{2}$ to the first excited state $^{4}T_{2}$ via spin-orbit coupling and the external magnetic field is taken into account. The effect of covalent overlap of impurity and ligand orbitals is to reduce the spin-orbit

Table 4.2

## E.P.R. measurements

| Ion | | AgCl | AgBr | | Reference |
|---|---|---|---|---|---|
| $Ni^{2+}$ (4.2K) | g-value | 2.281 | 2.20 | (axial centre) | 6,7 |
| | Line width | 10mT | 18mT | (cubic line) | |
| | Zero field splitting | $-2.96cm^{-1}$ | $-2.92cm^{-1}$ | (axial centre) | |
| $Co^{2+}$ (4.2K) | g-values | $g_{//} = 5.88$ $g_{\perp} = 3.87$ | - | (axial centre) | 5 |
| | Line width | 1.5mT | 3mT | | |
| $Fe^{3+}$ (77K) | g-value | 2.0156 | 2.045 | | |
| | Line width | 0.5mT | 1.4mT | | 3 |
| | Cubic field splitting | $75 \times 10^{-4}cm^{-1}$ | - | | |
| | 'A' value | $3.3 \times 10^{-4}cm^{-1}$ | $16.2 \times 10^{-4}cm^{-1}$ | | |

## Optical absorption measurements

| Ion | | AgCl | AgBr | Reference |
|---|---|---|---|---|
| $Ti^{3+}$ (20K) | $^2T_2 \rightarrow 2E$ upper level | $12740cm^{-1}$ | $11290cm^{-1}$ | 11 |
| $Cr^{3+}$ (20K) | Dq | $1310\ cm^{-1}$ | $1202\ cm^{-1}$ | 11 |
| $V^{2+}$ (20K) | Dq | $815\ cm^{-1}$ | $737\ cm^{-1}$ | 11 |
| | B | $605\ cm^{-1}$ | $565\ cm^{-1}$ | |

---

| | |
|---|---|
| Lattice parameters | AgCl : 2.77Å, AgBr : 2.88Å |
| Ionic radii | $Ag^+$ : 1.26Å, $Cl^-$ : 1.81Å, $Br^-$ : 1.95Å, $Cr^{3+}$ : 0.65Å (24) |
| Polarizability in an ionic lattice | $Cl^-$ : 2.96, $Br^-$ : 4.16 (30) |

coupling parameter by mixing of ligand orbital wave-functions into the $Cr^{3+}$ spin only ground state. The g-value may now be expressed as

$$g = 2 - \frac{8N_\sigma^2 \lambda}{\Delta}$$

where $(1 - N_\sigma)$ is the proportion of ligand $\sigma$ bonding present. This expression, and the measured g-values, leads to

$$N_\sigma \simeq 0.6 \quad \text{for} \quad AgCl$$

$$N_\sigma \simeq 0.4 \quad \text{for} \quad AgBr.$$

The increase in covalency in AgBr satisfactorily explains the g-value of $AgBr:Cr^{3+}$ having a value closer to 2.

### 4.8.3  Crystal field splittings

The D values observed in AgBr are generally four times as large as those in AgCl. The optical results show that, in general, the cubic field splitting decreases from AgCl to AgBr and indeed this is the trend usually observed as the ligand ion changes[25]. The only crystal field splitting measured in the two lattices is that for $Ni^{2+}$ where the two results are very similar. However, the processes by which the crystal field will act upon the $Ni^{2+}$(S = 1) ion will be different to those acting in $Cr^{3+}$, and in addition $Ni^{2+}$ has only one excess positive charge.

An increase in the covalent overlap of orbitals in AgBr could explain an increase in D. However, since the cubic field splitting of $Cr^{3+}$ in AgBr is less than that in AgCl, any covalent effect must be small and would not give the observed large numerical change in the crystal field splittings.

A striking difference between the $Br^-$ and $Cl^-$ ions is the greater polarizability of the $Br^-$ ion (table 4.2). The small $Cr^{3+}$ ion with double excess charge over the lattice will certainly cause a local relaxation and reduction of the separation of the $Cr^{3+}$ and the halide ions. This movement reduces the 'a' value to be used in the crystal field calculation. Polarization of the ligand ions will correspond to a further decrease in a and the value appropriate to $AgBr:Cr^{3+}$ may be sufficiently smaller than that for $AgCl:Cr^{3+}$ to explain the increase in all the observed $|D|$ values.

$|D|$ and $|E|$ for the principal centre in $AgCl:Cr^{3+}$ increase on warming from 95K to 300K, whereas $|D|$ and $|E|$ for $AgBr:Cr^{3+}$ decrease. If the lattice expands on warming a simple point charge model predicts a decrease in the crystal field splittings. In AgCl the ions surrounding the $Cr^{3+}$ ion must in some way be able to relax inwards towards the trivalent ion as the temperature rises.

## 4.8.4   The 'L' lines

The similar temperature dependence of these lines in the two lattices suggests that they arise from the same source. The single line observed in AgBr suggests an $S = \frac{1}{2}$ centre, and it might be possible to explain the three lines in AgCl as an $S = \frac{1}{2}$ centre with the magnetic field parallel to X, Y and Z. However, the relative intensity of the three lines in AgCl (3:4:3) rules out this possibility.

The possibility of the lines arising from interstitial $Cr^{3+}$ is also ruled out because of the way in which the lines disappear. If interstitial $Cr^{3+}$ were seen at 95K due to an increased spin-lattice

relaxation time following a reduction in lattice phonons, then on warming the lines would be expected to broaden abruptly and disappear, probably at quite low temperatures.

The manner in which the lines disappear can best be explained by a centre which is abruptly destroyed as the temperature rises above a value where the activation energy of the necessary process is of the order of kT.

Neither the AgCl lines nor the AgBr line are cubic and it seems, therefore, that the centre present will only give a detectable spectrum with the magnetic field parallel to one axis. Possibly it is a planar centre involving large ligand overlap so that the lines are broadened and cannot be seen except when the external magnetic field is perpendicular to the plane. The $S = \frac{1}{2}$ line observed in AgBr might then be a single transition observed because of the very large zero field splitting.

## 4.8.5  The lattice site

The only other trivalent ion studied directly in AgCl is $Fe^{3+}$. This is incorporated interstitially with four silver ion vacancies at low temperatures. The Goldschmidt radii of $Cr^{3+}$ and $Fe^{3+}$ are $0.65\overset{o}{A}$ and $0.67\overset{o}{A}$ respectively[24]. It is, therefore, certainly possible for the $Cr^{3+}$ ion to fit into the interstitial space. The reason why it does not do so is clear if the orbital levels of the $3d^3$ ($Cr^{3+}$) ion are compared with the $3d^5$ ($Fe^{3+}$) ion. Griffith[26] gives a table of ligand field stabilization energies of the $d^n$ ions in octahedral field. In the free ion the $d^n$ energy levels are degenerate. In a ligand field the $dt_2$ and de orbits split resulting in an overall lowering of the energy of the ion over the free ion according to the filling of the energy levels.

For $Cr^{3+}$ in an octahedral field the reduction in energy is $-\frac{6}{5}\Lambda$ where $\Lambda$ is the optical level splitting. This is the largest stabilization energy in the 3d series. $Fe^{3+}$ is an S-state ion with zero orbital angular momentum and, therefore, the energy levels are not affected, to first order, by the ligand field. The stabilization energy is zero. Rado and Suhl[27] also calculate site preference energies for the iron transition series, taking into account the Madelung, polarization and ligand field energies. The values for octahedral site preference energies are $\frac{76}{9}Dq$ for $Cr^{3+}$ and zero for $Fe^{3+}$.

It is probable that for small ions the lattice energy is lowest for interstitial incorporation in AgCl and AgBr. However, the high preference of $Cr^{3+}$ for octahedral coordination forces it into the substitutional site. The lattice strain in this position will be large and will account for the $\eta$ and $\varepsilon$ values observed, which are larger than for $NaCl:Mn^{2+}$, and for the large line widths at all angles away from B//<100>. Low and Suss note a similar effect with small radius ions in CaO[28].

## 4.9    References

1    S.U. Cheema and M.J.A. Smith, J. Phys. C. 2, 1751 (1969).

2    M. Daehler, Ph.D. Thesis, University of Wisconsin (1962).

3    W. Hayes, J.R. Pilbrow and L.M. Slifkin, J. Phys. Chem. Solids, 25, 1417 (1964).

4    K.A. Hay, D.J.E. Ingram and A.C. Tomlinson, J. Phys. C. 1, 1205 (1968).

5    T.R. Sliker, Phys. Rev. 130, 1749 (1963).

6    J. Busse, Phys. Stat. Sol. 3, K65, and 1892 (1963).

7    M. Höhne, M. Stasiw and A. Wattesich, Phys. Stat. Sol. 34, 319 (1969).

8    R.F. Tucker, Phys. Rev. 112, 725 (1958).

9    I.S. Ciccarello, M.B. Palma-Vitorelli and M.A. Palma, Phil. Mag. 5, 723 (1960).

10   D.C. Burnham and F. Moser, Phys. Rev. 136A, 744 (1964), Phys. Stat. Sol. 15, 129 (1966).

11   W. Ulrici, Phys. Stat. Sol. 27, 333 and 489 (1968).

12   I. Kunze and P. Müller,   (a) Phys. Stat. Sol. 33, 91 (1969)
                              (b) Ibid. 38, 271 (1970).

13   H. Böttger, Phys. Stat. Sol. 4, 669 (1964).

14   G.H. Dieke, Spectra and Energy Levels of Rare Earth Ions in Crystals, J. Wiley, N.Y. (1968).

15   K.W.H. Stevens, Proc. Phys. Soc. A65, 209 (1952).

16   J.W. Orton, Electron Paramagnetic Resonance, Iliffe (1968).

17   W. Low, Solid State Physics Suppl. 2, Academic Press (1960).

18   A.J.B. Codling and B. Henderson, J. Phys. C. 4, 1242 (1971).

19   G.D. Watkins, Phys. Rev. 113, 91 (1959).

20   Yu Ting, L.D. Farringer and D. Williams, Phys. Rev. 97, 1037 (1955).

21   D.M.S. Bagguley, B. Bleaney and J.H.E. Griffiths, Proc. Phys. Soc. 51, 551 (1948).

22   S.U. Cheema, Ph.D. Thesis, University of Warwick (1971).

23     F. Bassani and F.G. Fumi,   Il Nuovo Cimento, 11, 274 (1954).

24     R.W. Gurney and N.F. Mott,   Electronic Processes in Ionic Crystals, Dover, New York (1948).

25     J. Owen and J.H.M. Thornley,   Rep. Prog. Phys. 29, 675 (1966).

26     J.S. Griffith,   The Theory of Transition Metal Ions,   Cambridge University Press (1964).

27     G.T. Rado and H. Suhl,   Magnetism III,   Academic Press (1963).

28     W. Low and J.T. Suss,   Solid State Comm. 2, 1 (1964).

29     J.E. Wertz and P. Auzins,   Phys. Rev. 106, 484 (1957).

30     J.R. Tessman, A.H. Kahn and W. Schockley,   Phys. Rev. 92, 890, (1953).

Chapter Five :   The E.P.R. of ytterbium, erbium and dysprosium
                 in AgCl

## 5.1    Introduction

Some rare earth metals (cerium, praseodymium, neodymium, samarium
and europium) were added to the silver halides by Moser, Nail and Urbach
in 1959[1] but were found to produce no striking effect on the optical or
photochemical properties of the halide.  More recently, Cheema and
Smith[2,3] investigated the E.P.R. of europium and gadolinium in silver
chloride.  They found that europium in silver chloride, after annealing
under a non-oxidising atmosphere, considerably increased the amount of
silver colloid produced on exposure to light.  E.P.R. showed that the
$Eu^{2+}$ ion was incorporated substitutionally in the lattice and was
associated with a silver ion vacancy in the nearest-cation position.  On
exposure to light the $Eu^{2+}$ acted as a trap for photoproduced holes and
was converted to $Eu^{3+}$.

In this work the rare earths other than europium and gadolinium
were studied in silver chloride.  This chapter describes the E.P.R.
results for those ions ($Yb^{3+}$, $Er^{3+}$, $Dy^{3+}$) for which resonances were
observed, and the conclusions which could be made about the incorporation,
site symmetry, and vacancy association of these ions in AgCl.

The ions studied by Cheema and Smith ($Eu^{2+}$, $Gd^{3+}$) both have half-
filled 4f shells.  The ground state of the free ions is $^{8}S_{7/2}$ with zero
orbital angular momentum.  These ions are only coupled to the crystal
field by second order and higher terms, and resonance can be observed at
room temperature since the spin-lattice relaxation times are long.  The

other rare earth ions have finite orbital angular momentum and temperatures of 20K or less are required for the observation of resonances.

The samples were doped as described in Chapter Three using the appropriate rare earth metal. E.P.R. traces were recorded at 77 and 4.2K after annealing the samples in chlorine or nitrogen atmospheres. For dysprosium, erbium and ytterbium E.P.R. observed after the two anneals was the same. The only changes observed were slight increases in the overall intensity of the spectrum after annealing in chlorine. These are believed to arise because the chlorine anneal encourages precipitates of the impurity to diffuse into the crystal. Altering the rate of cooling of the samples after annealing and changing the concentration of the impurity ion did not affect the structure of the spectra. Changes in the optical spectra of AgCl:Au as a result of heat treatment were observed by Edmonds[26]. The rare earth doped samples were irradiated at room temperature, 77K and 4.2K after annealing in nitrogen and no appreciable changes were observed in the spectra at 4.2K by comparison with a coke specimen attached to the sample.

## 5.2 Ytterbium

### 5.2.1 Ytterbium spectra

Ytterbium ions diffused readily into AgCl and samples containing up to 0.5% of ytterbium were easily prepared. The grown crystals were clear with a very slight yellow colour. The E.P.R. signals were observed at 4.2K and the signal intensity was usually high. Typical

line widths were 0.8mT and the line shapes were Gaussian at 4.2K. The resonance signals decreased sharply in intensity by broadening as the temperature rose above 25K. With low doped samples (500ppm of Yb) care had to be taken to avoid saturation broadening of the lines which occurred at only moderate microwave power levels (about 1mW).

E.P.R. spectra were recorded as the sample was rotated in the {100} and {110} planes. The spectra obtained with the magnetic field parallel to the <100> and <110> axes are shown in figs. 5.1 and 5.2. Fig. 5.3 shows the angular dependence of the spectrum as the magnetic field is rotated in the {100} plane. Fig. 5.4 shows the spectrum at low field with B//<100> on an expanded field scale. The hyperfine structure of two lines due to the odd isotope $Yb^{171}$ (14.3% abundant) and of six lines due to $Yb^{173}$ (16.1% abundant) can be clearly identified. The resonance lines broaden as they move to fields above 0.3T near to B//<100>. Broadening probably occurs because the line position changes very quickly with $\theta$ over this range. A misalignment of $0.5^{\circ}$ in the microcrystal grains, or local strains causing distortions in the crystal fields of this order, will give line widths of about 0.5mT for most of the low field lines and of 2mT above 0.3T.

5.2.2  <u>Analysis of the principal spectrum</u>

The movement of the lines as the sample is rotated in the {100} and {110} planes shows that the principal lines arise from a centre of tetragonal symmetry. They are interpreted using the axial spin Hamiltonian

$$H = g_{/\!/} \beta B_z S_z + g_{\perp} \beta (B_x S_x + B_y S_y) \qquad (1)$$

where $S = \frac{1}{2}$.
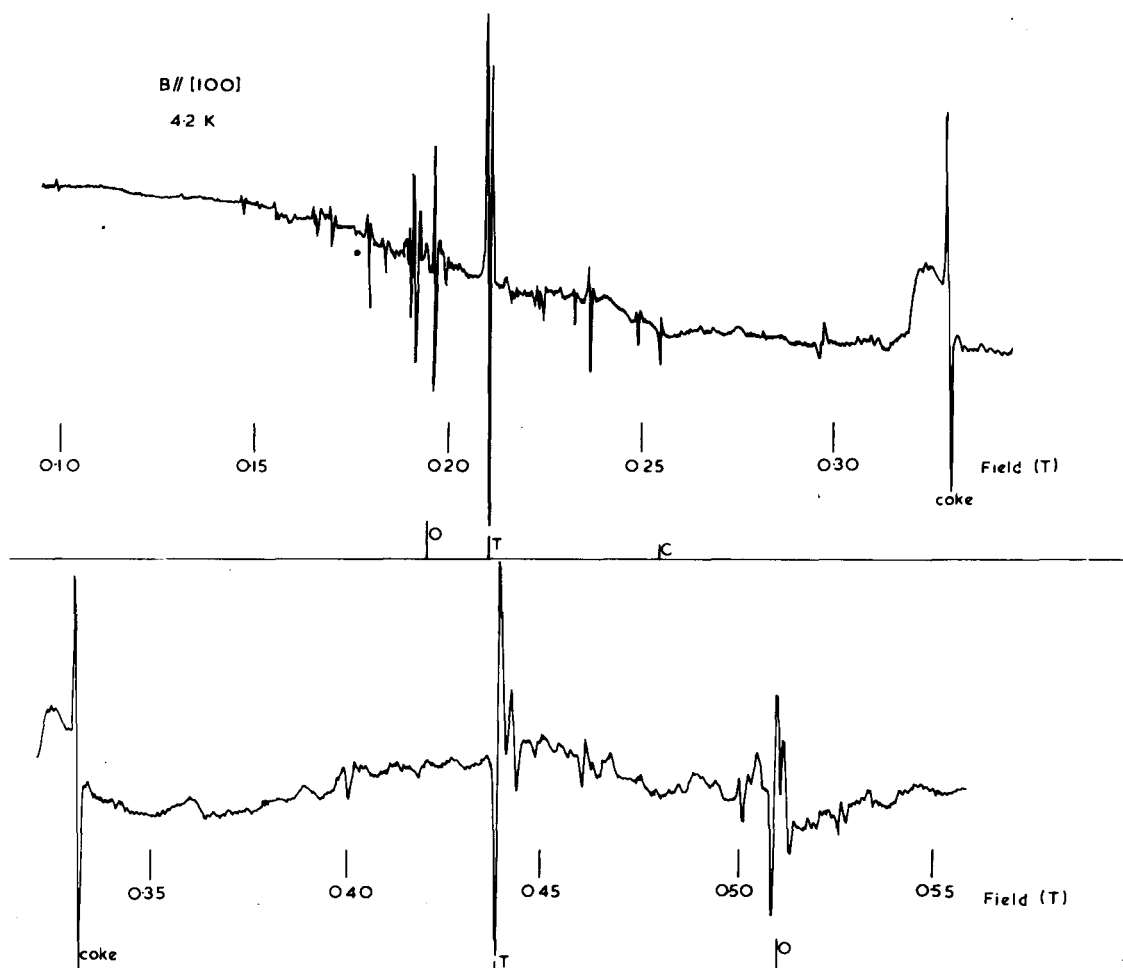
Fig. 5.1. The E.P.R. of Yb$^{3+}$ in AgCl at 4.2K with B $//<100>$.
The line positions calculated using the spin Hamiltonian
parameters given in the text are shown for the principal tetragonal
centre (T) and the orthorhombic centre (0) . The isotropic line
is labelled C .
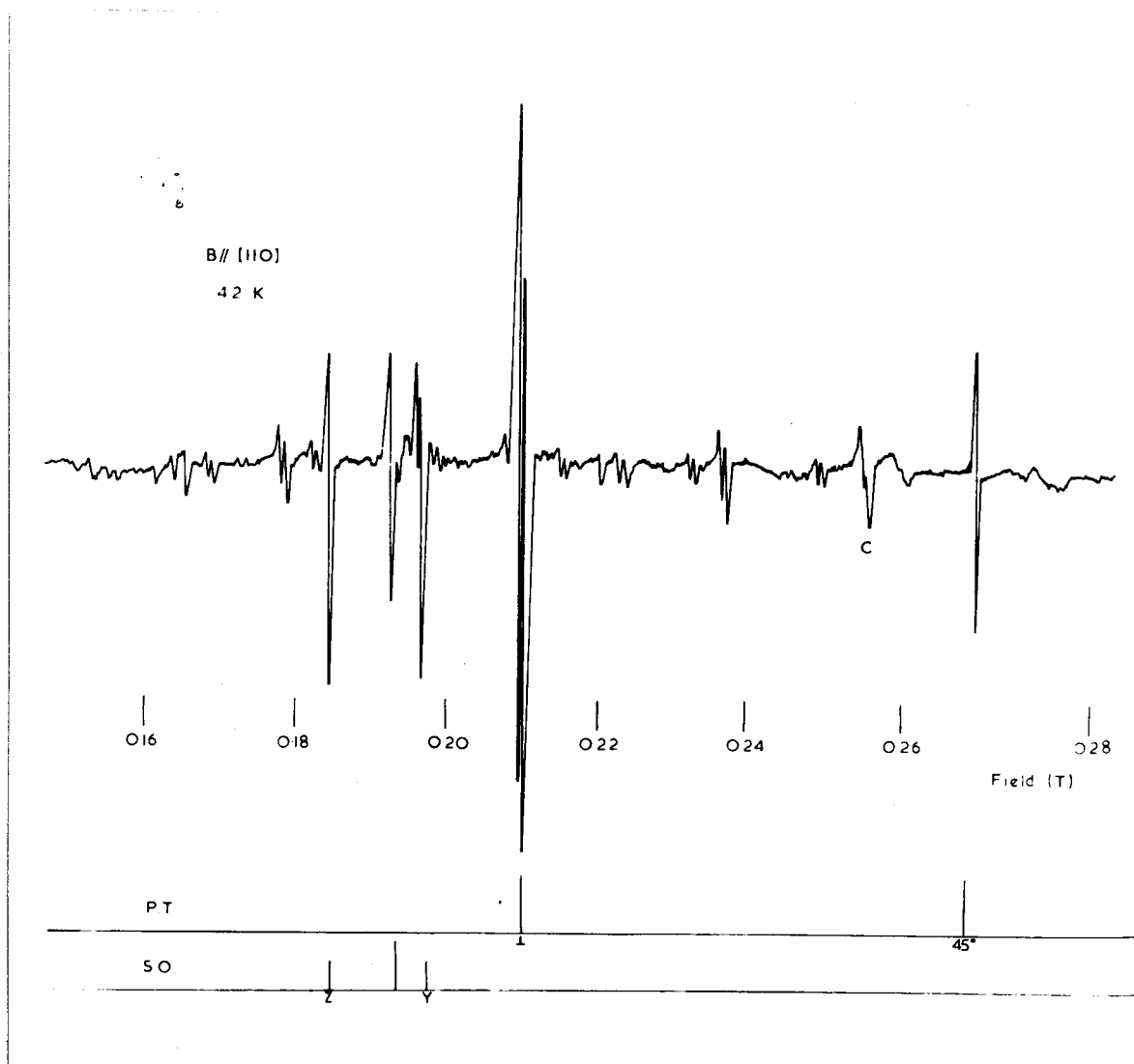
Fig. 5.2. The E.P.R. of $Yb^{3+}$ in AgCl at 4.2K with B $//\langle 110 \rangle$.

The line positions calculated using the spin Hamiltonian

parameters given in the text are shown for the principal tetragonal

centre (P.T.) and the subsidiary orthorhombic centre (S.O.) .
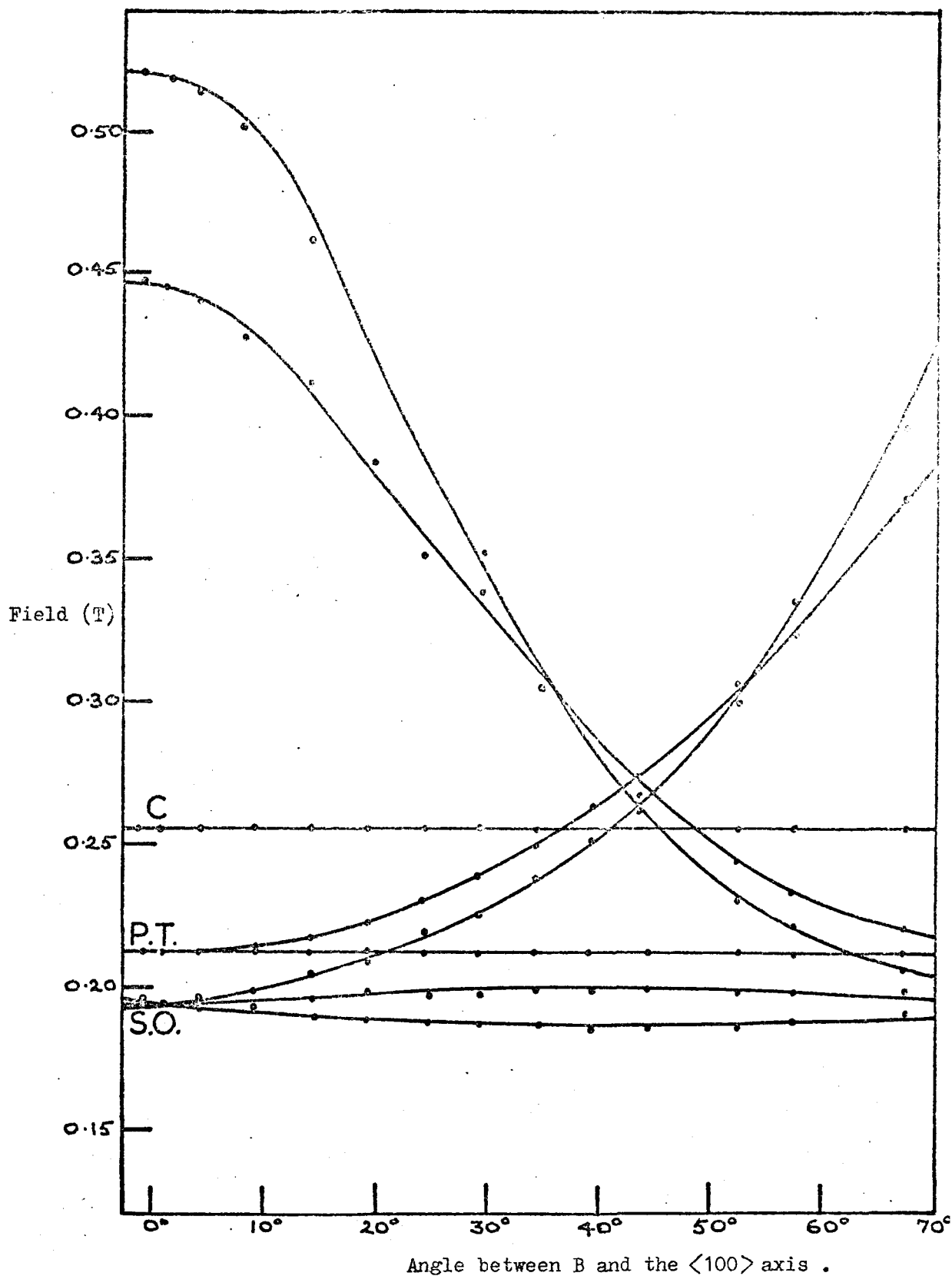
Fig. 5.3. The angular dependence in the {100} plane of the principal
tetragonal spectrum (P.T.), the subsidiary orthorhombic spectrum (S.O.)
and the isotropic line (C) of $AgCl:Yb^{3+}$. The full lines indicate the
theoretical values and the circles the experimental ones.
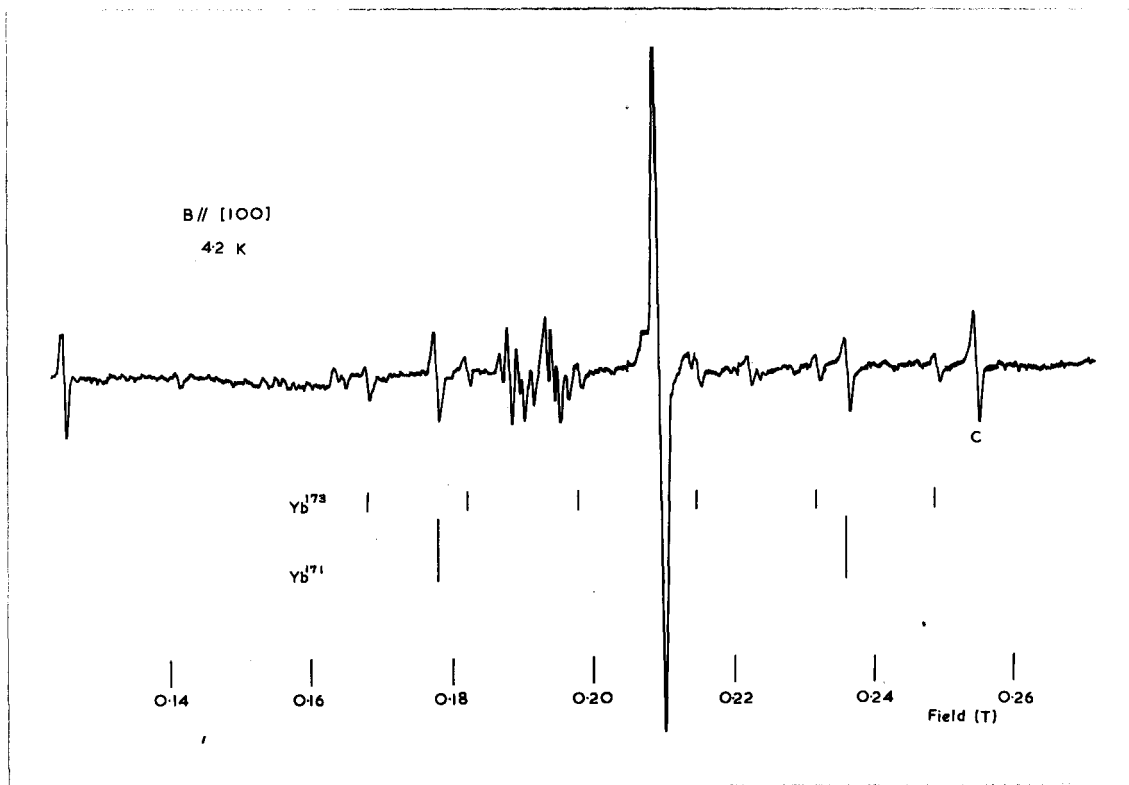
Fig. 5.4.. The E.P.R. of $Yb^{3+}$ in AgCl at 4.2K with B // $\langle 100 \rangle$.

The figure shows the low field region of the principal tetragonal spectrum and the hyperfine structure from the isotopes $Yb^{171}$ and $Yb^{173}$ can be seen .

Resonance occurs when

$$h\nu = g\beta B \quad \text{with} \quad g^2 = g_{//}^2\cos^2\theta + g_{\perp}^2\sin^2\theta$$

$\theta$ is the angle between the external field and the z axis of the centre which is a $\langle 100 \rangle$ crystal direction.

The g-values were calculated from the spectrum with $B//\langle 100 \rangle$ in which the line at 0.209T is from centres with the z axis at $90°$ to B, and the line at 0.441T is from centres with z parallel to the external magnetic field. The values obtained are $g_{//} = 1.501 \pm 0.007$ and $g_{\perp} = 3.162 \pm 0.005$. These values are used to calculate the resonant fields for $\theta = 45°$ and $55°$ (0.268T and 0.243T respectively) and the values agree well with those obtained experimentally. The tetragonal centre accounts for approximately 65% of the total intensity present.

5.2.3 <u>Analysis of the subsidiary spectra</u>

The angular dependence of the resonant lines of smaller intensity than those of the tetragonal centre shows that there is an orthorhombic centre present with intensity about 28% of the total. This centre is interpreted using the orthorhombic spin Hamiltonian

$$H = \beta(g_z B_z S_z + g_y B_y S_y + g_x B_x S_x) \tag{2}$$

where $S = \frac{1}{2}$.

Transitions are observed at

$$h\nu = g\beta B \quad \text{with} \quad g^2 = g_z^2 l^2 + g_y^2 m^2 + g_z^2 n^2$$

where l, m, n are the direction cosines of the external magnetic field, B,

with the Z, Y and X axes respectively. The axes used to interpret the spectrum are Z as $\langle 110 \rangle$, Y as $\langle 1\bar{1}0 \rangle$ and X as $\langle 001 \rangle$. With $B/\!/\langle 110 \rangle$ two lines are seen to reach minimum fields as the sample is rotated in the $\{110\}$ plane. These lines arise from centres with $B/\!/Z$ and $B/\!/Y$ and are used to calculate $g_z$ and $g_y$. With $B/\!/\langle 100 \rangle$ a broad line is seen to reach an extreme position at high field. This line arises from centres with $B/\!/X$ and is used to determine an approximate value for $g_x$. The calculated g-values are

$$g_z = 3.57 \pm .02$$
$$g_y = 3.34 \pm .02$$
$$g_x = 1.27 \pm .04$$

The field positions for the other lines observed at $B/\!/\langle 100 \rangle$ with $l^2 = \frac{1}{4}$, $m^2 = \frac{1}{4}$ and $n^2 = \frac{1}{2}$ and at $B/\!/\langle 110 \rangle$ with $l^2 = \frac{1}{2}$, $m^2 = \frac{1}{2}$, $n^2 = 0$, were calculated as a check on the interpretation and agree well with the experimental values.

There is also a line at $B = 0.254T$ which does not move as the sample is rotated in either a $\{110\}$ or a $\{100\}$ plane. This resonance, which accounts for about 4% of the total intensity, arises from a cubic centre with a g-value of $2.603 \pm .005$. There are also some lines of lower intensity from centres whose symmetry could not be determined. Approximately 3% of the total intensity is not accounted for by the centres described above.

## 5.2.4 Hyperfine structure

The hyperfine structure in the principal spectrum due to the odd isotopes of ytterbium is analysed using the Hamiltonian given in

equation (1) with the additional terms

$$A_{\parallel}S_z I_z + A_{\perp}(S_x I_x + S_y I_y) \tag{3}$$

where $I = \frac{1}{2}$ for $Yb^{171}$ (14.3% abundant)

and $I = \frac{5}{2}$ for $Yb^{173}$ (16.1% abundant).

The position of the transition $E_{M,m} \longrightarrow E_{M-1,m}$ is found using the expression given by Bleaney[4]

$$h\nu = g\beta B + Km + \frac{A_{\perp}^2}{4g\beta B_o}\left[\frac{A_{\parallel}^2 + K^2}{K^2}\right]\left[I(I+1) - m^2\right] \tag{4}$$

where $K^2 = \dfrac{A_{\parallel}^2 g_{\parallel}^2}{g^2}\cos^2\theta + \dfrac{A_{\perp}^2 g_{\perp}^2 \sin^2\theta}{g^2}$ ,

M is the Z component of S, and m is the Z component of I,

$$g^2 = g_{\parallel}^2\cos^2\theta + g_{\perp}^2\sin^2\theta \quad \text{and} \quad B_o = \frac{h\nu_o}{g\beta}$$

Those terms which are zero for $M = \frac{1}{2}$ and $\theta = 0^{\circ}$ or $90^{\circ}$ have been omitted. For the isotope with $I = \frac{1}{2}$ and for $\theta = 0^{\circ}$, transitions occur at

$$B_1 = B_o + \frac{A_{\parallel}}{2g_{\parallel}\beta} - \frac{A_{\perp}^2}{4(g_{\parallel}\beta)^2 B_o}$$

$$\tag{5}$$

$$B_2 = B_o - \frac{A_{\parallel}}{2g_{\parallel}\beta} - \frac{A_{\perp}^2}{4(g_{\parallel}\beta)^2 B_o}$$

For $\theta = 90^{\circ}$ transitions occur at

$$B_1 = B_o + \frac{A_{\perp}}{2g_{\perp}\beta} - \frac{A_{\parallel}^2 + A_{\perp}^2}{8(g_{\perp}\beta)^2 B_o}$$

$$\tag{6}$$

$$B_2 = B_o - \frac{A_{\perp}}{2g_{\perp}\beta} - \frac{A_{\parallel}^2 + A_{\perp}^2}{8(g_{\perp}\beta)^2 B_o}$$

In these expressions $A_{\parallel}$ and $A_{\perp}$ are in energy units.

The separation of the $Yb^{171}$ hyperfine lines at $\theta = 0^{\circ}$ and $90^{\circ}$ was used to calculate $A_{/\!/}$ and $A_{\perp}$. The shift of the central position of the two lines from the $I = 0$ line $(B_1 + B_2 - 2B_o)$ was calculated and compared with the experimental value. The hyperfine separation was about 0.06T for $\theta = 0^{\circ}$ and $90^{\circ}$ and the calculated values of $A_{/\!/}$ and $A_{\perp}$ were

$$|A_{/\!/}| = 1240 \pm 20 \text{ MH}_z = (413 \pm 8) \times 10^{-4} \text{cm}^{-1}$$

$$|A_{\perp}| = 2580 \pm 20 \text{ MH}_z = (860 \pm 7) \times 10^{-4} \text{cm}^{-1}$$

The experimental values of $(B_1 + B_2 - 2B_o)$ agree with the calculated values to within the experimental error.

The six hyperfine lines from $Yb^{173}$ are analysed using equations (1) and (3) with $I = \frac{5}{2}$. Expressions similar to equations (5) and (6) are found. The separation of the pairs of lines with $m = \pm \frac{5}{2}$, $m = \pm \frac{3}{2}$ and $m = \pm \frac{1}{2}$ is not affected by the second order terms and so these separations were used to find $A_{\perp}$. Unfortunately, the $Yb^{173}$ hyperfine lines for centres with $\theta = 0^{\circ}$ are not clearly distinguished in the spectra and so $A_{/\!/}$ was calculated from the second order terms at $\theta = 90^{\circ}$. The value of $A_{/\!/}$ is, consequently, less accurate than the value of $A_{\perp}$. The results give

$$|A_{\perp}| = 720 \pm 10 \text{ MH}_z = (240 \pm 3) \times 10^{-4} \text{cm}^{-1}$$

and $\quad |A_{/\!/}| = 400 \pm 50 \text{ MH}_z = (133 \pm 17) \times 10^{-4} \text{cm}^{-1}$

### 5.2.5 Ground states and g-values

The resonances in AgCl:Yb are attributed to the $Yb^{3+}$ ion. The only other valence attained by ytterbium is $Yb^{2+}$ which has a filled 4f shell and is not expected to be paramagnetic[5]. $Yb^{3+}$ $(4f^{13})$ is a Kramers ion with a $^2F_{7/2}$ ground state. The calculations of Lea, Leask and Wolf (L.L.W.)[6] show that a $\Gamma_6$ doublet level is expected to lie lowest in an octahedral field. The $\Gamma_6$ configuration occurs only once in the decomposition of the $J = \frac{7}{2}$ level and so the eigenvectors of the ground state in an octahedral field are not a function of the ratio of the fourth and sixth order terms in the crystal field expression (fig. 5.5). The ground state given by L.L.W. for octahedral symmetry is

$$0.6455 \left| \pm \frac{7}{2} \right\rangle + 0.7638 \left| \mp \frac{1}{2} \right\rangle$$

with a theoretical g-value of 2.667.

The experimental g-value for the isotropic line from $Yb^{3+}$ in AgCl is $2.603 \pm .005$. The decreased g-value may be accounted for by assuming a degree of covalent bonding between the $Yb^{3+}$ and the ligand $Cl^-$ ions. The covalency reduces the orbital magnetic moment contribution to the g-value as described by Low and Rubins[7]. For $Yb^{3+}$ in a general cubic field there can be no mixing of the $^2F_{5/2}$ level with the ground state since $J = \frac{5}{2}$ does not contain a state with $\Gamma_6$ symmetry[6]. (The $\Gamma_6$ ground state differs in this respect from the $\Gamma_7$ doublet discussed by Lowther and Killingbeck[8] since $^2F_{5/2}$ does contain a state with $\Gamma_7$ symmetry.) The wavefunction may, therefore, be taken as exactly that given above which has a theoretical g-value of $\frac{7}{3}g_J'$. The Landé g-factor, $g_J$, is reduced to $g_J'$ by an orbital reduction factor k. For a ground state of spin S and angular momentum L the expression for $g_J'$ is[7] :
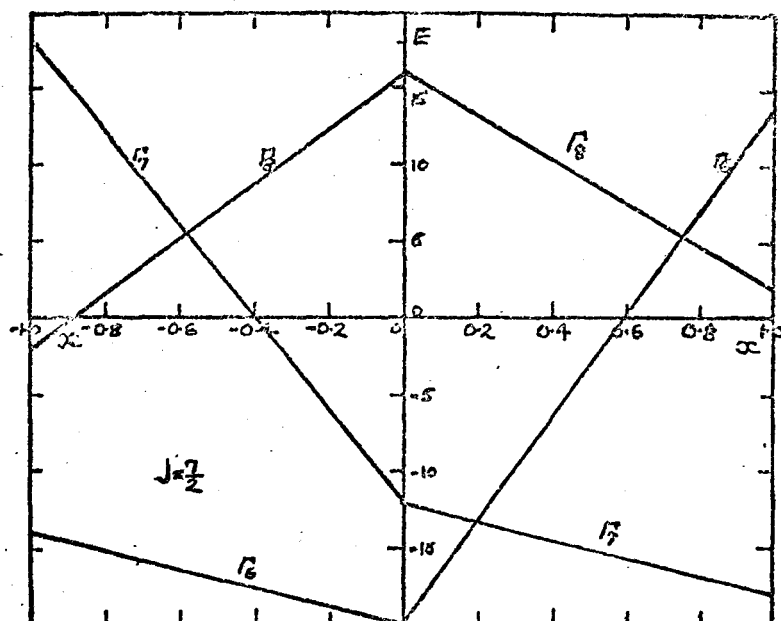
For Yb$^{3+}$ in an octahedral environment x is negative .
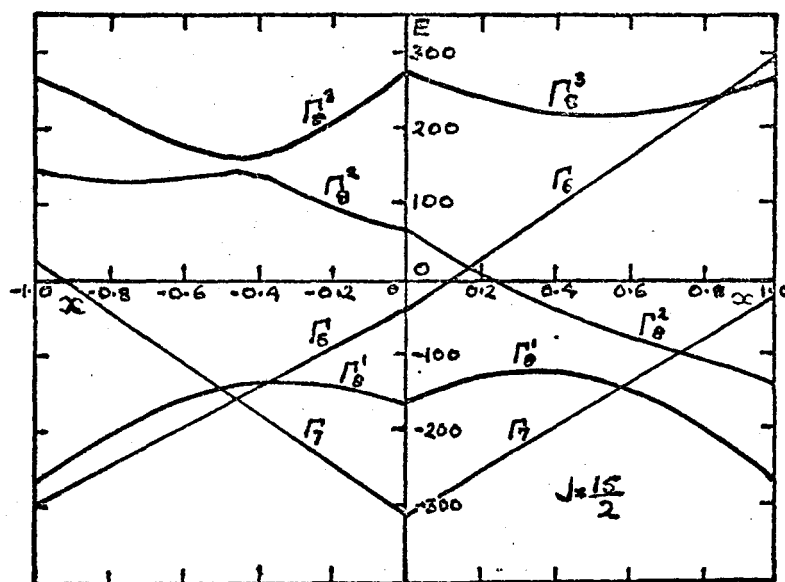


For Er$^{3+}$ in an octahedral environment x is positive .

For Dy$^{3+}$ in an octahedral environment x is negative .

Fig. 5.5. The energy levels for $J = 7/2$ and $J = 15/2$ from Lea, Leask and Wolf .

$$g'_J = g_J - (1 - k) \frac{J(J + 1) - S(S + 1) + L(L + 1)}{2J(J + 1)} \qquad (7)$$

$J = L + S$ in the second half of the rare earth series and for $Yb^{3+}$, $^2F_{7/2}$ equation (7) becomes

$$g'_J = \frac{8}{7} - \frac{6}{7}(1 - k) \quad \text{since } g_J = \frac{8}{7} \text{ for } Yb^{3+} \quad (6).$$

The value of $(1 - k)$ required to fit the observed g-value is $(1 - k) \simeq 0.032$ since

$$\triangle g = g \text{ (theoretical)} - g \text{ (experimental)} = 2(1 - k)$$

The value for $(1 - k)$ calculated by Low and Rubins[7] for $Yb^{3+}$ in an octahedral environment in CaO was 0.041. A value of $(1 - k) = 0.009$ was obtained for the isoelectronic ion $Tm^{2+}$ in $CaF_2$[7]. The relative values show that the covalent effect in AgCl is less than that in CaO but greater than that in $CaF_2$, as expected. The double excess charge present in $AgCl:Yb^{3+}$ will attract the ligands more strongly towards the $Yb^{3+}$ ion than in the other lattices and probably accounts for the covalent parameter being relatively close to the value for CaO. Lowther and Killingbeck[8] have estimated the covalency parameter k expected from overlap of the $Yb^{3+}(4f)$ and $S^{--}$ orbitals in CdS and they obtain $k > 0.997$ for pure $\sigma$ bonding. The space available for the $Yb^{3+}$ ion is greater in AgCl than in CdS and so the overlap is not expected to be much greater in spite of the double excess charge. However, it is usual for experimental k values to be smaller than those expected theoretically for both octahedral and tetrahedral sites. Some mixing of f-orbitals with the 5s and 5p outer orbitals may have to be invoked to explain the observed values.

Lewis and Sabisky[9] have shown that the average g-value $\bar{g} = \frac{1}{3}(g_{//} + 2g_{\perp})$ of a $\Gamma_6$ or a $\Gamma_7$ doublet in an axial field should be equal to the g-value ($g_c$) appropriate to the particular cubic field from which the axial field is derived. This relationship will hold provided that the axial distortion is small compared to the cubic field so that the total perturbation energy (or shift of the doublet levels from their cubic field positions) is much less than the separation of the doublet from the nearest quartet (since an axial distortion can only mix a $\Gamma_8$ state with a $\Gamma_6$ or a $\Gamma_7$ state). From fig. 5.5 it can be seen that this condition should hold well for $Yb^{3+}$, and $\bar{g}$ for the tetragonal centre is 2.608 ± .006 which is the same as the isotropic g-value within the experimental error.

Elliott and Stevens[10] have shown that there is a relation between the g-values and hyperfine constants of an axial centre provided that the ground state is accurately represented by a single value of J. If this is so then

$$\frac{A_{//}g_{\perp}}{A_{\perp}g_{//}} = 1 \qquad\qquad (8)$$

Optical measurements[11] show that the ground state of $Yb^{3+}$ in crystals is usually 10,000 cm$^{-1}$ below the $J = \frac{5}{2}$ excited state. There should be little mixing of J states even when an axial field is present. The value of $\frac{A_{//}g_{\perp}}{A_{\perp}g_{//}} = 1.01 ± .03$ for $Yb^{171}$ in tetragonal symmetry in AgCl and is unity within the experimental accuracy, confirming that the ground state is a pure $J = \frac{7}{2}$ state.

The wavefunctions of the $\Gamma_6$ ground state of the tetragonal centre should then be of the form given by L.L.W.:

$$\psi(\pm) = a \left| \pm \tfrac{7}{2} \right\rangle + b \left| \mp \tfrac{1}{2} \right\rangle$$

where a and b are constants to be determined and $a^2 + b^2 = 1$ from the normalisation condition. The g-values for a general axial field are given by[12]

$$g_{/\!/} = 2g_J' \left\langle \psi + \left| J_z \right| \psi + \right\rangle$$

$$(9)$$

and $\quad g_x = g_y = g_\perp = g_J' \left\langle \psi + \left| J_+ \right| \psi - \right\rangle$

where J is the total momentum operator and $J_+ = J_x + iJ_y$ is the raising operator. The reduced Landé g-factor $g_J'$ is used with $k = 0.032$. It follows that

$$g_{/\!/} = g_J'(7a^2 - b^2),$$

$$g_\perp = g_J' \, 4b^2 \qquad \text{and} \qquad g_J' = 1.115$$

The observed axial g-values may be fitted with $a = 0.545$, $b = 0.845$, and, as $a^2 + b^2 = 1.011$, the normalisation condition is satisfied.

The average g-value of the orthorhombic centre is $\bar{g} = \tfrac{1}{3}(g_x + g_y + g_z) = 2.73 \pm .03$. The ground state of this centre is clearly a $\Gamma_6$ state since the alternative $\Gamma_7$ state has a theoretical g-value of 3.429. However, the average g-value is rather higher than the other g-values obtained. This may be due to the low symmetry of the site mixing part of the excited J state into the ground state. The anisotropy of the g-value is slightly larger than that observed for the tetragonal centre, which indicates that the departure from octahedral symmetry is greater for this centre. Lowther and Killingbeck[8] have discussed in detail the effects of a small rhombic distortion and a large trigonal distortion on the $\Gamma_7$ ground state of $Yb^{3+}$ in a tetrahedral environment. For the small rhombic distortion they show that $\bar{g} = g_c$. The same derivation should apply to the $\Gamma_6$ ground state. For the case where the

trigonal distortion is large compared to the separation of the cubic energy levels, they derive expressions for $g_{//}$ and $g_{\perp}$ for both the $\Gamma_6$ and $\Gamma_7$ states. The average g-value is not equal to $g_c$ and for the $\Gamma_6$ state it will be

$$\bar{g} = \frac{7}{3}g_J(m^2 + \frac{3}{7}l^2 - \frac{3}{7}n^2 - \frac{8}{7}\sqrt{3}ln)$$

$$= \frac{7}{3}g_J(1 - \frac{4}{7}l^2 - \frac{10}{7}n^2 - \frac{8}{7}\sqrt{3}ln) \quad \text{since } m^2 = 1 - n^2 - l^2$$

(10)

The trigonal field mixes some of the $\Gamma_7$ and $\Gamma_8$ states into the $\Gamma_6$ state so that the new eigenstate is

$$|\gamma_1 +\rangle = l|\gamma_1(E'') +\rangle + m|\gamma_1(E') +\rangle + n|\gamma_1(U') +\rangle$$

where $m > l, n$ since in the notation of reference (8) :

$|\gamma_1(E'')+\rangle$ is the cubic field state derived from $E'' = \Gamma_7$ ,

$|\gamma_1(E')+\rangle$ is the cubic field state derived from $E' = \Gamma_6$ and

$|\gamma_1(U')+\rangle$ is one of the cubic field states from $U' = \Gamma_8^{(1)}$ .

The $\bar{g}$-value in a field with a large orthorhombic distortion should also not be equal to $g_c$ since the orthorhombic symmetry may be expressed as a sum of trigonal and tetragonal components. For $Yb^{3+}$ in octahedral symmetry, l is expected to be greater than n since $\Gamma_7$ is closer to the ground state than $\Gamma_8'$. However, equation (10) will give a value for $\bar{g}$ which is less than $g_c$ whatever the values of l, m and n. The observed increase in $\bar{g}$ over $g_c$ may arise as a result of the effects of the actual symmetry present. The majority of reported results give $\bar{g} \leqslant g_c$, although a spectrum was observed for $Dy^{3+}$ in natural Zircon[13] for which $\bar{g} - g_c = + 0.257$.

It is not obvious whether the axial distortion present in AgCl is expected to be 'large' in this context for a rare earth ion or not. However, the asymmetry of the g-values ($g_z - g_x$) observed here is 2.3. The value is comparable in magnitude, although smaller than the values for $Yb^{3+}$:ZnS ($g_\perp - g_{//} = 3.20$) and $Yb^{3+}$:CdS (3.25) for which Lowther and Killingbeck use the large trigonal field analysis. The values of $\bar{g} - g_c$ for AgCl:$Yb^{3+}$ (0.06) are correspondingly slightly smaller than those for ZnS and CdS (0.08). The axial distortions found in AgCl may, therefore, be taken as large relative to the separations of the energy levels in a general cubic field.

## 5.2.6 Lattice site and vacancy association

The majority of the $Yb^{3+}$ ions are most probably incorporated substitutionally. The anisotropic centres observed are derived from a $\Gamma_6$ state which is expected to lie lowest for $Yb^{3+}$ in all six co-ordinated sites. The centres of tetragonal and orthorhombic symmetry can be explained by choosing appropriate positions for the two charge compensating silver cation vacancies. The isotropic resonance observed is from a $\Gamma_6$ state and may arise from $Yb^{3+}$ ions in substitutional sites which are not associated with silver cation vacancies, or from precipitates of $YbCl_3$. For $Yb^{3+}$ in an interstitial site the crystal field parameter x, defined in section 2.7, is positive. A $\Gamma_6$ state lies lowest if $|x| < 0.2$ (fig. 5.5). $|x| = 0.2$ would imply a ratio of the fourth to sixth degree cubic field terms of 5.25 for $Yb^{3+}$ since $\dfrac{B_4}{B_6} = \dfrac{x}{1 - |x|} \cdot \dfrac{F(6)}{F(4)}$ and $\dfrac{F(6)}{F(4)} = 21$. This is an extremely unusual value since the ratio of $\dfrac{B_4}{B_6}$ is usually of order $10^2$ and, therefore, interstitial incorporation is considered a very unlikely explanation even for the isotropic resonance.

The tetragonal centre is most probably due to a substitutional $Yb^{3+}$ ion associated with two next-nearest cation vacancies in the same $\langle 100 \rangle$ line from the impurity ion. The vacancies are likely to lie on opposite sides of the trivalent ion because of their mutual repulsion. There are a number of possible explanations for a centre of orthorhombic symmetry with axes in $\langle 110 \rangle$, $\langle 1\bar{1}0 \rangle$, and $\langle 001 \rangle$ directions as shown in fig. 4.13 of Chapter Four. In this case the g-values in the $\langle 110 \rangle$ directions are similar in magnitude, while the g-value in the $\langle 100 \rangle$ direction is considerably smaller. The arrangement of vacancies should then give a fairly symmetrical pattern in the $\{100\}$ plane in which the Z and Y axes lie. Of the three orthorhombic centres listed in fig. 4.13, the most likely is that with two nearest cation vacancies at $90^{\circ}$.

## 5.3    Erbium

### 5.3.1   Erbium spectra

The erbium-doped crystals were clear and colourless. E.P.R. was observed at 4.2K and the intensity of the spectrum was high with many narrow lines of width about 0.8mT. The resonant intensity became very small as the temperature of the sample rose above 20K. With the magnetic field at a general orientation to the crystal axes the spectrum consisted of very many overlapping lines in the magnetic field range 0.02 - 0.22T. Some simplification occurred with the magnetic field parallel to a $\langle 100 \rangle$ or a $\langle 110 \rangle$ crystal axis (fig. 5.6 and 5.7). The pattern of the line positions at $B/\!/\langle 100 \rangle$ was quite different to that at $B/\!/\langle 110 \rangle$. A careful orientation in the $\{100\}$ plane was made which enabled the movement of the more intense lines to be followed as the sample was rotated (fig. 5.8).
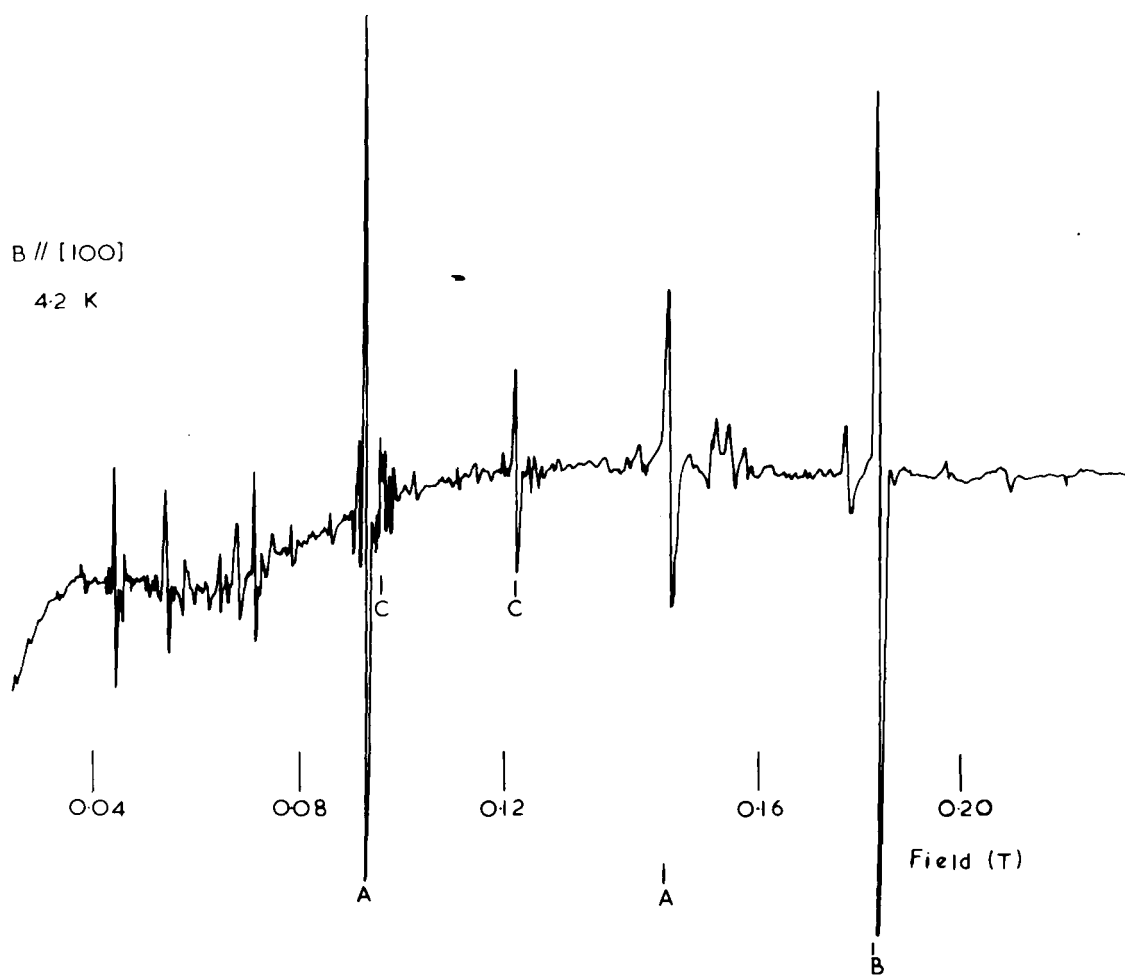
Fig. 5.6. The E.P.R. of $Er^{3+}$ in AgCl at 4.2K with B // $\langle 100 \rangle$ .
The lines from the principal orthorhombic centre, the trigonal
centre and the possible subsidiary centre are labelled A,B and
C respectively .
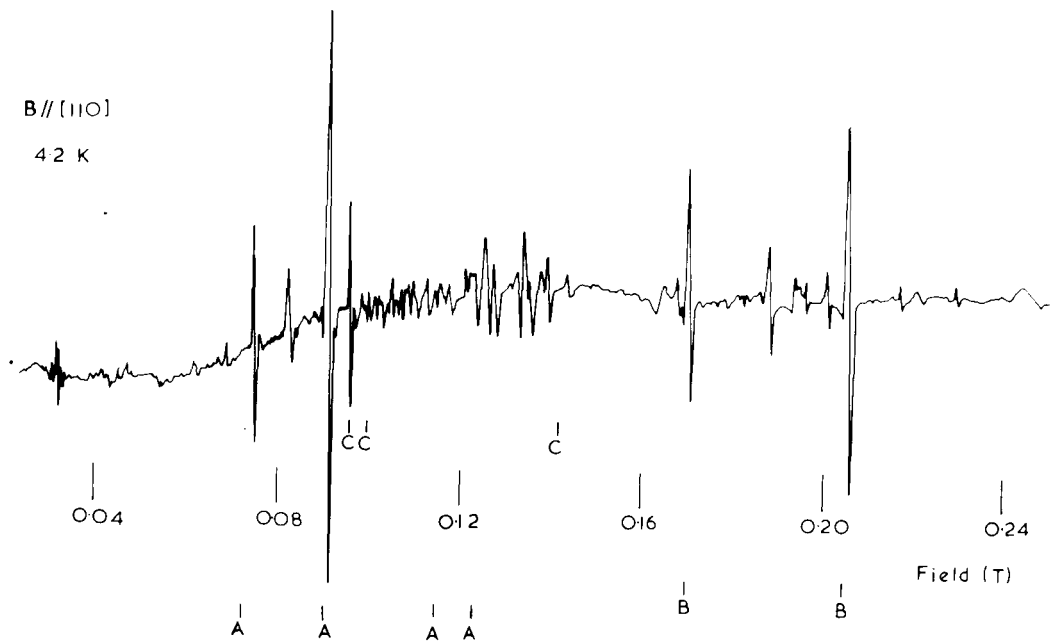
Fig. 5.7. The E.P.R. of $Er^{3+}$ in AgCl at 4.2K with B $// \langle 110 \rangle$.
The lines from the principal orthorhombic centre, the trigonal
centre and the possible subsidiary centre are labelled A,B and
C respectively .
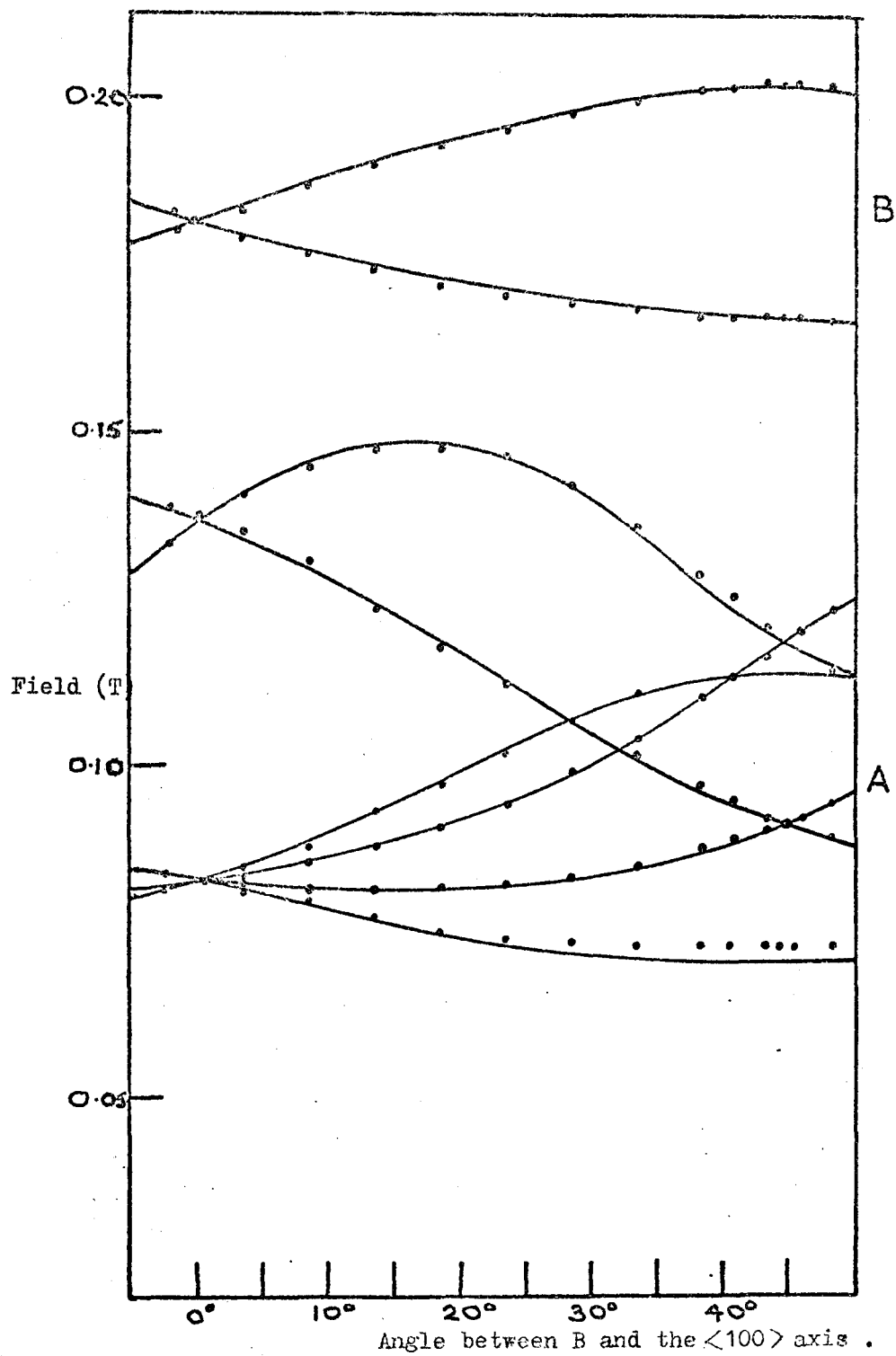
Fig. 5.8. The angular dependence in the {100} plane of the principal

orthorhombic spectrum (A) and the trigonal spectrum (B) in $AgCl:Er^{3+}$.

The angular variation shows that there are several independent centres present, and also that one of the main sets of lines (A) do not reach extreme fields at B//$\langle 100 \rangle$ or B//$\langle 110 \rangle$. Crystals were oriented to rotate on a $\{110\}$ plane and some lines could be seen to extreme at the B//$\langle 111 \rangle$ and B//$\langle 112 \rangle$ positions although the orientations obtained were not good enough for the movement of the lines to be followed as the crystal was rotated.

5.3.2  Analysis of the principal spectra

One prominent set of lines (A) was analysed using the orthorhombic Hamiltonian

$$H = \beta (g_z B_z S_z + g_y B_y S_y + g_x B_x S_x)$$

with the Z axis in a $\langle 111 \rangle$ direction, the X axis along $\langle \bar{1}\bar{1}2 \rangle$ and the Y axis along $\langle 1\bar{1}0 \rangle$. At a general orientation of the magnetic field in the $\{100\}$ plane there are six non-equivalent orientations of this centre. With the magnetic field parallel to a $\langle 100 \rangle$ axis four of the centres have the same orientation with $l^2 = \frac{1}{3}$  $m^2 = \frac{1}{2}$  $n^2 = \frac{1}{6}$ and the other two centres have  $l^2 = \frac{1}{3}$  $m^2 = 0$  $n^2 = \frac{2}{3}$ , where the resonant positions and effective g-values are given in section 5.2.3. With B//$\langle 110 \rangle$ the six non-equivalent centres reduce to four. Two centres have

$$l^2 = \frac{2}{3} \qquad m^2 = \frac{1}{4} \qquad n^2 = \frac{1}{12} \, ,$$

two have $\qquad\qquad l^2 = 0 \qquad m^2 = \frac{1}{4} \qquad n^2 = \frac{3}{4} \, ,$

and there is one with $\quad l^2 = \frac{2}{3} \qquad m^2 = 0 \qquad n^2 = \frac{1}{3} \, ,$

and one with $\qquad\qquad l^2 = 0 \qquad m^2 = 1 \qquad n^2 = 0 \, .$

The g-values of the resonant lines are used to construct simultaneous equations for $g_z$, $g_y$ and $g_x$. Since there are six equations and three unknowns the g-values are overdetermined, which provides a check on the interpretation used. The g-values which were found to give the best fit were

$$g_z = 6.73 \pm 0.1$$
$$g_y = 9.36 \pm 0.1$$
$$g_x = 3.60 \pm 0.4$$

The values are less accurate than is usual because of the indirect method of determination. The X, Y and Z axes were assigned to the site axes in the way described above because of the interpretation of the centre to be made in 5.3.5. The calculated line positions at $B/\!/\langle 100\rangle$ and $B/\!/\langle 110\rangle$ are shown in fig. 5.6 and 5.7, and the angular variation calculated for the lines is shown in fig. 5.8. This set of lines accounts for about 53% of the total spectrum.

Another set of high intensity lines (B) in the erbium spectrum apparently arise from a centre with axial symmetry along the $\langle 111\rangle$ axis. These are analysed using the Hamiltonian

$$H = g_{/\!/}\beta B_z S_z + g_\perp\beta(B_x S_x + B_y S_y)$$

and resonances are observed at $B = \dfrac{h\nu}{g\beta}$ with $g^2 = g_{/\!/}^2\cos^2\theta + g_\perp^2\sin^2\theta$ as before. At $B/\!/\langle 100\rangle$ $\theta = 55^\circ$ for all the $\langle 111\rangle$ axes and a single resonance line is observed. At $B/\!/\langle 110\rangle$ two equally intense sets of lines are expected with $\theta = 35^\circ$ and $\theta = 90^\circ$. The line position at $B/\!/\langle 100\rangle$ is midway between these two. The g-values cannot be unambiguously defined by these three field values alone since the $\theta$ values of the two lines at $B/\!/\langle 110\rangle$ can be interchanged. However, inspection of the resonances in

the {110} plane showed that the lines from this centre did not move to higher fields than the high field line observed at B//<100>. This line is, therefore, assigned to $\theta = 90°$ and the calculation of $g_{//}$ and $g_\perp$ is made to give

$$g_{//} = 4.25 \pm .05 \qquad g_\perp = 3.23 \pm .01$$

The calculated resonant fields are shown in figs. 5.6, 5.7 and 5.8. Again, the g-values are not highly accurate because of the method of determination. The lines are slightly less intense in samples less heavily doped than the one used to obtain the resonances in figs. 5.6 and 5.7. In this sample they account for about 24% of the $Er^{3+}$ ions present, whereas in the least heavily doped samples ( 0.05% Er) the intensity of the <111> centre lines was about 17% of the whole spectrum.

### 5.3.3 Analysis of the subsidiary spectra

There are numerous other lines present with a total intensity less than 20% of the A and B centres. Some of these lines (C) may be fitted to an orthorhombic Hamiltonian with axes in the <110>, <1$\bar{1}$0> and <001> directions. The assignment of these lines is tentative since the angular dependence of the low intensity lines could not be followed with certainty where they intersected the principal lines. Fitting the line positions to the Hamiltonian at B//<100> and B//<110> as for the $Yb^{3+}$ orthorhombic centre gives

$$g_z \ (<110>) = 4.71 \pm 0.1$$
$$g_y \ (<1\bar{1}0>) = 6.97 \pm .05$$
$$g_x \ (<001>) = 7.7 \pm 0.1$$

## 5.3.4 Hyperfine structure

A hyperfine structure of eight lines due to the $Er^{167}$ isotope ($I = \frac{7}{2}$, 22.8% abundant) is expected with an intensity in each line of about 3% of the principal lines. Hyperfine structure is seen around the main lines of centres A and B but it is difficult to analyse because orientations with the magnetic field parallel to all the principal axes were not clearly obtained for these centres. Also, the number of overlapping lines made it difficult to distinguish all eight lines of the hyperfine set. The relationship $\dfrac{A_{//}g_{\perp}}{A_{\perp}g_{//}} = 1$ between the hyperfine constants and the g-values implies that the hyperfine structure should have the same field splittings whatever the orientation of the axial centre to the magnetic field[9]. The relationship was shown to hold well for $Yb^{3+}$ in AgCl. Optical data show that the first excited state ($J = \frac{13}{2}$) of the $Er^{3+}$ ion in crystals is usually about 6,000 $cm^{-1}$ above the ground state[11]. The separation of the two lowest J states can be expected to be less for $Er^{3+}$ than for $Yb^{3+}$ in AgCl, but nevertheless the deviation of $\dfrac{A_{//}g_{\perp}}{A_{\perp}g_{//}}$ from unity should be small.

The hyperfine lines which can be fairly clearly seen on the high field side of the $\langle 111 \rangle$ axial centre lines have the same separations as the sample is rotated. The hyperfine structure for $B//\langle 110 \rangle$ and perpendicular to the Z axis of this centre was used to derive an approximate value for $A_{\perp}$, taking second order shifts into account. $A_{//}$ was then calculated assuming $\dfrac{A_{//}g_{\perp}}{A_{\perp}g_{//}} = 1$. The values obtained are

$$|A_{//}| = 650 \pm 50 \text{ MH}_z = (216 \pm 15) \times 10^{-4} \text{ cm}^{-1}$$

$$|A_{\perp}| = 500 \pm 30 \text{ MH}_z = (167 \pm 10) \times 10^{-4} \text{ cm}^{-1}$$

The hyperfine splittings of the main orthorhombic centre are considerably smaller in terms of field units ($\sim 8mT$). However, assuming again that the structure is isotropic, similar values to those obtained above are found for $A_x$, $A_y$ and $A_z$. The value of $\frac{1}{3} (A_{//} + 2A_{\perp})$ for the axial centre is similar to the values of A for $Er^{3+}$ in a general cubic environment tabulated on page 331 of reference (12).

## 5.3.5  Ground state and g-values

The resonances observed are attributed to the $Er^{3+}$ ion as erbium is not expected to attain any other valence. The free $Er^{3+}$ ($4f^{11}$) ion has a $^4I_{15/2}$ ground state and in a cubic field this is expected to split into a $\Gamma_6$, a $\Gamma_7$ and three $\Gamma_8$ levels. The calculations of L.L.W. show that, for $Er^{3+}$ in an octahedral environment, x is expected to be positive and a $\Gamma_7$ or a $\Gamma_8$ level may lie lowest according to the value of x (fig. 5.5). The $\Gamma_7$ ground state in an octahedral field is given by L.L.W. as

$$0.6332 \left| \pm \frac{15}{2} \right\rangle + 0.5819 \left| \pm \frac{5}{2} \right\rangle - 0.4507 \left| \mp \frac{3}{2} \right\rangle - 0.2393 \left| \mp \frac{11}{2} \right\rangle$$

and has a theoretical g-value of 6.772. If the parameter x of the field is larger than 0.58, a $\Gamma_8$ quartet is expected to be lowest. Since the $\Gamma_8$ level occurs more than once in the decomposition of $J = \frac{15}{2}$ in a general cubic field, the g-values are functions of x and of the crystal orientation. If an axial distortion is also acting on the $\Gamma_8$ level, it is split into two doublets and a resonance may be observed from either or both of these.

The g-values expected for the case of a tetragonal distortion greater than the Zeeman energy are given by Abragam and Bleaney[12]. For the $\left|\pm\frac{3}{2}\right\rangle$ doublet

$$g_{/\!/} = -2P \qquad\qquad |g_\perp| = \tfrac{1}{2}|(P - 3Q)|$$

and for the $\left|\pm\frac{1}{2}\right\rangle$ doublet

$$g_{/\!/} = 2Q \qquad\qquad |g_\perp| = \tfrac{1}{2}|(3P - Q)|$$

P and Q are defined in terms of the tetragonal crystal field potential $V_z$ by

$$\left\langle \tfrac{3}{2}\right| V_z \left|\tfrac{3}{2}\right\rangle = P$$

$$\left\langle \tfrac{1}{2}\right| V_z \left|\tfrac{1}{2}\right\rangle = Q$$

$Er^{3+}$ has been studied in octahedral sites in CaO, SrO and MgO. In CaO and SrO tetragonal resonances are also seen[14]. The octahedral resonances are fitted to the $\Gamma_8$ states given by L.L.W. and the corresponding values of x are found to be 0.732 for CaO and 0.744 for SrO. The average g-values of the tetragonal resonances are 6.65 (CaO) and 6.63 (SrO). The $\bar{g}$-values are in close agreement with the $\Gamma_7$ value if $g'_J$ is reduced by the same factor as it is for $Er^{3+}$ in MgO[15]

$$(1 - k) = 0.025 \qquad \text{and} \qquad \bar{g} = 6.65$$

In MgO the $\Gamma_8$ resonances are explained with x = 0.72[15]. An axial spectrum is also seen and is attributed to the $\left|\pm\frac{3}{2}\right\rangle$ doublet derived from the $\Gamma_8$ state. Resonance from the $\left|\pm\frac{1}{2}\right\rangle$ doublet is not not detected. If the values of P and Q given by Descamps and D'Aubigne[15] for $MgO:Er^{3+}$ are used to predict the g-values of the $\left|\pm\frac{1}{2}\right\rangle$ transition in tetragonal symmetry then

$$g_{/\!/} = 4.62 \qquad \text{and} \qquad g_\perp = 7.70.$$

$\bar{g} = 6.67$ which is again in agreement with the value for the $\Gamma_7$ state.

It appears, therefore, that if an axial distortion small with respect to the cubic term but large with respect to the Zeeman energy is present, then it is not possible to distinguish between a $\Gamma_7$ ground state with $x < 0.58$ or a doublet derived from a $\Gamma_8$ state. The observed symmetry of the main orthorhombic centre seen in $Er^{3+}$:AgCl can be explained most simply if the $Er^{3+}$ ion is substitutional. The average g-value of this centre is $\bar{g} = \frac{1}{3}(g_x + g_y + g_z) = 6.56 \pm 0.2$. The resonant doublet is almost certainly a $\Gamma_7$ state since the alternative $\Gamma_6$ state has a theoretical g-value of 6.0. The value of $\bar{g}$ is lower than the g-value (6.62) calculated for the $\Gamma_7$ wave function with an orbital reduction factor $k = 0.97$ as for AgCl:$Yb^{3+}$. The effect of tetragonal and lower symmetry fields on $Er^{3+}$ has not been investigated theoretically. However, the same general conclusions discussed for $Yb^{3+}$ should still apply. The value (0.06) of $g_c - \bar{g}$ is probably due to the low symmetry field mixing in a proportion of the $\Gamma_8$ wavefunctions since the $\Gamma_8$ and $\Gamma_7$ levels are not widely separated in $Er^{3+}$ (fig. 5.5).

It is quite reasonable to propose that the ratio of fourth to sixth order terms in the crystal field of AgCl is smaller than that in CaO, as will be discussed in 5.5.1. Resonances from ions of the iron transition series in AgCl do not usually show axial distortions large compared with the Zeeman energy, unlike the distortions for these ions in oxide lattices[16,17]. Thus, it seems most likely that the main orthorhombic resonance is associated with the $\Gamma_7$ ground state of substitutional $Er^{3+}$ with a small axial distortion on a cubic field with $x < 0.58$.

The value of $\bar{g}$ for the axial centre with a $<111>$ distortion is 3.57, which does not fit with any of the expected ground states of $Er^{3+}$.

The intensity of the resonance is also too large for it to be from an excited state. The $<111>$ symmetry can be explained most simply if the $Er^{3+}$ is in an interstitial site. For this site the co-ordination is tetrahedral and a $\Gamma_7$ or $\Gamma_6$ state is expected to be lowest. However, if the x-value for this site is close to -0.45 where the $\Gamma_6$ and $\Gamma_7$ levels cross and where the $\Gamma_8$ level may be only a few $cm^{-1}$ higher in energy, then the axial field may produce a very mixed ground-state with unknown g-values. A trigonal resonance from $Er^{3+}$ in a tetrahedral environment in $CaF_2$ for which $\bar{g} \neq g_c$ was observed by Weber and Bierig[18] but no explanation was proposed. They reported values of $g_{//} = 6.31 \pm .05$, $g_{\perp} = 2.14 \pm 0.04$ and $\bar{g} = 3.53$. The temperature dependence of the resonance indicated that there was an excited state at $\sim 50$ $cm^{-1}$ above the resonant level. The average g-value is close to that observed here for the trigonal spectrum in AgCl. The deviation of $\bar{g}$ from $g_c$ has been analysed rigorously for the case of $Er^{3+}$ in axial $<111>$ symmetry by Thoria[19]. The deviation, of only 2.5%, was fitted to $-0.355 \leqslant x \leqslant -0.335$. The deviation observed in AgCl could only be explained if x were very much closer to -0.45.

The average g-value of the possible orthorhombic centre with $<110>$, $<1\bar{1}0>$ and $<001>$ axes is $6.46 \pm 0.2$ which indicates that the centre also has a $\Gamma_7$ ground state.

The g-values for axial symmetry are not sufficient to determine the eigenstate of the $Er^{3+}$ ground level since the $\Gamma_7$ and $\Gamma_6$ states are made up of four $|J_z>$ states and there are four unknown constants. An axial centre gives three g-values and with the normalisation condition this gives four equations for four unknowns. However, the calculation of the eigenstates would be lengthy and not very informative.

## 5.3.6 Lattice site and vacancy association

The ground-state of the $Er^{3+}$ ion does not determine the nature of the lattice site directly since the $\Gamma_7$ ground state can occur for both positive and negative x. However, the symmetry of both the orthorhombic centres can be explained for a substitutional site. The centre with $\langle 111 \rangle$, $\langle 1\bar{1}0 \rangle$ and $\langle \bar{1}\bar{1}2 \rangle$ axes could arise if the $Er^{3+}$ were associated with two nearest cation vacancies in the {111} plane, and if the lines joining the vacancies to the trivalent ion made an angle of $120^{\circ}$. The Z axis is, therefore, chosen as the $\langle 111 \rangle$ direction and the Y axis as the $\langle 110 \rangle$ direction to one of the vacancies. The X axis is then the direction at right-angles to Y and Z in the plane of the two vacancies. The centre bears some resemblance to that seen for $Cr^{3+}$ in AgCl, except that the two vacancies are in the {100} plane in $AgCl:Cr^{3+}$ instead of the {111} plane.

The orthorhombic centre with $\langle 110 \rangle$, $\langle 1\bar{1}0 \rangle$ and $\langle 001 \rangle$ axes can be explained by one of the orthorhombic centres listed for substitutional chromium in fig. 4.13. The g-values for the two $\langle 110 \rangle$ axes of this centre are not similar, unlike the orthorhombic centre found in $AgCl:Yb^{3+}$. In $AgCl:Er^{3+}$ $g_x$ and $g_y$, where X and Y are $\langle 001 \rangle$ and $\langle 1\bar{1}0 \rangle$ directions, are close in value which suggests that the centre is either that with one nearest cation vacancy and one next nearest cation vacancy making $90^{\circ}$ at the $Er^{3+}$ ion, or that with two nearest cation vacancies along the same $\langle 110 \rangle$ axis through the $Er^{3+}$ ion. In the latter case the $g_z$ value would correspond to an orientation with the magnetic field parallel to the line joining the two vacancies.

A simple explanation for the $\langle 111 \rangle$ axial centre cannot be found for a substitutional impurity ion. The only centre which might give this symmetry if $Er^{3+}$ were in a silver ion position would be an arrangement of three nearest cation vacancies in a $\{111\}$ plane such that the lines joining the $Er^{3+}$ to the vacancies made angles of $120°$. This is a somewhat artificial centre since only two silver ion vacancies are needed to completely compensate for the excess charge present. Also, this model does not help to explain the unusual g-values observed unless the ratio of $\frac{B_4}{B_6}$ of this site is such that the $\Gamma_7$ and $\Gamma_8$ energy levels are close to their intersection.

A more probable explanation is that the $Er^{3+}$ ion is interstitial in this case. Three silver ion vacancies are then required for charge compensation since the $Er^{3+}$ is not replacing a $Ag^+$ ion. The site symmetry will be trigonal if the three vacancies are at three of the four corners of the tetrahedron of $Ag^+$ ions surrounding the interstitial erbium.

A centre of this kind has been observed for $Fe^{3+}$ in AgCl when $Fe^{3+}$ is formed at low temperatures by irradiation of the $Fe^{2+}$ ion[20]. A further possibility is that precipitates of $ErCl_3$ form in the crystal and give rise to a trigonal site for the erbium ion.

## 5.4 Dysprosium

### 5.4.1 Dysprosium spectra

Dysprosium did not diffuse easily into silver chloride. The polycrystalline samples were cloudy white and brittle when heavily doped and the grown crystals were usually clear and colourless. The resonances in

fig. 5.9 were observed at 4.2K. The spectrum was always of low intensity even in heavily doped samples. The line widths were quite narrow (1mT) with the magnetic field parallel to $\langle 100 \rangle$ or $\langle 110 \rangle$ directions, but increased slightly in width as the crystal was rotated. The microwave level and 100 KHz amplifier gain had to be increased to observe the spectra. The increased microwave level did not cause saturation broadening of the lines, but the increased gain settings resulted in a considerable level of background signal, presumably arising from the modulation coils, which increased as the magnetic field increased. This made the resonance lines difficult to observe and a background level proportional to the external magnetic field has been subtracted from the spectra to give the traces in fig. 5.9. The dysprosium spectrum disappeared rapidly as the sample temperature rose above 18K.

## 5.4.2 Analysis of the spectrum

The dysprosium resonance consisted of only a few lines unlike the spectra of ytterbium and erbium. As a result, although the quality of the E.P.R. traces was poor, the angular variation of the line positions could be quite easily followed. Fig. 5.10 shows the characteristic angular dependence of an orthorhombic centre with axes in the $\langle 110 \rangle$, $\langle 1\bar{1}0 \rangle$ and $\langle 001 \rangle$ directions. The spectrum was analysed using the orthorhombic Hamiltonian already described for similar centres in $AgCl:Yb^{3+}$ and $AgCl:Er^{3+}$. With the magnetic field parallel to a $\langle 110 \rangle$ axis two lines reach minima and arise from centres with B//Y and B//Z. $g_z$ and $g_y$ are calculated from these line positions. At B//$\langle 100 \rangle$ the line seen clearly at low field arises from centres with the magnetic field at $45^{\circ}$ to Z and Y and $90^{\circ}$ to X. There should also be a line from a centre with B//X.

B 2° off
⟨100⟩

0.05    0.06    0.09 (T)
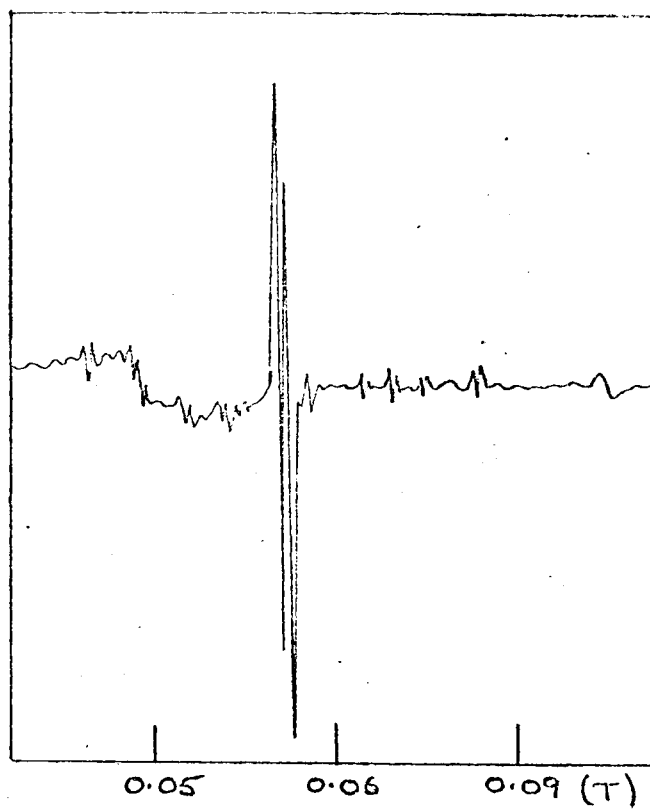
B // ⟨110⟩
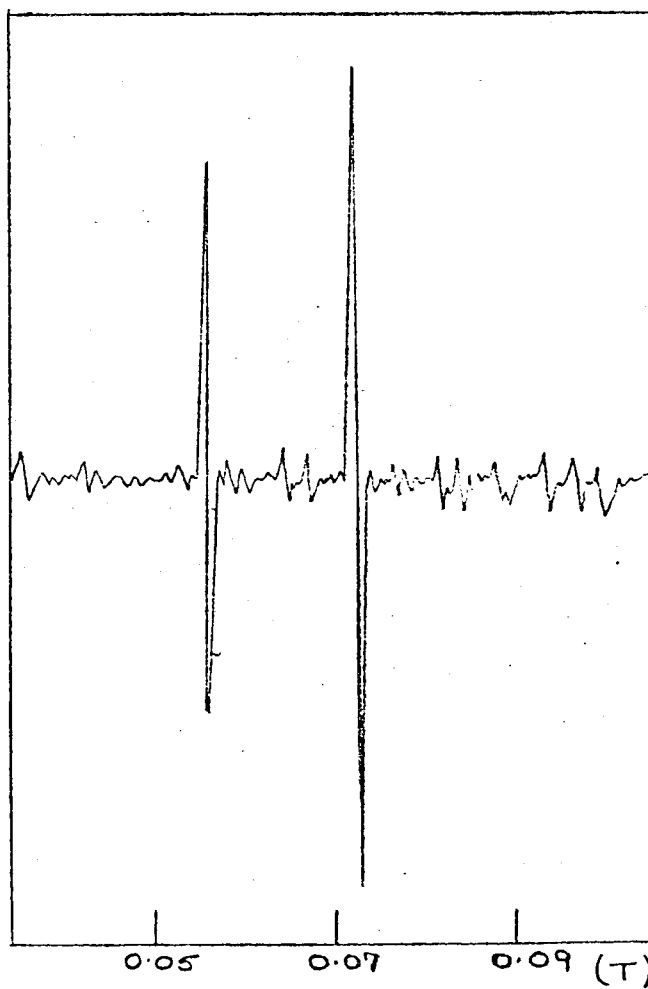
Fig. 5.9. The E.P.R.
of Dy³⁺ in AgCl
at 4.2K .

0.05    0.07    0.09 (T)
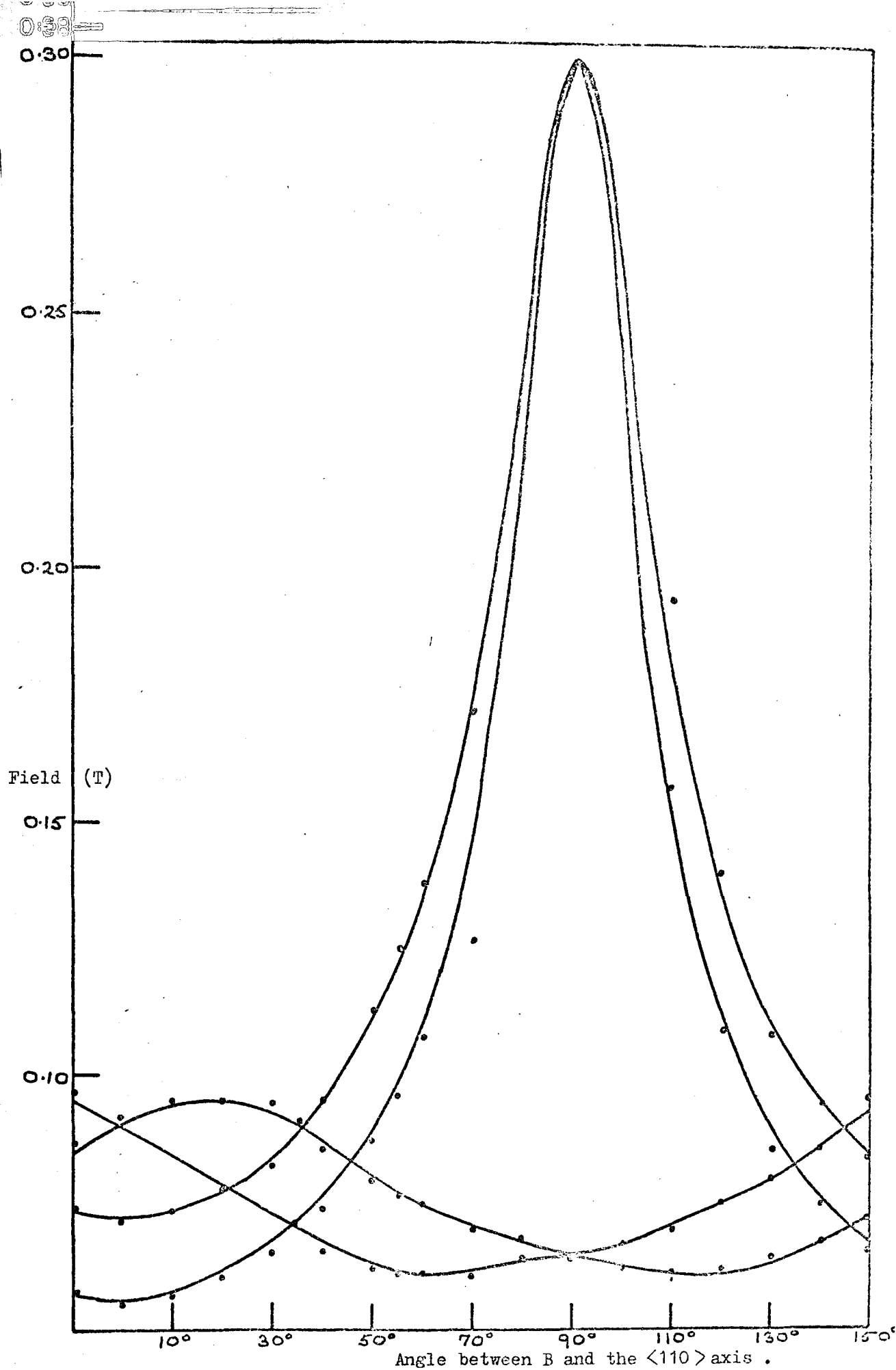
Fig. 5.10. The angular dependence in the $\{110\}$ plane of the spectrum

Several attempts were made to follow the lines moving to high fields as the magnetic field was rotated away from the $<110>$ axis. However, the line width observed on the oscilloscope display increased greatly as the sample was rotated and eventually made the lines impossible to detect. The $g_x$-value was, therefore, calculated from the line positions obtained with the field at $55°$ and $70°$ to $<100>$.

The resonant lines from centres with B//Y and B//Z are at low fields where the proton resonance device for measuring the magnetic field cannot be used. This region below 0.2T was calibrated with a Hall probe. A correction was then made for the residual field at zero magnet current which affected the linear field sweep of the integrating magnetometer.

The g-values obtained are

$$g_z = 11.0 \pm 0.2$$
$$g_y = 8.66 \pm 0.1$$
$$g_x = 2.2 \pm 0.2$$

The $g_x$ value is less accurate than $g_z$ and $g_y$ because of the indirect calculation. The solid lines in fig. 5.10 represent the theoretical resonant field positions as the sample is rotated in a $\{110\}$ plane.

$Dy^{162}$ has a zero nuclear magnetic moment but the isotopes of dysprosium $Dy^{161}$ and $Dy^{163}$ have $I = \frac{5}{2}$ and are 18.7% and 25% abundant respectively. Each of the isotopes should give a hyperfine structure of six lines and of intensity about 3% and 4% of the central line. The structure was observed on the clearer resonant spectra (for example with B//$<100>$) and could be most easily distinguished from the noise level at small angles away from $<100>$ where the splitting of the lines made them

readily identifiable (fig. 5.9). Approximate values for A were obtained, as in the case of $Er^{3+}$, by assuming the hyperfine splittings to be isotropic. This assumption is reasonable since optical spectra show that the excited $J = \frac{13}{2}$ level of $Dy^{3+}$ usually lies about 3,500 $cm^{-1}$ above the ground state. The average $\bar{A}$ values for the isotopes, taking $\bar{A} = \frac{1}{3} (A_x + A_y + A_z)$, are

$$Dy^{161} \quad |\bar{A}| = 600 \pm 50 \text{ MH}_z = (200 \pm 20) \times 10^{-4} \text{ cm}^{-1}$$

$$Dy^{163} \quad |\bar{A}| = 900 \pm 50 \text{ MH}_z = (300 \pm 20) \times 10^{-4} \text{ cm}^{-1}$$

### 5.4.3 Ground state, and vacancy association

$Dy^{3+}$ resonances have not been seen in as large a number of different host materials as $Yb^{3+}$ and $Er^{3+}$. Dysprosium is not expected to attain other valent states under normal conditions, although resonances from excited states of $Dy^{2+}$ in $CaF_2$ have been observed after reduction of the $Dy^{3+}$ by annealing in calcium vapour. The resonance observed in AgCl is not affected by annealing in nitrogen or chlorine and it is assigned to $Dy^{3+}$ ($4f^9$) with a $^6H_{15/2}$ ground state. For $Dy^{3+}$ in an octahedral environment the x parameter of the field is expected to be negative. The ground state may then be a $\Gamma_6$ state with a theoretical g-value of 6.67 if $|x| > 0.45$, or a $\Gamma_7$ state with a g-value of 7.55 if $|x| < 0.45$. Assuming a covalent correction to the Landé g-factor of the same magnitude as that assigned to $Yb^{3+}$ (k = 0.97), the theoretical g-values become 6.56 and 7.43.

The observed centre has an average g-value of $7.3 \pm 0.2$. Assuming, as before, that $\bar{g}$ for the low symmetry centres should be only slightly less than the cubic g-value, the centre has a ground level derived from

the cubic $\Gamma_7$ ground state. The symmetry of the site is best explained by assuming a substitutional site in association with two nearest cation vacancies such that the lines joining the $Dy^{3+}$ ion to the vacancies make an angle of $90°$. The relative similarity of the g-values for the two $\langle 110 \rangle$ axes compared to the g-value for the $\langle 001 \rangle$ axis makes this orthorhombic centre the most likely. It is the same centre as the subsidiary centre in $AgCl:Yb^{3+}$. The deviation of $\bar{g}$ from $g_c$ in $AgCl:Dy^{3+}$ is larger than in $AgCl:Yb^{3+}$, and slightly larger than $\bar{g} - g_c$ for the orthorhombic centre in $AgCl:Er^{3+}$. However, the g-values of the centre in $AgCl:Dy^{3+}$ show great asymmetry and the axial distortion of the field is probably larger than in $AgCl:Yb^{3+}$ or $AgCl:Er^{3+}$.

The $\Gamma_7$ ground state could occur for $Dy^{3+}$ in an interstitial site (fig. 5.5) but the symmetry of the resonance would then be hard to explain. In CaO the octahedral surroundings give rise to a $\Gamma_6$ ground state for $Dy^{3+}$ [7] and the ratio of $\dfrac{B_4}{B_6}$ must be lower ($< 190$) in AgCl than in CaO since a $\Gamma_7$ state is lowest.

## 5.5     Discussion

### 5.5.1     Lattice site

The vast majority of E.P.R. measurements reported for the rare earths, other than the S-state ions, have involved sites of cubic or axial symmetry. The rare earths are often found in crystals of low symmetry (for example, the ethyl sulphates and double nitrates), but the environment of the paramagnetic ions is usually of at least tetragonal or trigonal

symmetry. Few E.P.R. measurements have been made on trivalent ions in simple monovalent cubic lattices. $Yb^{3+}$ has been studied in KCl and $NaCl^{(21)}$ and a broad line with g = 3.5 was seen at 77K. Measurements were not made at 4.2K and no inference was made as to the site symmetry or lattice site. Extensive optical studies on $Sm^{2+}$, $Eu^{2+}$ and $Yb^{2+}$ in the alkali halides have been made by Wagner and $Bron^{(22)}$ and others. $Eu^{2+}$ has also been studied by E.P.R. in KCl, NaCl and $KBr^{(23)}$ and the site symmetry was shown to be orthorhombic. All three divalent ions are believed to be substitutional in the alkali halides and associated with a single nearest cation $vacancy^{(22)}$.

The E.P.R. results for $Yb^{3+}$, $Er^{3+}$ and $Dy^{3+}$ in AgCl show that the majority of the ions in each case are in substitutional sites. The radii of the rare earth ions are relatively large compared to those of the iron transition series and interstitial sites would not be expected to be favoured. The radii are

$$Yb^{3+}:0.85\overset{\circ}{A} \qquad Er^{3+}:0.87\overset{\circ}{A} \qquad Dy^{3+}:0.91\overset{\circ}{A} \qquad (5)$$

The crystal (Goldschmidt) radius of $Ag^{+}$ is $1.13\overset{\circ}{A}$ and the interstitial site is expected to have a radius of about $1.0\overset{\circ}{A}$. The interstitial site possibly observed for a proportion of the $Er^{3+}$ ions is unusual. There is slight evidence that the number of these trigonal sites increases as the total impurity concentration increases. It may be that $Yb^{3+}$ or $Dy^{3+}$ can be found in interstitial sites but the resonances were not detected either because the impurity concentration was too low, or the relaxation time was too short.

## 5.5.2  The octahedral crystal field

The $Dy^{3+}$ and $Er^{3+}$ results suggest that the ratio of $\dfrac{B_4}{B_6}$ for the

AgCl octahedral sites is less than 200 and is smaller than for the

octahedral cubic sites in CaO, MgO and SrO which are the only lattices for

which the trivalent rare earths have been studied in octahedral fields[14,15].

Values of $|x|$ for the oxide lattices are of the order of 0.7, which

corresponds to $\left|\dfrac{B_4}{B_6}\right| \approx 540$. Comparison of the fields in AgCl and CaO may be

made by considering the E.P.R. results reported for $Eu^{2+}$ in these

lattices[2,24]. The results for $Eu^{2+}$ in CaO give $\left|\dfrac{B_4}{B_6}\right| = 320$ and those for

$Eu^{2+}$ in AgCl give $\left|\dfrac{B_4}{B_6}\right| = 248$, for the ions in an octahedral field at room

temperature. The mechanism by which the cubic field affects the S-state

$Eu^{2+}$ ion is not the same as that which applies to the other 4f ions and

the absolute magnitudes of $\dfrac{B_4}{B_6}$ are not important. However, the relative

values give some indication of the change expected in going from a CaO to

an AgCl matrix. For AgCl a reduction about $\frac{1}{3}$ over CaO is indicated for

$Eu^{2+}$ at room temperature. The other rare earth measurements are made at

4.2K and the contraction of the two lattices at the low temperatures may

alter the magnitude of $\dfrac{B_4}{B_6}$ although not necessarily by the same amount in

the two lattices since the misfit of the impurity ion and its excess

charge are not the same in CaO as in AgCl. In the case of $Eu^{2+}$ in CaO

the ratio decreases at 77K and then increases again at 4.2K. However, the

accuracy of the measurement of $B_6$ by Shuskins is low and these variations

are not very significant. The double excess positive charge or the low

temperature must cause the octahedral field to alter so that the ratios

of $\dfrac{B_4}{B_6}$ in AgCl:$Dy^{3+}$ and AgCl:$Er^{3+}$ at 4.2K are about 0.4 of the values

found in the oxide lattices.

### 5.5.3 g-values

The g-values obtained are used to establish the ground states of the impurity ions. The assumption is made that the average g-value of an asymmetric centre should be only slightly less than the g-value of the particular cubic state from which the new state is derived. The covalent reduction factor can only be estimated for $Yb^{3+}$ since an isotropic resonance is only observed in this case.

Ranon and Low[25] have shown that the relative sizes of $g_{//}$ and $g_{\perp}$ for an axial centre can be related to the charge of the ion producing the axial distortion. The axial field can be taken as a single extra term in the expansion of the general cubic field in terms of the usual operator equivalents. The general cubic field Hamiltonian is

$$H = B_4 (O_4^0 + 5.O_4^4) + B_6 (O_6^0 - 21.O_6^4)$$

and the axial field adds an additional term $B_2^0 O_2^0$. $O_2^0$ is the operator given by Elliott and Stevens[10] as $\langle J\|\alpha\|J\rangle[J_z^2 - \frac{1}{3}J(J + 1)]$ where $\langle J\|\alpha\|J\rangle$ is a factor relating the crystal field operators to the original potential functions and values of $\langle J\|\alpha\|J\rangle$ are given in ref.(10). The sign of $B_2^0$ may be found by a simple point charge calculation to determine the effect of the vacancy, which is equivalent to a negative charge in place of an $Ag^+$ ion. In Appendix II the tetragonal part of the crystal field potential (D or $B_2^0$) is calculated and for a next-nearest cation vacancy the sign of D is predicted as negative. D is positive for a nearest cation vacancy. Ranon and Low[25] argue that, for positive $B_2^0$ and positive $\langle J\|\alpha\|J\rangle$, the coefficients of the cubic field eigenfunctions of smallest $|J_z\rangle$ values will be increased by the axial distortion. Since the total eigenfunction must remain normalised, the coefficients of the

wavefunctions of large $|J_z\rangle$ are reduced. The $g_{/\!/}$ of an axial centre is given by $g_{/\!/} = 2g_J\langle\psi^*|J_z|\psi\rangle$ and will be reduced from the cubic field value $g_c$. If $(g_{/\!/} + 2g_\perp)\frac{1}{3} = g_c$, then $g_{/\!/} < g_c < g_\perp$. Conversely, if the product $B_2^o \langle J\|\alpha\|J\rangle$ is negative, $g_{/\!/} > g_c > g_\perp$.

The spectrum of $Dy^{3+}$ in AgCl is not axial. However, since the two vacancies are believed to lie along the Z and Y axes of the centre, the effective $g_{/\!/}$ of the centre may be taken as $\frac{1}{2}(g_z + g_y)$. The value of $g_\perp$ is $g_x$ since X is the $\langle 001\rangle$ direction perpendicular to the plane of the two vacancies. Hence for $Dy^{3+}$ $g_{/\!/} = 9.83$, $g_\perp = 2.2$ and the above analysis implies that $B_2^o \langle J\|\alpha\|J\rangle$ is negative since $g_{/\!/} > g_c > g_\perp$. For $Dy^{3+}$, $\langle J\|\alpha\|J\rangle$ is negative and so $B_2^o$ should be positive which fits with two nearest cation vacancies.

For the principal $Er^{3+}$ centre, $g_z = g_\perp$ since the Z ($\langle 111\rangle$) direction is perpendicular to the plane of the vacancies. It follows that $g_{/\!/} = \frac{1}{2}(g_y + g_x)$ which gives $g_{/\!/} = 6.46$, $g_\perp = 6.73$. For the $\Gamma_7$ state $g_c = 6.65$ when corrected for $k = 0.975$. For $Er^{3+}$ $\langle J\|\alpha\|J\rangle$ is positive and $g_{/\!/} < g_c < g_\perp$ implies that $B_2^o$ is also positive, which agrees with the nearest cation vacancy model.

The main $Yb^{3+}$ centre is axial with $g_{/\!/} < g_c < g_\perp$ and $\langle J\|\alpha\|J\rangle$ positive. The g-values imply, therefore, that $B_2^o$ is positive. The simple crystal field calculation shows that $B_2^o$ is negative for a next nearest cation vacancy and two such vacancies can be shown to double the size of $B_2^o$ but not to alter its sign. The proposed centre does not, therefore, fit with the g-values. A possible explanation is that the two vacancies are not in a straight line but make an angle of $90^o$ at the $Yb^{3+}$ ion. A simple crystal field calculation shows that this centre is approximately

axial, and that $g_{//}$ given above will apply to the direction at right angles to the plane of the two vacancies. Thus, in order to apply the above argument relating to the g-value, $g_{//}$ and $g_{\perp}$ must be interchanged so that $g_{//} > g_c > g_{\perp}$ and $B_2^0$ is negative as expected for a next nearest cation vacancy.

### 5.5.4 Vacancy association

The complexity of the $Yb^{3+}$ and $Er^{3+}$ spectra is not unusual for rare earth ions. $Er^{3+}$ in $CaF_2$ is found in cubic, trigonal and tetragonal sites[18]. There are numerous possible arrangements of two vacancies within the nearest and next-nearest cation shells about the impurity ion. The dielectric loss spectra of the trivalent ions of the iron transition series are complex and indicate that several centres are often present when a double excess charge is compensated. There are probably other centres present in $AgCl:Dy^{3+}$, since the intensity of the spectrum is low in comparison to the doping levels. Short relaxation times may account for the difficulty of seeing the other spectra in AgCl and the fact that E.P.R. from $Dy^{3+}$ has not been seen in as large a number of lattices as $Er^{3+}$ and $Yb^{3+}$.

There appears to be a change in the vacancy association pattern observed as the 4f series progresses. The radius of the rare earth ions decreases as the number of 4f electrons increases (lanthanide contraction), as reflected in the radii quoted above. The overall energy levels of the rare-earth ions are not greatly affected by the symmetry of the surrounding field since the outer shells (5s and 5p) are closed shells and they shield the inner 4f shell. The vacancy association and lattice

site are likely to be determined mainly by size factors, in contrast to

the iron transition series.


The coulombic binding energy of vacancy to impurity will increase

as the distance between the two decreases. The energy of the complex is

expected, therefore, to be lowest when the vacancy is as near as possible

to the impurity ion. There are two factors which mitigate against the

vacancies always being in the nearest cation shell. If the impurity

ion is smaller than the $Ag^+$ ion, as is frequently the case, then the $Cl^-$

ions will relax inwards and the neighbouring $Ag^+$

ions will also move slightly inwards since they are attracted by the $Cl^-$

ions. As a consequence the average anion-cation distance in the cube

next to the impurity ion will decrease, the ionic orbitals will overlap

more and the $Ag^+$ ions will be more tightly held in the first cation

shell. Thus the smaller the impurity ion the less likely a nearest

cation vacancy. The second factor which may encourage the vacancies to

stay further away from the impurity ion is their mutual repulsion.

However, this factor does not seem to be very important except that it

prevents the vacancies being in adjacent silver ion positions.


Thus 65% of the smallest rare earth ion, $Yb^{3+}$, are associated with

two next nearest cation vacancies at either $180^o$ or $90^o$ and only 28% with

nearest cation vacancies. About 70% of the erbium ions are substitutional

with nearest cation vacancies, and the majority of the dysprosium ions

are associated with nearest cation vacancies. The larger ion, $Eu^{2+}$, of

radius 1.09Å, is also entirely associated with a single nearest cation

vacancy in $AgCl$[2].


It is not easy to explain the change in the probable arrangement

of the vacancies in going from $Er^{3+}$ to $Dy^{3+}$. In the former case the two

vacancies make an angle of $120^\circ$ at the erbium ion, whereas in the latter case they are believed to make an angle of $90^\circ$ at the dysprosium ion. It may be that the vacancies can in some way lower their energy by being relatively close together, and that the larger impurity ion makes this possible. The three g-values for the orthorhombic centre in $AgCl:Dy^{3+}$ differ by quite large amounts as compared to the orthorhombic centre in $AgCl:Er^{3+}$. The spread of the g-values in $AgCl:Dy^{3+}$ indicates a larger asymmetry in the crystal field which is probably a result of the greater ionic radius of $Dy^{3+}$ as compared to $Er^{3+}$.

## 5.6    <u>References</u>

1    F. Moser, N.R. Nail and F. Urbach,  J. Phys. Chem. Solids, 9, 217 (1959).

2    S.U. Cheema and M.J.A. Smith,  J. Phys. C., 4, 1231 (1971).

3    S.U. Cheema,  Ph.D. Thesis, University of Warwick (1970).

4    B. Bleaney,  Phil. Mag.  42, 441 (1951).

5    F.H. Spedding and A.H. Daane,  The Rare Earths,  J. Wiley & Sons, N.Y. (1961) Chapter 1.

6    K.R. Lea, M.J.M. Leask and W.P. Wolf,  J. Phys. Chem. Solids, 23, 1381 (1962).

7    W. Low and R.S. Rubins,  Phys. Rev. 131, 2527 (1963).

8    J.E. Lowther and J.P. Killingbeck,  J. Phys. C., 3, 1621 (1970).

9    H.R. Lewis and E.S. Sabisky,  Phys. Rev. 130, 1370 (1963).

10   R.J. Elliott and K.W.H. Stevens,  Proc. Roy. Soc. A218, 553 (1953).

11   G.H. Dieke,  Spectra and Energy Levels of Rare Earth Ions in Crystals,  Interscience, N.Y. (1968).

12   A. Abragam and B. Bleaney:  E.P.R. of Transition Ions, Clarendon Press, Oxford (1970).

13   D. Ball,  Phys. Stat. Sol. 46, 635 (1971).

14   I.C. Chang and W.W. Anderson,  Phys. Lett. 13, 112 (1964).

15   D. Descamps and Y.M. D'Aubigne,  Phys. Lett. 8, 5 (1964).

16   J.E. Wertz and P. Auzins,  Phys. Rev. 106, 484 (1957).

17   J. Lambe and C. Kikuchi,  Phys. Rev. 118, 71 (1960).

18   M.J. Weber and R.W. Bierig,  Phys. Rev. 134, A1492 (1964).

19   J. Michoulier and A. Wasiela,  C.R. Acad. Sci. Paris, 271, 1002 (1970).

20   K.A. Hay, D.J.E. Ingram and C.A. Tomlinson,  J. Phys. C., 1, 1205 (1968).

21   G.D. Sootha, T.C. Tripathi and S.K. Agarwal,  Phys. Stat. Sol.(b) 44, K61 (1971).

22    M. Wagner and W.E. Bron,   Phys. Rev. 139, A223 (1965).

23    R. Rohring,   Phys. Lett., 16, 20 (1965).

24    A.J. Shuskins,   Phys. Rev. 127, 2022 (1962).

25    U. Ranon and W. Low,   Phys. Rev. 132, 1609 (1963).

26    I.R. Edmonds,   Ph.D. Thesis, University of Warwick (1972).

Chapter Six :   Review of the E.P.R. and optical properties of
4f, 4d and 5d ions in silver chloride

## 6.1   E.P.R. of the rare earths

### 6.1.1   Introduction

The rare earth metals europium and gadolinium were studied in
silver chloride by Cheema and Smith[13].   E.P.R. was detected at room
temperature from $Eu^{2+}$ and $Gd^{3+}$ which have half-filled 4f shells.   The
seven 4f electrons have an $^8S_{7/2}$ ground state and the spin-lattice relaxa-
tion times are long.   $Eu^{2+}$ was found to sensitize AgCl on exposure to
light.   The other rare earths, and some members of the 4d and 5d series,
are reviewed in this chapter.   E.P.R. studies were made to investigate
the ground states and environments of the ions.   Optical studies were
carried out to determine whether the ions sensitized AgCl for silver
colloid formation.   All the rare earths except promethium, which is not a
naturally occurring element, were added to silver chloride by metallic or
chloride doping.   E.P.R. was searched for at 4.2K after annealing the
samples in nitrogen and chlorine atmospheres.

### 6.1.2   The second half of the 4f series

E.P.R. was only detected from the ions $Yb^{3+}$, $Er^{3+}$ and $Dy^{3+}$.   The
results are given in Chapter Five and the other ions with more than seven
4f electrons will be discussed here.   The trivalent state will be
considered first as it is the most common valent state of all the rare
earths.

No E.P.R. was detected from the non-Kramers ions $Tm^{3+}$, $Ho^{3+}$ and $Tb^{3+}$. A general cubic crystal field can split the J-states of a non-Kramers ion into singlet levels ($\Gamma_1$, $\Gamma_2$), non-Kramers doublets ($\Gamma_3$) and triplet states ($\Gamma_4$, $\Gamma_5$) which can be represented by an effective spin $S = 1$. The tables of Lea, Leask and Wolf[1] show the relative energy levels of the states for each J value in general cubic fields. The energy parameter W, defined in Chapter Two, is negative for these three ions and the energy level diagrams of L.L.W. must be reversed. The singlet states can give no resonance. The $\Gamma_3$ doublet has no first-order Zeeman interaction in a general cubic field but can be split by a low symmetry crystal field. Resonance can be observed provided that the splitting is smaller than the microwave quantum. The triplet states will give resonance in general cubic fields but can be split into singlets by low symmetry fields. In AgCl at 4.2K the majority of the trivalent ions present are expected to be associated with two silver ion vacancies at sites of low symmetry. The lowest J-level can be expected to be split into singlet levels and the resonance will be described by a spin-Hamiltonian[2]

$$H = g\beta\underline{B}.\underline{S} + A.\underline{I}.\underline{S} + \Delta xSx + \Delta ySy$$

$\Delta = (\Delta x^2 + \Delta y^2)^{\frac{1}{2}}$ describes either the static crystal field splitting or a Jahn-Teller splitting where the crystal field symmetry leaves an orbital doublet lowest.

Resonances from $Tm^{3+}$ ($4f^{12}$, $^3H_6$) have not been widely seen. Low[3] reported an axial spectrum in $CaF_2$ but subsequent searches by Weber and Bierig[4] showed no E.P.R. They concluded that $\Gamma_2$ singlet was lowest in an 8-coordinated cubic field, and that the x parameter, defined in Chapter Two, was equal to 0.6. In an octahedral field L.L.W. show that a $\Gamma_1$ or $\Gamma_2$ level is lowest and no E.P.R. is expected.

$Ho^{3+}$ $(4f^{10}, {}^5I_8)$ has been observed in trigonal sites. Kirton[5] reported an axial spectrum in $CaWO_4$ with $g_{//} = 13.691$, $g_\perp = 0$ and a Jahn-Teller splitting $\Delta = 0.05$ cm$^{-1}$ resulting in asymmetric line shapes. Broad lines were observed when the magnetic field was not parallel to the crystal C axis. All the $Ho^{3+}$ ions have $I = \frac{7}{2}$ and a large hyperfine splitting parameter $A = 0.299$ cm$^{-1}$ was observed. In $CaF_2$ no E.P.R. was seen and a $\Gamma_3$ singlet level is taken to be lowest in 8-coordinated fields $(x = -0.5)$[4]. In an octahedral field a $\Gamma_3$ doublet is expected lowest provided that $x < 0.8$ and $\frac{B_4}{B_6} < 924$ which is reasonable in view of the values discussed in Chapter Five. A resonance is expected from this state but it seems likely that the crystal field splitting in a low symmetry site will be large and a higher microwave frequency will be needed for observation of the resonance. Also, the large A value and large g anisotropy expected (since $g_\perp = 0$ for the doublet states before the crystal field mixes in small amounts of higher states) may make the resonant intensity in each line low and the line widths large.

$Tb^{3+}$ $(4f^8, {}^7F_6)$ has been studied in axial sites in several lattices. Forrester and Hempstead[6] saw resonances in $CaWO_4$ and $CaF_2$ from a ground state doublet $(J_z = \pm 6)$ of $Tb^{3+}$ in tetragonal and trigonal sites. Weber and Bierig estimated $x > 0.8$ in $CaF_2$. A $\Gamma_3$ doublet is lowest and is split by the axial fields in $CaF_2$ giving values of $g = 17.77$, $\Delta = 5.134$ GHz and $g = 17.28$, $\Delta = 31.67$ GHz, for the two sites. Frequencies of 4-50 GHz were used to observe the resonances[6]. In octahedral symmetry L.L.W. give $\Gamma_1$ or $\Gamma_2$ states lowest and a resonance is not expected.

Several divalent rare earths have been seen in $CaF_2$[4], and $Eu^{2+}$ and $Sm^{2+}$ have been studied in the alkali halides. Those ions in this part

of the series, which become Kramers ions after reduction, are most likely to be detected in AgCl if they can be reduced. $Ho^{2+}$ and $Tm^{2+}$ are iso-electronic with $Yb^{3+}$ and $Er^{3+}$ and have been seen in $CaF_2$[4]. Isotropic spectra are most commonly seen and are fairly simple except for the large hyperfine constant of holmium which introduces forbidden transitions, particularly at X-band.

### 6.1.3 The first half of the 4f series

Although all the elements in the first half of the 4f series were added to AgCl in both nitrogen and chlorine atmospheres, no E.P.R. was detected. Three of these ions are Kramers ions ($Sm^{3+}$, $Nd^{3+}$, $Ce^{3+}$) and numerous resonances have been reported from them in 8-coordinated cubic and trigonal sites although none have been reported in octahedral sites. $Sm^{3+}$ ($4f^5$, $^6H_{5/2}$) has a $\Gamma_8$ quartet lowest for both types of cubic field. The quartet is split by axial or lower symmetry fields and the g-values usually observed are low since $g_J$ for $Sm^{3+}$ is $\frac{2}{7}$. In $CaF_2$ Low has seen an axial spectrum with $g_{//} = 0.907$, $g_{\perp} = 0.544$ [7] and another axial spectrum with $g_{//} = 0$, $g_{\perp} = 0.823$ [8] has been reported. Similar g-values would be expected for charge-compensated sites in AgCl. At X-band frequencies fields of 0.7T to 15.T or higher are needed to observe these resonances. The magnet used gave fields up to 1.2T, but it seems probable that $Sm^{3+}$ was not observed because of the experimental difficulty in detecting resonances at high fields, and the large anisotropy of g-values which is expected.

$Nd^{3+}$ ($4f^3$, $^4I_{9/2}$) resonances have been seen in many lattices in cubic and low symmetry sites. Rhombic resonances were seen in several

garnets by Wolf et al[9] with g-values in the region 1.7 - 3.8. In $CaF_2$ a $\Gamma_8$ state is lowest for all x values and the g-values will depend on the ratio $\dfrac{B_4}{B_6}$ . Low reported an axial spectrum with $g_{//} = 4.412$, $g_\perp = 1.301$ [3] McLaughlan[10] has seen an orthorhombic spectrum with $g_x = 5.136$, $g_y = 1.201$ and $g_z = 0.596$ in $CaF_2$. In an octahedral field a $\Gamma_8$ state will lie lowest for x < 0.8 and, if x > 0.8, a $\Gamma_6$ state is lowest with cubic g-value $g_c = 1.33$. A value of x < 0.8 corresponds to $\dfrac{B_4}{B_6} < 168$ which is possible and in axial or lower symmetry the g-values would be similar to those quoted above and E.P.R. is expected to be detectable in AgCl.

$Ce^{3+}$ ($4f^1$, $^2F_{5/2}$) resonances have been reported in many lattices and, as for $Sm^{3+}$, a $\Gamma_8$ level is lowest for all x in 8-coordinated of octahedral fields. In tetragonal fields in $CaF_2$ values of $g_{//} = 3.038$ and $g_\perp = 1.396$ have been reported[11] and similar values would be expected in AgCl.

There would seem to be no paramagnetic property of these last two ions, particularly of $Nd^{3+}$, which would make resonance hard to detect in AgCl. It is probable that sufficiently high impurity concentrations were not obtained. $Ce^{3+}$ and $Nd^{3+}$ are the largest of the rare earth ions with radii 1.02Å and 0.99Å as compared to $Eu^{3+}$ (0.96Å) and $Yb^{3+}$ (0.85Å). The E.P.R. obtained in AgCl suggests that dysprosium is harder to incorporate in large concentrations than ytterbium. It is difficult to maintain high concentrations of europium in either the di- or trivalent state in AgCl. Europium precipitates out of the lattice in a few hours if the samples are not carefully annealed[13]. AgCl was doped with cerium and neodymium using both the metal and the metal chloride. Crystals were grown under chlorine. Parts of the crystals were cloudy and brittle

indicating that impurities were certainly present but, even after careful annealing and cooling, a large proportion of the impurity ions were probably present in precipitate form. The largest ion which has been added to AgCl is $Au^+$ (radius 1.37Å) and, although this is a special case because of the similarity of the gold and silver ions, precipitation of the impurity can be detected[14]. The spin sensitivity of the low temperature system corresponds to 5 - 10ppm of impurity in the small samples provided that all the spins give a single resonance line.

The other ion studied in this part of the series was $Pr^{3+}$ ($4f^2$, $^3H_4$). This is again a large ion but in any case a $\Gamma_1$ singlet state is expected to be lowest in an octahedral field.

## 6.2 Optical studies of the rare earth ions

### 6.2.1 Photosensitivity

In addition to the E.P.R. measurements experiments were carried out to determine if any of the rare earths sensitized AgCl to light in the same way as europium and to detect any absorption at visible or infra-red wavelengths which would confirm the presence of or suggest the site symmetry of the impurity. Europium is believed to sensitize AgCl after a non-oxidising anneal because the $Eu^{2+}$ formed is a trap for photoproduced holes. The photoproduced electrons are then able to form $Ag^o$ atoms and subsequently stable silver colloid. This work was carried out, therefore, to see if any of the other rare earths acted in a similar way.

The silver chloride containing the rare earth impurity was reduced for several hours by vacuum or nitrogen anneal, usually in the presence of metallic silver. The samples were then cleaned and exposed to blue light of peak wavelength 434nm using a mercury light and filter. At intervals of about 30s measurements of the optical absorption in the range 700 - 450 nm were made in the Perkin-Elmer spectrophotometer and were compared with corresponding measurements on pure samples. In clear samples none of the rare earth dopants made a significant change in the photolytic darkening over the pure samples. In heavily doped and brittle samples a slight increase of darkening was sometimes observed which could be accounted for by the internal strains and precipitates in these samples. The high doping levels increased the number of dislocations and grain boundaries in the samples which could act as hole traps or as sites for the build up of silver colloid[15]. In the most heavily doped and cloudy samples dark lines could be clearly seen along grain boundaries after prolonged exposure.

The problem of the apparent sensitivity of the heavily doped samples does not commonly arise in studying the photosensitivity of the iron transition series ions. A number of the ions studied do not sensitize AgCl (Ti, V, Cr, Mn, Co, Ni). These ions are all fairly readily incorporated in the halide lattice and the colour (Ti, V, Cr) and fairly readily observed E.P.R. (V, Cr, Cu, Fe) of the specimens can be used to detect the presence of the ions at medium concentrations. In addition, a number of these ions (V, Cr, Ni) all attain two different valent states and are believed to act as recombination centres for electrons and holes. In heavily doped and in sensitized samples these ions will help to recombine photoproduced electrons and holes and will reduce the sensitivity of the material over that expected from the

presence of any sensitizing impurities[13]. By contrast, the rare earths

other than europium are thought to play a neutral role with regard to

electron or hole trapping when dispersed in the halide lattice.


## 6.2.2  Divalent state formation


The E.P.R. and the optical spectra of the rare earth ions

studied here are not significantly altered by annealing in chlorine or

in nitrogen.  This, and the lack of photosensitivity, suggest that the

lanthanides other than europium do not attain the divalent state in AgCl

to a significant extent.  A divalent ion concentration of 1ppm

corresponding to a reduction of about 0.5% of the ions present in the

samples used would cause significant photolytic darkening if the divalent

ion were to act as a hole trap.  The divalent rare earths, except for

$Yb^{2+}$, $Eu^{2+}$ and $Ce^{2+}$, are expected to give strong absorption at visible

wavelengths and they produce colouration in $CaF_2$[16].  No colours were

observed in the rare earth doped silver chloride after annealing in a

reducing atmosphere.  The surface was cleaned as it was sometimes grey or

pink coloured from reduced silver.


The chemical properties of the 4f series show that the reduction

of the rare earths to the divalent state in AgCl is unlikely.  Reduction

to $Sm^{2+}$, $Ho^{2+}$, $Er^{2+}$, $Tm^{2+}$ and $Yb^{2+}$ in $CaF_2$ has been achieved by annealing

in calcium vapour, by electrolytic reduction and by irradiation with

X-rays, U.V. light and $\gamma$-rays[4,16,17].  However, exposures to reduce

the trivalent rare-earths in $CdF_2$ by annealing in cadmium vapour failed

to produce concentrations of divalent rare earths, other than $Eu^{2+}$, that

could be detected optically or by E.P.R.[18].  Weller and Scardefield

argued that the chemical oxidation potentials of the elements can be used to determine if reduction will take place[19]. The conversion of the rare earth from the trivalent to the divalent state does not take place to a measurable extent in $CdF_2$ or AgCl because $Ag^+$ and $Cd^+$ are more easily reduced to the metal than the rare earths are to the divalent state. The oxidation potentials of several relevant reactions given by Latimer[20] are shown in Table 1. Values are included for the reduction of the trivalent rare earth where these are known. The potentials are measured in acidic solution by comparison with a standard hydrogen electrode. A positive value indicates that the reaction is favoured as written.

## Table 1

| Reaction | Potential (Volts) | Reaction | Potential (Volts) |
|---|---|---|---|
| $Ca \rightarrow Ca^{2+} + 2e$ | + 2.87 | $Ag \rightarrow Ag^+ + e$ | − 0.799 |
| $Cr^{2+} \rightarrow Cr^{3+} + e$ | + 0.41 | $Eu^{2+} \rightarrow Eu^{3+} + e$ | + 0.43 |
| $Cd \rightarrow Cd^{2+} + e$ | + 0.403 | $Yb^{2+} \rightarrow Yb^{3+} + e$ | + 0.578 |
| $Ti^{2+} \rightarrow Ti^{3+} + e$ | + 0.37 | $Sm^{2+} \rightarrow Sm^{3+} + e$ | > 0.9 |
| $V^2 \rightarrow V^{3+} + e$ | + 0.255 | | |

In a reducing atmosphere or in vacuo chlorine ions leave the surface of the crystal as $Cl_2$ molecules and electrons diffuse into the crystal which is effectively conducting at these temperatures (just below the melting point)

$$AgCl(S) \rightarrow Ag^+(S) + Cl^- \rightarrow \tfrac{1}{2}Cl_2(g) + Ag^+(C) + e$$
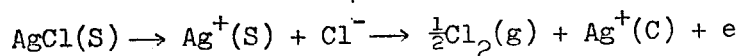
where (S) represents the surface,

(g) the gas phase and (C) a cation position.

The electron can be trapped at a silver ion or an impurity ion site. By reversing the equations given in Table 1, it can be seen that the reaction $Ag^+ + e \rightarrow Ag^o$ (E = + 0.799V) is more likely to occur than any of the other reductions listed. However, optical and E.P.R. measurements show that the reduction of $V^{3+}$ to $V^{2+}$, for example, does take place[13]. The absolute values of the potentials quoted cannot be applied directly to the AgCl system since they are measured in solution. Some values of oxidation potentials for elements in fused salts are available and, in general, the elements occupy the same relative positions. There is evidence that an element in contact with its own salt has a more positive electrode potential[21]. It follows that silver will be more likely to remain ionic when in contact with silver chloride than when it is in acidic solution, but that the other elements in AgCl should remain in the relative positions of Table 1. The figures indicate that it will be harder to convert $Cr^{3+}$ to $Cr^{2+}$ than $V^{3+}$ to $V^{2+}$ and indeed prolonged annealing in vacuo in contact with metallic silver is needed to produce complete conversion to $Cr^{2+}$ [21]. $Eu^{2+}$ can be formed, and is well known chemically, in the divalent state since $Eu^{3+}$ achieves a half-filled 4f shell by gaining an electron. However, dielectric loss experiments suggest that complete conversion of $Eu^{3+}$ to $Eu^{2+}$ in AgCl does not take place. The E.P.R. of AgCl:$Yb^{3+}$ after annealing in vacuum does show a reduction in intensity of 10% or less over the samples annealed in chlorine and this may be due to a reduction of a proportion of the ions to $Yb^{2+}$. E.P.R. is not expected from $Yb^{2+}$ since it has a filled 4f shell. The reduction of Sm and all the other rare earths is expected to be less well favoured than for Yb and they are not expected to attain divalent states in AgCl.

Although the chemical theory supports the experimental observations, the oxidation potentials cannot be used, a priori, to dismiss the possibility of the reduction since there are a number of unknown factors in the incorporation of the ions in AgCl. Indeed, on the figures alone, the conversion of $Eu^{3+}$ to $Eu^{2+}$ is not expected whereas the reduction of $Ti^{3+}$ to $Ti^{2+}$ might be thought more likely but it is not observed (probably because the divalent state of titanium is unstable at temperatures above 700K).

## 6.2.3 Gadolinium

The previous argument implies that the formation of $Gd^{2+}$ in AgCl is very unlikely. $Gd^{2+}$ is unknown chemically and has not been formed in $CaF_2$. $Gd^{3+}$ has the stable configuration of a half-filled 4f shell. The question arises as to how gadolinium can sensitize AgCl as suggested by S.U. Cheema[13]. A single crystal of gadolinium doped AgCl was prepared and cut into three slices. The impurity concentration was expected to vary between the slices owing to the zone-refining action of crystal growth. Experiments were carried out to see if doping with gadolinium increased the sensitivity of the material, if there was a relationship between sensitivity and dopant concentration and if the E.P.R. was affected by annealing in chlorine or nitrogen. Quantitative measurements were difficult because the sample had to be removed from the single crystal mount for annealing and very slight changes in the orientation of the sample could cause marked changes in the relative intensities of the resonant lines. Furthermore, the large number of intense lines made identification of iron or copper impurity levels uncertain.

The top slice of the crystals gave a slight increase in photolytic darkening, but the sensitivities of the second and third slices were negligible although the gadolinium concentration was reduced by less than 10%. No variation in the pattern of the spectrum which could not be accounted for by slight changes in the orientation of the sample and the external field was observed after annealing in nitrogen and chlorine or after irradiation.

The experiments are not conclusive but certainly suggest that the photo-effects of gadolinium are much less than those of $Eu^{2+}$ and may arise from residual impurities introduced with the gadolinium. These may include europium since the two ions are neighbours in the rare earth series and are, therefore, hard to separate.

### 6.2.4 Optical spectra of erbium, holmium and dysprosium

The absorption spectra of the rare earths in AgCl were studied in the visible and infra-red. For the majority of the ions no strong absorption lines were seen. Ytterbium gave a yellow colouration apparently due to the tail of an absorption band at wavelengths just below the AgCl band edge. Dysprosium, holmium and erbium gave a few absorption lines of low intensity. The strongly allowed transitions are those from the $4f^n$ to higher configurations (for example 4f to 5d). For the trivalent rare earths the configuration nearest to $4f^n$ is $4f^{n-1}5d^1$ and is separated from $4f^n$ by at least $5 \times 10^4 cm^{-1}$. These transitions will lie in the U.V. and far U.V. where they cannot be seen because of the lattice absorption of AgCl which is strong at wavelengths below 410nm. Transitions in the visible and I.R. will be between different states

within the $4f^n$ configuration and will only be allowed when elements of odd parity are present in the crystal field and will usually have oscillator strengths of the order of $10^{-8}$ [23]. At room temperature the lines observed are often broad because of vibrations of the crystal lattice and temperatures of 4.2K are needed to resolve the structure. Cooling to 77K or 4.2K also reduces the intensity of transitions from states higher than the ground J-state and helps to analyse the spectrum. The spectrophotometer used does not have the very high resolution usually needed for rare earth work and no Zeeman apparatus was available to establish the symmetry of the site giving rise to the lines. The spectra were investigated mainly as evidence for the presence of the impurity and the effect, if any, of annealing in chlorine or reducing atmospheres.

The spectrum observed for $Er^{3+}$ (fig. 6.1) consisted of a small group of low intensity lines near 525nm superimposed on a steadily rising background due in part to reflections from the sample. No other lines could be distinguished and the relative intensities and widths of the lines were not affected by cooling to 90K. The lines are probably due to transitions from the ground J-state of $Er^{3+}$ to higher states in a low symmetry field. The general pattern of lines for a given rare earth is expected to remain the same as the surrounding lattice changes, since the crystal field effects on the rare earths are small. However, the relative intensities of the lines will alter markedly as the precise site symmetry varies. Comparison with the tables of Dieke[23] for $Er^{3+}$ in various lattices shows that a group of lines near 525nm ($19050cm^{-1}$) could arise from transitions from the ground level $^4I_{15/2}$ to $^2H_{11/2}$. $Er^{3+}$ spectra from approximately orthorhombic sites in $YCl_3$ show a strong set of lines between 19,018 $cm^{-1}$ and 19,185 $cm^{-1}$ [24]. Rakestraw and
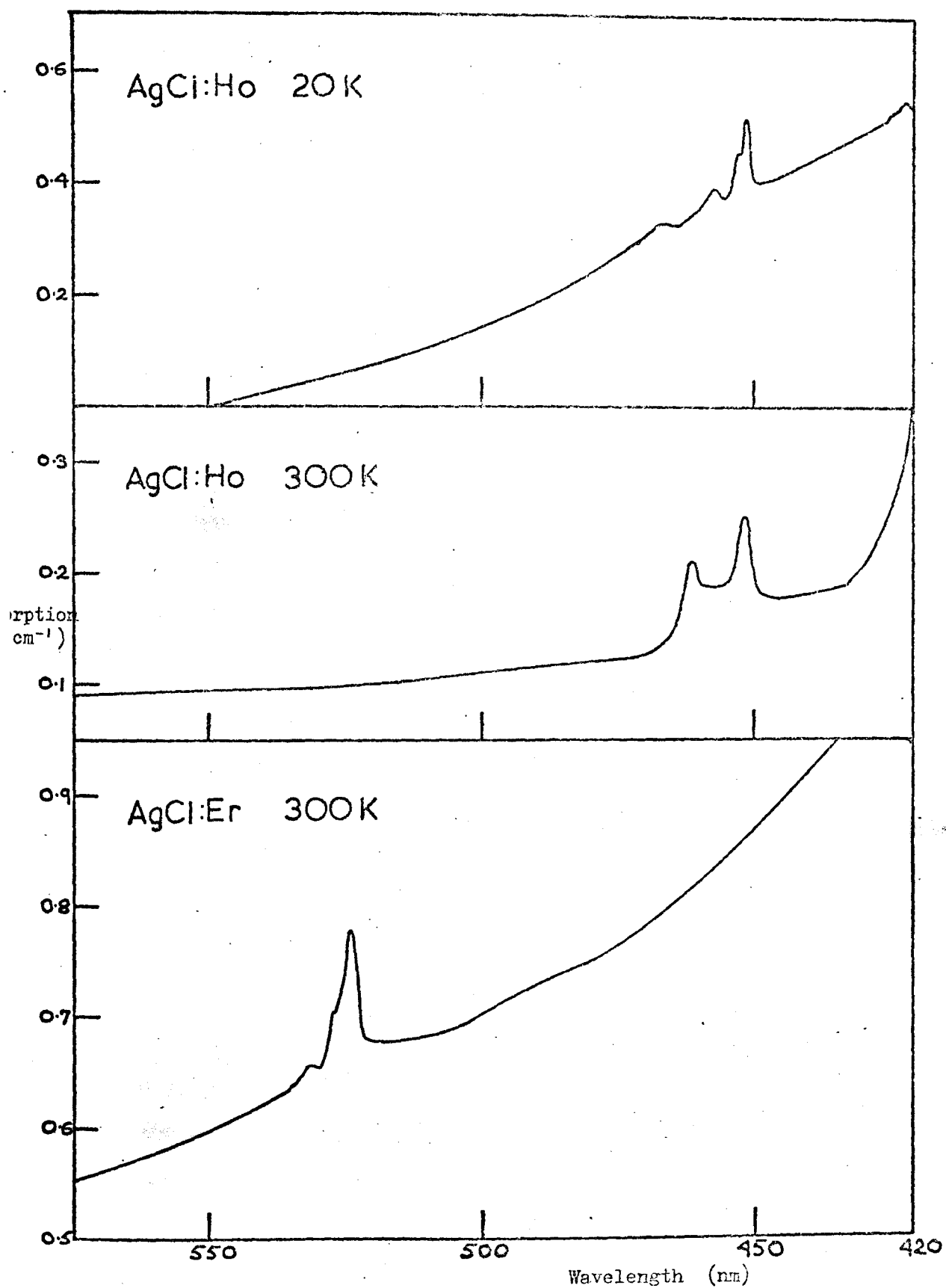
Fig. 6.1. The optical absorption of AgCl:Ho and AgCl:Er .

Dieke comment that the crystal field splittings in $YCl_3$ are larger than those in $LaCl_3$, but that the centre of gravity of each excited level is lowered with respect to the mean of the lowest J level. Both lattices provide approximately octahedral sites and the average cation to $Cl^-$ bond distance in $LaCl_3$ is 3.01Å and in $YCl_3$ it is 2.63Å which accounts for the lowering of the levels in $YCl_3$[24]. In AgCl the cation-anion bond distance is 2.773Å and the centre of gravity of the excited J states should lie between the values in $LaCl_3$ and $YCl_3$. If the observed lines are assumed to span the $F(^2H_{11/2})$ level, the mean energy is $18,950 \pm 10$ cm$^{-1}$ lying between the value for $YCl_3$ (18,949 cm$^{-1}$) and the probably value for $LaCl_3$ ($19,040 \pm 20$ cm$^{-1}$). In $CaF_2$:$Er^{3+}$ lines are observed for $Er^{3+}$ in tetragonal sites and the $^2H_{11/2}$ lines are seen in the region 19,231 to 19,300 cm$^{-1}$ [25] but are not so markedly more intense than the other lines in the visible as compared to the orthorhombic $YCl_3$:$Er^{3+}$ case. The cation to anion distance in $CaF_2$ is smaller than in the lattices considered above, but the erbium ion is 8-coordinated to the fluorine ions which may account for the higher $^2H_{11/2}$ level.

At room temperature the holmium spectra consists of two broad lines at 451 and 461 nm and on cooling to 90K the intensity of the 461 line is reduced. By cooling to 20K the line at 461 is lost and lines at 451, 453 and 457 nm are clearly resolved (fig. 6.1). Two low intensity lines are also present at 468 and 421 nm at 20K. The 461nm line is probably from an excited J state and the group of lines near 453nm (22,170; 22,080; 21,880 cm$^{-1}$) probably correspond to transitions from the $^5I_8$ ground level to the $^5G_6$ level which give a strong set of lines between 22,290 cm$^{-1}$ and 22,064 cm$^{-1}$ in $LaCl_3$. As expected, the AgCl level lies 100 cm$^{-1}$ or so below the level in $LaCl_3$. Again by comparison with the spectrum observed in $LaCl_3$:$Ho^{3+}$ tabulated in Dieke[23], the 468nm (21,370 cm$^{-1}$)

line may arise from transitions from $^5I_8$ to $^3K_8$ and the line at 421nm

(23,750 cm$^{-1}$) may be $^5I_8$ to $^5G_5$ transitions.

The only line seen in the dysprosium spectrum was a broad low intensity

line in the infra-red at $1.30 \pm .01\mu$ with a possible smaller line at

$1.27 \pm .01\mu$. Measurements in the infra-red were not made at low temperatures

These lines would correspond to energies of 7,690 cm$^{-1}$ and 7,870 cm$^{-1}$

respectively. By comparison with LaCl$_3$:Dy$^{3+}$ they may be $^6H_{15/2}$ to $^6F_{11/2}$

transitions but the fit is not as clear as in the Ho$^{3+}$ and Er$^{3+}$ cases.

It is surprising that no other lines were seen and that the lines

which were observed did not become clearer at low temperatures. However,

as the oscillator strengths of these optical transitions are expected to

be low even in the low symmetry fields, a study using larger samples might

reveal other lines. Yb$^{3+}$ [26] and Dy$^{3+}$ [27] have been studied in NaCl

and KCl and in neither case was any optical absorption observed in the

visible. Local random strains in the lattice may prevent the lines in

AgCl from becoming narrower at 4.2K. A very much more lengthy study of

the optical absorption and luminescence would be needed to establish the

energy levels and crystal fields of the ions, but the results given here

do produce confirmation of the presence of Ho$^{3+}$ in AgCl and suggest that

an E.P.R. search at Q-band and at 4.2K or below would be worthwhile.

## 6.3    The palladium and platinum transition groups

Transition series ions with unfilled inner electron shells are

expected to give E.P.R. in certain valent states and, since these ions

are known chemically to have variable valencies, they are ions which

could take some part in electron or hole trapping in the silver-halide
lattice. The 4d and 5d series ions have not been studied in AgCl
previously. Their paramagnetic properties are similar to the iso-
electronic members of the 3d series. The main difference between the
two series is that the 4d and 5d ions tend to form strong covalent bonds
with the surrounding ligands and are usually in a strong crystal field
configuration[27]. Hund's rules no longer apply and the spin states of
the $d^4$, $d^5$, $d^6$ and $d^7$ ions are altered. $d^5$ and $d^7$ will both have $S = \frac{1}{2}$
whereas in weak fields spins of $S = \frac{5}{2}$ and $S = \frac{3}{2}$ are expected using Hund's
rules. The 4d and 5d ions have generally been incorporated in complex
covalent matrices and few results are reported for simple ionic lattices.
A number of these ions were added to AgCl by the methods described in
Chapter Three, and optical sensitivity tests were made by eye and in the
spectrophotmeter. E.P.R. was looked for in most of the samples and single
crystals were grown in some cases. The series will be discussed in
order of increasing numbers of d electrons in the atoms.

Samples doped with yttrium metal were clear or pale yellow and
brittle. They were not affected by annealing in chlorine or nitrogen
atmospheres and no E.P.R. was detected at temperatures from 300K to 4.2K
in polycrystalline samples. Lanthanum is a very unstable metal and
doping was not attempted. $Y^{2+}$ $(4d^1)$ is paramagnetic and resonance was
seen in $CaF_2$ at 20K after electron irradiation of $CaF_2:Y^{3+}$ [29]. The
chemically stable state of yttrium is trivalent and the divalent form is
unlikely to occur in AgCl. O'Connor and Chen[30] discuss the colouration
of $CaF_2:Y^{3+}$ by ionising radiation and observe that the presence of $Sm^{3+}$
prevents this colouration because $Sm^{3+}$ traps the electrons in preference
to $Y^{3+}$. It has already been shown that $Sm^{3+}$ will not reduce to $Sm^{2+}$
to AgCl and, from the evidence of $CaF_2$, $Y^{2+}$ is even less likely to form.

Zirconium and hafnium in metal form were added to AgCl and appeared to be incorporated in the crystals but gave no colouration nor any increase in photosensitivity. A single crystal containing zirconium gave no detectable E.P.R. at temperatures from 300K to 4.2K. The stable valent state of zirconium is $Zr^{4+}$ although divalent and trivalent halides are known[31]. Little is known about the chemistry of hafnium. $Ha^{2+}$ and $Zr^{2+}$ are likely to be harder to form than $Ti^{2+}$ since titanium is the first member of this subgroup and the valence of these ions in AgCl is probably 3+ or 4+. No E.P.R. has been definitely reported for hafnium or zirconium although $Zr^{3+}$ $(4d^1)$ is suggested to explain one of the resonance lines observed in Zirconia[32].

Niobium and tantalum metal appeared to dissolve in AgCl and gave cloudy white or colourless samples. No changes were observed on annealing the samples in chlorine or nitrogen atmospheres and no E.P.R. was detected from AgCl:Nb polycrystals at 300K and 77K, or from a single crystal of AgCl:Ta at 300K, 77K or 4.2K. The most common valent states of these ions are 3+ and 5+ and the trivalent state is thought most likely to form in AgCl and is not expected to be paramagnetic $(4d^2, 5d^2)$. Niobium dihalides are not known and $TaCl_2$ is unstable[31] and conversion to the divalent state in AgCl would not be expected. E.P.R. has been observed from $Nb^{4+}$ $(4f^1)$ and $Ta^{4+}$ $(5f^1)$ in $TiO_2$ at 4.2K[33]. The tetravalent state forms naturally in $TiO_2$:Ta and after oxidation of $TiO_2$:Nb samples. The 4+ states may not be formed in AgCl because of their triple excess charge in a monovalent lattice.

Molybdenum and tungsten metal appeared to dissolve in AgCl and gave clear or pale yellow samples which were not affected by annealing in chlorine or nitrogen. No E.P.R. was detected in polycrystalline

samples and a slight optical sensitivity in tungsten doped samples could be accounted for by the height of the $Fe^{3+}$ impurity E.P.R. signal. Molybdenum forms complex dihalides and trihalides and $WCl_2$ is known but is very easily oxidised. No simple ionic compounds are known[31]. Molybdenum and tungsten are found in 3+, 4+ and 5+ states but the trivalent state is thought most likely to be stable in AgCl. E.P.R. has been observed from $Mo^{3+}$ ($4d^3$) in $K_3InCl_3 \cdot 2H_2O$ [34] at 90K and 20K with $S = \frac{3}{2}$ and a zero-field splitting of more than $1$ $cm^{-1}$. If this state is formed in AgCl a single crystal would be needed to observe a resonance.

As the number of d electrons in the atom increases, higher valent states become more common. Technetium was not used as it is radioactive. Rhenium metal was added to AgCl and, as colourless samples, sometimes with visible black specks of metal were produced the rhenium metal may not dissolve in AgCl. No photosensitivity was found nor was any E.P.R. detected at 300K and 77K. The lowest valent state of rhenium is $Re^{3+}$ and this is probably the stable valence in AgCl. E.P.R. is not expected from $Re^{3+}$ ($5d^4$) but has possibly been seen from $Re^{4+}$ in $K_2PtCl_6$ at $4°K$ [35].

Ruthenium and Osmium metal were added to AgCl and gave colourless samples often with black specks of the metal or metal chloride. $RuCl_3$ is stable and black and $Ru^{3+}$ would be expected to be formed in AgCl since $Ru^{2+}$ does not usually occur. E.P.R. has been seen from $Ru^{3+}$ ($4d^5$) in $Al_2O_3$ at 20K with $g_{//} < 0.06$ and $g = 2.430$ [36] and in other compounds [34] and is always in the strong field ($S = \frac{1}{2}$) configuration. No E.P.R. was observed in a polycrystalline sample at 300K or 4.2K and it was thought that the ruthenium had not been successfully dissolved in the lattice since the samples were fairly soft to cut and colourless. No photo-sensitivity was observed from the ruthenium or osmium doped samples. No

E.P.R. has been reported from osmium and none was seen in AgCl:Os. Osmium is usually found in 4+ or higher valent states.

Rhodium has been studied in AgCl by Wilkens et al[37] who report no photosensitization and attribute a single line spectrum to $Rh^o$ ($4d^9$) and a broad background line to $Rh^+$ ($4d^8$). Iridium metal added to AgCl gave a pale yellow colour to the samples and the optical absorption in the visible showed some structure (fig. 6.2). The chief valent state of iridium is $Ir^{3+}$ ($5d^6$) which is not paramagnetic, although $Ir^{4+}$ ($5d^5$) is often formed. There are many reports of E.P.R. from $Ir^{4+}$ at 20K which usually shows clear ligand hyperfine structure[34]. However, since no E.P.R. was seen in AgCl, the iridium is probably present in the trivalent state. The energy levels of the excited states of an $(IrCl_6)^{3-}$ complex have been measured by Jørgensen and are quoted by Griffith[38]. They give two $^3T_1$ bands at 16,300 and 17,900 cm$^{-1}$ above the ground state ($^1A_1$) and a $^1T_1$ band at 24,100 cm$^{-1}$. The observed bands overlap and the peak positions are not clear. However, the absorption may be approximately resolved into two bands superimposed on the AgCl lattice absorption (fig.6.2b). The peak wavelengths are 550 ± 10nm (18,100 ± 300 cm$^{-1}$) and 415 ± 10nm (24,000 ± 500 cm$^{-1}$) which are compatible with the transitions quoted above.

Palladium and platinum were added to the silver chloride using the metal form. A current had to be used to dissolve platinum in the molten halide. Palladium doped samples were red when heavily doped and orange when lightly doped. The colour was often slightly paler after annealing in nitrogen and precipitation or a change in valent state may be taking place. Palladium can form 2+, 3+ and 4+ states. $PdCl_2$ exists as red crystals and is fairly stable up to 900K. Trivalent compounds are known
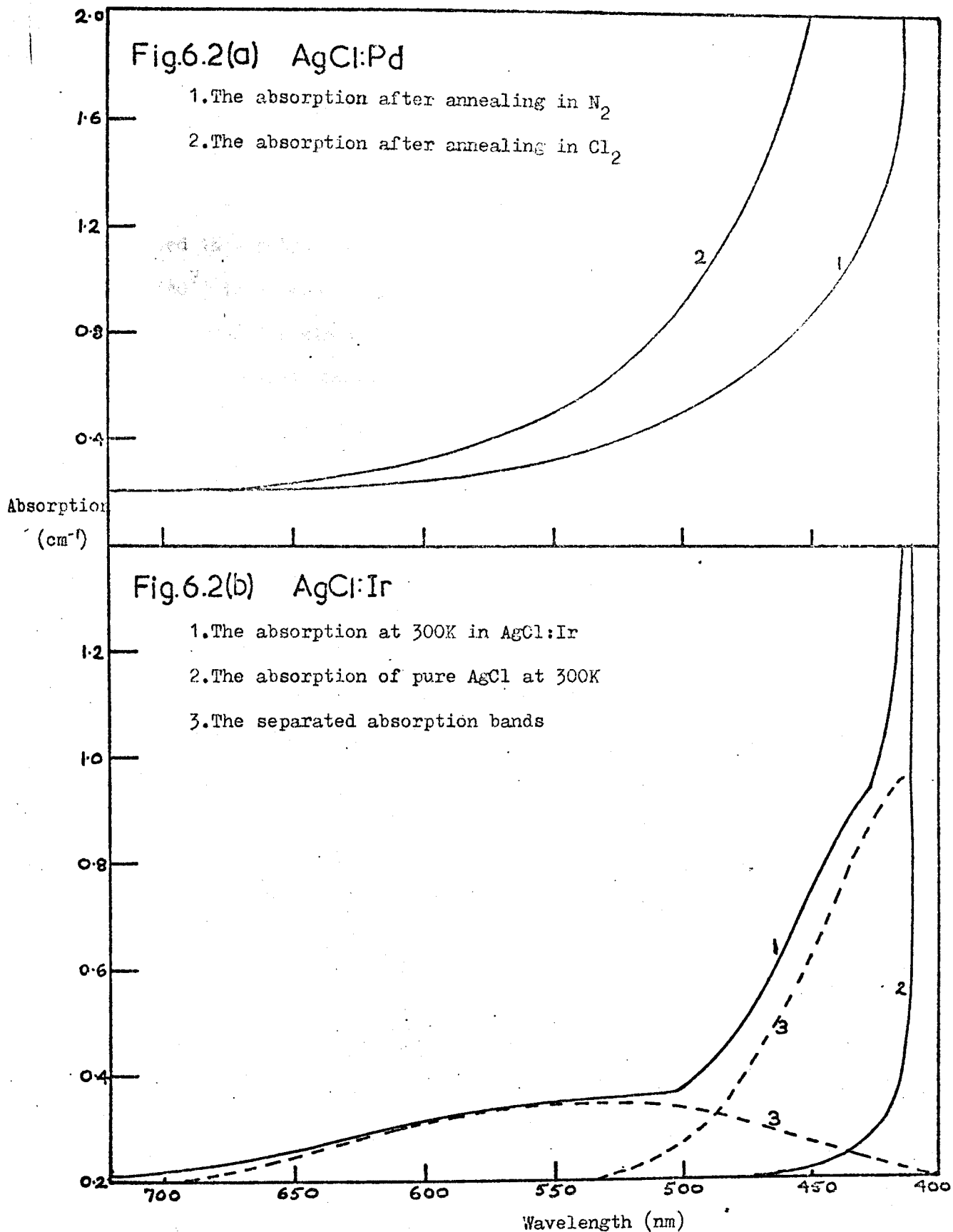
Fig. 6.2. The optical absorption of AgCl:Pd and AgCl:Ir .

but are not very stable, and both 3 and 4 valent states are strong

oxidising agents and convert easily to the divalent state or the metal.

$Pd^{2+}$ is thought to be the stable state in AgCl, and reduction to the

metal may take place when the samples are annealed in nitrogen. Palladium

gave no enhanced photosensitivity to the material and no E.P.R. was

observed in a polycrystalline sample at 300K, 77K or 4.2K. E.P.R. from

$Pt^{3+}$ ($4d^7$) in a strong crystal field has been reported in $Al_2O_3$[39] from

77K to 4.2K and a single isotropic line with g = 2.163 is observed. The

E.P.R. and optical absorption of $Pd^{2+}$ in KCl and KI has been reported[40].

The optical absorption and conductivity of the samples show that $Pd^{2+}$ is

present but the interpretation of the E.P.R. is not certain. The

resonance is a single, isotropic, broad line (half-width 50mT) with

g = 1.995 at 300K and 77K, with a superimposed hyperfine structure of

separation about 8mT. $Pd^{2+}$ ($4d^6$) is isoelectronic with $Ni^{2+}$ and the

theoretical behaviour of the resonance is not well known. However, an

anisotropic spectrum would be expected for both interstitial and

substitutional incorporation. The line observed in (40) may be due to

some precipitated or separate phase of $Pd^0$ or $Pd^{2+}$ and the six line

hyperfine structure could be due to manganese. In KI:Pd only the six

hyperfine lines are seen at room temperature[41]. The optical

absorption spectrum of AgCl:Pd shows no structure in the visible (fig.

6.2a) and it is probably the long wavelength tail of absorption bands

hidden in the lattice absorption below 410nm, similar to those seen in

KCl:Pd[40].


Platinum doped samples were orange in colour when prepared in a

chlorine atmosphere. Single crystals grown in vacuo were pale yellow and

reverted to an orange colour after annealing in chlorine. A prolonged

anneal in vacuo in contact with metallic silver was then needed to remove

the orange colour. No E.P.R. was detected in a single crystal at 300K or 4.2K. No increase in photolytic darkening was observed on exposure of a sample annealed in nitrogen, but a slight increase in the orange colour, particularly on the surface and grain boundaries, could be seen by eye. $PtCl_2$ can be made and is brown green in colour. $PtCl_3$ is thought to exist over a very limited temperature range (637-647K) and is green. $PtCl_4$ forms as reddish brown crystals[31]. The $Pt^{4+}$ state is usually considered to be the most stable valent state of platinum and the orange colour seen in AgCl may be due to this state. It is possible that $Pt^{2+}$ is formed after prolonged reduction. A resonance from $Pt^{3+}$ $(5d^7)$ has been seen below 120K in yttrium aluminium garnet[42] in orthorhombic sites. A resonance in $Al_2O_3$ which showed a static Jahn-Teller distortion at 4.2K and a dynamic splitting at 77K was assigned to $Pt^{1+}$ $(5d^9)$ or to $Pt^{3+}$ [36]. Resonance from the divalent or tetravalent states has not been reported.

Although none of the 4d and 5d group ions considered were found to give an increase in silver colloid production on exposure to blue light, some of the systems might be worthy of further investigation. AgCl:Ru should give E.P.R. from $Ru^{3+}$ if sufficient concentration of ruthenium can be incorporated, although photosensitization by hole trapping at $Ru^{2+}$ or $Ru^{3+}$ is not thought likely. The AgCl:Pd and AgCl:Pt systems can be studied optically since they give visible colouration to the specimens. Pd and Pt are adjacent to Ag and Au respectively in the transition series and have some similarities in chemical behaviour to the noble metals, although their ionic radii are much smaller. Further experiments on these systems in the light of the recent work on AgCl:Au[14] might be valuable.

## 6.4 References

1    K.R. Lea, M.J.M. Leask and W.P. Wolf,  J. Phys. Chem. Solids, 23, 1381 (1962).

2    A. Abragam and B. Bleaney,  Electron Paramagnetic Resonance of Transition Ions,  Clarendon Press, Oxford (1970).

3    W. Low,  J. Phys. Soc. Japan, 17, Supp.BI, 440 (1962).

4    M.J. Weber and R.W. Bierig,  Phys. Rev. 134, A1492 (1964).

5    J. Kirton,  Phys. Rev. 139, A1930 (1965).

6    P.A. Forrester and C.F. Hempstead,  Phys. Rev. 126, 923 (1962).

7    W. Low,  Phys. Rev. 134, A1479 (1964).

8    A.A. Antipin, I.N. Kurkin, L.D. Livanova, L.Z. Potvorova and L. Y.A. Shekun,  Sov. Phys. Sol. State, 7, 1271 (1965).

9    W.P. Wolf, M. Ball, M.T. Hutchings, M.J.M. Leask and A.F.G. Wyatt, J. Phys. Soc. Japan, Vol.17, Suppl. B-I, 443 (1962).

10   S.D. McLaughlan,  Phys. Lett. 20, 486 (1966).

11   J. M. Baker, W. Hayes and D.A. Jones,  Proc. Phys. Soc. (London) 73, 942 (1959).

12   F.H. Spedding and A.H. Daane,  The Rare Earths,  J. Wiley N.Y. (1961).

13   S.U. Cheema,  Ph.D. Thesis,  University of Warwick, 1970, and S.U. Cheema and M.J.A. Smith,  J. Phys. C., 4, 1231 (1971).

14   I.R. Edmunds,  Ph.D. Thesis,  University of Warwick, 1972.

15   C.E.K. Mees and T.H. James,  The Theory of the Photographic Process,  Macmillan N.Y. (1966).

16   Z.J. Kiss and P.N. Yocom,  J. Chem. Phys. 41, 1511 (1964).

17   J.W. Twidell,  J. Phys. Chem. Solids 31, 299 (1970).

18   P.F. Weller,  Inorg. Chem. 4, 1545 (1965).

19   P.F. Weller and J.E. Scardefield,  J. of Electrochem. Soc. 111, 1009 (1964).

20   W.M. Latimer,  Oxidation Potentials,  Prentice-Hall (1952).

21   I.U.K. Delimarskii and B.F. Markov,  Electrochemistry of Fused Salts,  The Sigma Press, Washington D.C. (1961).

22   H. Böttger,  Phys. Stat. Sol. 4, 669 (1964).

23    G.H. Dieke,  Spectra and Energy Levels of Rare Earth Ions in Crystals,  J. Wiley (1968).

24    J.W. Rakestraw and G.H. Dieke,  J. Chem. Phys. 42, 873 (1965).

25    C.W. Rector, B.C. Pandey and H.W. Moos,  J. Chem. Phys. 45, 171 (1966).

26    G.D. Sootha, T.C. Tripathi and S.K. Agarwal,  Phys. Stat. Sol. (b) 44, K61 (1971).

27    V.F.  issarenko and S.V. Voropaeva,  Phys. Stat. Sol. 15, K95 (1966).

28    J.H.E. Griffiths, J. Owen and I.M. Ward,  Proc. Roy. Soc. (London), A219, 526 (1953).

29    J.R. O'Connor and J.H. Chen,  Appl. Phys. Lett. 5, 100 (1964).

30    J.R. O'Connor and J.H. Chen,  Phys. Rev. 130, 179 (1963).

31    P.J. Durrant and B. Durrant,  Introduction to Advanced Inorganic Chemistry,  Longmans (1962), Chapter 24.

32    J.S. Thorp, A. Aypar and J.S. Ross,  J. Materials Sci. 7, 729 (1972).

33    P.F. Chester,  J. of Appl. Phys. 32, 866 (1961).

34    K.D. Bowers and J. Owen,  Rep. Prog. Phys. 18, 304 (1955).

35    J.W. Orton,  Rep. Prog. Phys. 22, 204 (1959).

36    S. Geschwind and J.P. Remeika,  J. of Appl. Phys. Suppl. to Vol.33, 370 (1962).

37    J. Wilkens, D.P. de Graag and J.N. Helle,  Phys. Lett.19, 178 (1965).

38    J.S. Griffith,  The Theory of Transition-Metal Ions,  C.U.P. (1964), page 425.

39    R. Lacroix, U. Höchli and K.A. Müller,  Helv. Phys. Acta. 37, 627 (1964).

40    S.C. Jain, S.K. Agarwal, G.D. Sootha and R. Chander,  J. Phys. C. 3, 1343 (1970).

41    G.D. Sootha,  T.C. Tripathi and D.C. Parashar,  Phys. Stat. Sol. (b) 48, K45 (1971).

42    J.A. Hodges, R.A. Serway and S.A. Marshall,  Phys. Rev. 151, 196 (1966).

Chapter Seven : <u>Conclusions</u>

The E.P.R. results presented in this thesis have established the lattice site of $Dy^{3+}$, $Er^{3+}$ and $Yb^{3+}$ in AgCl and of $Cr^{3+}$ in AgCl and AgBr. The symmetry of the resonances has been used to derive the probable arrangement of charge compensating silver cation vacancies at low temperatures. Tables 7.1 and 7.2 give the results obtained so far for the iron and rare earth transition series ions in silver chloride. There are very few results for the ions in silver bromide and these are not given in the tables. The lattice sites and symmetries found hitherto in AgBr are the same as those in AgCl. To make the comparisons more valid all the ionic radii are taken from the same source[13] and they are the radii appropriate to these ions in ionic lattices.

The information available on the behaviour of the 3d and 4f transition series in AgCl enables some general trends to be followed. The simple Coulombic binding energy of an impurity-vacancy complex will have the form
$$\frac{e^2}{4\pi\epsilon r} \qquad (14)$$
where e is the effective charge of impurity and vacancy, $\epsilon$ is the permittivity of the crystal, and r is the impurity-vacancy separation. The binding energy will be greatest for the least distance of approach. In Chapter Five it is argued that the vacancy will form in the nearest cation shell when possible but that the relaxation of the lattice around a small impurity ion will make the formation of a vacancy in the nearest cation shell more difficult.

Bassani and Fumi[15] have made a quantitative estimate of the binding energies of $Cd^{2+}$, $Ca^{2+}$ and $Sr^{2+}$ to a nearest cation vacancy in

NaCl and KCl. They use the Born and Mayer model for the ionic lattice and include the effect of electronic and displacement polarisation of the lattice about the centre. Tosi and Airoldi[16] have calculated binding energies for a next nearest cation vacancy. They show that polarisation of the halide ion between the impurity and the vacancy considerably increases the binding energy of this complex over its coulombic value. The results of the two papers[15,16] for $Sr^{2+}$ may be summarised as follows:

| Vacancy position | Binding energy (eV) | |
| --- | --- | --- |
| | KCl | NaCl |
| Nearest cation | 0.38 | 0.43 |
| Next nearest cation | 0.49 | 0.41 |

Ionic radii (Å)    $Sr^{2+}$ : 1.12    $K^+$ : 1.33    $Na^+$ : 0.97

The binding energies indicate that in KCl, where $Sr^{2+}$ may be considered to be a small ion, a next nearest cation (N.N.C.) vacancy is expected. In NaCl, where $Sr^{2+}$ is a comparatively large ion, the nearest cation (N.C.) vacancy is favoured. These deductions are confirmed by experiment and agree with the qualitative conclusions of Chapter Five.

The largest divalent ion in table 7.1 ($Eu^{2+}$) is associated with a N.C. vacancy as expected. The iron series ions are all smaller and are associated with N.N.C. vacancies. $Cu^{2+}$ is the only ion seen by E.P.R. to be partly associated with a N.C. vacancy which does not fit with the suggested pattern as $Cu^{2+}$ is a relatively small divalent ion. E.P.R. results for the transition metal impurities in the alkali halides have been reviewed by Sootha and Agarwal[17]. Only the spectra for $V^{2+}$, $Cr^{2+}$ and $Mn^{2+}$ in NaCl have been analysed. The radius of $Na^+$ is 0.97Å as compared to 1.27 for $Ag^+$ and so $V^{2+}$, $Cr^{2+}$ and $Mn^{2+}$ will be relatively large in NaCl. Nearest vacancy association is observed for all three ions in NaCl.

All the trivalent ions in AgCl give more complex spectra than the divalent ions. The special case of iron, which is incorporated in an interstitial position, is discussed in section 4.8.5. Thermal depolarisation currents (T.D.C.) and E.P.R. results suggest that the substitutional ions are present in several different centres. There are numerous possible arrangements of two vacancies within the first two cation shells and these are listed in fig. 4.13. The binding energies of some of these arrangements must be comparatively close in value. A difference of only 0.02eV will result in populations in the ratio $10^4$:1 at 95K. An increase in the probability of a nearest cation vacancy association with increasing ionic radius was noted for the rare earths. Although there are fewer results available for the trivalent 3d ions the pattern may again be present within this series and would predict two N.C. vacancies as the likely arrangement for $Ti^{3+}$, As shown below, this is compatible with the dielectric loss measurements, which also suggest two N.C. vacancies for $Eu^{3+}$.

The values in tables 7.1 and 7.2 for the activation energy for jumping of the vacancy around the impurity $(E_a)$ and the binding energy of the complex $(E_b)$ are restricted to those obtained from E.P.R. measurements. Vacancy association models and values for $E_a$ may be obtained from T.D.C.[3] and dielectric loss[18,19] experiments. The T.D.C. peak temperatures and related $E_a$ values are given in table 7.3 with the values for $E_a$ and $E_b$ obtained from dielectric loss measurements. Watkins[20] has shown for $Mn^{2+}$ in NaCl that the E.P.R. and electrical results are in agreement and Edmonds[19] has discussed the relation between the different measurements in the silver halides.

The analysis of electrically active relaxation modes is relatively simple for the divalent impurities associated with a single vacancy. The

reorientations affecting the electrical measurements are taken to be those which preserve the symmetry of the site. For example, a N.N.C. vacancy jumping to a N.C. site and then to a new N.N.C. site. An E.P.R. fine structure line may be broadened by any vacancy jump which temporarily or permanently alters the local crystal field. The temperatures at which line broadening is observed in AgCl (typically 250-350K) are higher than the temperatures involved in T.D.C. and dielectric loss. There may be considerable jumping of the vacancies to more distant cation shells at the higher temperatures. The activation energy for motion of an unassociated vacancy is $0.39eV$[21]. Motion of the vacancy around the impurity is usually found to have a lower activation energy and is assumed to be the predominant line broadening mechanism.

The measurements of Kunze and Muller[3] in table 7.3 show that a N.C. vacancy is expected to have a value for $E_a$ of $0.30 \pm 0.05eV$ and a N.N.C. vacancy a value of $0.35 \pm 0.05eV$. The N.N.C. vacancy has the higher activation energy as it can only jump via an intermediate N.C. or more distant cation position. The T.D.C. results are in reasonable agreement with the E.P.R. values for the divalent ions. The $E_a$ results for $Cu^{2+}$ and $Eu^{2+}$ are unusually low. The $Cu^{2+}$ value is not accurate as it was determined from a single line width and temperature correlation. $E_a$ for $Eu^{2+}$ found from a plot of excess line width against temperature has an error quoted and the low value is probably due to the relatively large ionic radius.

Analysis of the vacancy jumps for the trivalent ions associated with two vacancies is difficult. Kunze and Muller have discussed their results for $Ti^{3+}$, $V^{3+}$ and $Cr^{3+}$ in AgCl and predict the $Cr^{3+}$ centre described in Chapter Four. The subsidiary orthorhombic $AgCl:Cr^{3+}$ centre

has $E_a = 0.32 \pm 0.04$eV which is reasonable for a centre involving two N.C. vacancies. A similar value (0.33eV) is found for $Eu^{3+}$ [19] by dielectric loss measurements and suggests that $Eu^{3+}$ is associated with two N.C. vacancies. The single T.D.C. peak obtained for $Ti^{3+}$ is at a temperature typical for a N.C. vacancy jump. It is suggested that this ion also associated with two N.C. vacancies which are arranged in a line thus giving the single reorientation peak.

The low $E_a$ value for the principal $Cr^{3+}$ centre found in E.P.R. and dielectric loss is almost certainly caused by motion of the N.C. vacancy around the line joining $Cr^{3+}$ to the N.N.C. vacancy. The presence of the second vacancy evidently makes this movement easier than for a single N.C. vacancy. The high $E_a$ value (0.41 $\pm$ 0.04eV) found for the tetragonal centre is similar to the value found for the smaller dielectric loss peak[19]. This peak is thought to be due to simultaneous motion of both of the vacancies of the principal centre[3]. It may be that the energy barrier is dominated by the movement of the N.N.C. vacancy, which will also be involved in broadening of the tetragonal centre lines.

The dielectric loss curves[19] show two peaks for $AgBr:Cr^{3+}$, with $E_a = 0.34$ and 0.25eV, but with slightly different relative sizes as compared to the $AgCl:Cr^{3+}$ peaks. Edmonds[19] has suggested that the principal centre present in $AgBr:Cr^{3+}$ is not the same as that in $AgCl:Cr^{3+}$. The E.P.R. spectra of $Cr^{3+}$ in the two halides show the same symmetry, but the relative sizes of D and E are very different. The analysis of Tosi and Airoldi[16] shows that a N.N.C. vacancy will have a greater binding energy in AgBr than in AgCl because of the greater polarisability of the $Br^-$ ion. It is possible that in AgBr both vacancies are in the N.N.C. shell. However, the low symmetry of the E.P.R. and the two

dielectric loss peaks can only be explained if the two vacancies are not exactly in the true cation sites.

Few measurements of $E_b$ are available from E.P.R. studies. $E_b$ is difficult to estimate as measurements of line intensities over a range of temperatures, where line broadening may also be taking place, are involved. $E_b$ may also be estimated from conductivity results provided that an activation energy for vacancy motion in the lattice is assumed. It can be noted that $E_b$ for $Cr^{3+}$ to the first vacancy is unusually low. Ulrici[2] has commented that the remaining vacancy must effectively compensate for more than one excess charge on the $Cr^{3+}$ ion. The conductivity value of $E_b$ for AgCl:Eu probably applies to $Eu^{3+}$. The $Eu^{2+}$ spectrum[9] shows relatively few associated ions at room temperature which indicates a value of $E_b$ close to 0.20eV as in AgCl:$Cu^{2+}$.

None of the ions studied in detail in the thesis significantly enhanced the photosensitivity of AgCl or AgBr. The chemical properties of the rare earths are used to show that only europium will be present in the divalent state in AgCl. The oxidation potentials of europium also show that $Eu^{2+}$ will readily accept a positive hole, and that $Eu^{3+}$, once formed, will be reluctant to trap an electron. The low activation energy for jumping of the vacancy at room temperature may be significant in more effectively neutralising the excess positive charge so that a hole approaching from any direction can be trapped at the $Eu^{2+}$ ion.

Of the 3d ions $Cu^+$ increases the silver colloid formation markedly and $Fe^{2+}$ is a less effective sensitizer. The chemical properties of the elements will not, on their own, explain why these two ions act as sensitizers. In contrast to the rare earths the iron series form numerous

valent states. Titanium, manganese and cobalt are only found in one valent state in the silver halides ($Ti^{3+}$, $Mn^{2+}$, $Co^{2+}$) and probably do not take part in the photographic process. Nickel is believed to form $Ni^+$ after irradiation at low temperatures[22] but $Ni^{2+}$ is chemically the usual valent state and at room temperature nickel probably remains divalent on exposure. Chromium and vanadium, however, readily form divalent and trivalent states and are thought to act as centres for recombination of electrons and holes on exposure to light[12]. The photosensitivity of $Cu^+$ and $Fe^{2+}$ cannot be explained on the basis of oxidation potentials[22] as these show that $Cu^{2+}$ and $Fe^{3+}$ are less likely to form than $V^{3+}$ and $Cr^{3+}$. $V^{2+}$ and $Cr^{2+}$ are, therefore, expected to be the better hole traps.

An explanation probably lies in the relative abilities of the higher valent states to trap an electron and return to the original valent state. In this respect $Fe^{3+}$ is unusual as it jumps into an interstitial site associated with four silver ion vacancies at room temperature. This complex is probably very stable and the number and distribution of negative vacancies surrounding the ion make electron trapping unlikely. The stability of $Cu^{2+}$ with respect to electron trapping is harder to explain. However, copper is the last member of the transitions series and can be considered as a noble metal. Copper may, therefore, have slightly unusual chemical properties as compared to the remainder of the series. It forms a stable monovalent state, unlike the other 3d ions, and the divalent state produced after trapping a hole has only to be compensated by one cation vacancy. The relatively low activation energy of the associated vacancy may result in fast vacancy motion around the $Cu^{2+}$ ion at room temperature and effective neutralisation of the cupric ion to the approach of an electron.

The properties of some $4d$ and $5d$ ions in silver chloride are also discussed. None of these ions are observed to sensitize the halide to the formation of silver colloid. Some impurities gave optical absorption in the visible (Pt, Pd, Ir) and some changes in valent state were thought to be taking place.

## Table 7.1

### Divalent impurities in AgCl

| Ion | Lattice site | Cation vacancy association at low temperatures | $E_a$(eV) (E.P.R.) | $E_b$(eV) (E.P.R.) | Ionic Radius (Å) | References |
|-----|------|------|------|------|------|------|
| $V^{2+}$ | S | N.N.C. | $0.30 \pm 0.05$ | - | 0.88 | 1 |
| $Cr^{2+}$ | $S^a$ | N.N.C.[b] | - | - | 0.89 | 2,3 |
| $Mn^{2+}$ | S | N.N.C. | $0.29 \pm 0.05$ | $0.42 \pm 0.05$ | 0.80 | 4 |
| $Fe^{2+}$ | S | N.N.C. | 0.35 | - | 0.74 | 5 |
| $Co^{2+}$ | S | N.N.C. | - | - | 0.72 | 6 |
| $Ni^{2+}$ | S | N.N.C.[c] | - | - | 0.69 | 7 |
| $Cu^{2+}$ | S | 70% N.N.C. 15% N.C. | 0.18 | 0.20 | 0.72 | 8 |
| $Eu^{2+}$ | S | N.C. | $0.22 \pm 0.05$ | - | 1.09 | 9 |

Radius of $Ag^+$ : 1.26Å.

$E_a$ represents the activation energy for reorientation of the impurity-vacancy dipole.

$E_b$ represents the impurity-vacancy binding energy.

S :  substitutional lattice site.

I :  interstitial lattice site.

a :  inferred from optical absorption curves.

b :  inferred from T.D.C. measurements.

c :  isotropic spectra from unassociated ions are also seen.

## Table 7.2

### Trivalent impurities in AgCl

| Ion | Lattice site | Cation vacancy association at low temperatures | $E_a(eV)$ (E.P.R.) | $E_b(eV)$ (E.P.R.) | Ionic Radius (Å) | References |
|---|---|---|---|---|---|---|
| $Ti^{3+}$ | $S^a$ | Two N.N.C. or [b] Two N.C. in a line | - | - | 0.76 | 2,3 |
| $V^{3+}$ | $S^a$ | N.N.C. & N.C.[b] | - | - | 0.74 | 2,3 |
| $Cr^{3+}$ | S | 80%: N.N.C. & N.C. at 135° | $0.21 \pm 0.04$ | $0.18 \pm 0.05$ | 0.63 | 2,3,10 |
| | | 10%: Two N.C. at 90° or 180° | $0.32 \pm 0.04$ | | | |
| | | 5% : Two N.N.C. at 180° | $0.41 \pm 0.04$ | | | |
| $Fe^{3+}$ | I | $(FeCl_4)^-$ complex | - | - | 0.64 | 11 |
| $Gd^{3+}$ | S | Complex | | | 0.94 | 12 |
| $Dy^{3+}$ | S | Two N.C. at 90° or 180° | - | - | 0.91 | 10 |
| $Er^{3+}$ | S | 70%: Two N.C. at 120° | - | - | 0.88 | 10 |
| $Yb^{3+}$ | S | 65%: Two N.N.C. at 90° or or 180°[c] | - | - | 0.86 | 10 |

## Table 7.3

### Electrical measurements[1,9]

| AgCl: | $E_a$ (dielectric loss) (eV) | $E_b$ (conductivity) (eV) | |
|---|---|---|---|
| $Cr^{2+}$ | $0.30 \pm 0.02$ | 0.28 | 0.08 |
| $Cr^{3+}$ | $0.34 \pm 0.02$ <br> $0.25 \pm 0.02$ | 0.41 | 0.08 |
| $Eu^{2+}$ ) <br> $Eu^{3+}$ ) | $0.30 \pm 0.02$ | 0.38 | 0.08 |

| AgBr: | | | |
|---|---|---|---|
| $Cr^{2+}$ | $0.34 \pm 0.02$ | 0.26 | |
| $Cr^{3+}$ | $0.34 \pm 0.02$ <br> $0.25 \pm 0.02$ | 0.32 | |

### Thermal depolarisation currents[3]

| Ion | Temperature of principal maximum (K) | $E_a$ (eV) | Temperature of subsidiary maxima | $E_a$ (eV) |
|---|---|---|---|---|
| $V^{2+}$ | 113.2 | 0.34 | 101.8 | 0.29 |
| $Cr^{2+}$ | 113.2 | 0.34 | 106.5 | 0.30 |
| $Mn^{2+}$ | 111.0 | 0.31 | 105.1 | 0.29 |
| $Fe^{2+}$ | 111.4 | 0.34 | 103.6 | 0.27 |
| $Co^{2+}$ | 113.2 | 0.35 | 101.8 | 0.29 |
| $Ni^{2+}$ | 113.1 | 0.34 | - | - |
| $Ti^{3+}$ | 103.5 | - | | |

$V^{3+}$ peaks at 99.5, 109.0, 117.5 with intensity ratio 1:2:1.

$Cr^{3+}$ peaks at 99.0 and 117.5 with intensity ratio 2:1.

## References

1    S.U. Cheema and M.J.A. Smith,   J. Phys. C., 2, 1751 (1969).

2    W. Ulrici,   Phys. Stat. Sol., 27, 333 and 489 (1968).

3    I. Kunze and P. Müller,   Phys. Stat. Sol., 33, 91 (1969),
     and ibid., 38, 271 (1970).

4    M. Daehler,   Ph.D. Thesis, University of Wisconsin (1962).

5    D.H. Lindley and P.G. Debrunner,   Phys. Rev., 146, 199 (1966).

6    T.R. Sliker,   Phys. Rev., 130, 1749 (1963).

7    M. Höhne, M. Stasiw and A. Wattesich,   Phys. Stat. Sol., 34,
     319 (1969).

8    R.F. Tucker,   Phys. Rev., 112, 725 (1958).

9    S.U. Cheema and M.J.A. Smith,   J. Phys. C., 4, 1231 (1971).

10   This thesis.

11   W. Hayes, J.R. Pilbrow and L.M. Slifkin,   J. Phys. Chem. Solids,
     25, 1417 (1964).

12   S.U. Cheema,   Ph.D. Thesis, University of Warwick (1970).

13   Handbook of Chem. and Phys., The Chemical Rubber Co., Cleveland,
     Ohio (1969).

14   M.P. Tosi and F.G. Fumi,   Nuovo Cimento 7, 95 (1958).

15   F. Bassani and F.G. Fumi,   Nuovo Cimento 11, 274 (1954).

16   M.P. Tosi and G. Airoldi,   Nuovo Cimento 8, 584 (1958).

17   G.D. Sootha and S.K. Agarwal,   Phys. Stat. Sol. (a) 5, 293 (1971).

18   H. Böttger,   Phys. Stat. Sol., 4, 669 (1964).

19   I.R. Edmonds,   Ph.D. Thesis, University of Warwick (1972).

20   G.D. Watkins,   Phys. Rev., 113, 91 (1959).

21   P. Suptitz and J. Teltow,   Phys. Stat. Sol., 23, 9 (1967).

22   W.M. Latimer,   Oxidation Potentials,   Prentice-Hall.

## Appendix I

A calculation of the matrix elements and the relative energy levels of an $S=3/2$ ion with the spin Hamiltonian :

$$H_s = g\beta\underline{B}\cdot\underline{S} + D\left[S_z^2 - 1/3S(S+1)\right] + E(S_x^2 - S_y^2) + K(S_xS_y + S_yS_x)$$

The calculation will use the operators $S_+$, $S_-$ where

$$S_+ = S_x + iS_y \quad \text{and} \quad S_- = S_x - iS_y .$$

Therefore

$$S_x = 1/2 (S_+ + S_-) \quad \text{and} \quad S_y = -i/2 (S_+ - S_-)$$

The Hamiltonian will have off diagonal elements of $g\beta\underline{B}\cdot\underline{S}$ if the usual base states $|3/2,3/2\rangle$, $|3/2,1/2\rangle$, $|3/2,-1/2\rangle$, $|3/2,-3/2\rangle$, are used. The Hamiltonian may be made diagonal in $g\beta\underline{B}\cdot\underline{S}$ by rotating the axes so that Z is parallel to the external magnetic field but is not parallel to the crystal field Z axis.[1]

Perturbation theory may then be used if $D, E \ll B_o$ and then

$$H_s = H_o + H_1 \quad \text{where } H_o = g\beta\underline{B}\cdot\underline{S}$$

and 
$$\begin{aligned} H_s\psi_n &= H_o\psi_n^o + H_1\psi_n^o \\ &= E_n^o\psi_n^o + H_1\psi_n^o \end{aligned} \quad \text{where } \psi_n^o \text{ are the usual base states .}$$
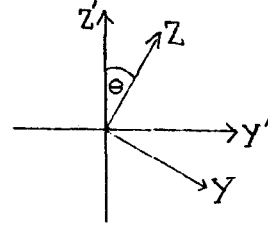
The eigenvalues, correct to second order, are

$$E_n = E_n^o + E_n^1 + \sum_{m\neq n} \frac{|H_{nm}|^2}{E_n^o - E_m^o}$$

where $E_n^1$ are the diagonal matrix elements of $H_1$ .

**(1). The external magnetic field in the (ZY) plane.**

The transformation of the Hamiltonian from the crystal field axes $Z', Y', X'$, to the new axes $Z, Y, X$, is made using the following substitutions :

$$S_{x'} = S_x$$
$$S_{y'} = S_y \cos\theta + S_z \sin\theta$$
$$S_{z'} = S_z \cos\theta - S_y \sin\theta$$

The Hamiltonian becomes

$$H = g\beta B S_z + D\left[S_y^2 \sin^2\theta + S_z^2 \cos^2\theta - (S_y S_z + S_z S_y)\sin\theta\cos\theta\right] - \frac{D}{3}S(S + 1)$$
$$+ E\left[-S_y^2 \cos^2\theta - S_z^2 \sin^2\theta - (S_z S_y + S_y S_z)\sin\theta\cos\theta + S_x^2\right]$$
$$+ K\left[(S_x S_y + S_y S_x)\cos\theta + (S_x S_z + S_z S_x)\sin\theta\right]$$

The following matrix is obtained using the usual base states.

|  | $\left\|+\frac{3}{2}\right\rangle$ | $\left\|+\frac{1}{2}\right\rangle$ | $\left\|-\frac{1}{2}\right\rangle$ | $\left\|-\frac{3}{2}\right\rangle$ |
|---|---|---|---|---|
| $+\frac{3}{2}\rangle$ | $\frac{3}{2}g\beta B$ $+\frac{D}{2}(3\cos^2\theta - 1)$ $-3\frac{E}{2}\sin^2\theta$ | $-\sqrt{3}i(D + E)\sin\theta\cos\theta$ $+\sqrt{3}K\sin\theta$ | $-\sqrt{3}\frac{D}{2}\sin^2\theta$ $+\sqrt{3}\frac{E}{2}(1 + \cos^2\theta)$ $+\sqrt{3}iK\cos\theta$ | $0$ |
| $+\frac{1}{2}\rangle$ | $\sqrt{3}i(D + E)\sin\theta\cos\theta$ $+\sqrt{3}K\sin\theta$ | $\frac{1}{2}g\beta B$ $-\frac{D}{2}(3\cos^2\theta - 1)$ $+3\frac{E}{2}\sin^2\theta$ | $0$ | $-\sqrt{3}\frac{D}{2}\sin^2\theta$ $+\sqrt{3}\frac{E}{2}(1 + \cos^2\theta)$ $+\sqrt{3}iK\cos\theta$ |
| $-\frac{1}{2}\rangle$ | $-\sqrt{3}\frac{D}{2}\sin^2\theta$ $+\sqrt{3}\frac{E}{2}(1 + \cos^2\theta)$ $-\sqrt{3}iK\cos\theta$ | $0$ | $-\frac{1}{2}g\beta B$ $-\frac{D}{2}(3\cos^2\theta - 1)$ $+3\frac{E}{2}\sin^2\theta$ | $\sqrt{3}i(D + E)\sin\theta\cos\theta$ $-\sqrt{3}K\sin\theta$ |
| $-\frac{3}{2}\rangle$ | $0$ | $-\sqrt{3}\frac{D}{2}\sin^2\theta$ $+\sqrt{3}\frac{E}{2}(1 + \cos^2\theta)$ $-\sqrt{3}iK\cos\theta$ | $-\sqrt{3}i(D + E)\sin\theta\cos\theta$ $-\sqrt{3}K\sin\theta$ | $-\frac{3}{2}g\beta B$ $+\frac{D}{2}(3\cos^2\theta - 1)$ $-3\frac{E}{2}\sin^2\theta$ |

The separations between the energy levels, correct to second order, are

$$E_1 - E_2 = g\beta B + D(3\cos^2\theta - 1) - 3E\sin^2\theta + \frac{6[(D + E)^2\sin^2\theta\cos^2\theta + K^2\sin^2\theta]}{g\beta B}$$

$$E_2 - E_3 = g\beta B - \frac{6[(D + E)^2\sin^2\theta\cos^2\theta + K^2\sin^2\theta]}{g\beta B}$$

$$+ \frac{3[\{-D\sin^2\theta + E(1 + \cos^2\theta)\}^2 + 4K^2\cos^2\theta]}{4g\beta B}$$

$$E_3 - E_4 = g\beta B - D(3\cos^2\theta - 1) + 3E\sin^2\theta + \frac{6[(D + E)^2\sin^2\theta\cos^2\theta + K^2\sin^2\theta]}{g\beta B}$$

Spin resonance transitions will take place when $\triangle E = h\nu$ where $\nu$ is the microwave frequency used. The substitution $B_o = \frac{h\nu}{g\beta}$ is used in which $g\beta$ is the spin magnetic moment of the ion. For $D, E \ll B_o$ the transition field B appearing in the denominator of the second order term can be replaced by $B_o$ correct to second order of $\frac{D}{B}$. The resonant fields obtained are given in section 4.4.1.

These expressions may be compared with those given by Codling and Henderson from calculations of Low[2]. For the external magnetic field confined to the (ZY) plane the angles $\theta'$ and $\gamma$ used by (2) are related to $\theta$ by

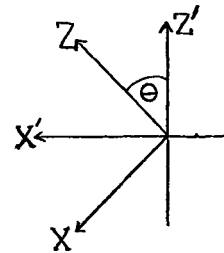$$\theta' = \theta \quad , \quad \text{and} \quad \gamma = 90^o \ .$$

If I = 0 and K is zero these expressions agree with those of reference (2).

(2) For the magnetic field in the (ZX) plane the transformations are

$$S_{x'} = S_x\cos\theta + S_z\sin\theta$$

$$S_{y'} = S_y$$

$$S_{z'} = -S_x\sin\theta + S_z\cos\theta$$

and the angles for comparison with reference (2) are $\theta' = \theta$ and $\gamma = 0^o$. The calculation proceeds as above to give the resonant fields quoted in section 4.4.1.

(3) For the magnetic field in the (XY) plane the transformations are
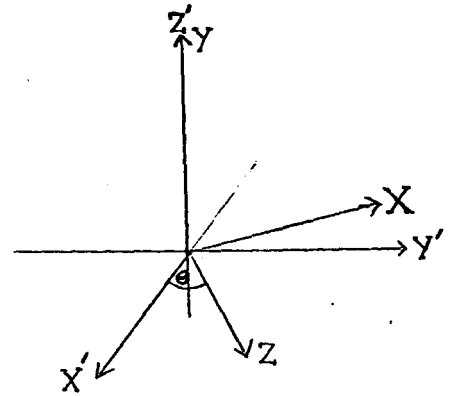
$$S_{x'} = -S_x \sin\theta + S_z \cos\theta$$

$$S_{y'} = S_x \cos\theta + S_z \sin\theta$$

$$S_{z'} = S_y$$

and the angles for comparison with

reference (2) are $\qquad \theta = 90^{\circ}$

$$\gamma = \theta$$

The calculation proceeds as before to give the resonant fields quoted

in section 4.4.1.

References

1. J.W. Orton, Electron Paramagnetic Resonance, Iliffe (1968).

2. A.J.B. Codling and B.Henderson, J. Phys. C. 4, 1242 (1971).

## Appendix II

A calculation of the crystal field potential for a centre in which a trivalent impurity ion is associated with a next nearest cation vacancy and a nearest cation vacancy. The lines joining the vacancies to the impurity ion are at an angle of $135^{\circ}$.

(1) The cubic field potential.

The origin of the coordinates is taken as the impurity ion. The potential at a general point $(x,y,z)$ due to the nearest neighbour halogen ion, $A$, of charge $e$ is

$$V_A = \frac{e}{(r^2 + a^2 - 2ax)^{\frac{1}{2}}}$$

where $r^2 = x^2 + y^2 + z^2$ .
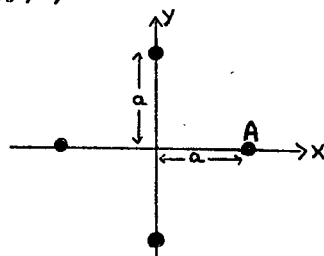
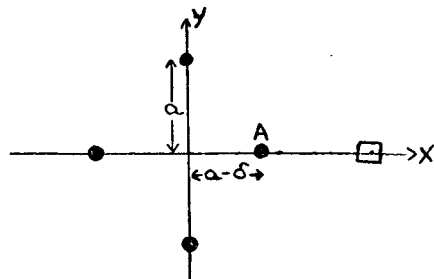The other halogen ions will give similar expressions in $-x, \pm y, \pm z$. A binomial expansion of $V$ in powers of $\frac{x}{a}$ is made and is valid for $x \ll a$. For 3d ions only the terms up to 4th order in x are needed.

(2) The effect of a next nearest cation vacancy.

The potential due to the halide ion A which is displaced by $\delta$ towards the impurity ion is given by

$$V_A = \frac{e}{(r^2 + b^2 - 2bx)^{\frac{1}{2}}}$$

where $b = a - \delta$ .

The potential due to A, and due to the other halide ions which are assumed to be undisplaced, is expanded in powers of $\frac{a}{x}$ and $\frac{b}{x}$ . The terms quadratic in x are not present in the cubic field potential and give rise to terms in $s^2$ in the Spin Hamiltonian.

The tetragonal potential due to the displacement of

A is $\qquad$ $V_T = \dfrac{3e(3x^2 - r^2)}{2a^3}\eta$ $\qquad$ where $\eta = \dfrac{\delta}{a}$

The potential due to the effective negative charge of the vacancy is

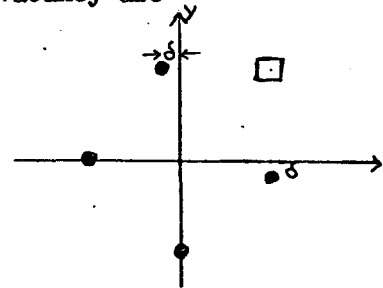$$V_\square = \dfrac{e}{(r^2 + 4a^2 - 4ax)^{\frac{1}{2}}}$$

Expanding and collecting quadratic terms gives

$$V_\square = \dfrac{3e}{16a^3}\left(x^2 - \dfrac{1}{3}r^2\right)$$

(3) The effect of a nearest cation vacancy.

The two halide ions nearest to the vacancy are

displaced by $\delta$. The potential due to A is given by

$$V_A = \dfrac{e}{\left[(a - x)^2 + (y + \delta)^2 + z^2\right]^{\frac{1}{2}}}$$

The ion B will give a similar expression and

after expanding the quadratic part of the potential due to A and B is

$$V_{A,B} = \dfrac{e}{a^3}(-6xy\,\varepsilon) \quad \text{where } \varepsilon = \dfrac{\delta}{a}$$

The potential due to the negative charge of the vacancy gives a

quadratic contribution

$$V_\square = \dfrac{e}{\sqrt{2}a^3}\left[\dfrac{-r^2}{4} + \dfrac{3}{8}(x + y)^2\right]$$

(4)The combined effect of the two vacancies.

The potentials given in (2) and (3) are written in the form suitable to the positions of the vacancies shown in the diagram. A combination of the quadratic potentials gives
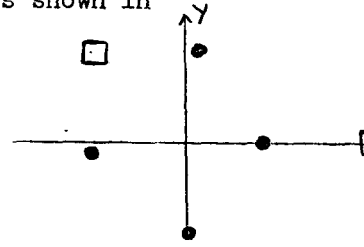
$$V = \frac{e}{16a^3} (3 + 72\,\Omega)(x^2 - \frac{r^2}{3}) + \frac{e}{a^3}\, 6\,\varepsilon\,(xy)$$
$$+ \frac{3e}{8\sqrt{2}a^3}\left[\frac{-2r^2}{3} + (y - x)^2\right]$$

The potential can be expressed in the form of the spin Hamiltonian :

$$V = D'(z^2 - \frac{r^2}{3}) + E'(x^2 - y^2) + K'(xy)$$

and then
$$D' = -\left[\frac{3e}{8\sqrt{2}a^3} + \frac{e}{32a^3}(3 + 72\,\Omega)\right]$$

$$E' = \frac{e}{32a^3}\,(3 + 72\,\Omega)$$

$$K' = \frac{e}{a^3}6\,\varepsilon - \frac{6e}{8\sqrt{2}a^3}$$